Compliant Aerial Manipulation

Author Alejandro Suárez Fernández-Miranda

Supervisors Professor Aníbal Ollero Baturone

Professor José Guillermo Heredia Benot

University of Seville, Spain – July 2018

Compliant Aerial Manipulation

PhD Thesis Dissertation

Alejandro Suárez Fernández-Miranda

Supervisors
Professor Anibal Ollero Baturone
Professor José Guillermo Heredia Benot

University of Seville, Spain – July 2018

Tesis Doctoral: Compliant Aerial Manipulation

Autor: Alejandro Suárez Fernández-Miranda
Directores: Aníbal Ollero Baturone
José Guillermo Heredia Benot

El tribunal nombrado para juzgar la Tesis arriba indicada, compuesto por los siguientes doctores:

Presidente

Vocales

Secretario

Acuerdan otorgar la calificación de:

El secretario del Tribunal

Fecha

Index

Abstract iii
Resumen v
Acknowledgment vii
List of figures ix
List of tables xvii
Acronyms xix
Symbols xxi

1. Introduction

1.1. Aerial manipulation 1
1.2. Design and development of aerial manipulators 1
1.3. Applications of aerial manipulators 4
1.4. Bimanual aerial manipulation 6
1.5. Compliance 7
1.6. Scope of this work 9
1.7. Contributions of this work 12
1.8. List of publications 17
1.9. Organization of this thesis 18

2. Design and development of lightweight and compliant aerial manipulators

2.1. Design requirements in aerial manipulation 19
2.2. Compliant joint: design and mechanics 21
2.3. Lightweight and compliant joint arm prototypes 23
2.4. Compliant and lightweight anthropomorphic finger module 29
2.5. Lightweight and human-size dual arm aerial manipulator 31
2.6. Anthropomorphic, compliant and lightweight dual arm 38
2.7. Long reach aerial manipulators 47
2.8. Conclusion 54

3. Functionalities of lightweight and compliant aerial manipulators

3.1. Benefits of mechanical joint compliance 55
3.2. Payload mass estimation with compliant joint arm 58
3.3. Passive/active compliance in compliant manipulators 59
3.4. Soft collision detection and contact-based obstacle localization 60
3.5. Monitoring force/displacement in grabbing situations 61
3.6. Operations with dual arm aerial manipulator 62
3.7. Functionalities of flexible link long reach aerial manipulators 64
3.8. Conclusion 70

4. Modelling, estimation and control of compliant aerial manipulators

4.1. Considerations and notation 71
4.2. Compliant joint dynamics and control 74
4.3. Force/position control in 3-DOF compliant arm 79
4.4. Position-force control in compliant finger module 82
4.5. Lightweight and human-size dual arm aerial manipulator 85
4.6. Anthropomorphic, compliant and lightweight dual arm 92

4.7. Flexible link, long reach aerial manipulators **102**
4.8. Conclusion **109**

5. Experimental results with compliant joint manipulators (single arm)

5.1. Compliant joint: identification, estimation and control **111**
5.2. Compliant joint arm with compliant finger module **113**
5.3. Passive/active compliance and payload mass estimation **116**
5.4. Control, grasping, and detection with compliant finger module **121**
5.5. Long reach aerial manipulator in passive pendulum configuration **124**
5.6. Conclusion **129**

6. Experimental results with dual arm aerial manipulators

6.1. Lightweight and human-size dual arm aerial manipulator **131**
6.2. Flexible long reach link with lightweight dual arm **138**
6.3. Anthropomorphic, compliant and lightweight dual arm **142**
6.4. Long reach aerial manipulators **154**
6.5. Conclusion **158**

7. Conclusion and future work

7.1. Conclusions **159**
7.2. Future work **160**

References **163**

Abstract

The aerial manipulation is a research field which proposes the integration of robotic manipulators in aerial platforms, typically multirotors – widely known as “drones” – or autonomous helicopters. The development of this technology is motivated by the convenience to reduce the time, cost and risk associated to the execution of certain operations or tasks in high altitude areas or difficult access workspaces. Some illustrative application examples are the detection and insulation of leaks in pipe structures in chemical plants, repairing the corrosion in the blades of wind turbines, the maintenance of power lines, or the installation and retrieval of sensor devices in polluted areas. Although nowadays it is possible to find a wide variety of commercial multirotor platforms with payloads from a few gramps up to several kilograms, and flight times around thirty minutes, the development of an aerial manipulator is still a technological challenge due to the strong requirements relative to the design of the manipulator in terms of very low weight, low inertia, dexterity, mechanical robustness and control.

The main contribution of this thesis is the design, development and experimental validation of several prototypes of lightweight (<2 kg) and compliant manipulators to be integrated in multirotor platforms, including human-size dual arm systems, compliant joint arms equipped with human-like finger modules for grasping, and long reach aerial manipulators. Since it is expected that the aerial manipulator is capable to execute inspection and maintenance tasks in a similar way a human operator would do, this thesis proposes a bioinspired design approach, trying to replicate the human arm in terms of size, kinematics, mass distribution, and compliance. This last feature is actually one of the key concepts developed and exploited in this work. Introducing a flexible element such as springs or elastomers between the servos and the links extends the capabilities of the manipulator, allowing the estimation and control of the torque/force, the detection of impacts and overloads, or the localization of obstacles by contact. It also improves safety and efficiency of the manipulator, especially during the operation on flight or in grabbing situations, where the impacts and contact forces may damage the manipulator or destabilize the aerial platform. Unlike most industrial manipulators, where force-torque control is possible at control rates above 1 kHz, the servo actuators typically employed in the development of aerial manipulators present important technological limitations: no torque feedback nor control, only position (and in some models, speed) references, low update rates (<100 Hz), and communication delays. However, these devices are still the best solution due to their high torque to weight ratio, low cost, compact design, and easy assembly and integration. In order to cope with these limitations, the compliant joint arms presented here estimate and control the wrenches from the deflection of the spring-lever transmission mechanism introduced in the joints, measured at joint level with encoders or potentiometers, or in the Cartesian space employing vision sensors. Note that in the developed prototypes, the maximum joint deflection is around 25 degrees, which corresponds to a deviation in the position of the end effector around 20 cm for a human-size arm. The capabilities and functionalities of the manipulators have been evaluated in fixed base test-bench firstly, and then in outdoor flight tests, integrating the arms in different commercial hexarotor platforms. Frequency characterization, position/force/impedance control, bimanual grasping, arm teleoperation, payload mass estimation, or contact-based obstacle localization are some of the experiments presented in this thesis that validate the developed prototypes.

Resumen

La manipulación aérea es un campo de investigación que propone la integración de manipuladores robóticos in plataformas aéreas, típicamente multirotores – comúnmente conocidos como "drones" – o helicópteros autónomos. El desarrollo de esta tecnología está motivada por la conveniencia de reducir el tiempo, coste y riesgo asociado a la ejecución de ciertas operaciones o tareas en áreas de gran altura o espacios de trabajo de difícil acceso. Algunos ejemplos ilustrativos de aplicaciones son la detección y aislamiento de fugas en estructura de tuberías en plantas químicas, la reparación de la corrosión en las palas de aerogeneradores, el mantenimiento de líneas eléctricas, o la instalación y recuperación de sensores en zonas contaminadas. Aunque hoy en día es posible encontrar una amplia variedad de plataformas multirotor comerciales con cargas de pago desde unos pocos gramos hasta varios kilogramos, y tiempo de vuelo entorno a treinta minutos, el desarrollo de los manipuladores aéreos es todavía un desafío tecnológico debido a los exigentes requisitos relativos al diseño del manipulador en términos de muy bajo peso, baja inercia, destreza, robustez mecánica y control.

La contribución principal de esta tesis es el diseño, desarrollo y validación experimental de varios prototipos de manipuladores de bajo peso (<2 kg) con capacidad de acomodación ("*compliant*") para su integración en plataformas aéreas multirotor, incluyendo sistemas bi-brazo de tamaño humano, brazos robóticos de articulaciones flexibles con dedos antropomórficos para agarre, y manipuladores aéreos de largo alcance. Puesto que se prevé que el manipulador aéreo sea capaz de ejecutar tareas de inspección y mantenimiento de forma similar a como lo haría un operador humano, esta tesis propone un enfoque de diseño bio-inspirado, tratando de replicar el brazo humano en cuanto a tamaño, cinemática, distribución de masas y flexibilidad. Esta característica es de hecho uno de los conceptos clave desarrollados y utilizados en este trabajo. Al introducir un elemento elástico como los muelles o elastómeros entre el los actuadores y los enlaces se aumenta las capacidades del manipulador, permitiendo la estimación y control de las fuerzas y pares, la detección de impactos y sobrecargas, o la localización de obstáculos por contacto. Además mejora la seguridad y eficiencia del manipulador, especialmente durante las operaciones en vuelo, donde los impactos y fuerzas de contacto pueden dañar el manipulador o desestabilizar la plataforma aérea. A diferencia de la mayoría de manipuladores industriales, donde el control de fuerzas y pares es posible a tasas por encima de 1 kHz, los servo motores típicamente utilizados en el desarrollo de manipuladores aéreos presentan importantes limitaciones tecnológicas: no hay realimentación ni control de torque, sólo admiten referencias de posición (o bien de velocidad), y presentan retrasos de comunicación. Sin embargo, estos dispositivos son todavía la mejor solución debido al alto ratio de torque a peso, por su bajo peso, diseño compacto y facilidad de ensamblado e integración. Para suplir estas limitaciones, los brazos robóticos flexibles presentados aquí permiten estimar y controlar las fuerzas a partir de la deflexión del mecanismo de muelle-palanca introducido en las articulaciones, medida a nivel articular mediante potenciómetros o codificadores, o en espacio Cartesiano mediante sensores de visión. Tómese como referencia que en los prototipos desarrollados la máxima deflexión articular es de unos 25 grados, lo que corresponde a una desviación de posición en torno a 20 cm en el efector final para un brazo de tamaño humano. Las capacidades y funcionalidades de estos manipuladores se han evaluado en base fija primero, y luego en vuelos en exteriores, integrando los brazos en diferentes plataformas hexartor comerciales. Caracterización frecuencial, control de posición/fuerza/impedancia, agarre bimanual, teleoperación de brazos, estimación de carga, o la localización de obstáculos mediante contacto son algunos de los experimentos presentados en esta tesis para validar los prototipos desarrollados por el autor

Acknowledgment

The research activity of Alejandro Suarez was supported by the Spanish Ministry of Education, Culture and Sport (*Ministerio de Educacion, Cultura y Deporte*) through its FPU Program. This work, developed within the Robotics, Vision and Control Group at the University of Seville (Spain), has been funded by the H2020 AEROARMS Project (Grant Number 644271), and by the AEROMAIN (DPI2014-5983-C2-1-R) the AEROCROS (DPI2015-71524-R) and the ARM-EXTEND (DPI2017-89790-R) Spanish projects. The three-month stay at the Robotics and Mechatronics Institute in the German Aerospace Center in Oberpfaffenhoffen (Germany) was also supported by the Spanish Ministry of Education, Culture and Sport.

The author wishes to acknowledge the collaboration and participation of several members of the Robotics, Vision and Control Group (GRVC) in the preparation and the realization of several experiments presented in this thesis: Victor Manuel Vega, Antonio Enrique Jimenez Cano, Fran Real, Pablo Ramon Soria, Pedro Sánchez Cuevas, Julián Delgado, Luis Manuel Ramirez, and Pedro Grau. The 3D model of the hexarotor platform shown in the cover of this thesis and along the different chapters is courtesy of Pedro Grau. The author wishes to thank Professors Angel Rodriguez Castaño and Begoña C. Arrue for providing the components and equipment required in the development of the prototypes, and to our secretary Ana Blasco for dealing with an uncountable number of invoices.

Special thanks to Dr. Konstantin Kondak, Alessandro M. Giordano and Max Laiacker from DLR for their kind attention and support during the three-month stay at the Robotics and Mechatronics Institute lead by Professor Alin Albu-Schäffer.

The author has to remark the contribution of Professors Anibal Ollero and Guillermo Heredia in the education and support of the author of this thesis, who started its research activity in the GRVC back in November 2012. I want to express my admiration and respect for these two great researchers who devote most part of their life in the robotics field.

List of figures

Chapter 1. Introduction

Figure 1.1. Two dual arm aerial manipulators: rendered view of hexarotor with anthropomorphic, compliant and lightweight dual arm (left), and lightweight dual arm integrated in a DJI Matrice 600 platform (right). 3

Figure 1.2. Two application examples of aerial manipulators: installation of inspection tool on pipe (left), and visual inspection of pipes for the detection of leaks using a long reach manipulator (right). 4

Figure 1.3. Two illustrative application examples of bimanual manipulation with lightweight dual arm: grasping long bars (left) and operating with one arm while the other holds a camera for visual servoing (right). 6

Figure 1.4. Process flow diagram followed in the design, development and experimental validation of a prototype of aerial manipulator. 11

Figure 1.5. Prototypes of lightweight and compliant manipulators developed by the author. 13

Figure 1.6. Dual arm aerial manipulators. Outdoor flight tests with different hexarotor platforms. 14

Figure 1.7. Spring-lever transmission mechanism introduced in the joint of the anthropomorphic dual arm. 15

Chapter 2. Design and development of lightweight and compliant aerial manipulators

Figure 2.1. Mass distribution (grams and %) of the anthropomorphic and compliant dual arm. 20

Figure 2.2. Compliant joint in spring-lever configuration. The lever attached to the servo shaft pushes the pair of compression springs depending on the rotation direction. The output link rotates w.r.t. the servo shaft thanks to the flange bearing. The joint deflection is measured with a potentiometer integrated in the frame. 22

Figure 2.3. Two different implementations of compliant joint: single side support with partial servo protection (left) and double flange bearing in side-by-side configuration for full servo protection (right). 23

Figure 2.4. 3-DOF compliant joint arm (left). Detailed view of the compliant joint corresponding to the elbow pitch joint (right). 24

Figure 2.5. Rendered view of the compliant mechanism integrated in the shoulder and elbow pitch joints. 25

Figure 2.6. Compliant finger module deflected due to a frontal collision against an obstacle. MCP joint deflection is measured with a potentiometer. 25

Figure 2.7. Compliant finger module integrated in 3-DOF compliant arm 26

Figure 2.8. Conversion from linear displacement to rotational motion in the elbow joint. The distance from joint to the contact point of the actuator in the forearm determines the rotational torque and speed 26

Figure 2.9. Different operation conditions of the tendon in the elbow joint. 27

Figure 2.10. Human size robot arm built with aluminium profiles. A Firgelli L16 linear servo moves elbow joint position, whereas two Futaba S3003 servos move wrist in roll and pitch angles. The arm weight is 325 g. 27

Figure 2.11. Detailed view of the compliant elbow joint mechanism based on linear servo. Two extension springs act as elastic tendon. 28

Figure 2.12. Kinematic model of the four degrees of freedom in anthropomorphic finger 29

Figure 2.13. Anthropomorphic finger module with compliant joints and 40 grams weight. 30

Figure 2.14. View of the components of the finger module in the 3D model. 30

Figure 2.15. Developed lightweight and human-size dual arm manipulator integrated in two different commercial hexarotor platforms. Outdoor flight tests **31**

Figure 2.16. Rendered view of the 10-DOF lightweight dual arm manipulator with the significant lengths and joint angles. **32**

Figure 2.17. Detailed view of the elbow joint mechanism and the wrist yaw servo. Radial loads exerted at the end effector are catch by the pair of igubal EFOM-08 bearings and supported by the aluminium frames. **33**

Figure 2.18. Detailed view of the shoulder and upper arm assembly, including the shoulder yaw and pitch servos, and the elbow pitch servo with the lever-bar transmission mechanism for moving the elbow joint. **33**

Figure 2.19. General and detailed view of the shoulder structure supporting the dual arm manipulator. **34**

Figure 2.20. Workspace covered by the shoulder pitch and the elbow pitch joints with collision constraints (left). Working space of the dual arm system with collision constraints and common operation area (right). **34**

Figure 2.21. Hardware/software components and architecture of the developed dual arm aerial manipulator. **35**

Figure 2.21. Three views of the dual arm aerial manipulation system integrated in the DJI Matrice 600 hexarotor. **37**

Figure 2.23. Lightweight dual arm manipulator integrated in the customized hexarotor platform manufactured by Drone Tools. **37**

Figure 2.24. Anthropomorphic, compliant and lightweight dual arm. **38**

Figure 2.25. Detailed view of the joints in the right arm. Hands-up pose. **39**

Figure 2.26-A. Kinematic configuration of the anthropomorphic dual arm and reference frames of both arms attached to the shoulder joint. **40**

Figure 2.26-B. Kinematic configuration of the anthropomorphic dual arm and reference frames of both arms attached to the shoulder joint. **41**

Figure 2.27. Components and architecture of the compliant dual arm. **41**

Figure 2.28. Relative distances between the center of mass of the links (left) and global center of mass of the left arm (right). Lengths in mm. **42**

Figure 2.29. CoM and dimensions (in mm) of the shoulder pitch structure. **43**

Figure 2.30. CoM and dimensions (in mm) of the shoulder roll structure. **43**

Figure 2.31. CoM and dimensions (in mm) of the shoulder yaw structure. **44**

Figure 2.32. CoM and dimensions (in mm) of the elbow pitch structure. **44**

Figure 2.33. CoM and dimensions (in mm) of the forearm structure. **45**

Figure 2.34. 3D model of the anthropomorphic dual arm integrated in a hexarotor. Take-off and landing (left) and operation (right) configurations. **45**

Figure 2.35. Anthropomorphic dual arm integrated in hexarotor platform along with a ZED stereo camera, an Intel NUC computer board, an Ubiquiti wireless link and the batteries. **46**

Figure 2.36. Integration of anthropomorphic, compliant dual arm in DJI Matrice 600 hexarotor. **46**

Figure 2.37. Dual arm aerial manipulation robot with flexible, long reach link. The batteries in the back act as counterweight of the arms. The flexible LRM increases safety in the physical interactions with the environment, avoiding potential collisions of the propellers against walls or obstacles. **47**

Figure 2.38. Lightweight, human size dual arm system installed at the tip of an 80 cm length flexible link (left). A Prosilica GC 1380H camera at the base provides direct measurement of tip deflection (right). **48**

Figure 2.39. Compliant joint, long reach aerial manipulator. The manipulator integrates magnetic encoders for joint deflection and passive joint rotation measurement, a range sensor for measuring the distance to a contact point, and a camera installed in the forearm link, close to the end effector. **50**

Figure 2.40. Wearable exoskeleton interface for arm teleoperation. **51**

Figure 2.41. Hardware components and architecture of the aerial manipulator. **52**

Figure 2.42. Two rendered views of the long reach aerial manipulator with the anthropomorphic, compliant and lightweight dual arm (left), and operation in outdoors (right). **53**

Chapter 3. Functionalities of lightweight and compliant aerial manipulators

Figure 3.1. Torque sensor based on strain gauges employed in industrial manipulators (up) and compliant joint with deflection encoder based on spring-lever transmission mechanism (down). **56**
Figure 3.2. Impedance behaviour of compliant manipulator to external load, assimilated to a mass-spring-damper system. **57**
Figure 3.3. Lightweight arm with compliant elbow joint (left) and geometric model (right). **58**
Figure 3.4. Three situations illustrating the passive compliance capability: unexpected impact against obstacle (left), flexible link deflection in grabbing situations (middle), and closed kinematic chain (right). **59**
Figure 3.5. Active compliance applied to the detection and reaction against impacts. **60**
Figure 3.6. Dual arm aerial manipulator carrying a long bar (1) – (2). Unexpected collision with obstacle in the environment, which causes a deflection in the compliant arms (3), releasing the bar for safety (4). **61**
Figure 3.7. Retrieval on flight of inspection tool installed on a pipe. The compliant dual arm apply a pulling force in the vertical axis while monitoring the displacement of the end effector to detect if the tool is blocked. **62**
Figure 3.8. Compliant dual arm aerial manipulator installing a sensor device with the left arm (operation arm) while the right arm is grabbed at a fixed point in the workspace measuring the relative position. **63**
Figure 3.9. Flexible link long reach manipulator with lightweight dual arm in test bench (left), and passive pendulum aerial manipulators, single arm (right) and dual arm (middle). **64**
Figure 3.10. The dual arm system executes a scan for detecting obstacles, rotating the shoulder yaw joint until a collision occurs. The contact force causes a deflection in the flexible link and a disturbance on the UAV. **66**
Figure 3.11. Evaluation in fixed test-bench of the obstacle detection capability based on the flexible link deflection measurement provided by the vision system. **67**
Figure 3.12. Sequence of images showing the obstacle localization method based on soft-collision detection. **67**
Figure 3.13. Contact force control scheme. The shoulder yaw joint determines the pushing force of the end effector against a surface in the direction of the flexible link tip deflection. **68**
Figure 3.14. Estimation and control of the contact force exerted by the left arm through the rotation around the shoulder yaw joint. The camera installed at the base of the link measures the deflection at the tip. **68**
Figure 3.15. Two different behaviours of the long reach aerial manipulator to an external force acting at the end effector: propagation of torque through rigid joint (up), and reaction force with passive joint (bottom). **69**
Figure 3.16. Recoil rotation in the passive joint caused by the motion of the manipulator attached at the tip of the long reach link (left, middle). Estimation and control of the pushing force applied at the end effector through the rotation angle of the passive joint exploiting the gravity force (right). **70**

Chapter 4. Modelling, estimation and control of compliant aerial manipulators

Figure 4.1. General control scheme of an aerial manipulation robot. **73**
Figure 4.2. Model of the compliant actuator and mechanical construction. **74**
Figure 4.3. Geometric model considered in the derivation of the torque-deflection relationship. **76**

Figure 4.4. Torque control scheme in a compliant actuator with joint deflection feedback. **77**

Figure 4.5. Virtual variable impedance actuator. Response to external load (up) and implementation (down). **78**

Figure 4.6. Geometric model considered in the kinematic model and in the derivation of the force-torque relationships (left). Developed prototype (right) with two compliant joints in elbow and shoulder. **79**

Figure 4.7. Position-torque control scheme in static (contact) conditions. The input references are the end effector position reference, the torque reference, and the maximum speed of the servos. **81**

Figure 4.8. Anthropomorphic, compliant and lightweight finger module. **82**

Figure 4.9. Model used in the computation of the MCP joint torque. The nylon tendon passes through P_1 and P_2 before it is rolled up on the reel. **83**

Figure 4.10. MCP joint position control. **84**

Figure 4.11. Reference frame, joint variables, sign criteria and lengths in the lightweight dual arm. **85**

Figure 4.12. Kinematic model of the lightweight dual arm. **86**

Figure 4.13. Reference frames, position vectors, mass and inertia parameters involved in the dynamic model of the dual arm aerial manipulator. **87**

Figure 4.14. Control structure of the dual arm aerial manipulator with arms torque compensation. **89**

Figure 4.15. Velocity profiles for the three operation modes of the Herkulex servos. In the Velocity Over-Ride (VOR) mode, the new profile (green) is re-computed from the velocity in the time instant the new reference is received, preventing acceleration peaks. **90**

Figure 4.16. Arms control structure based on inverse kinematics. Smooth trajectories are achieved sending the position references to the servos at the midpoint of the trapezoidal velocity profile, imposing that the play time is two times the way-point tracking time. **90**

Figure 4.17. Structure of the arms torque estimator. **91**

Figure 4.18. Inertia (blue), Coriolis and centrifugal (green) and gravity (red) terms in the XY axes for the 90° step in the shoulder pitch joint of the left arm. The components in the X-Z axes are due to the asymmetry in the motion of the arms. **91**

Figure 4.19. Kinematic configuration of the anthropomorphic dual arm and reference frames of both arms attached to the shoulder joint. **92**

Figure 4.20. Cartesian position/velocity controller based on inverse kinematics. **94**

Figure 4.21. Geometric model considered in the bimanual grasping task with visual servoing. **95**

Figure 4.22. Geometric model considered for deriving the force-torque relationships. **98**

Figure 4.23. Cartesian deflection measured on the left arm by means of a red color marker attached at the TCP and a stereo camera head. **99**

Figure 4.24. Contact force control scheme based on Cartesian deflection. **100**

Figure 4.25. Structure of the deflection estimation system. **101**

Figure 4.26. Geometric model and parameters in the flexible link manipulator. **102**

Figure 4.27. Reference frames and kinematic model of the flexible link dual arm manipulator. **103**

Figure 4.28. Kinematic model of the long reach aerial manipulator with single arm. **105**

Figure 4.29. Coordinated UAV-long reach manipulator control scheme. The goal is to control the position and force of the TCP of the arm. The pose and thrust of the UAV is adapted to achieve this reference. **107**

Figure 4.30. Force-position control scheme implemented in the compliant arm. The force is estimated from the Cartesian deflection $\boldsymbol{\Delta l_{TCP}}$ and stiffness $\boldsymbol{K_C}$. **108**

Figure 4.31. Reference frames, joint variables and position vectors of the long reach aerial manipulator with compliant dual arm in pendulum configuration. **108**

Chapter 5. Experimental results with compliant joint manipulators (single arm)

Figure 5.1. Frequency response of the compliant joint actuator to sine chirp signal generated by the servo. Validation of the mass-spring-damper model. **112**

Figure 5.2. Output link angular position for initial condition $q(0) = 90$ deg: variable damping for $k_v = k_n/4$ (left), and variable stiffness for $d_v = 20 \cdot d_n$ (right). Simulated desired response (up) and experimental (down). **113**

Figure 5.3. Frequency (up) and time (down) response of the shoulder and elbow compliant joints to a 10° amplitude sine chirp signal in the range 0 – 10 Hz. Excitation of the elbow (left) and shoulder (right) joints. **113**

Figure 5.4. Shoulder pitch joint position reference, feedback and deflection angle for different playtimes. The amplitude of the overshoot in the deflection increases as the speed of the servo is higher. **114**

Figure 5.5. XZ-axes force reference and estimation (up, left) and joints deflection (bottom, left) when the wrist point is in contact with the surface. The collision occurs at t = 0.7 s with $q_2 \approx 0$ and $q_3 \approx 90$ [deg]. **115**

Figure 5.6. Force (left) and torque (right) reference and feedback estimated from the joint deflection measured with the magnetic encoders. **115**

Figure 5.7. Tool Center Point (TCP) position w.r.t. arm base (blue), and collision points (black) on the XY-plane. The position of the obstacle was moved from position 1 to position 3 during the experiment. In 4, the arm retracts once the collision is detected by the finger module. **116**

Figure 5.8. Rotation of the compliant arm in its three joints: elbow (compliant, A.1 – A.3), wrist roll (stiff, B.1 – B.3), and wrist pitch (stiff, C.1 – C.3). **117**

Figure 5.9. Evolution of linear servo position and elbow joint position for different payloads. **117**

Figure 5.10. Estimated payload mass for different elbow joint angles in static conditions. **119**

Figure 5.11. Influence of elbow joint position over payload estimation for different payloads. The accuracy in the estimation is lower for joint angles close to zero, remaining almost constant for angles above 45 deg. **119**

Figure 5.12. Response of elbow joint without active compliance. The forearm is blocked at t = 1.5 s while the linear servo keeps moving, being released at 3.1 s. The extension springs recover their normal elongation at t = 3.7 s. **120**

Figure 5.13. Response of the elbow joint with active compliance. The forearm is blocked at t = 1.2 s while the linear servo keeps moving. The collision is detected at t = 1.9 s when the springs elongation exceeds the 25 mm threshold. The springs have released the excess of energy at t = 3. **120**

Figure 5.14. MCP joint position control and PWM signal. Stair reference for flexion and extension. The proportional gain of the controller is set to K_p = 2.5, and the PWM signal is saturated to 80%. **121**

Figure 5.15. Finger flexion motion performed by the three joints driven by the single DOF. **121**

Figure 5.16. MCP joint position and torque in force control mode for different PWM saturation values. **122**

Figure 5.17. Regulation of grasping force adjusting the saturation of the PWM signal. The finger module is grasping a deformable rubber cup. **122**

Figure 5.18. Stable grasping of different objects: bottle, screwdriver, pliers and ball. **123**

Figure 5.19. MCP joint response to hammer impact and to frontal collision, detected when the measured joint angle exceeds the upper or lower threshold. **123**

Figure 5.20. Sequence of images corresponding to the landing operation. **124**

Figure 5.21. Multirotor position, velocity, attitude, and pendulum joint angle during the take-off and landing. **125**

Figure 5.22. Multirotor position, velocity, attitude, and pendulum rotation when the tip of the long reach link hits an obstacle at t = 160 s while the hexarotor moves at 2 m/s, causing a 10° oscillation in the pitch angle. **125**

Figure 5.23. Visual display shown to the operator during the inspection task. The red line at the tip of the manipulator represents the distance to the pipe. **126**

Figure 5.24. Joint position reference and feedback of the compliant arm (left), pendulum rotation (right, up) and range sensor (right, down) during the visual inspection of a pipe using the exoskeleton interface in test-bench. **127**

Figure 5.25. Contact force (left), joint deflection and servo angular position (mid) and Cartesian stiffness (right). **127**

Figure 5.26. Rotation of the passive pendulum: free oscillation (black) and vibration attenuation using the arm with different compensation gains. **128**

Chapter 6. Experimental results with dual arm aerial manipulators

Figure 6.1. Circular trajectory followed by the wrist point of left and right arms in the YZ plane (left) and XZ plane (right). The arms performed five complete turns for evaluating repeatability and accuracy. Note the scale of the X-axis on the right figure. **132**

Figure 6.2. Tracking points given by the CAMShift algorithm in the frontal and side planes corresponding to the circular trajectory. **132**

Figure 6.3. Experimental setup considered in the visual servoing experiment. **133**

Figure 6.4. Cartesian position of the left and right arms in the visual servoing experiment. Each arm tracked an ARUCO tag. An offset distance of 10 cm in the Z-axis was introduced for avoiding occlusions. **133**

Figure 6.5. Position, speed and acceleration of the shoulder yaw (red), pitch (green) and elbow pitch (blue) joints of the left and right arms. **134**

Figure 6.6. Servo position, speed and PWM in the left (first row) and right (second row) arms during a sequence of rotations around the shoulder pitch and yaw joints. Oscillations in the platform are measured with a three axis gyroscope (third row). The amplitude and axes involved in the reaction of the platform depend on the joints speed and symmetry of the arms trajectory (cols 1 – 2 vs col 3). **135**

Figure 6.7. Sequence of images corresponding to the outdoor flight tests with the arms integrated in the DJI Matrice 600 platform. Platform landed (1), landing gear down – up transition (2 – 3), arms in operation position (4), rotation around the shoulder pitch joint (5 – 6), rotation around the shoulder yaw joint (7 – 8), and left arm fully stretched (9). **136**

Figure 6.8. Sequence of images of the outdoor flight tests with the customized hexarotor manufactured by Drone Tools. Arms in take-off position (1), transition to operation position (2 – 3), execution of different trajectories (4 – 9). **136**

Figure 6.9. Outdoor flight tests for bar retrieval. Both arms are teleoperated using a single 6-DOF joystick **137**

Figure 6.10. Flexible link tip deflection measured with the vision system. Response to initial condition $w(0, L) = 100\ pixels$ with no load and with load at the tip (left). Experimental setup (right). **138**

Figure 6.11. Detailed view of the flexible link tip deflection in 1 second interval (left). Sequence of images showing the displacement of the market attached at the tip of the flexible link (right). Saving the images as JPEG files reduced the frame rate. **139**

Figure 6.12. FFT of the flexible link tip deflection signal (left). Execution time of the vision system (right). **139**

Figure 6.13. Flexible link tip deflection (top) and shoulder yaw joint speed (bottom) in the vibration suppression experiment for different compensation amplitudes. The left arm generates a disturbance between t = 0 and t = 2.2 seconds (red area). Vibration suppression is enabled at t = 5 s (green line). **140**

Figure 6.14. Flexible link tip deflection measurement and reference (top), shoulder yaw joint angle (middle), and control flags (bottom) corresponding to the collision detection experiment with contact force control. **141**

Figure 6.15. Trajectory followed by the wrist point of left and right arms for the obstacle localization experiment. The obstacle firstly impacts in the forearm of the left arm (1). Then both **141**

arms are retracted and an inner to outer scan phase is executed until the collision at the wrist point (2).

Figure 6.16. Flexible link tip deflection and thresholds for collision detection. The two impacts of the left arm against the obstacle are marked. Vibration suppression is executed after the impacts for removing tip oscillation. **142**

Figure 6.17. Elbow pitch (blue) and shoulder pitch (green) joint deflection for a 15 deg chirp signal generated by the elbow pitch servo (black). **143**

Figure 6.18. Detailed view of the servo position and the joints deflection. Before the first resonance peak the deflection is in phase with the servo (up), dropping 180 deg in the second resonance peak (down). **143**

Figure 6.19. FFT applied to the elbow pitch servo (black) and to the elbow pitch (blue) and shoulder pitch (green) joint deflection. The resonance frequencies are identified at $f_1 = 1.6\ Hz$ and $f_2 = 5.9\ Hz$. **144**

Figure 6.20. FFT applied to the elbow pitch servo (black), the elbow pitch (blue) and shoulder pitch (green) joint deflection. The spectrum and resonance frequencies have changed along with the mass of the arm. **144**

Figure 6.21. Impact response. Cartesian deflection and velocity measured with the vision system (left). Representation in the frequency domain (right). **145**

Figure 6.22. Representative signals in the contact force experiment: position of the platform (up, left), left arm force and reference (down, left), variation of the servos position (up, right), and left arm Cartesian stiffness (down, right). **145**

Figure 6.23. Approaching (left) and contact force control (middle) phases and images from onboard camera (right). The position of the left/right arms and the target contact point are measured with ARUCO tags. **146**

Figure 6.24. Force (left) and displacement (right) of the left/right arm markers when the grasped object is pulled in the Z-axis and this is lifted. **146**

Figure 6.25. Pulling force and displacement when the object cannot be lifted. The displacement is monitored (blue area) since $F_Z \geq 0.75 \cdot F_{Z,ref}$. **147**

Figure 6.26. Compliant dual arm integrated in DJI Matrice 600 hexarotor. Take-off (1), approaching to inspection tool installed on pipe (2 – 3), and visual servoing (4 – 6). The target points are out of the reach of the arms due to the displacement of the aerial platform (5 – 6). **148**

Figure 6.27 Bimanual object grasping on flight. The arms grasp the inspection tool installed over a pipe by a 50 cm length handle. **149**

Figure 6.28. TCP Cartesian position of left/right arms. Grasping points given by the vision (red), reference (black) and servo feedback (blue). **149**

Figure 6.29. Evaluation of the accuracy in the vision-based force estimation. Different payload masses were attached at the wrist point of the left arm. **150**

Figure 6.30. Application of dual arm aerial manipulator to pipe inspection with customized tool. **151**

Figure 6.31. Sequences of images taken from the on-board camera representing the bimanual grasping of the inspection tool stored at the tool bench. The arms are guided to the grasping points using the Vicon system. **151**

Figure 6.32. Trajectory followed by the aerial manipulator during the execution of the tool installation task. The numbers indicate the phase of the experiment according to the list indicated before. **152**

Figure 6.33. XYZ grasping point references (black) and current end effector position (blue) of the left and right arms. The grasping points are obtained from the position of the inspection tool given by Vicon. **152**

Figure 6.34. Grasping points obtained from Vicon (black) and current end effector position (blue) of both left and right arms in a 50 seconds evaluation period. **153**

Figure 6.35. Tracking error in mm of the left and right arms during the long term grasping experiment (left). Displacement of the multirotor in hovering state (right). **153**

Figure 6.36. Sequence of images from the on-board camera corresponding to the tool installation phase. **153**

Figure 6.37. Transportation operation performed by the long reach aerial manipulator with compliant dual arm. Sequence of images taken from the ground camera. **154**

Figure 6.38. Sequence of images of the long reach dual arm aerial manipulator taken from the DJI Phantom 3 camera. **155**

Figure 6.39. Dual arm aerial manipulator in passive pendulum configuration used in the sensor installation task. The left arm integrates magnetic encoders for estimating the contact forces in terms of joint deflection. **156**

Figure 6.40. Force reference and feedback (left), and joint angles and Cartesian stiffness on the left arm (right) during the application of the contact force. **156**

Figure 6.41. Hexarotor position (left) and displacement during the sensor installation operation (right). **157**

Figure 6.42. Installation of sensor on pipe applying a 2 N pushing force with the left arm. An adhesive tape located on the cage of the sensor maintains the device attached to the pipe. The pose of the arm (L-shaped configuration) results more favourable for the force controller since it is far from the kinematic singularities. **157**

Figure 6.43. Sequence of images from the on-board camera corresponding to the second experiment of contact force control. As it can be seen in (3) and (4), the arm is almost fully stretched in the contact phase, so it is not possible to control accurately the force. **158**

Figure 6.44. Force reference and feedback (left), joint variables and Cartesian stiffness (right) during the second contact force control experiment. Due to the displacement of the aerial platform w.r.t. the contact point, the left arm adopts a stretched pose close to the kinematic singularity, characterized by a high stiffness, so the servos are not capable to deliver the required torque. **158**

List of tables

Chapter 1. Introduction

Table 1.1. Comparison of several prototypes of aerial manipulators (single arm). 2
Table 1.2. Main specifications of different commercial multirotor platforms. 2
Table 1.3. Main specifications of different commercial robotic manipulators. 3
Table 1.4. Comparison of several dual arm aerial manipulation prototypes. 7
Table 1.5. Comparison of different prototypes of compliant joint arms for aerial manipulation. 8

Chapter 2. Design and development of lightweight and compliant aerial manipulators

Table 2.1. Materials employed in the prototypes of lightweight and compliant manipulators. 20
Table 2.2. Specifications of the 3-DOF compliant robot arm. 24
Table 2.3. Specifications of the compliant and lightweight robot arm. 28
Table 2.4. Specifications of the joints in the lightweight and human-size dual arm. 32
Table 2.5. Specifications of the aerial manipulation system considering two commercial hexarotor platforms. 36
Table 2.6. Specifications of the compliant dual arm. 39
Table 2.7. Specifications of the joints in the compliant dual arm. 39
Table 2.8. Mass and inertia parameters of the links in the compliant dual arm. 42
Table 2.9. Specifications of the lightweight and human-size dual arm system. 49
Table 2.10. Specifications of the vision sensor for tip deflection measurement. 49
Table 2.11. Specifications of the compliant joint, long reach aerial manipulator. 50
Table 2.12. Sensor devices integrated in the compliant arm. 51
Table 2.13. Mechanical specifications of the long reach aerial manipulator. 53

Chapter 3. Capabilities of lightweight and compliant aerial manipulators

Table 3.1. Pseudocode implementing the vibration suppression method. 65
Table 3.2. Criteria for identifying which arm and in which side a collision occurs based on flexible link tip deflection and the sign of the scan. 66

Chapter 4. Modelling, estimation and control of compliant aerial manipulators

Table 4.1. Parameters of the compliant joint actuator. 75

Chapter 5. Experimental results with compliant joint manipulators (single arm)

Table 5.1. Parameters of the compliant joint actuator depicted in Figure 5.1. 112
Table 5.2. Proportional, integral and derivative constants used in the virtual variable impedance controller. 112
Table 5.3. Static payload mass estimation for different elbow joint angles. 118

Acronyms

Abbreviation	Definition
CAD	Computer Aided Design
CAMShift	Continuously Adaptive Mean-Shift
CoM	Center of Mass
DIP	Distal Inter-Phalange
DOF	Degree of Freedom
EKF	Extended Kalman Filter
FFT	Fast Fourier Transform
GCS	Ground Control Station
GPS	Global Positioning System
HSV	Hue-Saturation-Value
IMU	Inertial Measurement Unit
LIDAR	Light Detection and Ranging
LRM	Long Reach Manipulator
MCP	Metacarpo-Phalangeal
PID	Proportional-Integral-Derivative
PIP	Proximal Inter-Phalange
PWM	Pulse Width Modulation
RTK	Real Time Kinematics
SLAM	Simultaneous Localization and Mapping
TCP	Tool Center Point
TTL	Transistor-Transistor Logic
UAV	Unmanned Aerial Vehicle
UDP	User Datagram Protocol
USART	Universal Synchronous and Asynchronous Receiver-Transmitter
VOR	Velocity Over-Ride
VTOL	Vertical Take-Off and Landing

Symbols

Symbol	Description
$\{\boldsymbol{E}\}$	Earth fixed frame
$\{\boldsymbol{B}\}$	UAV base frame
$\{\boldsymbol{M}\}$	Manipulator reference frame
$\{\boldsymbol{i}\}$	i-th manipulator reference frame
$i = \{1, 2\}$	Arm index (left, right)
$j = \{1, 2, 3, 4, \dots\}$	Joint index
θ	Servo shaft angular position
θ_{ref}	Servo shaft position reference
q	Output link angular position
$\Delta\theta$	Joint deflection angle
K_s	Compression spring stiffness
L_{lever}	Lever length (spring-lever mechanism)
L_{link}	Link length (spring-lever mechanism)
L_1	Upper arm link length
L_2	Forearm link length
D	Separation between left-right arms
$\boldsymbol{FK}$	Forward kinematics function
$\boldsymbol{IK}$	Inverse kinematics function
$\Delta\boldsymbol{l}$	Cartesian deflection at the end effector
$\boldsymbol{\tau}$	Torque vector
$\boldsymbol{F}$	Cartesian force at the end effector
τ_j^i	Joint torque (i-th arm, j-th joint)
k_j^i	Joint stiffness (i-th arm, j-th joint)
d_j^i	Joint damping (i-th arm, j-th joint)
K	Kinetic energy
V	Potential energy
$\boldsymbol{\xi}$	Vector of generalized coordinates
$\boldsymbol{\Gamma}$	Vector of generalized forces
$\boldsymbol{M}$	Generalized inertia matrix
$\boldsymbol{C}$	Coriolis and centrifugal terms
$\boldsymbol{G}$	Wrenches due to gravity potential
$\boldsymbol{K}$	Wrenches due to elastic potential

$\boldsymbol{D}$	Wrenches associated to damping
$\boldsymbol{K}_p$	Physical stiffness matrix (diagonal)
$\boldsymbol{D}_p$	Physical damping matrix (diagonal)
$\boldsymbol{K}_C$	Cartesian stiffness matrix (virtual)
$\boldsymbol{D}_C$	Cartesian damping matrix (virtual)
$\boldsymbol{J}$	Jacobian matrix of the manipulator
$\boldsymbol{r}_{\boldsymbol{UAV}} = [x, y, z]^T$	UAV position
$\boldsymbol{\eta} = [\phi, \theta, \psi]^T$	UAV orientation (roll, pitch, yaw)
$\boldsymbol{F}_{\boldsymbol{UAV}}$	Forces acting over the UAV
$\boldsymbol{\tau}_{\boldsymbol{UAV}}$	Torques acting over the UAV
$w(t, L)$	Flexible link tip deflection signal
$\varphi_k(x)$	Modal shape function, k-th vibration mode
$\delta_k(t)$	Generalized coordinate, k-th vibration mode
$\boldsymbol{x} = \left[x, y, z, v_x, v_y, v_z\right]^T$	State vector: marker position-velocity (EKF)
Δt	Elapsed time since last measurement
$\boldsymbol{Q}$	Process noise covariance matrix (EKF)
$\boldsymbol{R}$	Measurement noise covariance matrix (EKF)
$\boldsymbol{c}_{M,i}^k$	i-th marker centroid projected on k-th camera

Chapter 1 – Introduction

1.1. Aerial manipulation

The aerial manipulation is a robotics research field that proposes the integration of one or more robotic arms in vertical take-off and landing (VTOL) unmanned aerial vehicles (UAVs), typically multirotors or autonomous helicopters, in such a way that the manipulator is capable to perform certain operations in workspaces at high altitude or in areas out of the reach for ground robots. The development of this technology is motivated by the convenience to simplify and reduce the time and cost associated to inspection and maintenance tasks that are typical in a wide variety of industrial scenarios. Some application examples are detection and the repair of leaks in pipe structures in chemical plants, the insulation of cracks in the blades of wind turbines caused by the corrosion, the installation and retrieval of sensor devices in polluted areas, or the inspection of power lines.

Unlike fixed base or wheeled base manipulators, the development and application of an aerial manipulation robot is strongly affected by three constraints associated to the aerial platform: payload, flight time, and workspace. Although nowadays it is possible to find a wide variety of commercial multirotor platforms with payloads from a few grams up to several kilograms, and flight times around 15 – 30 minutes (depending on the load), the size and cost of these platforms increase rapidly with the payload, and so, the difficulty for their transportation and operation. The effective reach and workspace of the arms are also reduced due to the legs of the landing gear and the propellers, limiting in practice the performance to movements of relatively small amplitude. As consequence, the aerial platform has to operate very close to the point of interest, maintaining its position stable with deviations smaller than the reach of the manipulator. Additionally, the physical interactions between the aerial robot and the environment (contact forces, grabbing situations or impacts) may cause the destabilization of the UAV and thus the potential risk of crashes. In this sense, the mechanical compliance is a highly desirable feature for the manipulator, since it increases the tolerance of the system to overloads during the operation on flight, allows the estimation and control of the contact forces through the deflection of an elastic element integrated in the joints or links, and protects the actuators against impacts. Most robotic arms commercially available are not suitable for their integration in multirotors since they are not specifically designed for this purpose. This is evidenced in the mass distribution, the design of the frame structure, and the lack of mechanical compliance. Note that the weight of a robotic arm intended to aerial manipulation is typically below 1 kg, that is, around 20 times lower than the so called "lightweight" industrial manipulators, whereas the stiffness is 2 – 3 orders of magnitude lower in a compliant arm. The strong mechanical constraints imposed by the aerial platform in the design of the arms, the dynamic coupling, the effect of the interaction forces with the environment, and the need of a highly accurate positioning system for outdoor operation make the development of the aerial manipulation technology still a technological challenge.

1.2. Design and development of aerial manipulators

Although its precise definition may vary according to the author, the term "aerial manipulator" usually refers to a flying robot consisting of an aerial platform (multirotor or helicopter) equipped with some kind of gripper, robotic arm or tool, and which is intended to perform certain operations or tasks involving physical interactions with the environment or with objects within this. There is a wide variety of morphologies associated to the manipulator. This may be a multi-link arm [1][2][3][4], a dual arm manipulator [5][6][7][8], a long reach manipulator [9][10], a gripper [11][12][13], a parallel manipulator [14][15], a surface or net carried by multiple quadrotors [16], or even the body of the multirotor may become the manipulator itself [17]. The aerial platform in most cases is a quadrotor [1][2][5][11][16] or hexarotor [4][6][7][8][15][18]. Tilted-rotor hexarotors, also known as fully actuated hexarotors [19][20][21], allow the translation of the platform maintaining the orientation constant, which is convenient to increase the positioning accuracy of the manipulator when this is close to the point of interest. Autonomous helicopters provide higher payload capacities [13][22] since the thrust of the propellers increases with the length of the blades. **Table 1.1** compares the features of different prototypes of single arm aerial manipulators, indicating the type of platform, arm, weight and payload.

Table 1.1. Comparison of several prototypes of aerial manipulators (single arm).

Ref./Year	**Aerial platform**	**Manipulator**				
		Type	**DOF**	**Reach [m]**	**Weight [k]**	**Lift load [kg]**
[1] / 2013	Quadrotor	Arm	2	0.32	0.37	NA
[2] / 2015	Quadrotor	Arm	5	0.3	0.25	0.2
[3] / 2013	Quadrotor	Arm	2	NA	0.4	0.2
[28] / 2015	Quadrotor	Arm	6	0.45	1.4	NA
[13] / 2011	Helicopter	Gripper	NA	NA	NA	NA
[22] / 2014	Helicopter	Industrial	7	0.8	22	7

Two approaches can be adopted in the development of an aerial manipulation robot: 1) integrating commercial robotic arms designed for fixed base operation [22][23], or 2) develop robotic arms which are specifically designed for aerial platforms [2][7][8][15]. This second option is the solution adopted in most research works, where the effort is focused in reducing as much as possible the weight, but ensuring a certain level of dexterity, reach and payload capacity. The payload and flight time in a multirotor is closely related with its size and weight. **Table 1.2** compares the specifications of several commercial multirotor platforms, whereas **Table 1.3** presents the main features of some industrial manipulators. Higher size/weight platforms involve higher effort in the maintenance, transportation and operation. It is necessary to remark that a 5 kg weight aerial platform may cause serious injuries or even death in case of accident with a human. In order to prevent the injuries associated to the blades, several protection mechanisms have been proposed and validated experimentally [24][25].

Table 1.2. Main specifications of different commercial multirotor (quadrotors, hexarotors) platforms.

Manufacturer	**Model**	**Weight/MTOW [kg]**	**Payload [kg]**	**Flight time [min]**	**Size [mm]**
Ascending Technologies	AscTec Hummingbird	NA / 0.71	0.2	20 (with payload)	540 × 540 × 85
Ascending Technologies	AscTec Pelican	NA / 1.65	0.65	16 (with payload)	651 × 651 × 188
DJI	Matrice 200	3.8 / 6.14	2.34	13 – 27	887 × 880 × 378
DJI	Matrice 600	9.1 / 15.1	6.0	16 – 35	1668×1518×759
DroneTools	Hexarotor	3.4/ NA	2.5	30 (no load)	800 × 800 × 270

Table 1.3. Main specifications of different commercial robotic manipulators.

Manufacturer	Model	Num. Joints	Weight [kg]	Payload [kg]	Reach [m]
Robai	Cyton Epsilon 300	7	1.2	0.3	0.48
Robai	Cyton Epsilon 1500	7	3.0	1.5	0.63
Kinova Robotics	Jaco	6	6.2	1.6	0.9
Universal Robots	UR3	6	11.0	3.0	0.5
Franka Emika	Franka	7	18.5	3.0	0.85
KUKA	BLR iiwa 7 R800	7	22.0	7.0	0.8

This thesis is focused in the development of lightweight and compliant robotic arms intended to aerial manipulator with multirotor platforms, following a bioinspired design approach with the idea of replicating the human arm in terms of size, kinematics, mass distribution, and compliance. Several of the developed prototypes have been integrated in commercial hexarotor platforms and evaluated in outdoor flight tests, validating the low weight and inertia design and their application to grasping and other tasks involving physical contact with the environment. **Figure 1.1** shows two prototypes of dual arm manipulators developed by the author. The left image is a rendered view taken from the 3D model of the anthropomorphic, compliant and lightweight dual arm [8] installed over the landing gear of a hexarotor. The right image corresponds to the lightweight dual arm integrated [7] in a DJI Matrice 600 hexarotor.

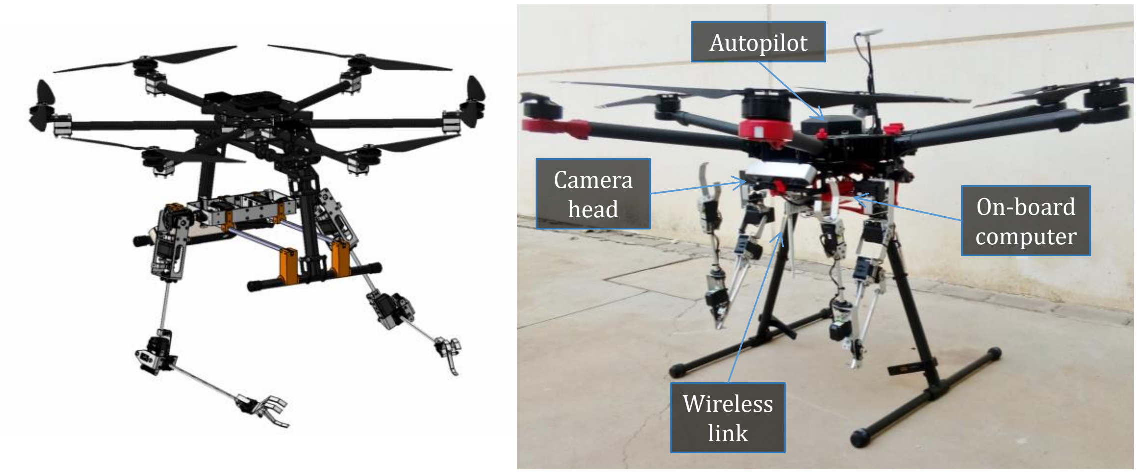

Figure 1.1. Two dual arm aerial manipulators: rendered view of hexarotor with anthropomorphic, compliant and lightweight dual arm (left), and lightweight dual arm integrated in a DJI Matrice 600 platform (right).

One of the main factors that determine the performance of an aerial manipulation robot is the level of dexterity of its manipulator. It is possible to find research prototypes of different degrees of freedom: one [26], two [1], three [27], five [2], six [28], seven [22][23], or dual arm systems with two [5], four [8] or five [7] joints per arm. In this sense, it would result highly convenient to provide the aerial platform with a human-like manipulation capability, in such a way that the operations or tasks can be done in way similar a human operator would do. However, the designer should deal with payload limitations imposed by the UAV, which affect for example to the number of joints in the arms, as well as to the motion constraints associated to the landing gear and the frame structure of the platform in which the arms are integrated. This motivated the development of long reach aerial manipulators [9][10], consisting of placing the arms at the tip of a flexible long link (~1 m length) that is attached at the base of the aerial platform through a passive joint, similarly to a pendulum [10].

In this thesis, the multirotor is considered as a mobile base that carries the manipulator and it is responsible of its transportation and positioning within the workspace, taking into account the dynamic coupling between both parts, the contact forces, and other effects that may affect the accuracy and reliability of the operation. It should be noted that the effective reach of a human-size arm is around 30 cm around its usual operation position, although its length is around 50 cm. Humans extend the reach of their arms through the torso and abdomen, or they approach to a certain grasping point walking, whereas in an aerial manipulator, the arms are placed at the base of the aerial platform, where the propellers and the landing gear limit their operation. The proximity between the aerial platform, the manipulator, and the obstacles in the environment increases the risk of crashes, especially if the controller of the UAV is not able to deal with the interaction forces. Therefore, it is essential that the multirotor is capable to maintain its position with small positioning errors, which implies the use of highly accurate position sensors or methods. Otherwise, the manipulator will not be able to conduct the operation. Vicon and OptiTrack systems have been extensively used in indoor testbeds [1][4][12][16][20]. Real Time Kinematic (RTK) GPS [29][30], vision-based SLAM [31][32][33][34], and range sensors [35][36] have been proposed to achieve accurate position and trajectory control of multirotor vehicles in outdoors, where the conditions are less favourable.

1.3. Applications of aerial manipulators

Many inspection and maintenance operations in industrial facilities require the deployment of human operators and tools in areas of difficult access, for example in high altitude pipe structures or in wind turbines. The lack of appropriate paths and stable support points in these scenarios requires the participation of additional personnel, vehicles, cranes, and equipment. This is not a cost effective solution for periodic measurement campaigns. An aerial manipulation robot however, is capable to reach easily and quickly distant and high altitude points with no risk for the human operator. **Figure 1.2** illustrates two application examples of the aerial manipulation related with the inspection of pipes. On the left side, an inspection tool is installed over a pipe is grasped by the handles using both arms, whereas the right image represents a long reach aerial manipulator performing the visual inspection of a pipe structure for detecting leaks, using a camera installed at the end effector of the arm for this purpose. As it can be seen, the inspection arm is attached at the tip of a long reach length link that rotates with respect to the base of the aerial platform, similarly to a pendulum. This configuration facilitates the access to narrow workspaces and at the same time improves safety as it reduces the probability of impact of the aerial platform with the environmental obstacles.

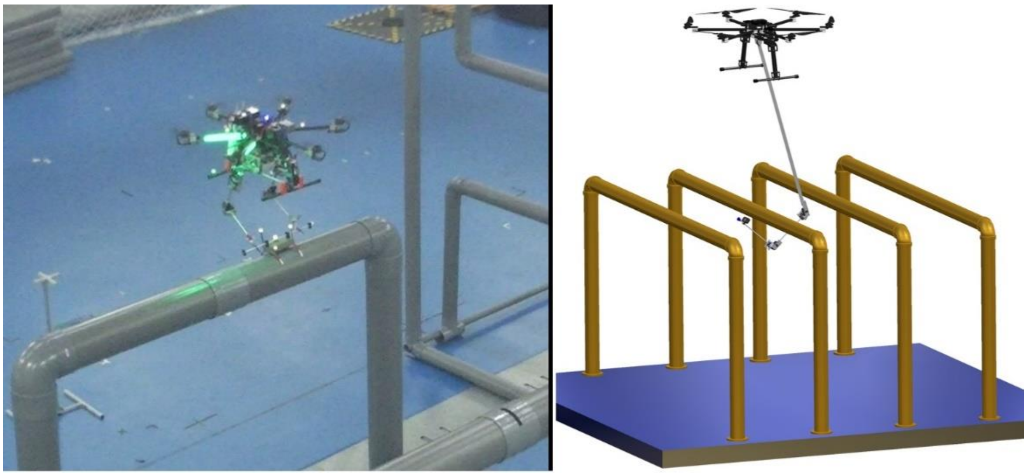

Figure 1.2. Two application examples of aerial manipulators: installation of inspection tool on pipe (left), and visual inspection of pipes for the detection of leaks using a long reach manipulator (right).

1.3.1. Operation in outdoors: perception and control

The application of the aerial manipulation technology in outdoor industrial scenarios requires the ability of perceiving and navigating in environments with obstacles. Once the aerial robot reaches the area of interest, it should be able to maintain its position stable with small deviations despite the presence of wind disturbances or interaction forces, so the arms can execute their task as if they were working in fixed base. On the one hand, both the navigation and operation phases require the use of an accurate and reliable positioning system, which typically involves different sensors such as GPS, IMU, on-board cameras, range sensors, or LIDAR. As mentioned before, since the effective reach of a human-size manipulator is around 30 cm, it is necessary that the positioning accuracy is around 5 cm, with update rates around 10 – 20 Hz, typical in most GPS sensors. Several methods for estimating the position of VTOL vehicles in outdoors have been proposed, including optical flow [37][38][39], monocular [31][32] and stereo [33][34] vision-based SLAM, or laser range sensors [40][41][42]. On the other hand, the UAV controller should be able to deal with the endogenous and exogenous forces acting over the aerial platform [43][44], including wind perturbations [23][45][46][47], the reaction wrenches associated to the motion of the arms [3][7][48][49][50], or interaction forces [51][52][53][54][55].

1.3.2. Long reach aerial manipulators

The realization of inspection and maintenance tasks in industrial scenarios using aerial robots is affected by the proximity between the blades of the aerial platform (either multirotors or autonomous helicopters) and the obstacles. The operation of the manipulator is also limited since its reach is usually inside the perimeter of the propellers and the landing gear reduces its workspace. Additionally, the interaction wrenches exerted over the manipulator during the operation on flight might compromise the stability of the aerial platform if the forces are rigidly propagated through a stiff-joint manipulator. Space robotics [75][76], nuclear waste cleanup, and civil infrastructure inspection and maintenance [77] are some usual application examples where the necessity to perform certain manipulation operations far away from the base of the robot motivated the development of long reach manipulators (LRM) [78] in the so called macro-micro configuration. However, achieving accurate position control of aerial vehicles becomes a hard task due to the dynamic coupling between the flexible link (macro part) and the dexterous manipulator installed at the tip (micro part), as any impact or contact force [79] or even the contactless motion of the arms [80] will cause a significant reaction of the flexible link that should be suppressed [81][82]. Although strain gauges are widely used in the measurement of link deflection, vision sensors have been applied for position control [83], giving direct and accurate measurements in one or two axes [84], resulting also in simpler setups.

Some works have used teams of UAVs that cooperatively carry platforms with end effectors or arms to extend the reach of the aerial manipulator. The position and orientation of the platform is set controlling the relative position of the aerial vehicles. A towed-cable system with a platform connected with cables to three quadrotors has been presented in [85]. A platform which consists of a rigid frame and multiple quadrotors that are connected to the frame through rigid bars with passive spherical joints is proposed in reference [86]. Although these configurations increase the payload of the system, they also have operational limitations coming from the large open space needed for the multiple quadrotors to fly safely. The idea of employing long reach manipulators in aerial manipulation was firstly proposed by the author in [9], presenting in [10] a prototype intended to pipe inspection (see **Figure 1.2**-right).

1.4. Bimanual aerial manipulation

A dual arm system extends the range of operations and tasks that an aerial manipulator is able to perform with respect to the single arm case [7] [8], allowing the execution of the following tasks:

- Manipulation of long bars or objects (**Figure 1.3**-left)
- Operating with one arm while the other holds a camera (**Figure 1.3**-right)
- The installation and retrieval of two sensor devices
- Grasping objects too heavy for a single arm
- Using one arm for compensating the reaction motions of the other arm
- Operating with one arm while the other is grabbed at a fixed point

This can be done at expenses of increasing the payload of the aerial platform, so additional care should be paid in reducing as much as possible the weight of each arm, removing for example those actuators which are not strictly necessary. Roughly speaking, a dual arm aerial manipulator can be built simply attaching two robotic arms at the base of an aerial platform, or well introducing a support frame as shoulder structure. This idea can be extended easily to an arbitrary number of arms. In any case, the mechanical design of a dual arm system is a relatively simple problem since it consists of attaching two identical arms side by side. The software integration is straightforward considering an implementation based on classes, in which there is one instance per arm of a class that implements the corresponding low-level control methods (update joint state, move joint, solve kinematics, etc.).

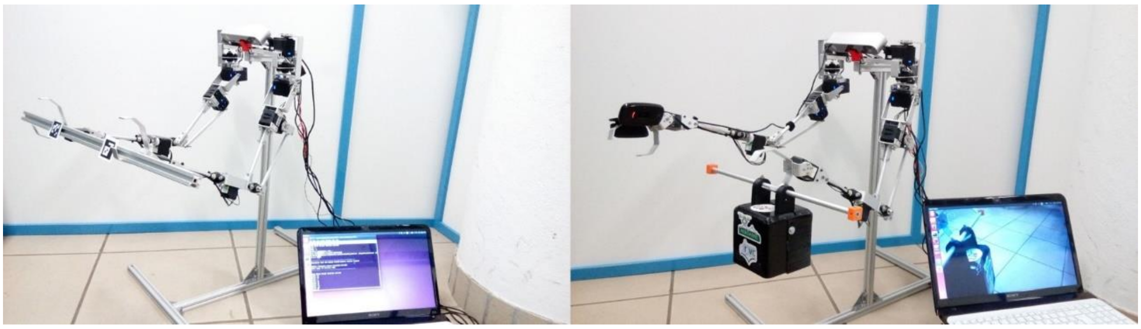

Figure 1.3. Two illustrative application examples of bimanual manipulation with lightweight dual arm: grasping long bars (left) and operating with one arm while the other holds a camera for visual servoing (right).

The control of a dual arm manipulator raises two problems with respect to the single arm case. On the one hand, the motion of the arms should be carefully planned in such a way that there are no collisions between them or with the aerial platform, as this might cause mechanical damages in any of their parts. Although it is expected that a high-level motion planner provides reliable trajectories to the arms, it is convenient that the low-level arms controller checks and prevents potential collisions in real time. On the other hand, the manipulation of an object using both arms requires a certain level of coordination or the ability to estimate and control the interaction forces associated to the bimanual operation. Consider for example a situation in which both arms are grasping a long bar in a closed kinematic chain (see **Figure 1.3**-left). The rotation of the bar involves a coordinated motion of the joints, but, in practice, some of them will be eventually overloaded due to the force exerted by some of the joints. This is a problem since the servo actuators typically employed in aerial manipulation do not provide direct torque feedback, and so, the gearbox or the motor might result damaged. In order to cope with the interaction forces associated to motion constraints in situations like this, it would be necessary to introduce some kind of elastic element between the object and the manipulator, or in the manipulator itself, whose purpose is to provide a certain level of mechanical tolerance against overloads.

Bimanual manipulation with multi-rotors has been addressed only in a few recent works [5][6][7][8], indicating their main specifications in **Table 1.4**. However, dual arm manipulators have been already considered in space applications for several decades [67]. In this sense, the redundancy provided by a second arm in a free-floating space robot can be exploited for optimizing the torque control of the whole manipulator [68], planning the trajectories of the arms in such a way that robot base is stabilized [69]. Several control methods have been developed and tested in dual arm systems with fixed or mobile base. Reference [70] deals with the cooperative control of two 3-DOF flexible link manipulators when holding an object in a closed kinematic chain. Dexterous manipulation with DLR humanoid robot Justin is shown in [71]. Impedance control is evaluated in [72] with two 6-DOF industrial manipulators. Cartesian impedance control is also applied for the real-time motion tracking in an anthropomorphic dual arm [73]. An extensive survey on other dual arm systems can be found in [74].

Table 1.4. Comparison of several dual arm aerial manipulation prototypes.

Ref. / Year	**Aerial platform**	**Manipulator**			
		Type	**DOF**	**Reach [m]**	**Lift load per arm [kg]**
[5] / 2014	Quadrotor	Stiff-joint	2	NA	NA
[6] / 2016	Octorotor	Commercial	NA	NA	NA
[7] / 2017	Hexarotor	Stiff-joint	10	0.5	0.75
[8] / 2018	Hexarotor	Compliant	8	0.5	0.2

1.5. Compliance

One of the current trends in aerial manipulation is the design and development of lightweight and compliant manipulators [8][10][18][26][27][56] (see **Table 1.5**), motivated in part by the convenience to increase safety during the physical interactions with the environment. Mechanical compliance not only protects the servo actuators and the aerial platform against impacts [8] and overloads, but it also provides a simple way to estimate and control the joint torque and the contact forces, just measuring the deflection of the elastic element, typically springs or elastomers [27][57]. The term "compliance" is usually associated to the mechanical elasticity or flexibility, but a stiff joint manipulator can also show a compliant behaviour. An actuator or manipulator is said to be compliant if it is capable to accommodate or adapt to the forces generated during the interactions with the environment or during the manipulation of an object, preventing that any component is damaged as result of the operation or due to unexpected impacts. This feature is closely related to safety in the context of human-robot collaboration. Imagine a work-cell shared by a human operator and an industrial manipulator. If, accidentally, the operator enters in the workspace of the robot and is hit by this, the consequences may vary drastically depending on the ability of the robot to detect the impact and react to it. The injury is caused by the transfer of the kinetic energy of the robot to the human body in a very short period of time. The capacity of an elastic element to absorb the excess of energy in a passive way at higher rates than the actuator may provide is the key concept in the development of mechanically compliant manipulators. Although most industrial robots are intrinsically stiff (the joint stiffness is 2 – 3 orders of magnitude higher than in a lightweight and compliant joint arms presented in this work), the accuracy of the force-torque sensors and the execution of control methods at rates above 1 kHz allow the implementation of impedance controllers with a compliant behaviour.

Table 1.5. Comparison of different prototypes of compliant joint arms for aerial manipulation.

Ref. / Year	Elastic element	DOF	Reach [m]	Joint stiffness [Nm/rad]	Max. torque [N·m]	Weight [kg]
[26] / 2015	Ext. springs	1	0.18	0.337	1.5	0.36
[56] / 2016	Elastomer	1	0.3	NA	NA	0.24
[88] / 2015	Ext. springs	1	0.25	X	NA	0.35
[57] / 2018	Compr. springs	1	0.25	1.2	1.17	0.25
[27] / 2016	Compr. springs	2	0.4	1.48	1.17	0.3
[8] / 2017	Compr. springs	8	0.50	2.93	2.34	1.3

This thesis is focused in the development of mechanically compliant lightweight manipulators designed for their integration in multirotor platforms [8][27][57], introducing an elastic element (springs) between the servo actuators and the output links. This is a particular implementation of the series elastic actuators [58][59] that allow the estimation and control of the forces/torques through the measurement of the deflection of the flexible element, what can be obtained integrating potentiometers or encoders in the mechanism. Thus, the force control is reduced to a position control problem in which the compliant sensor is characterized by a second order dynamics typical of a mass-spring-damper system. This behaviour affects the accuracy in the position control of the manipulator, and may be the cause of undesired oscillations when the arm suffers high accelerations. However, the benefits of a compliant manipulator are evidenced during the execution of certain tasks on flight like grasping. The experimental results reveal that the manipulator is much more tolerant than a stiff joint manipulator to overloads associated to interaction forces or motion constraints, preventing that the internal protection mechanisms of the servo actuators (based on monitoring the temperature or the PWM signal) are activated. This contributes to increase the lifespan of the manipulator, reducing also the probability of crashes of the platform, since the excess of energy generated during an impact can be stored in a passive way in the compliant joints and then released actively.

Variable stiffness actuators [60] are an extension of the series elastic actuators which employ two motors to control simultaneously the position and stiffness of the link, adjusting dynamically the relative compression of the springs. Consider for example the elbow joint in the human arm, where the biceps and triceps muscles are two antagonistic linear actuators connected to the fore-arm link through the respective elastic tendons. If both muscles contract, then the joint does not rotates, but the stiffness increases as the tendons are stretched. If the biceps is contracted while the triceps is relaxed, then the elbow rotates and lifts the forearm link. Several prototypes of antagonistic variable stiffness actuators have been proposed [61][62][63], demonstrating their ability to vary the stiffness of a robot manipulator during the execution of a trajectory. Unlike the antagonistic configuration, where two identical actuators are arranged symmetrically around the joint, other variable stiffness mechanisms make use of an actuator for moving the joint and a second actuator (typically smaller) for adjusting the stiffness of the spring [64][65][66]. In any case, these mechanisms require the use of two actuators for each joint, so they are not suitable for aerial manipulation in terms of weight. This has motivated the development of methods to vary the apparent impedance of a lightweight and compliant joint with a single actuator, exploiting the mechanical compliance for this purpose [57].

1.6. Scope of this work

1.6.1. Lightweight and compliant aerial manipulators

This thesis is focused in the development and experimental validation of different prototypes of lightweight and compliant manipulators designed for their integration in multirotor platforms. The success in the application of the aerial manipulation technology in outdoor scenarios depends largely on the mechanical properties of the robotic arms, especially when the operations to be performed involve contact forces with the objects or with the environment. Whereas most research works have treated extensively the modelling, estimation, control and planning of aerial manipulators, the design of lightweight and compliant robotic arms is much less extended. Actually, mechanical compliance, the key feature of the presented prototypes, arises from the need to provide the aerial robot a method to handle the interaction forces on flight without compromising the stability of the attitude controller, taking into account the technological limitations of the servo actuators typically employed in this field (no torque estimation/control, only position control, low update rates). Some works design the control system assuming that the joint torque control is possible, or they ignore the influence of the forces/torques generated in grabbing situations over the manipulator. If the shaft of the servos is directly exposed to the torques exerted over the respective links during the contact phases, it is highly probable that the gearbox is damaged after a few flight tests, since the manipulator must support the kinetic and potential energy of the whole aerial robot.

1.6.2. Design, development, and experimental validation of prototypes

The approach adopted by the author consists of developing manipulators whose mechanical features contribute to improve the performance of an aerial manipulation robot in outdoors, and at the same time extend the range of operations that can be executed. In this sense, the low weight and inertia features reduce the influence of the arms motion over the stability of the aerial base, which is also convenient in terms of positioning accuracy. Introducing a flexible element in the joints and measuring the deflection caused by external forces allow the detection and localization of close obstacles by contact, the estimation and control of contact forces, and the protection of the actuators and the aerial platform to impacts and in situations involving motion constraints (closed kinematic chains, grabbing, pushing/pulling). The frame structure of the manipulators is carefully designed in such a way that it protects the actuators against impacts and overloads, being robust, but low weight. The mechanical construction of the arms is closely related with the kinematics, since it is convenient that all the joint axes intersect in a common point in order to simplify the resolution of the kinematics and dynamics. The design and development of a robot manipulator is a complex iterative process that involves a general knowledge about mechanics, control, dynamics/kinematics, electronics, and manufacturing. The process can be decomposed in the phases represented in **Figure 1.4** and detailed below.

1. **Concept design**: the specifications of the manipulator are defined, including the number of joints, estimated weight, kinematic configuration, link lengths, the compliant element, and the control capabilities to be developed (position/trajectory control, force control, collision detection, grasping). Several preliminary designs are developed on paper, evaluating different frame structures that ensure robustness and very low weight. The mechanical design of the manipulator is determined by the geometry of the frame parts that can be manufactured (flat, L-shaped or U-shaped frames, circular hollow profiles). All the developed prototypes are built from standard and commercially available aluminium profiles, or manufactured by laser cut.

However, no CNC-machined part has been employed. This design constraint was imposed in order to simplify and reduce the cost and time of the manufacturing process.

2. **3D computer design**: the preliminary designs obtained in previous phase are evaluated and validated using 3D modelling software (Solid Edge, CATIA), generating all the individual frame parts and the assembly of the different structures (shoulder, upper arm, forearm, end effector). The 3D drawings of the servo actuators and other components employed in the prototypes are usually provided by the manufacturer. The mass density of all the parts is specified during the design process, so it is possible to estimate the weight of the assembly and obtain the moments of inertia. Almost the 40% of the development time of a prototype is devoted to refine the 3D design through successive iterations, requiring in most cases the manufacturing of some of its parts in order to evaluate the feasibility and convenience. Up to eight variations were proposed during the development of the anthropomorphic, compliant and lightweight dual arm manipulator, since it was hard to find a solution that satisfied all the design constraints (intersection of all axes in a common point, integration of a compliant transmission in all the joints, mechanical servo protection, high robustness, very low weight, and human-like kinematics).
3. **Manufacturing and assembly**: several prototypes have been completely manufactured by the author in the workshop from standard aluminium profile sections. The frame parts of the anthropomorphic, compliant and lightweight dual arm [8] were manufactured by laser cut. The stiff-joint dual arm [7] and the compliant dual arm [8] consists of around 50 – 60 frame parts, 100 – 200 screws, and around 16 flange bearings. The tolerance of the aluminium frame parts should be 0.1 mm in order to ensure the correct assembly with other parts or with the servo actuators. The manufacturer of the flange bearings extensively used in the prototypes, igus®, recommends an h7 tolerance for the crossing shafts, so the friction and clearance are minimal. The experience acquired with the development of the different prototypes of lightweight and compliant manipulators lead to the refinement of a design methodology based on four basic components: aluminium frame parts, servo actuators, flange bearings, and the springs.
4. **Development of software and electronics**: the software architecture of the manipulators has been completely developed from the scratch in C/C++ using the POSIX standard and the *cmake* tool. This facilitates the integration with different Linux distributions (Ubuntu, XUbuntu, LUbuntu, or Debian) in several computer boards (Odroid, Raspberry Pi, Intel NUC), whose small size and low weight make them suitable for aerial manipulation. The OpenCV library has been used for matrix operations and for image processing in the vision based deflection estimation methods described in [57][87]. The source code is decomposed in five main C++ classes (the servo state, the arm controller, the kinematics, the task manager, and data log class) and a number of threads running in parallel that handle the communication with the servo actuators, the sensors, the Ground Control Station, or with other executables like the UAV controller. An external control mode has been also implemented, in such a way that a MATLAB/Simulink model or a ROS node can send references and receive information from the manipulator through a UDP socket interface. A microcontroller board, also programmed in C, is used as data acquisition card, sending the measurements taken from the deflection potentiometers to the computer board through a serial port interface.
5. **Design and implementation of functionalities**: the interest in exploring new capabilities and functionalities that can be applied in aerial manipulation has motivated the design of the prototypes of lightweight and compliant manipulators presented in this thesis. Most of these functionalities are based on the deflection measurement, which allow the estimation of the weight of a grasped object [88], the detection of collisions [27][89], the control of the contact forces [27][57] and the localization of obstacles by contact [9][27]. Virtual variable impedance

control is proposed in [57], demonstrating that a single compliant joint can vary its apparent stiffness and damping without the need of a second actuator. Trajectory control and bimanual object grasping with visual servoing have been implemented with the two dual arm prototypes described in [7][18]. Simple feedback control schemes have been proposed and experimentally tested, taking into account the limitations of the servo actuators typically employed in aerial manipulation (only position control, no torque feedback, control rates below 100 Hz).

6. **Experimental validation in test-bench**: before their integration in the aerial platform, the prototypes and the implemented functionalities are extensively evaluated in fixed base test bench in order to reduce the probability of fault during the flight tests. In this phase, the actuators and sensors are calibrated, the parameters of the trajectory and force controllers are tuned, analysing graphically their performance, and several connectivity and boot tests are carried out.
7. **Integration in aerial platform**: this involves the installation of the manipulator, on-board computer, sensor devices, batteries and communication devices in the multirotor, as well as the installation of the different software modules in the computer. The assembly of the manipulator requires a customized support frame attached to the landing gear or at the base of the aerial platform, and it should be done with special care so the workspace of the arms is maximized, taking into account their kinematic configuration.
8. **Flight tests**: several experiments have been conducted in indoor-outdoor scenarios in order to evaluate the performance of the lightweight and compliant aerial manipulators presented in this thesis. The influence of high speed arms motion over a standard industrial autopilot is analysed in [7], proposing a method for estimating and compensating the reaction torques generated by the arms. Bimanual object grasping with the compliant dual arm is demonstrated in [8][18], whereas [57] shows its application to contact force control, evidencing the benefits of mechanical joint compliance during the physical interactions. The take-off and landing manoeuvres, and the response to impacts in a single arm, long reach manipulator in pendulum configuration is documented in [10].
9. **Documentation and publication**: the design, development and experimental validation of the lightweight and compliant manipulators has been documented in several conference and journal papers, including the corresponding videos.

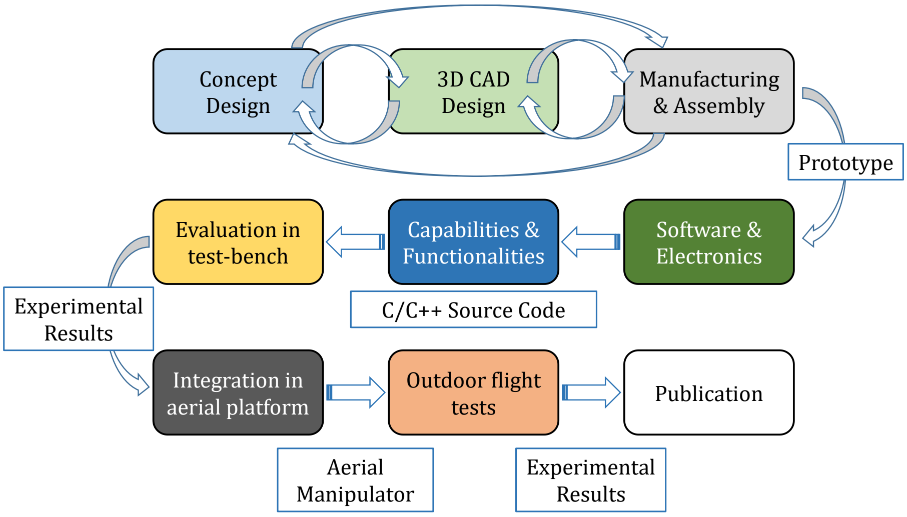

Figure 1.4. Process flow diagram followed in the design, development and experimental validation of a prototype of aerial manipulator.

1.6.3. Sensor fault tolerance in multi-UAV systems

The early detection of faults in the position and orientation sensors of an aerial manipulator may prevent risky situations involving damages in the platform, in the environment, or even potential injuries in case the robot hits a human. An aerial robot operating in outdoors may be affected by position sensor faults due to GPS signal loss if the aerial robot passes under a bridge, occlusions in a laser tracking system due to unexpected obstacles, variation in the light conditions in a vision-based localization system, or well interferences in the radio signal received by a range sensor due to multi-path. Most research works in this field are developed in indoor testbeds, using highly accurate and reliable positioning systems such as Vicon or OptiTrack, whereas the position estimation in outdoors is still a technological problem in these terms. Since the aerial robot is intended to operate at high altitudes or in remote areas far away from the reach of the human operators, it results convenient to provide a method for detecting and replacing the faulty sensors on flight, taking into account that the reaction time is critical to prevent potential collisions. The proposed solution consists of deploying one or more UAVs equipped with cameras, denoted as observers, whose mission is to track and stay visually focused on the aerial manipulator, monitoring its position so they can report any deviation and help the aerial robot to recover the control.

References [90][91] analyse the problem of sensor fault detection and identification in multi-UAV systems, proposing several methods and strategies that exploit the information provided by the vision sensors on-board the multirotors for this purpose. It is shown also that the faulty position sensor can be replaced by a cooperative virtual sensor that integrates the measurements of a group of observers focused on the affected platform, so it can be guided to a safe position and land.

1.7. Contributions of this work

The main contribution of this work is the design, development and experimental validation of several prototypes of lightweight and compliant manipulators intended to aerial manipulation with multirotor platforms. The prototypes manufactured by the author are listed below:

1. Lightweight and compliant arm (February 2015)
2. Compliant and lightweight anthropomorphic finger module (June 2015)
3. Lightweight and human size dual arm (September 2015)
4. Lightweight compliant arm with compliant finger (February 2016)
5. Flexible long reach link with lightweight dual arm (June 2016)
6. Anthropomorphic, compliant and lightweight dual arm (November 2016)
7. Lightweight and compliant arm for visual inspection (December 2017)
8. Long reach aerial manipulator with dual arm in pendulum configuration (January 2018)
9. Compliant long reach aerial manipulator for contact-based inspection (January 2018)

A picture of the developed prototypes can be seen in **Figure 1.5**. The lightweight dual arm (2015) and the anthropomorphic dual arm (2016) were integrated in different hexarotor platforms and tested in outdoor flights, as it can be seen in **Figure 1.6**, demonstrated bimanual object grasping. The main features of the developed prototypes are indicated below.

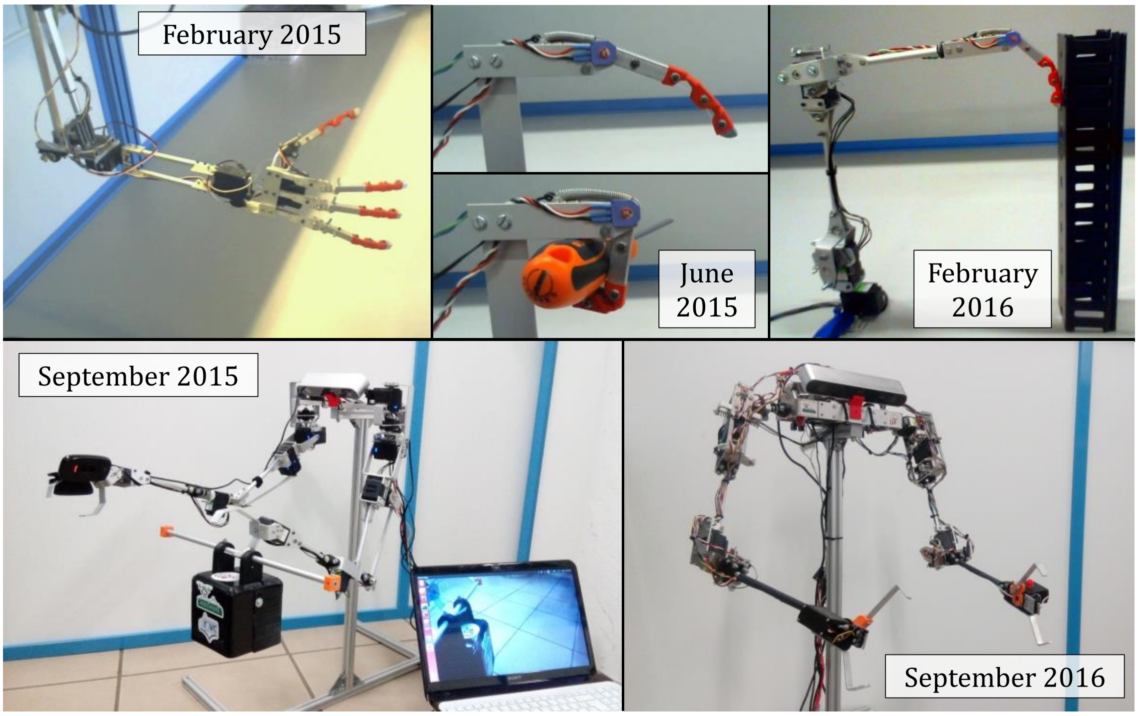

Figure 1.5. Prototypes of lightweight and compliant manipulators developed by the author.

1.7.1. Low weight

The design and development of robotic arms intended to aerial manipulation is a technological challenge since the maximum payload and flight time of the aerial platform is quite limited. The size and weight of the overall system is determined by the maximum lift load that the arms should support and by the number of joints in the desired kinematic configuration. With this, it is possible to estimate the weight of the manipulator and thus the required payload of the multirotor, taking into account the additional weight associated to the on-board computer, communication devices, sensors, and batteries. In general, the mass of the manipulator can be decomposed in two terms: one corresponding to the weight of the actuators, and other associated to the frame structure that supports the servos. It is convenient to remark this distinction since the only way to reduce the mass of the manipulator is through the second term, considering a particular combination of servo actuators. That is, most of the effort to achieve the low weight feature is in the design of the frame structure, which involves the choice of the materials (aluminium, carbon fibre, plastic) the geometry of the different frame parts, and the mechanical properties (compliance, servo protection, impact resistant). In the prototypes of lightweight and compliant manipulators developed by the author, the weight of the frame structure is around the 50 – 60% of the total mass. This ratio is relatively high due to the implementation of servo protection and joint compliance mechanisms.

1.7.2. Kinematic configuration

Since most industrial inspection and maintenance operations are conducted nowadays by human operators, it would be interesting that the aerial manipulator replicates the size and kinematics of the human arm, which provides four positioning joints (three at the shoulder and one at the elbow), and three joints at the wrist, whereas the kinematic configuration of the industrial manipulators usually consider three positioning joints (two at the shoulder and one at the elbow) and three joints for wrist orientation. The limitation in the payload imposed by the aerial platform constrains the number of joints in the manipulator, so, depending on the level of dexterity required by the task, some actuators should be removed in order to reduce the total weight. In this sense, the payload-to-weight ratio is a representative parameter of the efficiency of the arm that tends to decrease as the number of joints is higher. Due to the dynamic coupling between the aerial platform and the manipulator, it also results convenient that the inertia of the arms is as low as possible in order to reduce the effect of the reaction wrenches over the attitude controller. Taking into account that the inertia depends on the square of the distance from the center of mass to the rotation axis, it is preferable to avoid placing the actuators far away from the base of the manipulator, what can be achieved removing those joints which are not essential in the manipulation operation. The use of transmission mechanisms such as rigid bars, pulleys or gears should be avoided as these usually increase the weight or reduce the rotation range.

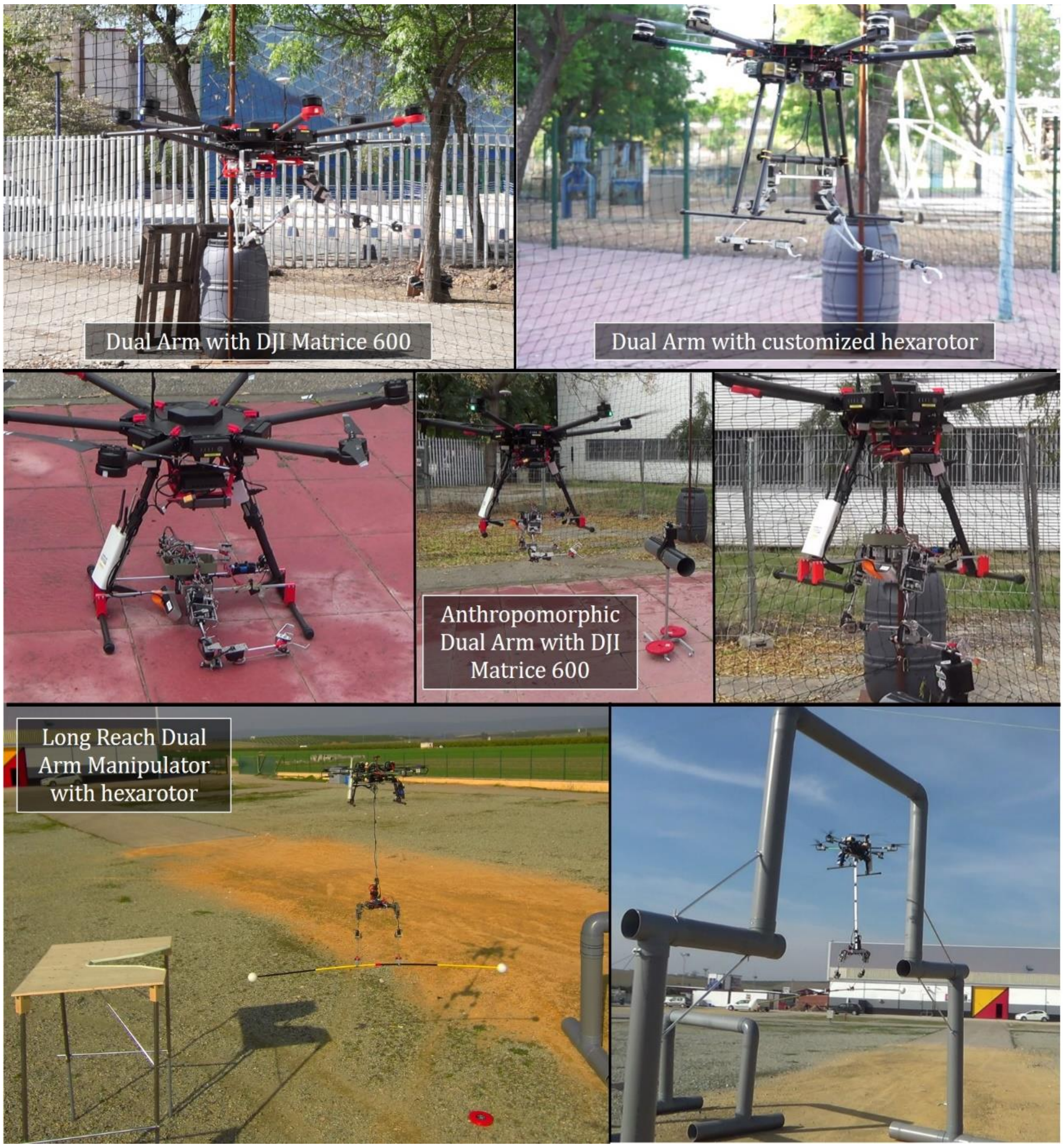
Dual Arm with DJI Matrice 600
Dual Arm with customized hexarotor
Anthropomorphic Dual Arm with DJI Matrice 600
Long Reach Dual Arm Manipulator with hexarotor

Figure 1.6. Dual arm aerial manipulators. Outdoor flight tests with different hexarotor platforms.

1.7.3. Mechanical joint compliance

Unlike most industrial manipulators, whose actuators allow the measurement and control of the join torque at rates above 1 kHz, the actuators typically employed in aerial manipulator (the so called "smart servos") only provide position or speed control at rates below 100 Hz. The use of these servos is justified by their high torque-to-weight ratio (7.6 N·m stall torque / 145 grams weight in the case of the Herkulex DRS-0602), ease of assembly in a frame structure, and because the motor, gearbox, sensors, and control electronics is embedded in a compact device interfaced through a serial port, allowing the connection of several servos in daisy chain. However, these actuators are not suitable in those applications involving physical interactions since the impacts between the aerial manipulator and the environment may damage the gearbox, and the contact forces cannot be estimated or controlled from the position of the servo unless a flexible element is introduced between the actuator and the environment. Motivated by the need to estimate and control the interaction forces/torques that affect the manipulator, this work proposes the integration of a simple and compact spring-lever transmission mechanism between the shaft of the servos and the output links, providing compliance with deflection feedback. **Figure 1.7** illustrates the implemented mechanism in the four joints of the anthropomorphic, compliant and lightweight dual arm.

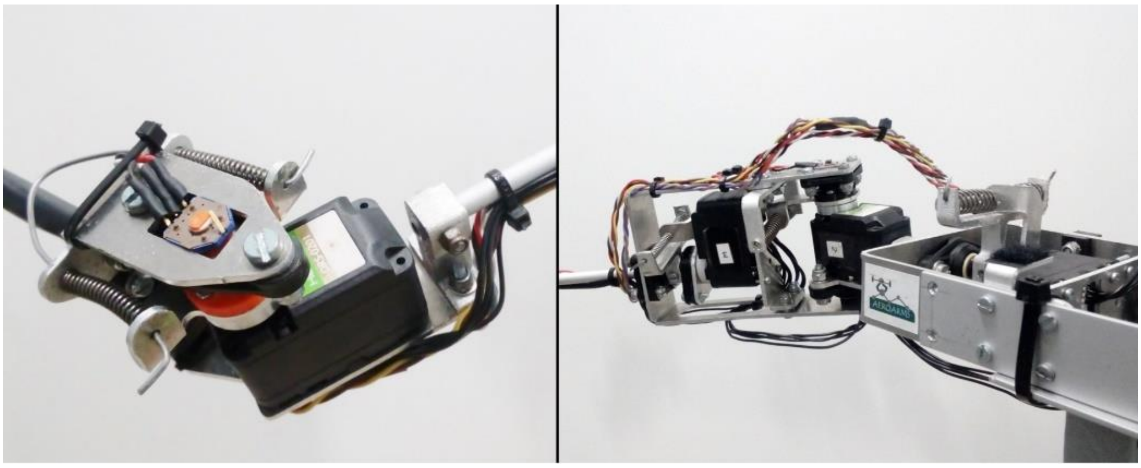

Figure 1.7. Spring-lever transmission mechanism introduced in the joints of the anthropomorphic dual arm.

Mechanical joint compliance is a highly desirable feature in aerial manipulation for two reasons. Firstly, it allows the estimation and control of the forces/torques by means of joint deflection. That is, measuring the deformation of the elastic element (a compression spring, in this case), it is possible to estimate the torque supported by the actuator, and at the same time control it through the position of the servo. Secondly, a spring-lever transmission mechanism acts as low pass filter due to the natural stiffness and damping of the springs and the flange bearings, which contributes to protect the servo actuators against peak forces and overloads that will arise during the operation on flight of the aerial manipulator. What is more, the tolerance of the arms associated to the deflection of the joints results especially useful when the motion of the arms is constrained, for example in closed kinematic chains or in grabbing situations. The excess of energy in these cases is stored temporarily in the compliant joints as elastic potential energy, and released later in an active way simply controlling the position of the servos. Different strategies on passive/active compliant control can be defined and implemented for improving the performance and reliability of the aerial robot. On the other hand, a compliant joint manipulator presents three inconveniences: 1) the positioning accuracy of the manipulator is significantly influenced by gravity and dynamic terms due to the deflection of the joints, 2) the design and integration of a compact spring-lever transmission mechanism is not easy due to space limitations and the lever-link length ratio (~1:10), requiring springs with relative high stiffness and low section, and 3) the dynamics of this compliant torque sensor cannot be ignored if the deflection of the joints is introduced in the control loop, since the dynamic terms may destabilize the controller of the arm. In any case, the evidenced benefits of compliance justify its application in aerial manipulation.

1.7.4. Human size

All the robotic arms developed by the author were designed in such a way that the forearm/upper arm link lengths is 20 – 25 cm and the separation between the arms is 30 – 35 cm. This design criteria is justified by the convenience to provide a human-like manipulation capability to the aerial robot, especially if the arms are intended to replace a human operator in certain inspection and maintenance tasks. Note however that although the length of the human arm from shoulder to wrist is around 50 cm, the effective reach with respect to its nominal operation position is around 30 cm, taking into account that the maximum rotation angle of the elbow joint is around 135º and that the robotic arm should not reach position references which are beyond the 95% of its length in order to avoid kinematic singularities. Although this might result surprising, it should be observed that humans extend significantly their reach thanks to the motion of the torso, abdomen and legs. Increasing the length of the links is not a convenient solution as the torque wasted by the servos in lifting the weight of the arm increases proportionally with the link length. It was also imposed as design requirement that the shape of the arms was as close as possible to the human arm for aesthetic reasons.

1.7.5. Mechanical robustness

During the physical interactions on flight between the aerial manipulator and the environment, it is expected that the robotic arms are affected by impacts, contact forces and overloads due to motion constraints. It should be noted that, in case of an impact, the arms will support the kinetic energy of the whole aerial robot. Therefore, it is important to prevent at hardware level that the servo actuators, which represent around the 70% of the total cost in materials of the manipulator, are damaged and have to be replaced frequently, with the corresponding waste of time. One of the novel design concepts introduced in the dual arm prototype developed in 2015 is the mechanical servo protection to axial-radial loads through the use of flange bearings attached to the aluminium frame structure. The loads, typically generated at the end effector due to the interaction with an object (supporting its weight) or the environment (contact forces or impacts), will be transmitted to the base of the UAV through the links and joints of the arm. The frame structure of the dual arm prototypes has been designed in such a way that the servos are partially or fully isolated against these loads.

1.7.6. Low manufacturing cost

In the developed prototypes of lightweight and compliant manipulators (see **Figure 1.5**), almost the 70% of the cost in materials corresponds to the servo actuators, whereas the rest corresponds to the aluminium frame structure, the flange bearings, screws, nuts and springs. One of the main design constraints imposed from the beginning was that the frame structure could be manufactured from standard aluminium profiles commercially available, or well produced by laser cut, whose cost is much lower compared to CNC machined parts. The malleability of this material facilitates the construction of L-shaped or U-shaped frame parts simply bending flat profile sections. Although the mass density of carbon fibre is a 57% lower, the cost of producing geometries like these is relatively high since it requires customized moulds and involves a more complex manufacturing process.

1.8. List of publications

Journal Papers

- A. Suarez, G. Heredia and A. Ollero, "Design of an Anthropomorphic, Compliant, and Lightweight Dual Arm for Aerial Manipulation," in *IEEE Access*, vol. 6, pp. 29173-29189, 2018.
- A. Suarez. A. E. Jimenez-Cano, V.M. Vega, G. Heredia, A. Rodriguez-Castaño, and A. Ollero, "Design of a lightweight dual arm system for aerial manipulation," in Mechatronics, vol. 50, pp. 30-44, 2018.
- A. Suarez, G. Heredia and A. Ollero, "Physical-Virtual Impedance Control in Ultralightweight and Compliant Dual-Arm Aerial Manipulators," in *IEEE Robotics and Automation Letters*, vol. 3, no. 3, pp. 2553-2560, July 2018.
- A. Suarez. G. Heredia, and A. Ollero, "Cooperative virtual sensor for fault detection and identification in multi-UAV applications, " in Journal of Sensors, vol. 2018, Article ID 4515828, 19 pages, 2018.

IROS / ICRA Conference Papers

- A. Suarez, P. Sanchez-Cuevas, M. Fernandez, M. Perez, G. Heredia, and A. Ollero, "Compliant joint, long reach aerial manipulation for contact-based inspection operations," in *2018 IEEE/RSJ International Conference on Intelligent Robots and Systems (IROS)*, Madrid.
- A. Caballero, A. Suarez, F. Real, V. Vega, M. Bejar, A. Rodriguez-Castaño, and A. Ollero, "Motion planning for transportation in aerial long reach manipulators with two arms," in *2018 IEEE/RSJ International Conference on Intelligent Robots and Systems (IROS)*, Madrid.
- A. Suarez, G. Heredia, and A. Ollero, "Physical-virtual impedance control in ultra-lightweight and compliant dual arm aerial manipulators," 2018 *IEEE International Conference on Robotics and Automation (ICRA+RAL)*, Brisbane, 2018.
- A. Suarez, P. R. Soria, G. Heredia, B. C. Arrue and A. Ollero, "Anthropomorphic, compliant and lightweight dual arm system for aerial manipulation," *2017 IEEE/RSJ International Conference on Intelligent Robots and Systems (IROS)*, Vancouver, BC, 2017, pp. 992-997.
- A. Suarez, G. Heredia and A. Ollero, "Lightweight compliant arm with compliant finger for aerial manipulation and inspection," *2016 IEEE/RSJ International Conference on Intelligent Robots and Systems (IROS)*, Daejeon, 2016, pp. 4449-4454.
- A. Suarez, G. Heredia and A. Ollero, "Cooperative sensor fault recovery in multi-UAV systems," *2016 IEEE International Conference on Robotics and Automation (ICRA)*, Stockholm, 2016, pp. 1188-1193.
- A. Suarez, G. Heredia and A. Ollero, "Lightweight compliant arm for aerial manipulation," *2015 IEEE/RSJ International Conference on Intelligent Robots and Systems (IROS)*, Hamburg, 2015, pp. 1627-1632.

Book Chapters

- "Aerial robotics manipulation" – Chapter 2.5 (Compliant aerial manipulation with dual arms). Editors: Anibal Ollero and Bruno Siciliano. Springer Transactions on Advanced Robotics – 2018.

ICUAS / ROBOT / MED / RobotSoft Conference Papers

- A. Suarez, A. M. Giordano, K. Kondak, G. Heredia, and A. Ollero, "Flexible link long reach manipulator with lightweight dual arm: soft-collision detection, reaction and obstacle localization," in *IEEE/RAS RobotSoft*, Livorno 2018.
- A. Suarez, A. E. Jimenez-Cano, V. M. Vega, G. Heredia, A. Rodríguez-Castaño and A. Ollero, "Lightweight and human-size dual arm aerial manipulator," *2017 International Conference on Unmanned Aircraft Systems (ICUAS)*, Miami, FL, USA, 2017, pp. 1778-1784.

- A. Suarez, G. Heredia, and A. Ollero, "Vision-based deflection estimation in an anthropomorphic, compliant and lightweight dual arm," in ROBOT 2017: Third Iberian Robotics Conference. Advances in Intelligent Systems and Computing, vol. 694, 2018.
- A. Suarez, G. Heredia, and A. Ollero, "Compliant and lightweight anthropomorphic finger module for aerial manipulation and grasping," in ROBOT 2015: Second Iberian Robotics Conference. Advances in Intelligent Systems and Computing, vol. 417. Springer, Cham. 2016.
- P. Grau, A. Suarez, A. Rodriguez-Castaño, and A. Ollero, "Design of a high performance dual arm aerial manipulator," in ROBOT 2017: Third Iberian Robotics Conference. Advances in Intelligent Systems and Computing, vol. 693, 2018.
- A. Suarez, G. Heredia, y A. Ollero, "Manipulador aéreo con brazos antropomórficos de articulaciones flexibles," en Jornadas de Automática de Gijón, 2017.

1.9. Organization of this thesis

The content of this thesis is organized in the following way. Chapter 2 describes the design and development of the lightweight and compliant manipulators created by the author, the integration in different multirotor platforms, and the hardware/software architecture. The criteria adopted in all the chapters is presenting the prototypes in order of complexity (compliant joint, compliant arm, dual arm, long reach manipulator with single/dual arm) rather than following the chronological order in their creation, so the coherence and clarity is maintained along the document. Chapter 3 explores the benefits compliant joint manipulators, remarking its functionalities and potential applications in aerial manipulation. The chapter describes several functionalities based on the deflection measurement of the flexible joint/link, including force-torque estimation and control, impact detection, zero torque control in grabbing situations, or obstacle localization. Chapter 4 covers the kinematics, dynamics and control of the compliant and lightweight prototypes, proposing a generalized control scheme for the whole aerial manipulation robot. The chapter also analyses the passivity properties of the flexible joints, the limits in the energy storage capacity, and the possibility to vary the apparent stiffness and damping controlling the deflection angle through the position of the servo. Chapter 5 presents the experimental results obtained from the evaluation of the different prototypes of lightweight and compliant single arm manipulators in test-bench and in outdoor flight tests, whereas Chapter 6 shows the results obtained in indoors and outdoors flight tests with dual arm manipulators, demonstrating their application in bimanual object grasping with visual feedback, contact force control, soft-collision detection and reaction, obstacle localization, virtual variable impedance control and teleoperation. The conclusions and future work are included at the end along with the references.

Chapter 2 – Design and development of lightweight and compliant aerial manipulators

This chapter describes the prototypes of lightweight and compliant manipulators developed by the author, presenting them in order of complexity, from the single joint case to the dual arm system, as well as the long reach manipulators. The design requirements relative to their application in aerial manipulation are firstly evaluated, considering the low weight and inertia features, the technological limitations associated to the servo actuators, the kinematic configuration of the manipulator, the materials for the frame structure, and the benefits of mechanical joint compliance. The integration of the manipulators in three different hexarotor platforms is also detailed, including the hardware and software architecture.

The rest of the chapter is organized as follows:

2.1. Design requirements in aerial manipulation
2.2. Compliant joint: design and mechanics
2.3. Lightweight and compliant joint arm prototypes
2.4. Lightweight and compliant finger module
2.5. Lightweight and human-size dual arm aerial manipulator
2.6. Anthropomorphic, compliant and lightweight dual arm
2.7. Flexible link, long reach aerial manipulators

2.1. Design requirements in aerial manipulation

2.1.1. Low weight and inertia features

The first two parameters that should be determined in the design of a robotic arm to be integrated in an aerial platform are its weight and maximum lift load. Let us call PL_{UAV} to the maximum payload that the UAV is able to lift, and m_{arm} and PL_{arm} to the weight and expected payload that the arm should lift, respectively. Then, the following equation can be defined:

$$m_{arm} + PL_{arm} \leq \eta \cdot PL_{UAV} \tag{2.1}$$

Here $\eta \cong 0.7$ is the dynamic margin constant that indicates how far away the brushless motors of the UAV are from the saturation. If the aerial platform is overloaded ($\eta > 0.8$), the propellers may suffer overheating and they might not respond properly to motion commands. In order to reduce the inertia of the arms, and thus the influence of arms motion over the aerial platform, it results convenient to place the servos as close as possible to the base of the aerial platform. Different transmission mechanisms can be employed for this purpose, including timing belts [2], pulley-wire [26] or rigid bars [7]. However, these solutions typically increase the weight of the manipulator, reduce the range of rotation of the joints, and complicate the design and assembly of the manipulator. The mass distribution of the different components employed in the construction of the compliant dual arm (see **Section 2.6**) are represented in **Figure 2.1**, whereas **Table 2.1** indicates the mass density of the different components and materials.

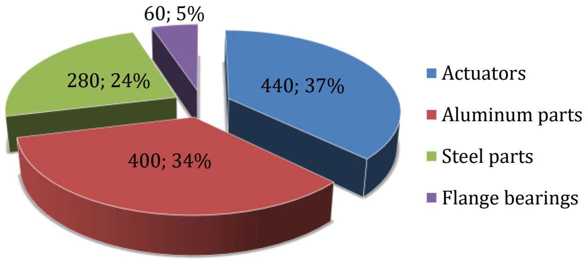

Figure 2.1. Mass distribution (grams and %) of the anthropomorphic and compliant dual arm.

Table 2.1. Materials employed in the prototypes of lightweight and compliant manipulators.

Material	**Mass density [g/cm³]**	**Description/Application**
Aluminium	2.8	Frame structure
Steel	7. 85	Screws, nuts, washers and springs
igus® polymers	1.4	EFOM/EFSM flange bearings
Servo actuators	1.5	Equivalent mass density of the servos

2.1.2. Actuators

The design and development of robotic arms intended to aerial manipulation is still a hard task due to the multiple design requirements imposed by the aerial platform in terms of very low weight, low inertia, mechanical robustness and dexterity. What is more, there are important technological limitations as only a few brands of actuators are suitable for this purpose. In this sense, the so called smart servos, such as Herkulex or Dynamixel, are nowadays the best option for building low weight manipulators [1][5][7][8][28]. These devices include the motor, gearbox, electronics, control and communications in a compact device that can be easily assembled in a frame structure, providing high torque to weight ratios. However, the performance of these actuators from the control point of view is quite limited, as they do not provide torque feedback or control, the control rates are usually low (<100 Hz), and the embedded servo controller has to be interfaced. Although the lift load of the arms should be determined by the application, its value is determined in practice by the combination of servo actuators employed, taking into account that the stall torque parameter provided by the manufacturer is usually 2 – 3 times higher than the maximum dynamic torque that the servo is able to provide.

2.1.3. Kinematics

The choice of the kinematic configuration of the arms is determined in the first place by the task that the aerial robot is expected to perform. Almost all aerial manipulators that can be found in literature consider at least two joints, shoulder pitch and elbow pitch, with the forearm and upper arm links. Some works exploit the rotation of the UAV around the yaw angle instead of employing a servo for this purpose [1]. Other works implement the typical configuration with three joints for positioning and two [2][7] or three [28] DOFs for wrist orientation. Motivated by the convenience of providing a human-like manipulation capability, this work follows a bio-inspired design approach, so the kinematics and size of the human arm are replicated [8]. The idea is that the application of the arms results more comfortable and intuitive for a human operator, without requiring special training. The mechanical construction of this configuration also results in a compact and robust design, as it will be seen later.

2.1.4. Frame structure

Aluminium and carbon fibre are widely used for building low weight robotic arms intended to aerial manipulation due to their mechanical robustness and low weight. ABS or PLA plastics should be avoided as they are not impact resistant and may suffer deformations for temperatures around 40 ºC. Note that in case of impact, the manipulator will support the kinetic energy of the whole aerial platform (0.625 J for a 5 kg weight platform moving at 0.5 m/s). Most aerial robots employ carbon fibre in the frame structure of the arms. However, the manufacturing cost and the material itself is quite expensive with respect to aluminium. Besides its low cost, aluminium is highly malleable, so L-shaped or U-shaped frames can be easily manufactured bending a flat frame. The possibility of introducing these geometries is important in the design of the frame structure and its parts.

2.1.5. Compliant transmission

As mentioned before, one of the main contributions of this work is the development of a simple, compact and low weigh spring-lever transmission mechanisms integrated in all joints of the arms for providing compliance. Conventional steel springs are preferred to other elastic materials like elastomers due to their high linearity and low hysteresis. The proposed mechanism makes use of the igus® flange bearings, screwed to the aluminium frame structure for supporting the rotation of the output links with respect to the servo shafts. These components provide low friction and vibration dampening, being also robust against impacts and radial/axial loads.

In most industrial manipulators, the torque is estimated from the current injected to the motor, or measuring the micro deflections of an aluminium structure attached between the motor shaft and the output link employing strain gauges. However, current-based torque estimation and control lacks of accuracy due to the friction of the gearbox, and torque sensors based on strain gauges require special electronics and a calibration process which increases the cost of the devices. What is more, although joint compliance and even variable stiffness/impedance can be achieved at software level controlling the torque at high rate (~1 KHz), the joint is intrinsically stiff and therefore less safe than a mechanically compliant joint in an environment shared with humans.

Introducing flexible elements like springs or elastomers for transmitting the motion of the motor to the output link is a simple and low cost method for providing compliance at hardware level. These components act as low pass filters, absorbing the energy of impacts and overloads in a passive way thanks to their natural dampening. This feature results of special interest for protecting the servo actuators against peak torques in those situations in which the manipulator enters in contact with the environment. A potentiometer or encoder can be introduced in the compliant joint for building a simple torque sensor based on the deflection of the springs.

2.2. Compliant joint: design and mechanics

A compliant joint manipulator can be considered as a chain of compliant joint actuators connected through rigid links, so it results convenient to describe the mechanical construction of the single joint as previous step in the development of a compliant and lightweight manipulator, either single arm or dual arm.

The compliant joint actuator presented here is a particular implementation of the series elastic actuators [58][59] consisting of a spring-lever transmission mechanism introduced between the servo shaft and the output link frame. A picture of a prototype built is shown in **Figure 2.2**. A lever rigidly attached to the servo horn pushes the compression springs that at the same time push the output link frame, which is supported by a flange bearing that rotates around the servo shaft [8]. A pair of springs is needed since the compression spring applies the pushing force only in one direction. The relative rotation of the output link with respect to the servo shaft is called the deflection angle and it is measured by a potentiometer or encoder aligned with the shaft. This sensor allows the estimation and control of the torque by means of the joint deflection, as described in [27][57]. Steel springs are preferred to elastomers or other flexible elements due to their high linearity, repeatability, and because they are less affected by permanent deformations in the long term. In particular, it is expected that the joint recovers the zero deflection position once the external loads cease in their application, so it may be necessary to set a slight pre-load of the springs in order to ensure the zero return. Torsion springs may result in more compact transmission mechanisms, although these components are less extended than compression springs

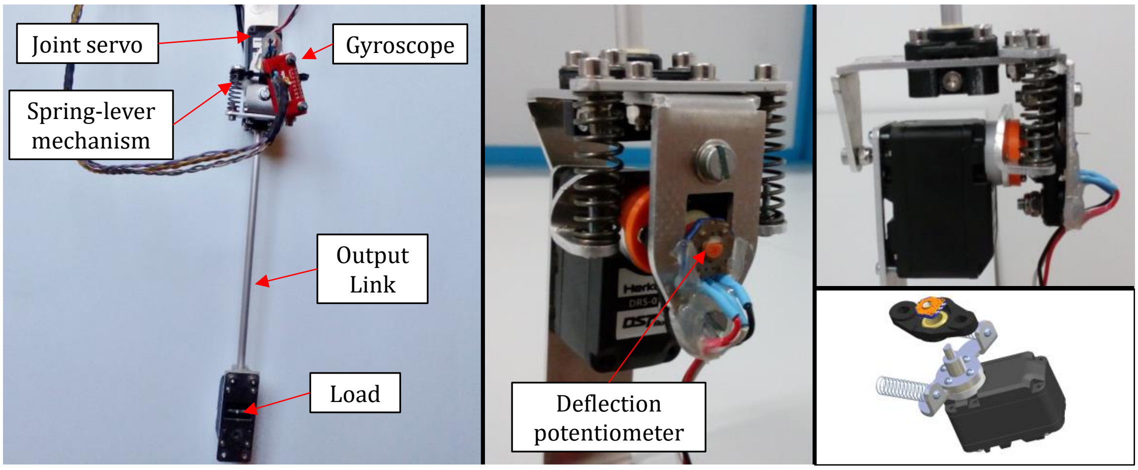

Figure 2.2. Compliant joint in spring-lever configuration. The lever attached to the servo shaft pushes the pair of compression springs depending on the rotation direction. The output link rotates w.r.t. the servo shaft thanks to the flange bearing. The joint deflection is measured with a potentiometer integrated in the frame.

The stiffness of the spring is related with the lever length and the output link lengths through the transmission ratio ρ defined as follows:

$$\rho = \frac{L_{link}}{L_{lever}} \sim 10 \tag{2.2}$$

This ratio indicates that the load supported by the springs is around 10 times the load at the tip of the link, considering typical values of the link/lever lengths (L_{link} ~250 mm, L_{lever} ~20 mm). The length of the lever should be small so the compliant transmission mechanism is compact (this is mainly an aesthetic criterion). Once the lever length is set, the stiffness constant of the compression spring, K_{spring}, can be computed knowing the stall torque of the servo, τ_{stall}, and the maximum joint deflection, $\Delta\theta_{max}$, allowed when the servo is stalled. The desired torsional stiffness of the spring-lever mechanism, denoted as k, is computed from these two parameters:

$$\tau_{stall} = k \cdot \Delta\theta_{max} \tag{2.3}$$

Now, assuming that the compression of the spring is proportional to the deflection angle, which is a valid approximation since the force is almost orthogonal to the lever, the spring stiffness can be obtained in the following way:

$$\tau \cong F_{spring} \cdot L_{lever} \cong K_{spring} \cdot (\Delta\theta \cdot L_{lever}) \cdot L_{lever} = K_{spring} \cdot L_{lever}^2 \cdot \Delta\theta \tag{2.4}$$

Combining these equations, it results that:

$$k = \frac{\tau_{stall}}{\Delta\theta_{max}} = K_{spring} \cdot L_{lever}^2 \rightarrow K_{spring} = \frac{k}{L_{lever}^2} \tag{2.5}$$

The mechanical protection of the servo actuator can be improved designing the frame structure of the compliant joint in such a way that the radial/axial loads and impacts are transmitted through the flange bearings and supported by the aluminium frame structure. **Figure 2.3** represents two levels of mechanical protection of the servo: partial (left) and full isolation (right). In the first case, the U-shaped frame of the output link is supported by the servo shaft and by the screw at its back, so the radial load is distributed on both sides. In the second case, the pair of flange bearings in side-by-side configuration support the crossing shaft of the output link in the radial and axial directions, so the servo does not support any load other than the torque transmitted through the spring-lever mechanism. Despite its benefits in term of mechanical protection, this structure may not be suitable for all the joints of the arm in terms of compactness and low weight, but it should be employed in the joints that support most of the load.

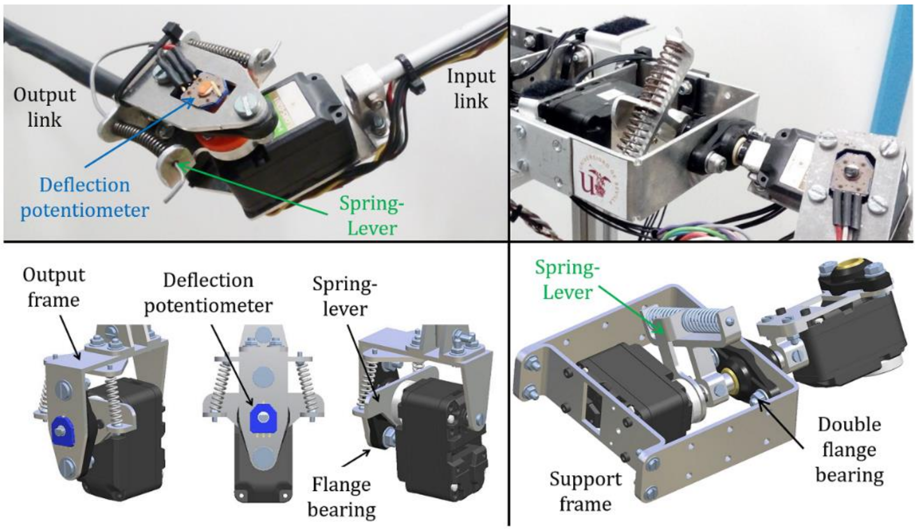

Figure 2.3. Two different implementations of compliant joint: single side support with partial servo protection (left) and double flange bearing in side-by-side configuration for full servo protection (right).

2.3. Lightweight and compliant joint arm prototypes

2.3.1. 3-DOF compliant arm

A picture of the 3-DOF compliant joint arm developed in [27] is represented in **Figure 2.4**. The kinematic configuration consists of the shoulder yaw joint at the base, followed by the shoulder pitch and elbow pitch joints. The actuators are three Herkulex DRS-0101 servos manufactured by Dongbu Robot, weighting 45 grams, with a stall torque of 1.17 N·m and a maximum speed of 360 deg/s. The frame structure of the manipulator consists of sixteen parts designed in such a way that they can be easily manufactured using simple hand tools from commercial anodized aluminium profiles, including 20×2 and 25×2 mm flat, and 8 mm hollow circular profiles. Aluminium is a well suited material due to its very low cost, low weight (2.8 g/cm^3), high mechanical resistance, and because it can be bended for building L-shaped or U-shaped frames.

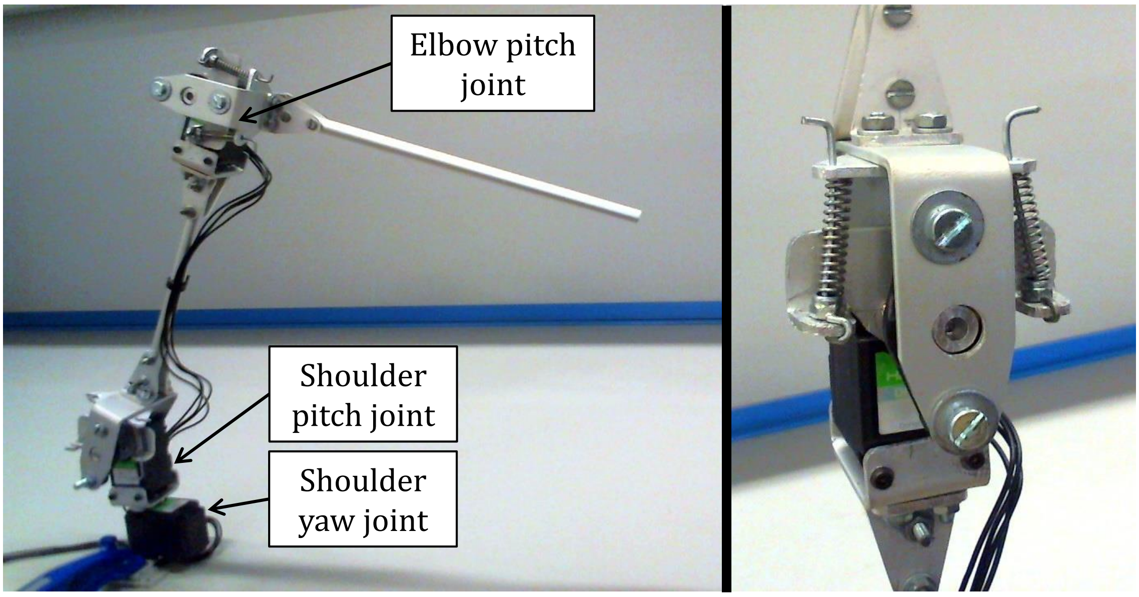

Figure 2.4. 3-DOF compliant joint arm (left). Detailed view of the compliant joint corresponding to the elbow pitch joint (right).

The specifications of the arm, including the weight, size, payload, or rotation range for each joint, can be found on **Table 2.2**. The volume of operation corresponds to a hollow semi-sphere generated by the revolution around the shoulder yaw axis of the circular ring that represents the points reachable by the tip of the forearm link. The lengths of the upper arm and forearm links have been chosen in such a way that the wrist point is out of the range of the propeller in a medium-scale quadrotor when the arm is fully stretched.

Table 2.2. Specifications of the 3-DOF compliant joint arm.

Weight	0.3 [Kg]
Max. lift load	0.2 [Kg]
Size	Upper arm: L_1 = 0.2 [m] Forearm: L_2 = 0.2 [m]
Volume of operation	0.12 [m^3]
Rotation range	Shoulder yaw: ±150 [deg] Shoulder pitch: ±90 [deg] Elbow pitch: ±120 [deg]
Max. joint deflection	±30 [deg]

A rendered view of the compliant mechanism integrated in shoulder pitch and elbow pitch joints is shown in **Figure 2.5**. A pair of compression springs transmit the motion from the servo shaft frame to the output link, and *viceversa*, in both rotation directions. If the output frame is deflected clockwise (counter clockwise) then the right (left) spring is compressed while the opposite spring is free of load. A Murata SV01 potentiometer is placed at the output frame, with its shaft attached to the servo shaft frame so the deflection angle can be measured. The output frame is supported by an 8 mm Ø shaft attached to servo horn frame through an igus EFOM-08 flange bearing in one side, and by a 3 mm Ø screw in the back side of the servo. This compliant mechanism has not been considered in the shoulder yaw joint due to space limitations.

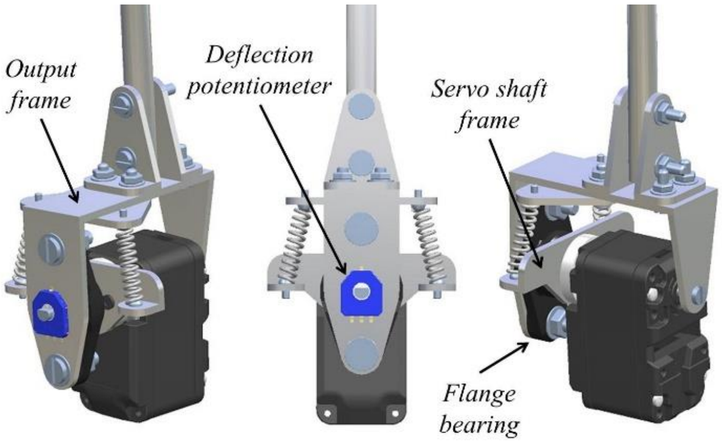

Figure 2.5. Rendered view of the compliant mechanism integrated in the shoulder and elbow pitch joints.

Finally, note that although the arm has been represented upwards, it can be installed either upwards or downwards in the multi-rotor platform. This is a relevant issue, as the landing gear, the propellers and the floor impose motion constraints that should be considered for preventing collisions.

2.3.2. Compliant finger module

The robot arm represented in **Figure 2.6** has been equipped with a 40 grams weight finger module [89] for object grasping and soft collision detection against obstacles or walls. A picture of the finger and its integration in the compliant arm can be appreciated in **Figure 2.6** and **Figure 2.7**. The 3 DOF anthropomorphic and compliant finger is driven by a nylon tendon rolled up into a 6 mm Ø reel for finger flexion. Finger extension is achieved by means of an extension spring and the heat shrink tube that maintains the three finger bones tied together. The potentiometer attached to the metacarpo-phalangeal (MCP) joint allows the position control of this joint, while proximal inter phalange (PIP) and distal inter phalange (DIP) joints are under-actuated. As the MCP joint provides low stiffness, any frontal collision will cause a deviation in its position that can be easily detected, without affecting significantly the stability of the UAV. This can be exploited for navigation in narrow spaces, using the arm-finger system for detecting obstacles in a similar way people do when they move through a room at night without seeing.

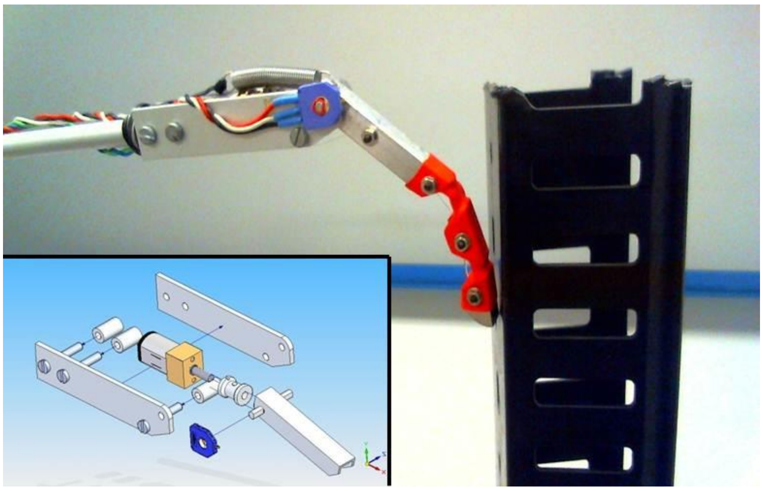

Figure 2.6. Compliant finger module deflected due to a frontal collision against an obstacle. MCP joint deflection is measured with a potentiometer.

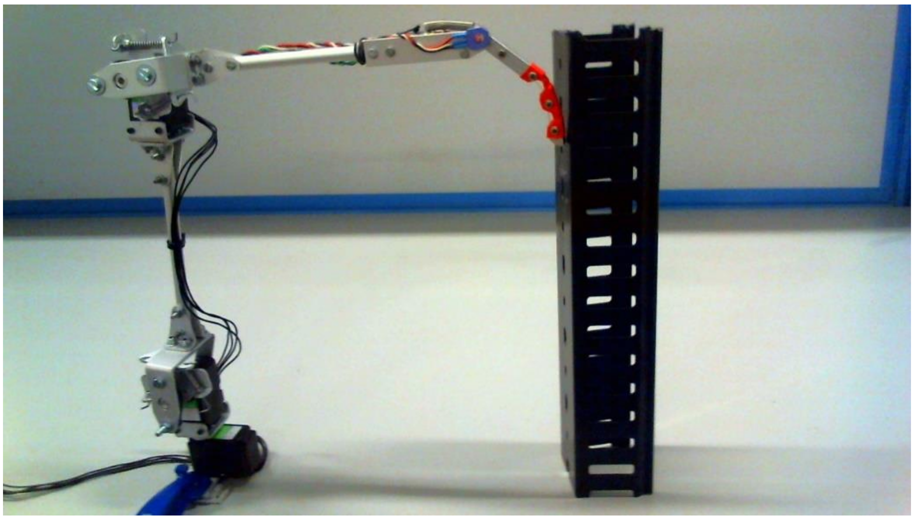

Figure 2.7. Compliant finger module integrated in 3-DOF compliant arm.

2.3.3. Lightweight arm with compliant elbow joint

In the human arm, the rotation of the forearm with respect the elbow joint is achieved with the contraction and extension of biceps and triceps, a pair of antagonistic muscles that can be considered as linear actuators. Compliance is provided by elastic tendons connecting the muscle with the skeleton. The distance from the elbow joint to the point where tendon is connected to the forearm determines the ratio between the force and linear speed of the muscle with respect to the torque and angular speed of the joint. For a given force and speed generated by the muscle, higher distances imply higher torques but lower speeds, and *vice versa*. This is graphically represented in **Figure 2.8**.

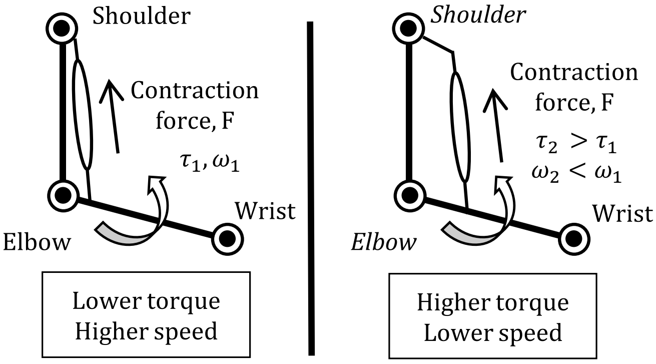

Figure 2.8. Conversion from linear displacement to rotational motion in the elbow joint. The distance from the joint to the contact point of the actuator in the forearm determines the rotational torque and speed.

When the human muscles contract, they generate a force in a single direction, like biceps when lifting the arm, so another muscle is required to apply a force in the opposite direction. In order to reduce the number of actuators in the arm, and therefore the total mass and inertia, the action of the gravity can be taken as advantage in a passive way for moving the arm downward, just allowing the actuator to extend. If the elbow joint is actuated with a single muscle, then the elastic tendon that connects it with the forearm may be in any of the three situations represented in **Figure 2.9**. In absence of any external force applied over the forearm, a minimum tension required for holding its mass is exerted over the tendon. If an impact or load is applied without retracting or releasing the actuator, then the tendon may become slack or elongated. In the last case, the energy of the impact is stored as potential energy in the elastic element, as the tendon can be seen as an extension spring. However, when the external force stops acting, the elbow joint will quickly tend to release the excess of potential energy, whether gravitational or elastic, involving a high acceleration of the forearm link. This can be avoided simply controlling actively tendon tension with the actuator, trying to minimize the energy stored in the elastic element. Therefore, the idea is to exploit the fast response of the elastic element to reduce the influence of sudden impacts over the arm, using the actuator to release the energy stored more slowly.

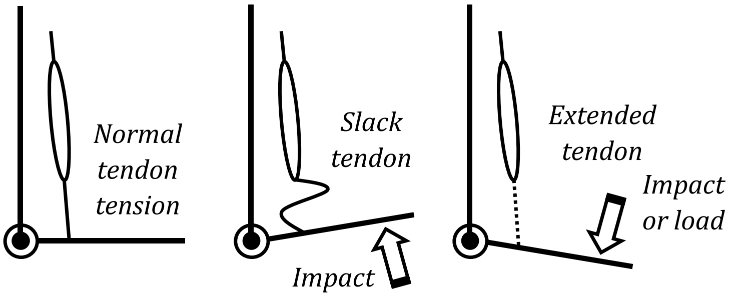

Figure 2.9. Different operation conditions of the tendon in the elbow joint.

The first prototype of lightweight and compliant arm developed in [88] is shown in **Figure 2.10** and **Figure 2.11**, summarizing its main specifications in **Table 2.3**. A Firgelli L16-100-63-12P linear servo acts as biceps for the elbow joint. This actuator is characterized by a 100 mm stroke, a maximum speed of 20 mm/s, a maximum force of 100 N, and a back-drive force of 46 N. This actuator provides position feedback, necessary to implement the payload mass estimation and the collision detection and reaction functionalities. The arm has been built using different aluminium profiles as basic material for the frame structure since it is a very low cost and lightweight material. The shaft of the elbow joint is attached to the upper arm frame through a pair of igus KSTM08 pillow block bearings. Two extension springs with elastic constant 0.2 N/mm are employed as tendons, connecting the forearm with the linear servo. With this, the actuator is not so directly exposed to impacts as occurs with conventional rotational mechanisms where the output link is rigidly attached to the servo shaft. This contributes to increase the lifespan of the actuator. Finally, the wiper of a rotational potentiometer is attached to the shaft of the joint for measuring its rotation with respect the forearm link.

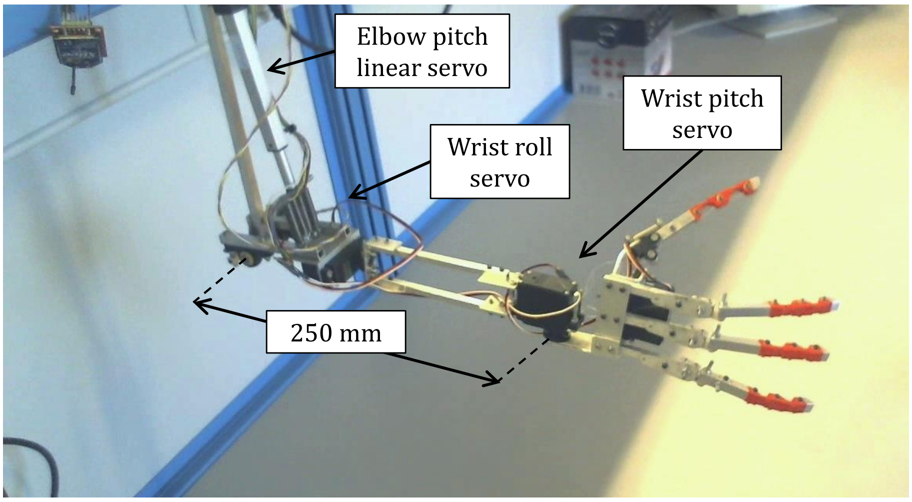

Figure 2.10. Human size robot arm built with aluminium profiles. A Firgelli L16 linear servo moves elbow joint position, whereas two Futaba S3003 servos move wrist in roll and pitch angles. The arm weight is 325 g.

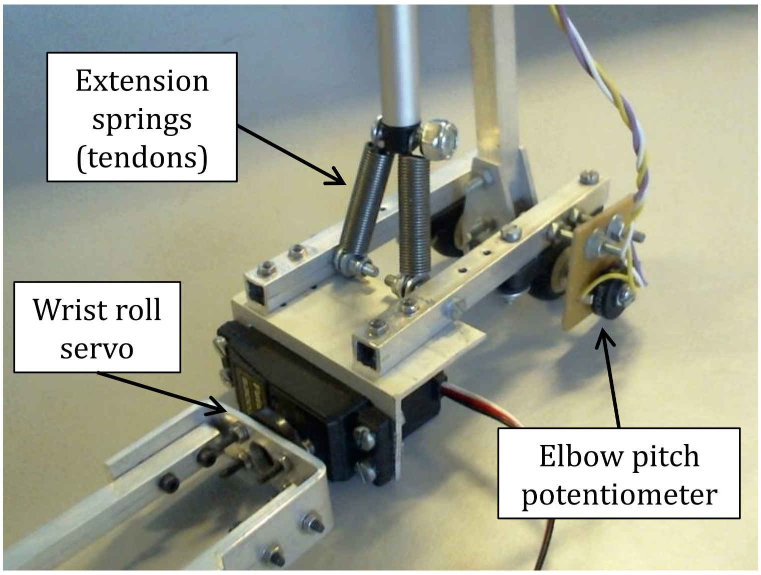

Figure 2.11. Detailed view of the compliant elbow joint mechanism based on linear servo. Two extension springs act as elastic tendon.

Table 2.3. Specifications of the compliant and lightweight robot arm.

Elbow joint actuator	Linear, Firgelli L16
Wrist roll and pitch actuators	Rotational, Futaba S3003
Range of motion	Elbow pitch: 0 – 135 deg Wrist roll and pitch: ±90 deg
Forearm length	25 cm (from elbow to wrist)
Compliant element	Extension springs (tendons)
Feedback	Elbow joint position Stroke position
Total weight	325 grams

Two Futaba S3003 servos (48 g weight each of them) allow the rotation of the wrist joint in the roll and pitch angles. The rolling servo was placed as close as possible to the elbow to minimize the inertia. The intention for the two parallel profiles of the forearm is that they can be used as support frames for the electronics and the motors in a wire-driven robot hand. The rotation in the yaw angle has not been implemented in order to reduce the total weight and complexity and because the orientation of the UAV around the vertical axis can be exploited for this purpose. The electronics consists of a STM32 VL Discovery board that takes care of the arm control, whereas the Firgelli Linear Actuator Control board (LAC) controls the L16 stroke position. The microcontroller board generates the PWM signals for the Futaba servos, measures the positions given by the two potentiometers (the one attached to the elbow shaft and the one integrated in the Firgelli), generates the reference position for the linear actuator, and communicates with a computer, receiving commands and sending measurements through a serial port interface.

2.4. Compliant and lightweight anthropomorphic finger module

2.4.1. Motivation

In the human hand, each finger provides four DOF's in a configuration similar to the one shown in **Figure 2.12**. The thumb, where up to seven DOF's can be identified, is a special case which is not considered here. The names of the links and joints correspond to the bones of the finger. The metacarpo-phalangeal joint (MCP) connects the finger with the palm of the hand, allowing the adduction/abduction and the flexion/extension of the finger, with a range of motion of 40º and 90º, respectively. The proximal inter-phalangeal (PIP) and the distal inter-phalangeal (DIP) joints have a rotation range around 80º and 110º, although DIP joint is typically considered as under-actuated by the PIP joint. In that case, each finger would require three actuated DOFs driven by a pair of tendons; that is, six actuators.

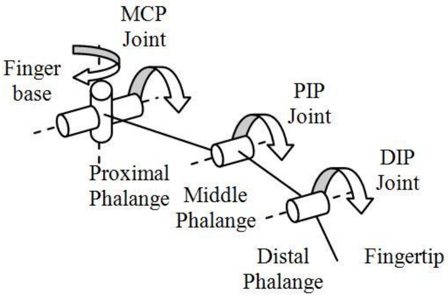

Figure 2.12. Kinematic model of the four degrees of freedom in an anthropomorphic finger.

As this work is focused on the design of a very low weight anthropomorphic finger module, it was found necessary to impose the following simplifications and constraints:

- Only flexion/extension is allowed, removing adduction/abduction at MCP joint.
- The three joints will be under-actuated by a single motor for finger flexion, driving a nylon tendon.
- The finger will stay extended by default.
- An elastic element disposed between the phalanges will cause the flexion of the finger in the following order: 1) MCP, 2) PIP, and 3) DIP.

The modular design of the fingers has a number of advantages and drawbacks with respect to the design of a full hand considered as a whole. Firstly, it simplifies and reduces the time required in the design and construction, as it avoids to waste time in the development and validation of the full hand. It also leads to highly efficient solutions as the work is focused on a more specific domain. It facilitates maintenance and replacement operations in case there is any fault, just removing the finger module from the frame structure of the hand palm. Finally, a number of finger modules can be considered for building hands with different configurations just changing the base frame where they are attached. On the other side, modularity usually implies higher weight, size and redundancy which could be reduced considering the hand as a whole, exploiting its geometrical structure for this purpose.

2.4.2. Mechanism description

A picture of the finger module and the assembly diagram of the mechanism from the 3D model are represented in **Figure 2.13** and **Figure 2.14**, respectively. The anthropomorphic finger consists of three 8 mm U-shape aluminium profile sections of 45 mm (proximal phalange), 20 mm (middle phalange) and 15 mm (distal phalange) length. A 50 mm section of heat shrink tube keeps the three bones tied together and at the same time it acts as elastic element for PIP and DIP joints, maintaining them extended by default. The elastic constant of both joints will depend on the heating process of the heat shrink tube and in the separation between the profile sections. The assembly of the case and the aluminium sections has been reinforced with three 2 mm Ø screws. The screw at the middle phalange and a fourth screw near the midpoint of the proximal phalange are used as pass points of the nylon tendon that drives the finger. Two 70×15×2 mm aluminium frames and three 11×6 mm cylinders support the finger and the Pololu 298:1 micro-motor, which is fixed to the surface of the frames through double sided adhesive tape. The Murata SV01 potentiometer is placed in the external side of one of the frames and aligned with the MCP joint shaft, while an extension spring that connects the proximal phalange with the frame is used to maintain this joint extended by default. Finally, an 8 mm Ø reel with 6 mm Ø internal section is attached to the motor shaft for rolling the tendon. At this point, it is important that the nylon tendon has the minimal length in order to avoid that the cable is unrolled if the tendon becomes slack.

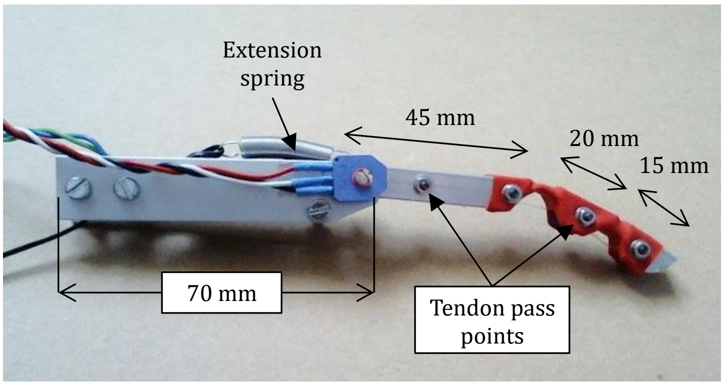

Figure 2.13. Anthropomorphic finger module with compliant joints and 40 grams weight.

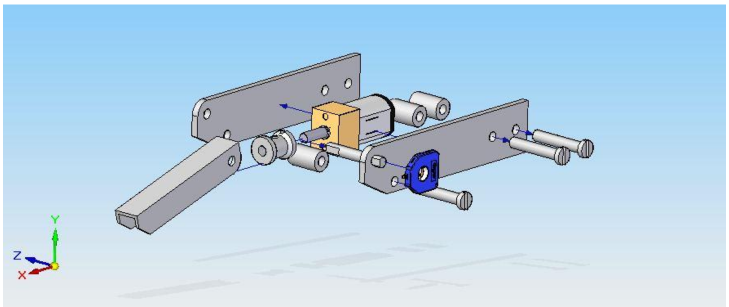

Figure 2.14. View of the components of the finger module in the 3D model.

2.4.3. Electronics

The electronics required for the control of the finger consists of an H-bridge implemented with the LM293B integrated circuit, a STM32 VL Discovery board and a USB-to-UART device for the communications with the computer. The H-bridge is employed for the torque/speed and direction control of the Pololu 298:1 micro metal gear motor. The microcontroller board generates the digital output and the PWM signal for motor control, gets the voltage given by the potentiometer attached to MCP joint from an analog input channel, and communicates with a computer through the USB-to-UART interface for data acquisition and parameters configuration.

2.5. Lightweight and human-size dual arm aerial manipulator

2.5.1. Overview

This section describes a dual arm aerial manipulator for outdoor operation consisting of a human size dual arm [7] integrated in a commercial hexarotor. Whereas most aerial manipulators that can be found in the literature are research prototypes evaluated in indoor testbeds, the proposed dual arm design extends the range of operations that can be accomplished with respect to the single arm case, satisfying four requirements essential in the successful application of the aerial manipulation technology in outdoors: 1) high payload (up to 0.75 kg per arm) for manipulating a wide variety of objects and tools, 2) high joint/Cartesian speed (300 deg/s, 2.5 m/s at end effector) for agile task execution, 3) positioning accuracy and reliability for object grasping, and 4) mechanical robustness for extending the lifespan of the actuators. The manipulator is built with smart servo actuators and a customized anodized aluminium frame structure that reduces the manufacturing cost. The accuracy, repeatability and smoothness in the operation of the arms is evaluated in test bench experiments. The integration of the arms in a hexarotor platform, including the identification of motion constraints and the electronics, is also addressed. The kinematics and dynamics of the dual arm aerial manipulator will be described in Chapter 4, proposing a control scheme that exploits the manipulator dynamics for compensating the reaction wrenches. The interactions between the manipulator and the aerial platform are experimentally identified in testbench in hovering conditions in Chapter 6. The dual arm design is validated through an extensive set of outdoor flight tests with two commercial hexarotor platforms equipped with standard industrial autopilots (**Figure 2.15**), showing that the influence of high speed motions of the arms over the aerial vehicle is low.

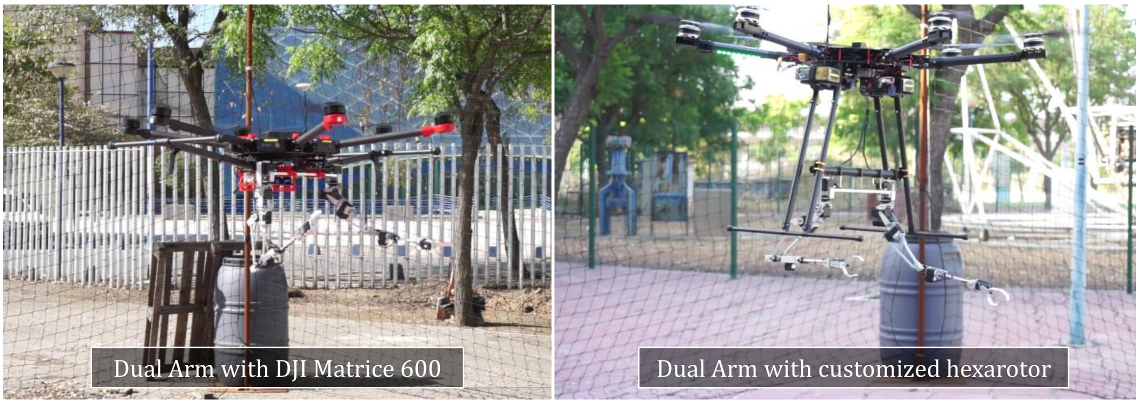
Dual Arm with DJI Matrice 600
Dual Arm with customized hexarotor

Figure 2.15. Developed lightweight and human-size dual arm manipulator integrated in two different commercial hexarotor platforms. Outdoor flight tests.

2.5.2. Motivation for a dual arm system

A dual arm system extends the grasping and manipulation capabilities that can be performed with an aerial platform with respect to the single arm case, allowing the simultaneous grasping and transportation of two objects, or large objects than cannot be handled with a single arm (see **Figure 1.3**-left). It makes possible the execution of certain tasks that are more suitable for a dual arm manipulator, like assembly or insertion operations. Manual operations assisted with visual feedback can be also performed with a camera in eye-in-hand configuration (see **Figure 1.3**-right). This is done at expenses of increasing the mass of the manipulator, although the payload to weight ratio is not significantly increased with respect to the single arm case.

2.5.3. Lightweight dual arm design

A rendered view of the 3D model of the arms is depicted in **Figure 2.16**. From top (shoulder) to bottom (wrist) the joints are: shoulder yaw, shoulder pitch, elbow pitch, wrist roll and wrist pitch. The kinematic configuration of the shoulder was chosen in such a way that the equations of the kinematic and dynamic models result in the simplest form, which reduces the computational cost and simplifies the control, and at the same time the working space is maximized. The actuators employed are the Herkulex smart servos from Dongbu Robot. These servos integrate the motor, gears, electronics and communications in a compact and robust device, providing very high torque to weight ratio and extensive information about the state of the servo, such like position, speed, PWM, temperature or voltage. The model of the servos and the main parameters associated to each joint are listed in **Table 2.4**. The different frames of the arms have been designed in such a way that they can be easily manufactured using hand tools from standard anodized aluminium profiles, including 15×2, 20×2 and 30×2 mm flat profiles, and 8 mm Ø hollow circular profile.

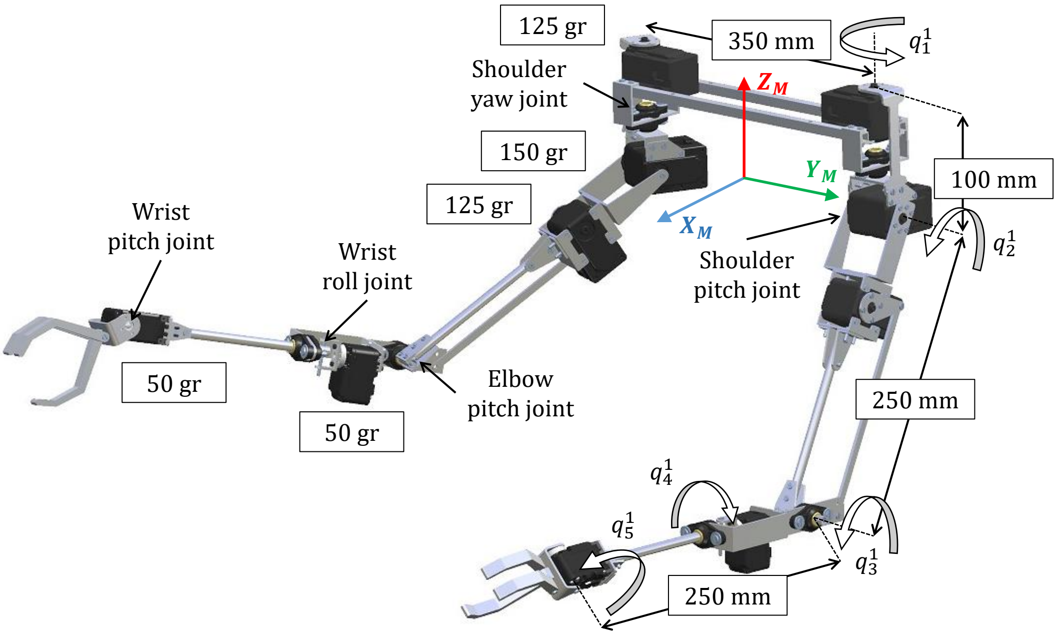

Figure 2.16. Rendered view of the 10-DOF lightweight dual arm manipulator with the significant lengths and joint angles.

Table 2.4. Specifications of the joints in the lightweight and human-size dual arm.

Joint	Servo Model	Stall torque [N·m]	Rotation range [deg]	Actuator weight [gr]
Shoulder Yaw	Herkulex DRS-0402	5,1	±90	125
Shoulder Pitch	Herkulex DRS-0602	7,6	±90	150
Elbow Pitch	Herkulex DRS-0402	5,1	[30, 150]	125
Wrist Roll	Herkulex DRS-0101	1,17	±150	50
Wrist Pitch	Herkulex DRS-0101	1,17	±135	50

As mentioned before, one of the key aspects in the design of the arms is protecting the servos against unexpected and undesired impacts and loads so they are not damaged. Some typical situations include crashes of the aerial platform against the floor, impacts of the arms against the landing gear, or, in the case of a dual arm, closed kinematic chains. Note that the cost of the servos represents approximately the 80% of the cost in materials. In the proposed design, six pairs of igus® EFOM-08 flange bearings in side-by-side configuration are employed for reducing the radial and axial load exerted over elbow pitch and wrist yaw servos (**Figure 2.17**), and over shoulder yaw servo (**Figure 2.18**). This simple and low weight mechanism (20 grams), distributes the load through the aluminium frames, isolating the servos from overloads. The space left between the servo shaft and the output link can be exploited for providing compliance introducing a flexible coupling element like springs [8]. This mechanism was not considered in the shoulder and wrist pitch joints due to space limitations.

The dual arm manipulator consists of fifty two aluminium frame parts. Some of them can be seen in **Figure 2.17** and **Figure 2.18**. The elbow pitch servo was attached directly under the shoulder pitch servo for reducing the inertia, using a lever mechanism for transmitting the motion to the elbow support frame, as it can be seen in **Figure 2.17**. Other transmission mechanisms like timing belts were avoided due to their drawbacks in terms of backlash and complexity in the assembly. The idea of placing the actuator at the top of the link is also applied to the wrist roll joint, which can be identified as the first joint in the human forearm. Its rotation is transmitted to the wrist pitch servo through a 140×8 mm hollow circular profile section. This frame structure may support the actuators in a tendon-driven hand.

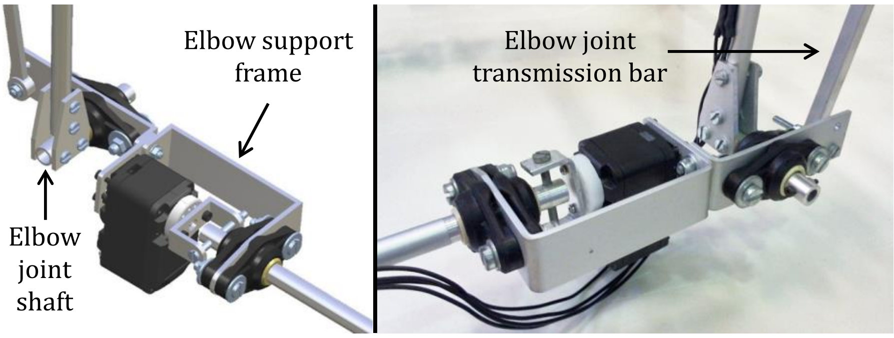

Figure 2.17. Detailed view of the elbow joint mechanism and the wrist yaw servo. Radial loads exerted at the end effector are catch by the pair of igubal EFOM-08 bearings and supported by the aluminium frames.

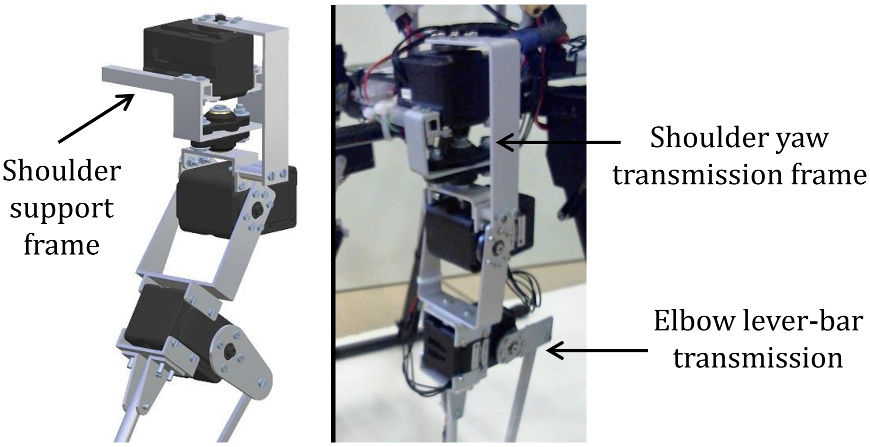

Figure 2.18. Detailed view of the shoulder and upper arm assembly, including the shoulder yaw and pitch servos, and the elbow pitch servo with the lever-bar transmission mechanism for moving the elbow joint.

The assembly of both arms is done through a pair of 260×8×8 mm square hollow profiles connecting the two shoulder yaw servos as illustrated in **Figure 2.19**, mounting the aluminium parts with the case of the servos. These two square bars will be attached to the multi-rotor base under the propellers. The separation between the arms was set to 35 cm, taking into account the dimensions of the landing gear and the structure of the base where the dual arm manipulator is attached.

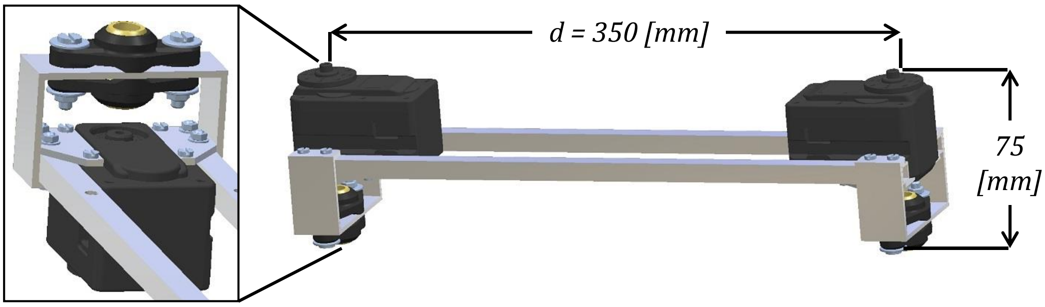

Figure 2.19. General and detailed view of the shoulder structure supporting the dual arm manipulator.

2.5.4. Workspace and motion constraints

The workspace of the developed manipulator is determined by the shoulder and elbow joints. Let us consider the transversal section on the XZ plane shown in **Figure 2.20**. As it can be seen, the area covered by the wrist point corresponds to a circular ring whose outer and inner limits are reached when the arm is fully stretched and retracted, respectively. The revolution of this section around the shoulder yaw axis generates a hollow semi-sphere whose volume, without considering any constraint, is $V_{arm} = 0.255\ [m^3]$.

There are two relevant considerations related with the integration of the arms in an aerial platform. First of all, it is critical that the arms rest in a position with the forearms above the floor before the UAV lands. Otherwise, the aerial platform will suffer a collision and the arms might result damaged. This corresponds to the shaded rectangle denoted as ground constraint in **Figure 2.20**. A possible solution for reducing the effect of potential accidents is introducing a mechanical fuse in the elbow joint transmission bar in such a way that this bar breaks when the forearm suffers a strong impact. The second consideration is related with the motion of the arms on flight, as it is necessary to plan carefully the trajectories to avoid collisions with the landing gear, but also with the arms themselves.

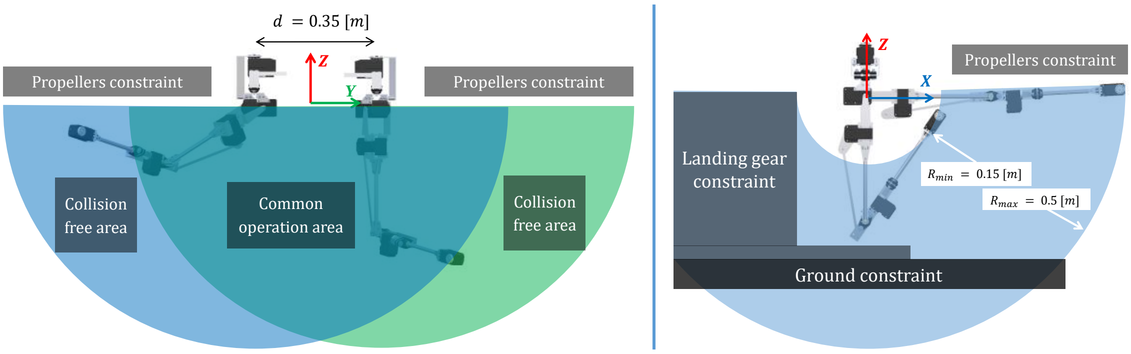

Figure 2.20. Workspace covered by the shoulder pitch and the elbow pitch joints with collision constraints (left). Working space of the dual arm system with collision constraints and common operation area (right).

2.5.5. Hardware/Software Architecture

The components and architecture of the developed dual arm aerial manipulator are depicted in **Figure 2.21**. The aerial platform comprises the hexarotor and the DJI A3 autopilot, which provides two flight modes: attitude stabilize, and position control. The manipulator consists of two groups of Herkulex servos, one for each arm, connected in daisy chain to the same TTL bus which ends in a USB-to-USART interface. Each servo is identified by a unique ID so the control program can access individually each actuator for reading its state and for commanding its position. Two types of data packets are transmitted through the bus. Request packets are sent from the computer board to a particular servo for commanding its position and for indicating which registers are going to be read. The response packets return the latest value of the specified registers, including the position, speed, PWM, temperature or voltage. All the servos are fed by a 3S LiPo battery, deriving a power line for feeding the computer board through a Recom 5V 1.5 A voltage regulator. The Odroid U3 computer board (with LUbuntu 13.04 OS) executes the C/C++ program that controls the arms and generates the data log files, interfacing with the servos through two USB ports.

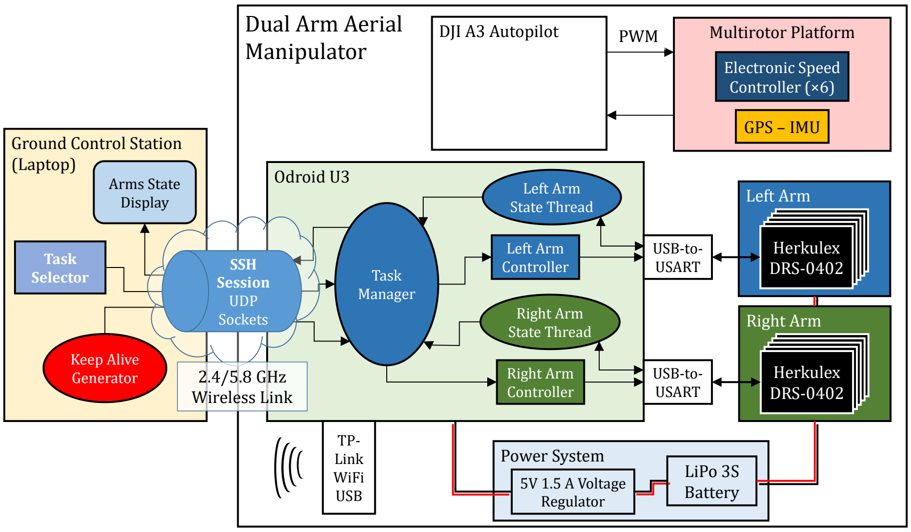
Dual Arm Aerial Manipulator
DJI A3 Autopilot
PWM
Multirotor Platform
Electronic Speed Controller (×6)
GPS – IMU
Ground Control Station (Laptop)
Arms State Display
Task Selector
Keep Alive Generator
SSH Session UDP Sockets
2.4/5.8 GHz Wireless Link
Odroid U3
Task Manager
Left Arm State Thread
Left Arm Controller
Right Arm State Thread
Right Arm Controller
USB-to-USART
USB-to-USART
Left Arm
Herkulex DRS-0402
Right Arm
Herkulex DRS-0402
TP-Link WiFi USB
Power System
5V 1.5 A Voltage Regulator
LiPo 3S Battery

Figure 2.21. Hardware/software components and architecture of the developed dual arm aerial manipulator.

The main software component is the Task Manager. It implements the different functionalities of the arms (go to rest/operation position, teleoperation, visual servoing…) and maintains the state of the servos updated through the Arm State Threads. The arm controller implements the inverse kinematics and the trajectory generation method described in Chapter 4. Two additional sensors were integrated in the DJI Matrice 600 platform: a ZED stereo camera intended to provide visual feedback at low frame rate to the ground control station (GCS), and a STM32F3 Discovery board used as external IMU for logging the attitude measurements. The GCS includes a display for monitoring the state of the aerial manipulator, a user interface for selecting the task to execute, and a Keep Alive Generator safety module that sends messages at 2 Hz so the arms control program is able to detect the communication loss and the arms can go to a safe state if necessary. The Odroid U3 is accessed through a SSH session, using UDP sockets for data interchange.

2.5.6. Integration of lightweight dual arm in hexarotor platforms

The developed dual arm manipulator was integrated and tested with two multirotor platforms: a Matrice 600 hexarotor manufactured by DJI, and a customized hexarotor manufactured by Drone Tools. The main features of both platforms and the arms are listed in **Table 2.5**. As mentioned before, one of the aims of this work is contributing to bring the aerial manipulation technology to the customer applications, showing how a lightweight dual arm system specifically designed for this purpose can be integrated in a commercial multirotor platform. In general, the most relevant requirements in the choice of a multirotor intended to aerial manipulation applications are the payload and flight time, which determine the size and weight of the platform. Then, the designer has to deal with the separation between the legs of the landing gear and the way of mounting the manipulator and other components (computer board, sensors, additional batteries, communication devices) to the frame structure of the multirotor, taking into account the motion constraints associated to the landing gear. What is more, the arms should rest above the floor before the take-off and landing operations to prevent undesired collisions.

Table 2.5. Specifications of the aerial manipulation system considering two commercial hexarotor platforms.

MULTIROTOR			**DUAL ARM MANIPULATOR**	
	DJI Matrice 600	**Drone Tools**		
Weight (no arms)	9,1 kg	10,8 kg	**Weight**	1,8 kg
Tip-toTip × Height	1,65 × 0,65 m	1,7 m × 0,55 m	**Max. lift load**	0,75 kg
Max. lift load	8 kg	8 kg	**Arms separation**	0,35 m
Propellers	8 × 16”	7,3 × 21,5”	**Max. joint speed**	360 deg/s
LiPo Battery	6S, 6 × 4.500 mAh	6S, 16.000 mAh	**LiPo Battery**	3S, 4.500 mAh
Max. flight time	16 min @6 kg	20 min @8 kg	**Operation time**	1 hour

The mechanical integration of the developed dual arm system in the mentioned platforms is detailed in **Figure 2.22** and **Figure 2.23**. As it can be seen, two different solutions were adopted: attaching the arms to the two carbon fibre bars under the central hub (DJI Matrice 600, **Figure 2.22**), and attaching the shoulder structure to a transversal bar disposed between the legs of the landing gear (customized hexarotor, **Figure 2.23**). Note that the first configuration is more convenient in terms of dynamic coupling, as the mass of the arms is closer to the center of gravity of the multirotor, whereas in the second case the workspace of the manipulator is less affected by the landing gear and there is more space left for integrating other devices. Both platforms use the DJI A3 industrial autopilot, showing a good performance in terms of positioning accuracy despite the controller had no feedback from the arms during the flight tests.

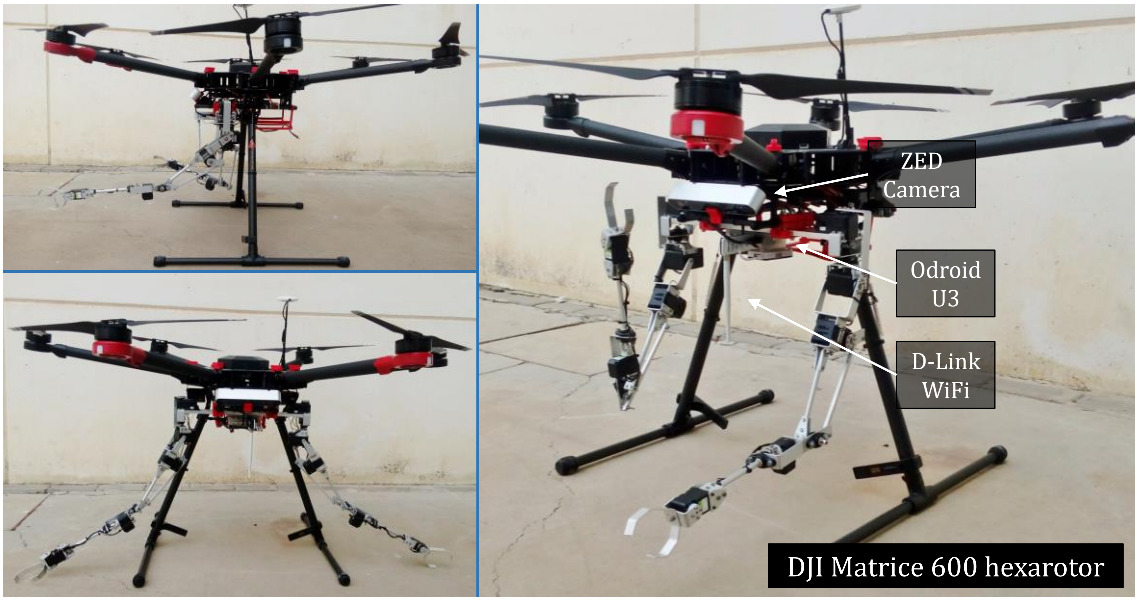
ZED
Camera
Odroid
U3
D-Link
WiFi
DJI Matrice 600 hexarotor

Figure 2.22. Three views of the dual arm aerial manipulation system integrated in the DJI Matrice 600 hexarotor.

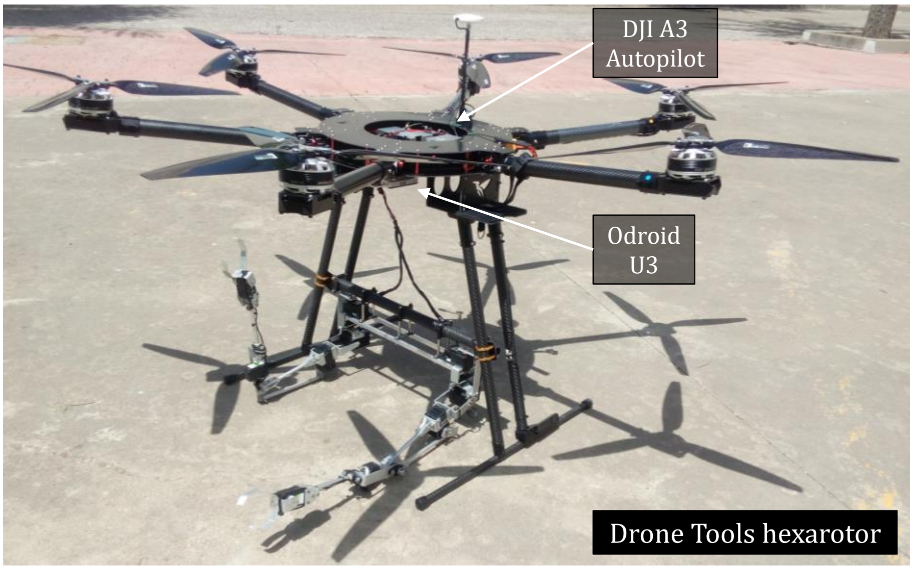
DJI A3
Autopilot
Odroid
U3
Drone Tools hexarotor

Figure 2.23. Lightweight dual arm manipulator integrated in the customized hexarotor platform manufactured by Drone Tools.

2.6. Anthropomorphic, compliant and lightweight dual arm

This section describes the development and experimental validation of an anthropomorphic, compliant and lightweight (1.3 kg weight) dual arm manipulator [8] designed for aerial manipulation applications. Each arm provides 4 DOF's for positioning the end effector in a human-like kinematic configuration. A simple and compact compliant transmission mechanism is integrated in all the joints with a deflection potentiometer, allowing the estimation and control of the joint torque and the contact forces. A customized and carefully designed aluminum frame structure manufactured by laser cut isolates the servo actuators against impacts and radial-axial overloads, supporting the rotation of the output links and the spring-lever transmission. The design and construction of the arms is also detailed, describing the kinematics, dynamics, and the force-torque relationships. Identification experiments have been conducted for evaluating the impact response and the frequency behavior. Deflection control experiments show how compliance can be exploited for reducing the interaction forces between the aerial manipulator and the environment on flight. The developed dual arm manipulator was integrated in a hexarotor platform, demonstrating bimanual aerial grasping.

2.6.1. Compliant dual arm design

A picture of the developed anthropomorphic, compliant and lightweight dual arm manipulator can be seen in **Figure 2.24**, with a detailed view of the right arm construction in **Figure 2.25**. The dual arm system was designed and developed completely from the scratch, although several design concepts are taken from previous designs. The actuators employed are the Herkulex DRS-0101 and 0201 smart servos from Dongbu Robot, introducing the igus® EFOM-08 and EFSM-06 flange bearings in the frame structure for isolating the servos from impacts and overloads and for building the compliant transmission mechanism. The frame structure of the arms consists of a set of 34 customized aluminum parts manufactured by laser cut, two 8 mm Ø shafts for the shoulder pitch joint, and four 6 mm Ø hollow profiles for the upper arm and forearm links. The laser cut frames include 2 mm, 8 mm and 10 mm thickness parts. The U-shaped aluminum frames in the shoulder pitch-yaw and in the elbow pitch structures are built bending 90 deg the 2 mm thickness flat profile sections. The frame structure has been designed in such a way that the cost and complexity of the manufacturing processes is reduced as much as possible.

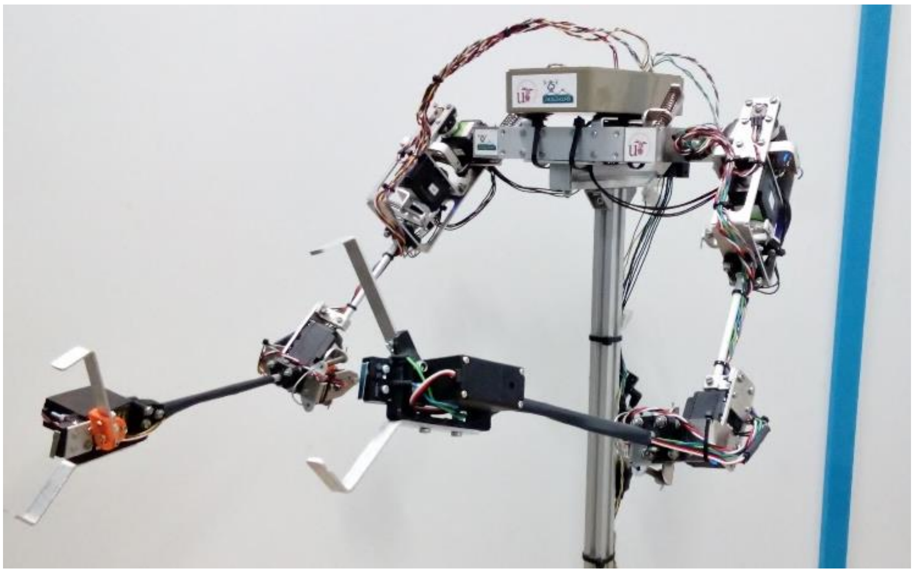

Figure 2.24. Anthropomorphic, compliant and lightweight dual arm.

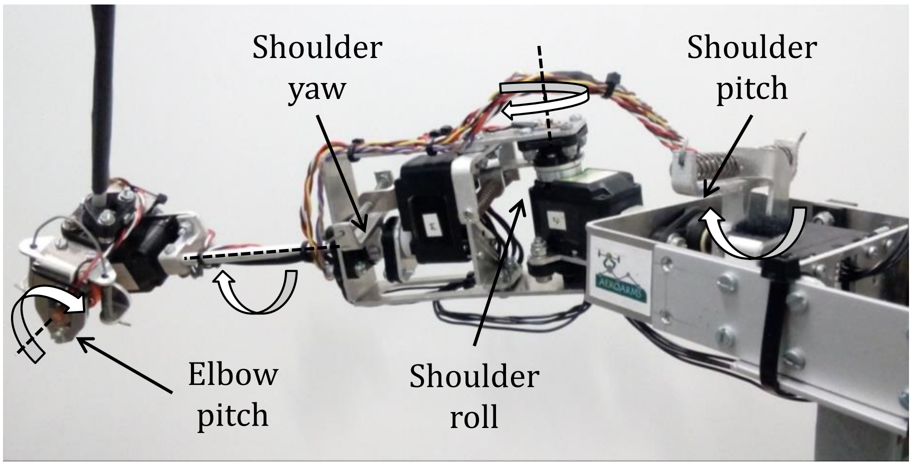

Figure 2.25. Detailed view of the joints in the right arm. Hands-up pose.

The main specifications of the dual arm manipulator are summarized in **Table 2.6**, providing additional information relative to each joint of the arms in **Table 2.7**. The maximum lift load was obtained placing a payload mass at the grippers with the arm fully stretched, rotating it from the vertical to the horizontal position so the torque due to gravity is maximum. The kinematic configuration, described in more detail in Chapter 4, as well as the dimensions are similar to the human arm motivated by the convenience of having human-like manipulation capabilities in an aerial platform. The shoulder roll joints are used for lifting the arms above the landing gear before the landing manoeuvre. Finally, two Futaba S3003 servos have been employed for building a simple gripper, integrating a micro switch in the palm for detecting the contact with the object to grasp.

Table 2.6. Specifications of the compliant dual arm

Total weight	1.3 kg (with grippers)
Dimensions	Forearm link length: 250 mm
	Upper arm link length: 250 mm
	Arms separation: 300 mm
Max. lift load	0.2 kg (per arm)
Rotation range	±90, [-30, 90], ±90, ±120 deg
Joint deflection	±30 deg approx..

Table 2.7. Specifications of the joints of the arms

Joint	Servo model	Stall torque [N·m]	Joint stiffness [N·m/rad]	Rotation range [deg]
Shoulder pitch	DRS-0201	2.34	2.93	±90
Shoulder roll	DRS-0201	2.34	2.1	[-30, 90]
Shoulder yaw	DRS-0101	1.17	0.8	±90
Elbow pitch	DRS-0201	2.34	1.48	±120

The developed manipulator satisfies the following design requirements imposed in the first stage of the design process:

1. Low weight and inertia.
2. Mechanical robustness, with high servo protection.
3. Intersection of the four joint axes in a common point, which simplifies the inverse kinematics.
4. Integration of compliant transmission mechanism.
5. Integration of deflection potentiometers in the joints.
6. Low clearance for increasing the accuracy in the positioning of the end effector.

All these features contribute to increase the probability of success in the application of an aerial manipulation robot to inspection and maintenance tasks in outdoor environments.

2.6.2. Kinematic configuration

The anthropomorphic dual arm provides 4 DOF's for end effector positioning in a human-like kinematic configuration with the shoulder pitch joint at the base, followed by the shoulder roll, shoulder yaw and elbow pitch joints. The corresponding joint variables of the output links are denoted by q_1^i, q_2^i, q_3^i, and q_4^i, respectively, with $i = 1, 2$ for the left and right arms. The wrist orientation joints have not been implemented in this version. A rendered view of the arms with the parameters of the kinematic model are represented in **Figure 2.26**, including the forearm and upper arm lengths, the separation between the arms, and the joint angles with the positive direction of rotation given by the right-hand criteria. A reference frame $\{\boldsymbol{X_0^i Y_0^i Z_0^i}\}$ attached to the intersection point of the joints of the shoulder of each arm is defined, so the tool center point (TCP) or any point in the workspace will be referenced to this frame. Each arm provides one redundant DOF that can be exploited for collision avoidance, null space control, or for orienting the end effector. In this work the shoulder roll angle is considered as a parameter, $q_2^i = \varphi_i$, which can be tuned according to the task. For example, in the take-off or landing operations, the arms should be in a position such that the elbow and wrist points are above the landing gear, so $\varphi_i = \pm 90$ degrees, whereas in a visual servoing task, this angle will take values around $\varphi_i = \pm 10$ degrees.

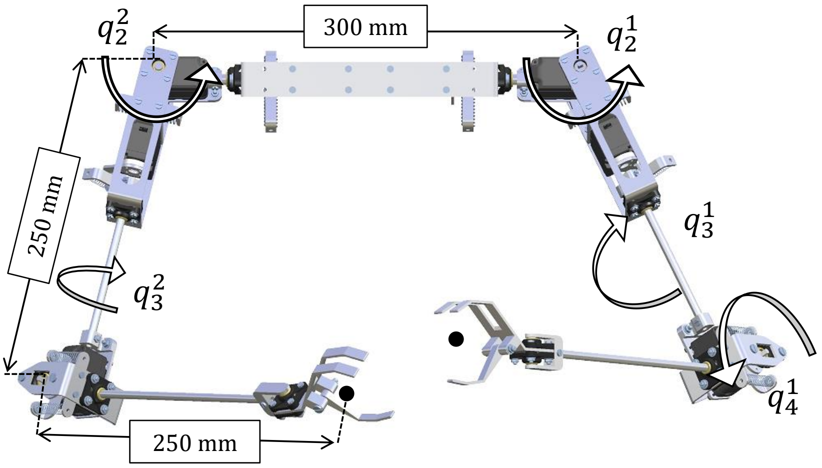

Figure 2.26-A. Kinematic configuration of the anthropomorphic dual arm and reference frames of both arms attached to the shoulder joint.

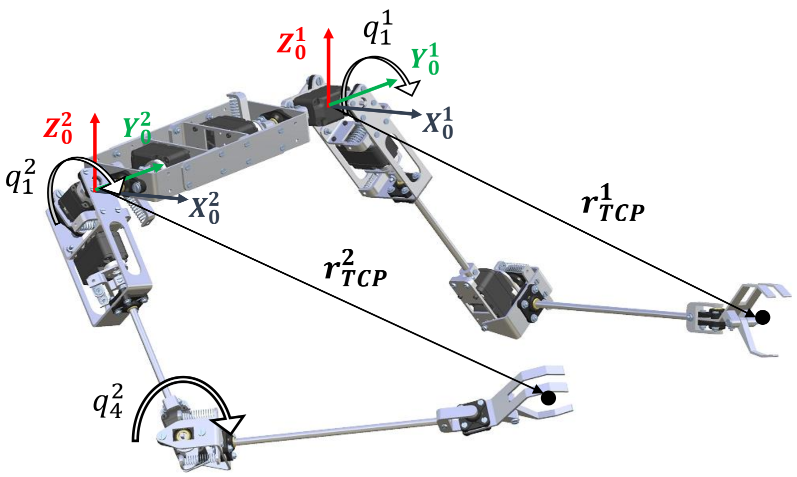
Z_0^1
q_1^1
Y_0^1
X_0^1
Z_0^2
Y_0^2
q_1^2
X_0^2
r_{TCP}^1
r_{TCP}^2
q_4^2

Figure 2.26-B. Kinematic configuration of the anthropomorphic dual arm and reference frames of both arms attached to the shoulder joint.

2.6.3. Hardware/Software architecture

The architecture of the compliant dual arm system is represented in **Figure 2.27**. The components of each arm are the four Herkulex servos indicated in **Table 2.7**, the Murata SV 01A deflection potentiometers attached to the joints, and a Futaba S3003 servo used in the gripper. The servos on each arm are connected in daisy chain to the Intel NUC board through an USB-to-USART device. As all the servos share the same TTL bus, the command/read rate is set to 50 Hz in order to prevent high packet loss. The analog signals provided by the deflection potentiometers are converted by the Analog to Digital Converter (ADC) in the STM32VL Discovery micro-controller board, which also generates the PWM signals that control the servos of the grippers. The micro-controller board is also connected to the Intel NUC computer through a USART interface. The control program executed in this board over Ubuntu 14.04 was developed in C/C++. The higher level class is the Task Manager, which implements several tasks or routines that can be selected by the operator from the Ground Control Station (GCS). The task manager gathers information from the state of the arms from the corresponding threads, providing the reference trajectories to the left/right arm controllers. These modules make use of the inverse kinematic model described in previous subsection for obtaining the joint references that are sent to the embedded servo controller through the serial port.

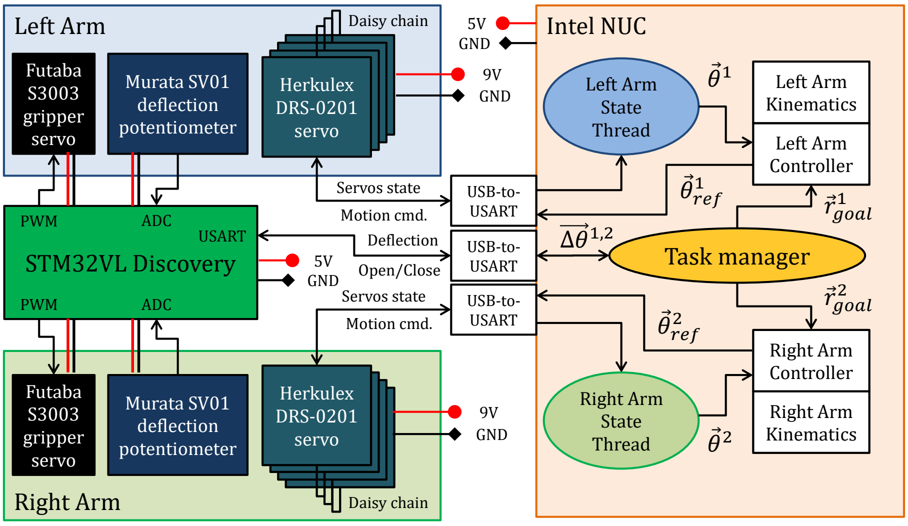
Left Arm
Futaba S3003 gripper servo
Murata SV01 deflection potentiometer
Herkulex DRS-0201 servo
Daisy chain
5V
GND
9V
GND
Intel NUC
Left Arm State Thread
$\vec{\theta}^1$
Left Arm Kinematics
Left Arm Controller
Servos state
Motion cmd.
USB-to-USART
$\vec{\theta}_{ref}^1$
$\vec{r}_{goal}^1$
PWM
ADC
USART
STM32VL Discovery
Deflection
Open/Close
5V
GND
$\Delta\vec{\theta}^{1,2}$
Task manager
USB-to-USART
PWM
ADC
Servos state
Motion cmd.
USB-to-USART
$\vec{\theta}_{ref}^2$
$\vec{r}_{goal}^2$
Right Arm Controller
Futaba S3003 gripper servo
Murata SV01 deflection potentiometer
Herkulex DRS-0201 servo
9V
GND
Right Arm State Thread
$\vec{\theta}^2$
Right Arm Kinematics
Right Arm
Daisy chain

Figure 2.27. Components and architecture of the compliant dual arm.

2.6.4. Arms frame structure

This section details the construction of the different links of the arms, providing the mass and inertia parameters obtained from the CAD model, which are summarized in **Figure 2.28** and **Table 2.8**. The definition of the XYZ axes associated to the CoM of each structure is shown in the figures below. This section does not consider the mass and inertia of the spring-lever transmission frames as these parameters are negligible with respect to the corresponding output links.

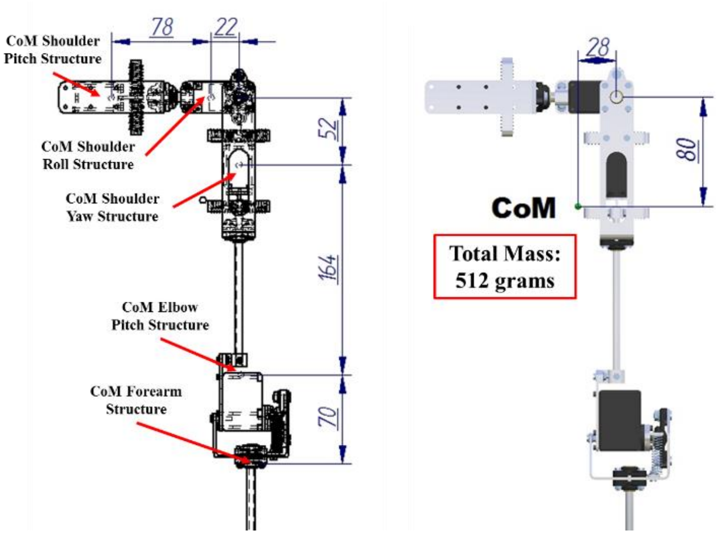
CoM Shoulder Pitch Structure
78
22
CoM Shoulder Roll Structure
52
CoM Shoulder Yaw Structure
164
CoM Elbow Pitch Structure
CoM Forearm Structure
70
28
80
CoM
Total Mass: 512 grams

Figure 2.28. Relative distances between the center of mass of the links (left) and global center of mass of the left arm (right). Lengths in mm.

Table 2.8. Mass in and inertia in parameters of the links in the compliant dual arm.

Structure	Mass [grams]	I_{xx} [g·cm^2]	I_{yy} [g·cm^2]	I_{zz} [g·cm^2]	I_{xy} [g·cm^2]	I_{xz} [g·cm^2]	I_{yz} [g·cm^2]
Sh. Pitch	127	853	750	1491	84	0	0
Sh. Roll	101	714	216	772	58	0	0
Sh. Yaw	121	1354	1813	611	0	38	0
E. Pitch	87	2055	2017	117	0	-79	-10
Forearm	53	1318	1187	177	0	0	-95

2.6.4.1. Shoulder pitch structure

This structure provides full protection to the Herkulex DRS-0201 servo. The radial and axial loads are supported by the igubal EFOM-08 flange bearings installed in side-by-side configuration, allowing the rotation of the shaft that connects the shoulder roll structure with the compliant transmission mechanism of the shoulder pitch joint. These components also provide vibration dampening and smooth rotation of the shaft. **Figure 2.29** shows a rendered view of this structure along with the XYZ axes to which the inertia moments are referred, as well as the dimensions in mm. The structure is built from two U-shaped aluminium parts manufactured by laser cut, 2 mm thickness and 25 mm width. The space left between the servo horn and the inner flange bearing (21 mm) is allocated for installing the spring lever mechanism and the deflection potentiometer.

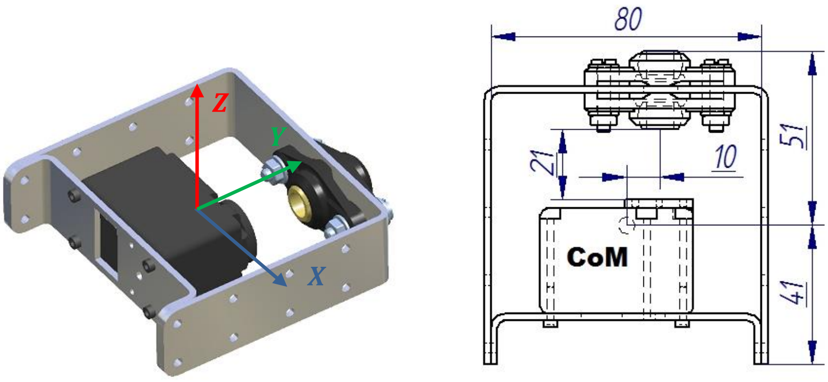

Figure 2.29. CoM and dimensions (in mm) of the shoulder pitch structure.

2.6.4.2. Shoulder roll structure

This structure, whose rendered view is depicted in **Figure 2.30**, provides partial protection to the Herkulex DRS-0201 servo through an igubal EFOM-08 flange bearing installed over the aluminium support frame on the back of the actuator. The shoulder yaw structure, described in next sub-section, is supported by this flange bearing and by the servo horn. The 8 mm Ø shaft crosses the EFOM-08 pair at the shoulder pitch structure, connecting the shoulder pitch transmission with the shoulder roll support frame. The shaft fits in a T-shaped frame in such a way that there is no clearance causing a dead-zone at the end effector.

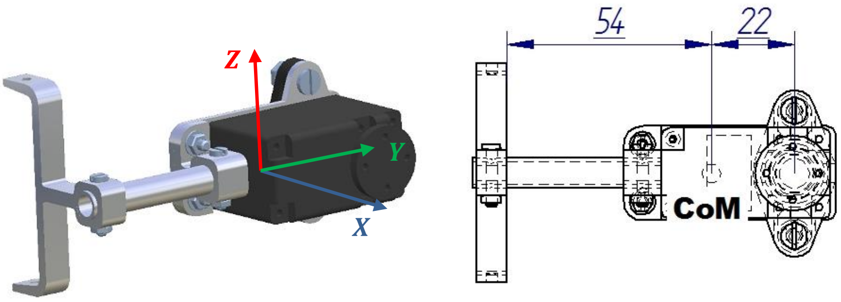

Figure 2.30. CoM and dimensions (in mm) of the shoulder roll structure.

2.6.4.3. Shoulder roll structure

A pair of igubal EFSM-06 flange bearings screwed into the base of a U-shaped frame support the rotation of the upper arm link and the compliant transmission. A third component attached to the inner side of the frame allows the rotation of this structure around the shoulder roll shaft, whereas the 8 mm Ø shaft in the opposite side is inserted in the EFOM-08 flange bearing of the shoulder roll structure. A rendered view of the assembly and the dimensions can be seen in **Figure 2.31**.

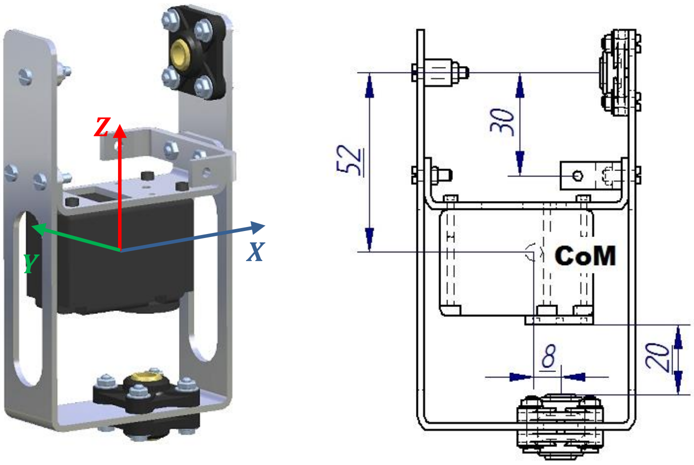

Figure 2.31. CoM and dimensions (in mm) of the shoulder yaw structure.

2.6.4.4. Upper arm link

This assembly, shown in **Figure 2.32**, is similar to the shoulder roll structure, although in this case, the transmission frame on the right of the 6 mm Ø profile is rotated 90 deg with respect to the servo support frame. This shaft passes through the pair of EFSM-06 flange bearings of the shoulder yaw structure. This solution, in which the elbow pitch servo is placed at the elbow joint, is not convenient in terms of inertia, but it avoids introducing a transmission mechanism, reducing the weight and complexity in the design and the assembly.

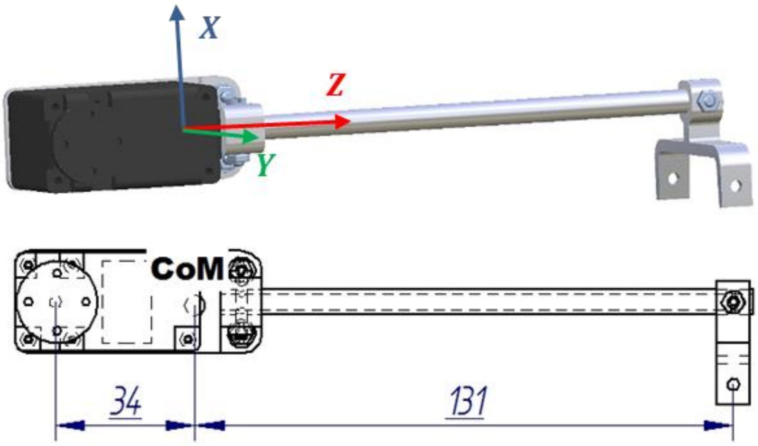

Figure 2.32. CoM and dimensions (in mm) of the elbow pitch structure.

2.6.4.5. Forearm link

The forearm link consists of a 6 mm Ø link connected to the elbow joint through a U-shaped frame and a pair of EFSM-06 flange bearings in side-by-side configuration. A rendered view of the assembly is represented in **Figure 2.33**. The EFOM-08 flange bearing is inserted into the servo shaft, using a M3 screw on the opposite side as second support point in the elbow pitch base frame. Although the current version does not implement the wrist orientation mechanism, the EFSM-06 pair allows the rotation of the end effector around the axis defined by the forearm link (wrist roll).

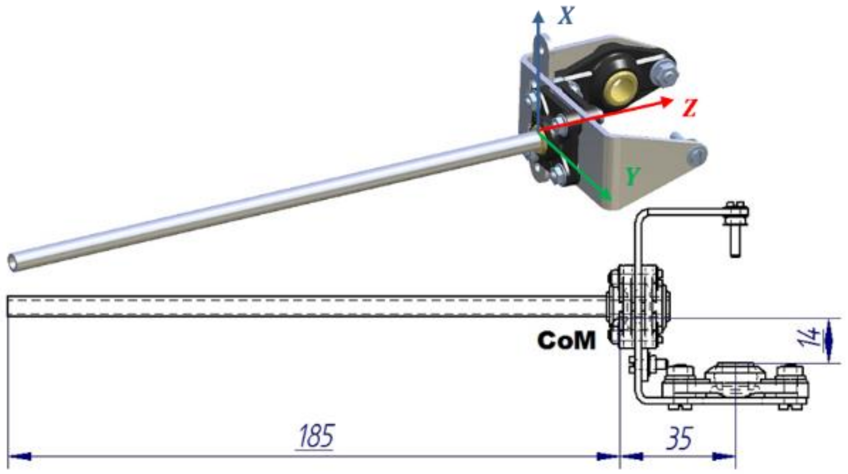

Figure 2.33. CoM and dimensions (in mm) of the forearm structure.

2.6.5. Integration of anthropomorphic dual arm in hexarotor platform

In order to maintain the symmetry of the aerial platform in terms of geometry and mass distribution, the manipulator is typically installed under the central hub of the UAV, trying to reduce the displacement of the center of mass (CoM) with respect to the vertical axis. This implies that the arms should be placed between the legs of the landing gear, what may reduce the workspace due to motion constraints. The solution adopted in this work is the one shown in **Figure 2.34** and **Figure 2.35**. Thanks to the anthropomorphic kinematic configuration, the arms can be lifted rotating the shoulder roll joints, so the upper arm and forearm links are above the landing gear when the UAV is landed. As it can be seen on the right side of **Figure 2.34**, the workspace of the manipulator is not affected by the landing gear, as occurred in previous dual arm prototype (see **Figure 2.20** and **Figure 2.22**). An adaptation frame consisting of two transversal hollow aluminium profiles is attached to the base of the landing gear. **Figure 2.36** shows the integration of the arms in a DJI Matrice 600 hexarotor platform, indicating the main components of the aerial manipulator.

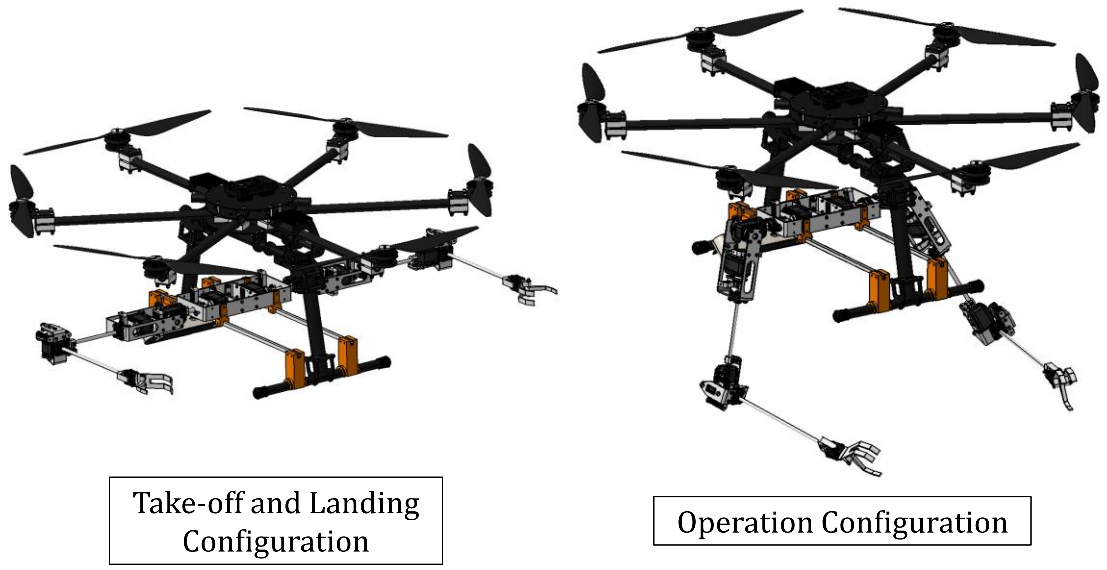
Take-off and Landing Configuration

Operation Configuration

Figure 2.34. 3D model of the anthropomorphic dual arm integrated in a hexarotor. Take-off and landing (left) and operation (right) configurations.

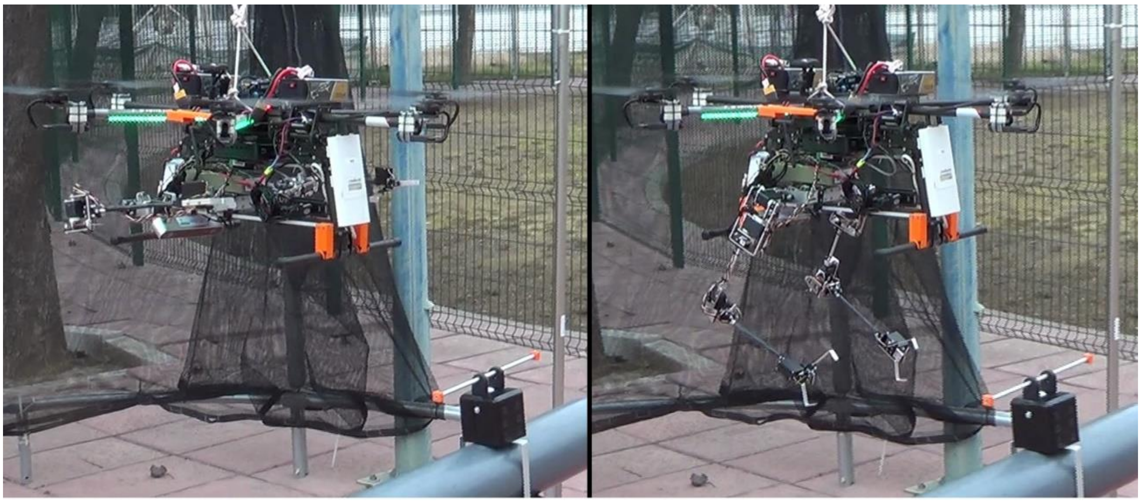

Figure 2.35. Anthropomorphic dual arm integrated in hexarotor platform along with a ZED stereo camera, an Intel NUC computer board, an Ubiquiti wireless link and the batteries.

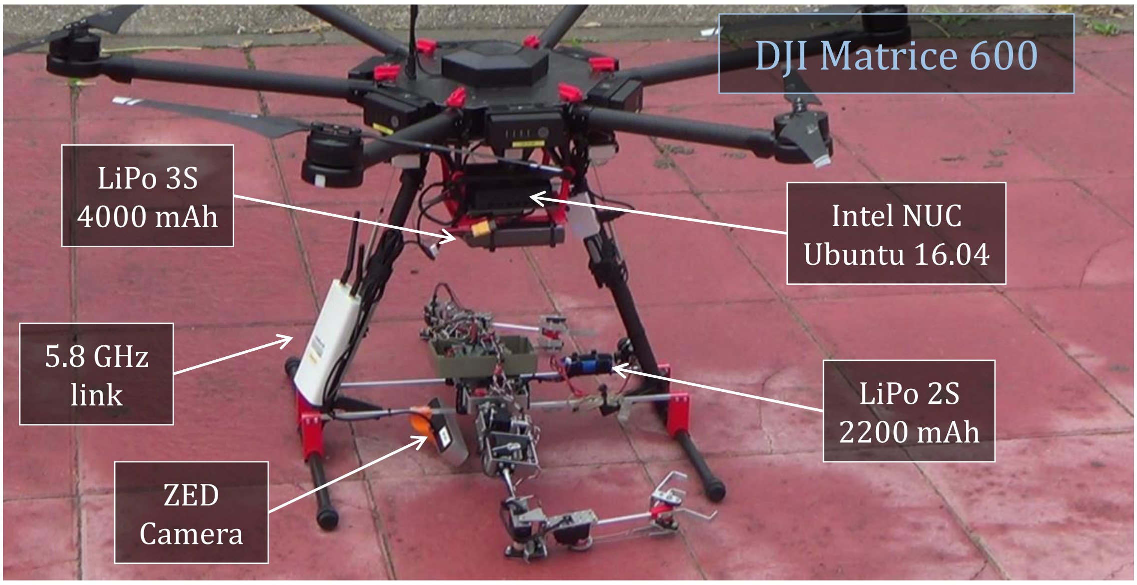
DJI Matrice 600
LiPo 3S 4000 mAh
Intel NUC Ubuntu 16.04
5.8 GHz link
LiPo 2S 2200 mAh
ZED Camera

Figure 2.36. Integration of anthropomorphic, compliant dual arm in DJI Matrice 600 hexarotor.

2.7. Long reach aerial manipulators

The proximity between the multirotor blades and the environmental obstacles restricts the use of aerial manipulators in inspection tasks due to the risk of impacts, the limitation in the reach of the arm, and the physical interactions in those operations involving contact forces. This section presents three prototypes of long reach aerial manipulators consisting of a hexarotor platform equipped with two different manipulators (single and dual arm systems) attached at the tip of a one-meter-length link in passive pendulum configuration.

2.7.1. Flexible long reach manipulator with lightweight dual arm

2.7.1.1. Introduction

This section analyses the possibility of integrating a long reach manipulator in an aerial platform, either multirotor or autonomous helicopter, motivated by the necessity of increasing the range and workspace of the manipulator (see **Figure 2.37**), whose motion is constrained by the landing gear and the propellers, as well as safety in those tasks involving physical interaction with the environment. The three mentioned functionalities are supported by a vision sensor providing direct measurements of tip deflection at 100 Hz, and a simple method based on zero cross detection of this signal for vibration suppression with the dual arm system. It is necessary to remark that, despite of increasing the total weight with respect to the single arm case, the benefits of a dual arm manipulator are significant in terms of performance. Several operations and tasks such like grasping large objects, installation of sensors with eye-in-hand camera configuration, assembling on flight with one arm while the aerial platform is stabilized with the other, or reaction torque compensation, are more suitable for a dual arm manipulator. Unlike space manipulators [75][76], the developed prototype of lightweight dual arm shown in this work has been specifically designed for its integration in multi-rotor vehicles and tested on flight (see experimental results in Chapter 6).

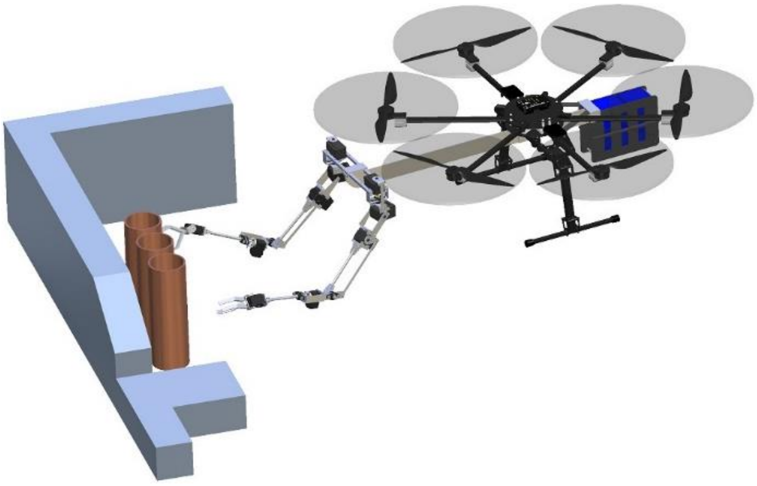

Figure 2.37. Dual arm aerial manipulation robot with flexible, long reach link. The batteries in the back act as counterweight of the arms. The flexible LRM increases safety in the physical interactions with the environment, avoiding potential collisions of the propellers against walls or obstacles.

2.7.1.2. Motivation

As mentioned before, the dexterity, workspace and reach of a robotic arm is strongly constrained by the landing gear and the propellers when integrated in an aerial platform, either multirotor or helicopter UAV. Let us consider a situation in which a helicopter equipped with a robotic arm is intended to perform some manipulation operation involving contact with a vertical surface. In case the manipulator is directly installed at the base of the rotorcraft, the propeller will impact against the surface before the end effector reaches the workspace. Extending the reach of the manipulator with a flexible link increases safety, not only because the risk of impact between the propeller and the obstacle is lower, but also because the mechanical flexibility avoids that contact forces are rigidly propagated to the aerial platform. In this way, the attitude-position controllers have more time for compensating the disturbances associated to the physical interaction during the aerial manipulation operation. This is possible at expenses of increasing slightly the total weight of the system due to the flexible link. Mass unbalance should be also compensated, using for example the batteries as counterweight. **Figure 2.37** illustrates this concept design with the developed prototype of dual arm flexible LRM installed in a hexarotor platform from. On the other hand, the control of the aerial platform becomes more complicated due to the dynamic coupling with the LRM, especially under the effect of lateral accelerations and rotations in the yaw angle inducing vibrations in the flexible link.

2.7.1.3. System description

The prototype of flexible link LRM with a lightweight, human size dual arm system installed at the tip is depicted in **Figure 2.38**. The flexible link consists of an 800 × 45 ×3 mm size aluminum profile, weighting 0.3 Kg, with its flat surface orthogonal to the direction of gravity. The dual arm system provides 5 DOF per arm, three for end effector positioning (shoulder yaw at the base, followed by shoulder pitch and elbow pitch) and two for orientation (wrist roll and pitch), although these two were not used in this case. The mechanical specifications have been summarized in **Table 2.9**. The dual arm system has been designed for aerial manipulation with multirotors, so special attention has been paid in reducing as much as possible the total mass and inertia. For that reason most part of the mass corresponding to the servos is placed close to the base. The frame of the arms has been manufactured using hand tools anodized aluminium. A Prosilica GC 1380H camera installed at the base of the LRM is focused in a marker attached at the back of the shoulder profile in order to measure tip deflection. The marker is a 10 mm Ø black dot drawn over a 300 × 50 mm size white panel acting as background. This configuration of the camera provides direct measurement of tip deflection with high accuracy.

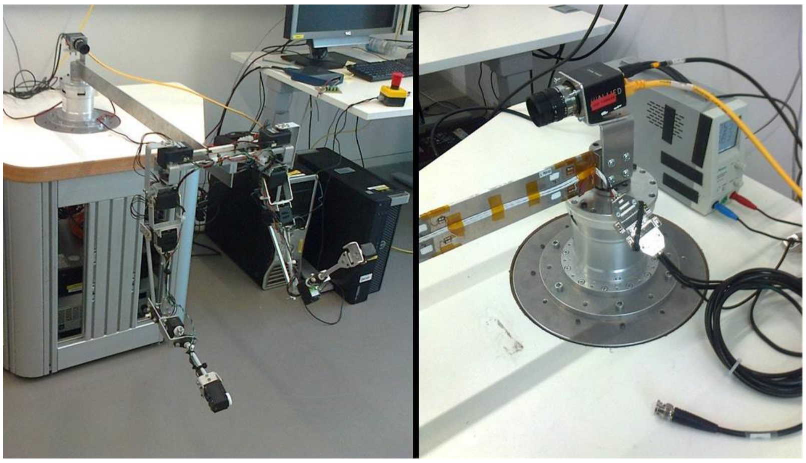

Figure 2.38. Lightweight, human size dual arm system installed at the tip of an 80 cm length flexible link (left). A Prosilica GC 1380H camera at the base provides direct measurement of tip deflection (right).

Table 2.9. Specifications of the lightweight and human-size dual arm system

Total mass	1.8 [kg]	
Max. lift load	0.75 [kg] per arm	
Size	Forearm length L_1: 25 [cm]	
	Upper arm length L_2: 25 [cm]	
	Separation between arms D: 25 [cm]	
Rotation range	Shoulder yaw	±90 [deg]
	Shoulder pitch	±90 [deg]
	Elbow pitch	10 – 150 [deg]
Actuators	Herkulex Servos, model DRS-0101, DRS-0402, DRS-0602	

The basis for the developed functionalities of the flexible link LRM with dual arm system is the high frame rate vision sensor that provides direct measurement of tip deflection. This sensor, whose features are listed in **Table 2.10**, consists of the Prosilica camera and a marker detector thread within the main program that controls the system. This program, coded in C++, makes use of the *OpenCV 2.4.2* library for image acquisition and processing. The Canny edge detector is applied over each frame for obtaining the contours found on the image. Geometrical information (contour length and area) is used for rejecting false positives in the detection. The region of interest (ROI) of the camera was set to the minimum size needed, 500×100 pixels, achieving 100 FPS, enough for tracking the marker which oscillates at 0.6 Hz.

Table 2.10. Specifications of the vision sensor for tip deflection measurement.

Frame rate	100 [FPS]
Resolution	500×100 [pixels]
Field of view	15 [cm]
Distance to marker	80 [cm]
Accuracy	0.28 [mm/pixel]
Delay	15 [ms]

The geometry of the flexible link prevents that deflections in the vertical axis happen. Although the effect of gravity can be neglected in space manipulators, it may affect significantly to the mechanical properties of an aerial manipulation system.

2.7.2. Lightweight and compliant long reach aerial manipulator

2.7.2.1. Long reach aerial manipulator with single arm

The developed long reach aerial manipulator consists of three components: the multirotor platform, the flexible long reach link attached at the base of the UAV through a passive joint in pendulum configuration, and the compliant joint arm placed at the tip of the link. A picture of the prototype is shown in **Figure 2.39**, summarizing its specifications in **Table 2.11**. The aerial platform is a hexarotor manufactured by Drone Tools, equipped with a PixHawk autopilot. The long reach link is a 1 m length flat profile section of anodized aluminum supported by a pair of igus® EFOM-08 flange bearings. An 8 mm Ø crossing shaft rigidly attached to the base of the multirotor allows the free rotation of the link similarly to a pendulum, measuring the angle with a magnetic encoder. The sensors integrated in the arm are indicated in **Table 2.12**.

One of the main features of this manipulator is the passive joint at the base of the pendulum. It prevents that the external wrenches generated during the physical interactions between the environment and the aerial manipulator are introduced as torques at the base of the multirotor. Instead, the components of the external wrenches contained in the plane orthogonal to the rotation axis of the passive joint are introduced as a force at the base of the aerial platform, whereas the components parallel to this axis will cause a deflection in the flexible link.

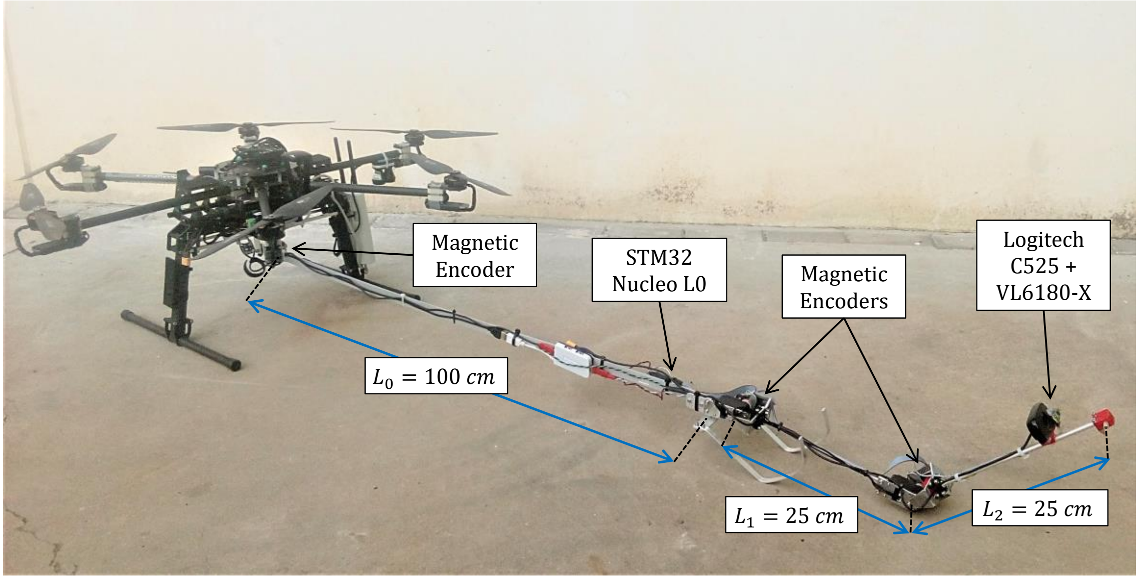

Figure 2.39. Compliant joint, long reach aerial manipulator. The manipulator integrates magnetic encoders for joint deflection and passive joint rotation measurement, a range sensor for measuring the distance to a contact point, and a camera installed in the forearm link, close to the end effector.

Table 2.11. Specifications of the compliant joint, long reach aerial manipulator.

Aerial Platform	Weight / Payload [kg]	3.4 / 2.5
	Flight time [min]	~30 (no load)
	Batteries (2 kg)	6S, 7000 mAh
Flexible Link + Integration frame	Dimensions [mm]	1000 × 25 ×2
	Weight [kg]	0.27
Compliant Joint Arm	Rotation range [°]	±120
	Weight / Lift load [kg]	0.5 / 0.2
	Link lengths [m]	0.25 / 0.25
	Joint stiffness [Nm/rad]	1.5 / 1.3

Table 2.12. Sensor devices integrated in the compliant arm.

Sensor	Range	Accuracy	Application
AS5048 magnetic encoder	±180°	0.2°	Deflection measurement in compliant joints, force torque estimation/control
VL6180X-SATEL ToF laser sensor	150 mm	3 mm	Measurement of distance from tool center point to the contact point
Logitech C525 camera	60° FoV	640×480 pixels	Visual inspection, eye-in-hand camera

2.7.2.2. Wearable exoskeleton interface

The exoskeleton interface shown in **Figure 2.40** consists of an anodized aluminum frame structure manufactured using standard 20 × 2, 25 × 2, and 30 × 2 mm flat profiles bended in such a way that they can fit as a backpack, supported over the shoulders and attached at the hip. The forearm and upper arm links are supported by igus® EFOM-08 flange bearings that allow the rotation of the shoulder and elbow joints, using the same magnetic encoders that in the compliant long reach arm for measuring the rotation angle. Two push-buttons have been included in a handle grasped by the user, connected to the wrist through a spherical joint. These buttons can be used to exert a pushing-pulling force with the compliant arm once the end effector is in contact with the inspection point. The motivation in the development of this device is to facilitate the teleoperation of the inspection arm for an untrained operator.

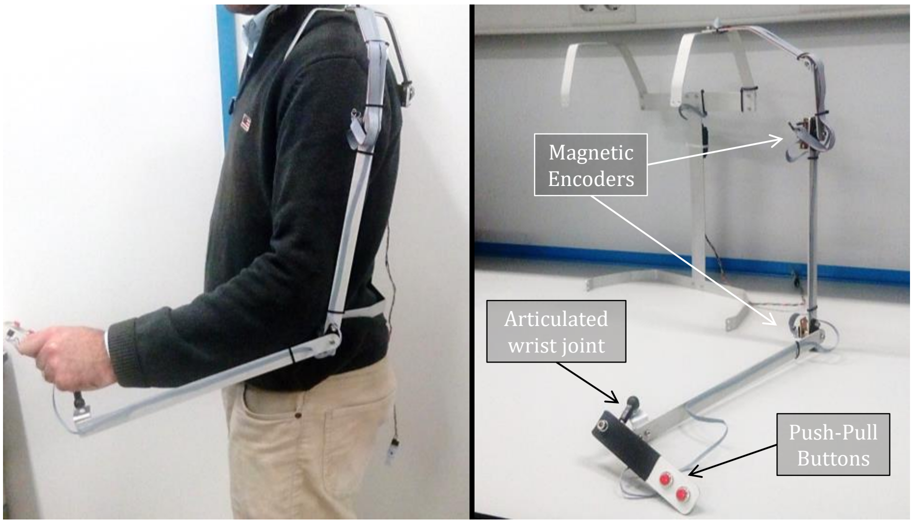

Figure 2.40. Wearable exoskeleton interface for arm teleoperation.

2.7.2.3. Hardware/Software architecture

The developed aerial manipulator can be decomposed in two main subsystems: the aerial platform and the compliant joint, long reach manipulator. The hardware components and the architecture is represented in **Figure 2.41**. The hexarotor integrates the PixHawk autopilot with the PX4 flight stack. The autopilot is connected to the Intel Nuc PC through a serial port. The communication between the two devices is based on the MAVROS protocol, whereas the mavros package of the Robot

Operating System (ROS) is used for logging the data of interest during the realization of the tests. The components of the LRM includes the Herkulex servos, three magnetic encoders for measuring the deflection of the joints and the rotation of the pendulum, and the camera and range sensors for the teleoperation. A STM32 Nucelo L0 board reads all the sensors and sends a single data packet to the Intel NUC through the serial interface at 200 Hz. The execution of the experiment is managed from a Ground Control Station through SSH sessions to the computer board.

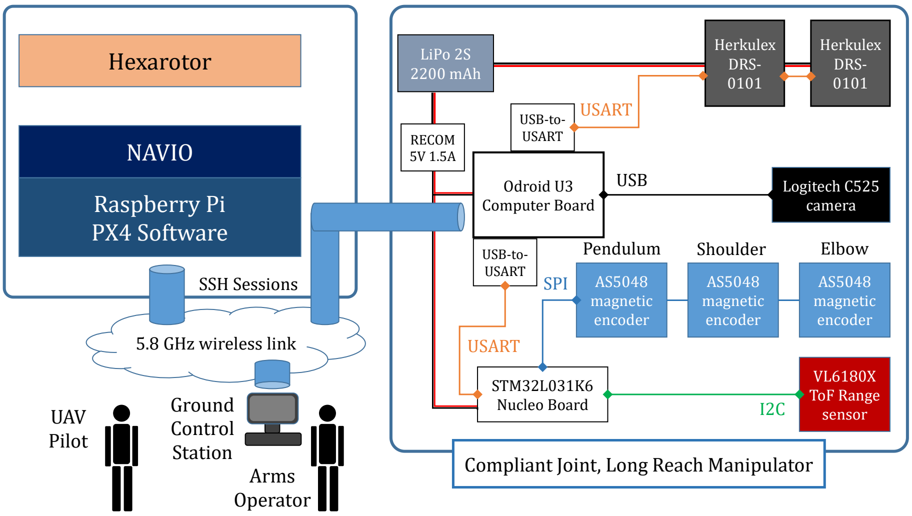
Hexarotor
NAVIO
Raspberry Pi
PX4 Software
SSH Sessions
5.8 GHz wireless link
UAV Pilot
Ground Control Station
Arms Operator
LiPo 2S 2200 mAh
Herkulex DRS-0101
Herkulex DRS-0101
USART
USB-to-USART
RECOM 5V 1.5A
Odroid U3 Computer Board
USB
Logitech C525 camera
USB-to-USART
Pendulum
Shoulder
Elbow
SPI
AS5048 magnetic encoder
AS5048 magnetic encoder
AS5048 magnetic encoder
USART
STM32L031K6 Nucleo Board
I2C
VL6180X ToF Range sensor
Compliant Joint, Long Reach Manipulator

Figure 2.41. Hardware components and architecture of the aerial manipulator.

2.7.3. Long reach aerial manipulator with dual arm

The aerial manipulator described here is an evolution of previous works. The idea of a long reach, dual arm aerial manipulator was firstly introduced in reference [18], presenting preliminary results with the lightweight dual system described in [3] in a fixed-base test bench. The new prototype is built from the anthropomorphic, compliant and lightweight dual arm aerial manipulation system presented in [4], although in this case, the arms were installed over the landing gear. Unlike [18], the flexible long reach link that supports the arms is not rigidly attached to the base of the hexarotor platform, but it is supported by a passive joint, similarly to a pendulum. This configuration prevents that the manipulator generates high torques over the base of the aerial platform that could not be compensated by the propellers.

The developed long reach dual arm aerial manipulator is depicted in **Figure 2.42**. The aerial vehicle is a hexarotor which provides 2.5 kg payload and around 30 minutes of flight time with no load. The tip-to-tip distance of the blades is 1.2 m, whereas the landing gear is 0.2 m height. The long reach link is a 25×80×2 mm anodized aluminum profile which can rotate freely in the pitch angle thanks to a pair of EFOM-08 flange bearings. An aluminum frame structure connects the link with the base of the hexarotor, supporting the pendulum joint. The manipulator is the anthropomorphic, compliant and lightweight dual arm described in Section 2.6. Each arm provides four degrees of freedom (DOF) in a human-like kinematic configuration, so its operation results more intuitive for an untrained operator. The mechanical specifications of the multirotor and the long reach dual arm manipulator are summarized in **Table 2.13**.

Table 2.13. Mechanical specifications of the long reach aerial manipulator.

HEXAROTOR PLATFORM		**COMPLIANT DUAL ARM**	
Max. payload	2.5 kg	**Weight/Max. lift load (per arm)**	1.5 / 0.2 kg
Flight time	<25 min	**Dimensions**	Forearm: 25 cm Upper arm: 25 cm Separation: 32 cm
Dimensions	1.2×0.3 m	**Kinematic configuration**	Shoulder pitch q_1 Shoulder roll q_2 Shoulder yaw q_3 Elbow pitch q_4
LONG REACH LINK			
Dimensions	80×2.5x0.2 cm	**Joint stiffness**	2.93 / 2.1 / 0.8 / 1.48 N·m
Mass	0.12 kg	**Max. deflection**	30 deg
Total weight	5 (aerial platform) + 1.5 (dual arm) + 0.12 (link) = 6.62 kg		

Two important points should be noted. On the one hand, the long reach manipulator can be assimilated to a classical pendulum that rotates freely around the pitch angle with a natural frequency of 0.5 Hz, determined experimentally. This implies that the displacement of the aerial vehicle or the motion of the arms themselves along the forward direction will induce an oscillation in the passive joint that could be coupled with the attitude controller. Thus, the trajectory of the aerial manipulator should be carefully planned in order to prevent undesired oscillations during the navigation and approaching phases. On the other hand, the acceleration of the platform as well as the contact forces exerted over the arms may also cause the deflection of the flexible link along the lateral direction. As stated in [78], the transfer function that relates the deflection at the tip with the torque at the base has associated non-minimum phase zeros that may convert into unstable poles in a closed loop control scheme.

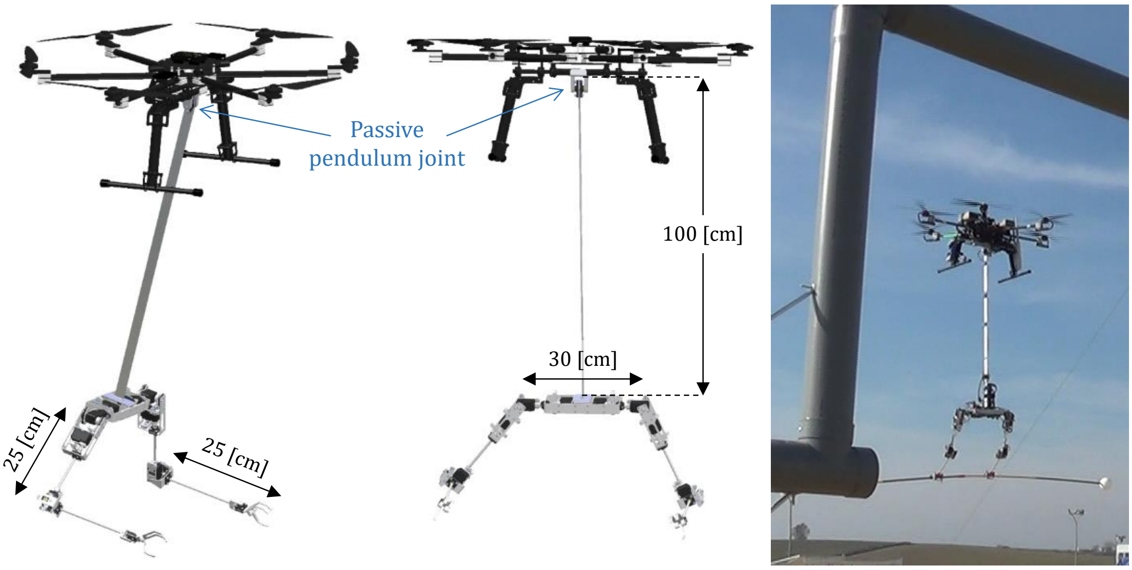

Figure 2.42. Two rendered views of the long reach aerial manipulator with the anthropomorphic, compliant and lightweight dual arm (left), and operation in outdoors (right).

Conclusion

This chapter has detailed the design, mechanical construction and hardware/software architecture of the different prototypes of lightweight and compliant manipulators developed by the author. These included the single compliant joint, two different implementations of compliant joint arms, a human-like finger module for object grasping, two dual arm systems (stiff and compliant joint), and three prototypes of long reach manipulators (flexible link in fixed base and two integrated in multirotor platform in pendulum configuration). Very low weight, low inertia, mechanical compliance, isolation of servo actuators against radial/axial loads, and intersection of joint axes are the main requirements imposed in the design of the arms. Mechanical joint compliance is implemented introducing a spring-lever transmission mechanism between the servo shaft and the output link, supporting the rotation of the link through a pair of flange bearings in side-by-side configuration. This mechanism allows the estimation and control of the torques and contact forces in terms of deflection, protecting the gears from peak forces due to impacts and overloads. The analysis of the workspace of the manipulators when integrated in the aerial platform evidences the motion constraints associated to the landing gear and the propellers and the risk of crash due to the proximity between these and the obstacles when the arms operate in contact with the environment. This has motivated the development of the long reach aerial manipulators, which extend the effective workspace of the arms and increase safety since the distance between the propellers and the obstacles within the workspace of the arms is higher.

Chapter 3 – Functionalities of lightweight and compliant aerial manipulators

The main purpose of this chapter is to illustrate the benefits of mechanical joint compliance and show how it can be exploited in aerial manipulation, although these capabilities also result suitable in ground service robotics. Two types of compliant manipulators are considered: flexible joint, where a spring-lever mechanism is introduced between the servo shaft and the output link, and flexible long reach link with passive joint. The use of a dual arm aerial manipulator is also motivated and compared with respect to the single arm case, showing that some tasks are more suitable for a dual arm system. The models and control methods that support the concepts proposed here are described in Chapter 4 and evaluated experimentally in Chapter 5 and Chapter 6.

The chapter is organized in the following way:

3.1. Benefits of mechanical joint compliance
3.2. Payload mass estimation with compliant joint arm
3.3. Passive/active compliance in compliant manipulators
3.4. Soft-collision detection and obstacle localization
3.5. Monitoring force/displacement in grabbing situations
3.6. Operations with dual arm aerial manipulators
3.7. Functionalities in flexible link long reach aerial manipulators

3.1. Benefits of mechanical joint compliance

3.1.1. Torque estimation and control

The torque sensors integrated in the joints of the industrial manipulators employ strain gauges to measure the micro-deflections of an aluminum structure consisting of two concentric rings connected by a number of transversal pads or beams. The inner ring is rigidly attached to the shaft of the motor, whereas the output link rotates rigidly with the output link, as illustrated in **Figure 3.1**-up. The strain gauges are disposed in this aluminum structure in such a way that their sensitivity to external loads acting over the output link is maximized, that is, at the weakest points of the structure, the pads. The signal provided by these devices is amplified and processed for obtaining the torque measurement at rates above 1 kHz, requiring a previous calibration process to improve the accuracy. The external load may also cause a very small deviation in the output link angular position, although the joint is intrinsically stiff, so the effect is almost negligible. The estimation and control of the torque also relies on the current injected to the motor, although the friction of the gearbox may affect the accuracy.

The spring-lever transmission mechanism employed extensively in this thesis consists of a pair of compression springs that transmit the motion of the servo shaft to the output link (see **Section 2.2**). The lever frame is screwed to the servo horn, pushing the springs that push the transmission frame of the output link. The design parameters of this mechanism are the lever length and the stiffness of the springs. The torque-deflection characteristic is described in more detail in **Section 4.2.2**, although it can be approximated in the following way assuming that the spring is orthogonal to the lever:

$$\tau_j^i \cong K_j^i \cdot \left(l_j^i\right)^2 \cdot \Delta\theta_j^i = k_j^i \cdot \Delta\theta_j^i \tag{3.1}$$

Here K_j^i is the stiffness of the compression spring, l_j^i is the lever length, k_j^i is the equivalent torsional stiffness, and $\Delta\theta_j^i$ is the deflection of the j-th joint of the i-th arm, defined as:

$$\Delta\theta_j^i = \theta_j^i - q_j^i \tag{3.2}$$

This angle is measured by the potentiometer attached at the frame structure, as depicted in **Figure 3.1**-down, allowing the estimation and control of the torque, as it will be described in **Section 4.2.3**.

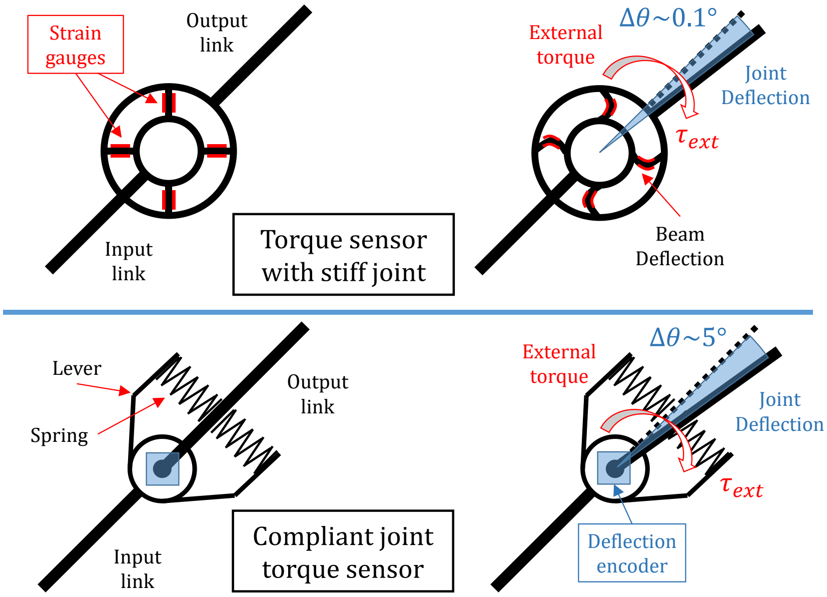
Strain gauges
Output link
Input link
Torque sensor with stiff joint
External torque
Δθ~0.1°
Joint Deflection
τext
Beam Deflection
Lever
Spring
Output link
Input link
Compliant joint torque sensor
External torque
Δθ~5°
Joint Deflection
τext
Deflection encoder

Figure 3.1. Torque sensor based on strain gauges employed in industrial manipulators (up) and compliant joint with deflection sensor based on spring-lever transmission mechanism (down).

Introducing flexible elements like springs or elastomers for transmitting the motion of the motor to the output link is a simple and low cost method for providing compliance at hardware level. These components act as low pass filters, absorbing the energy of impacts and overloads in a passive way thanks to their natural damping. This feature is especially interesting for protecting the servo actuators against peak forces or torques in those situations in which the manipulator enters in contact with the environment. A potentiometer or encoder can be introduced in the compliant joint for building a simple torque sensor based on the deflection of the springs.

3.1.2. Virtual variable impedance

In robot manipulation, the impedance is the opposition that the manipulator shows to an external force acting over it, at joint level or well at the end effector. According the diagram depicted in **Figure 3.2**, the impedance behaviour of the robotic arm can be assimilated as a mass-spring-damper system characterized by the physical stiffness k_p, damping d_p, and inertia J_p. The application of the external force F_{ext}, representing either an impact or contact force, will cause a deviation in the position of the manipulator with respect to its equilibrium point due to the mechanical elasticity, which is denoted in this thesis as deflection. The evolution of the deflection signal is determined by the second order dynamic model:

$$J_p \Delta\ddot{x} + d_p \Delta\dot{x} + k_p \Delta x = F_{ext} \tag{3.3}$$

where Δx represents the deflection. The impedance control of robotic manipulators has been well studied in several works [92][93][94][95][96], extending this concept to the control of multirotor vehicles affected by external wrenches [43][44][97]. During the execution of an aerial manipulation operation, it may result convenient to vary the impedance of the manipulator to improve the performance of the system. For example, in case of unexpected impacts with the environment it is preferable that the stiffness of the arm is low so the interaction does not affect the aerial platform significantly, whereas in a visual servoing task it is preferable that the stiffness is high to improve the positioning accuracy.

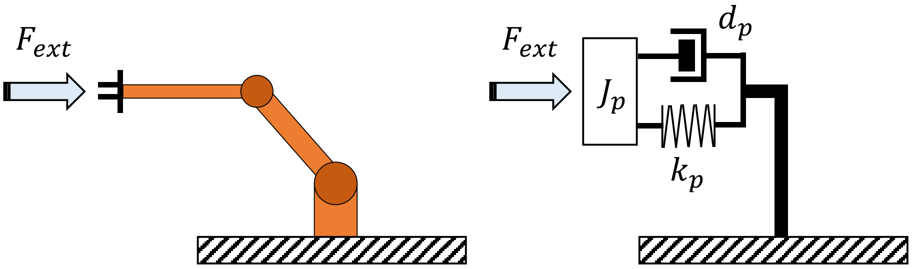

Figure 3.2. Impedance behaviour of compliant manipulator to external load, assimilated to a mass-spring-damper system.

This thesis explores the possibility to vary the apparent stiffness and damping of a lightweight and compliant joint manipulator at control level without the need of additional actuators [60][61][62], that is, without increasing the weight [57]. This can be achieved measuring and controlling adequately the deflection of the joints in such a way that the dynamic behaviour of the output links is similar to a virtual desired dynamics characterized by a virtual stiffness k_v, damping d_v, and inertia J_v. An important point here is that, unlike industrial robotic arms which have control frequencies of 1 kHz and higher, the low weight arms in the aerial manipulator are severely constrained by the servomotors used, which have a maximum control frequency of around 50 Hz. Thus, the passive response will be instantly but the active response will come at the control frequency of 50 Hz and with some delay. Then, the global compliant behavior of the arm can be seen as an instant response by the elastic element that is shaped later to adapt stiffness and damping with the controller. The main consequence is the different response to different interactions with objects or the environment. For an impact or collision of the arm, the initial response will come only from the passive elements, followed later by the controller action. On the other hand, other interaction tasks as applying forces or grabbing objects with slower variations of the external forces can fully benefit from the physical stiffness or impedance controller combination. Thus, when designing the compliant arms for safety of the physical interaction of the aerial manipulator, the physical stiffness should be used.

3.1.3. Energy storage capacity

One of the main benefits of the mechanical compliance is the ability of the joints to absorb the excess of energy due to motion constraints in grabbing tasks or associated to impacts between the aerial manipulator and the environment. However, the mechanical limit in the deflection of the joints, around 20 – 30 deg in the developed mechanisms, involves a limit in the maximum energy that the manipulator can store in a passive way. If it is imposed that $|\Delta\theta_j^i| \leq \Delta\theta_{max}$, then:

$$E_{PC}^{max} = \frac{1}{2}(\Delta\theta_{max})^2 \sum_{i=1}^{2}\sum_{j=1}^{4} k_{p,j}^i \tag{3.4}$$

where $k_{p,j}^i$ is the joint physical stiffness and E_{PC}^{max} is the maximum passive compliance energy.

Denoting by m_T to the total mass of the aerial manipulator, the maximum speed of the platform that can be supported by the arms in a strong impact is:

$$|v_{max}| \leq \sqrt{\frac{2 \cdot E_{PC}^{max}}{m_T}} = |\Delta\theta_{max}| \sqrt{\frac{\sum_{i=1}^{2} \sum_{j=1}^{4} k_{p,j}^{i}}{m_T}} \tag{3.5}$$

Considering the aerial manipulator depicted in **Figure 2.35**, whose weight is $m_T = 6.8\ kg$, with a maximum joint deflection $|\Delta\theta_{max}| = 20°$ and mean stiffness $k = 1.82\ Nm/rad$, it results that $E_{PC}^{max} = 0.89\ J$ and $|v_{max}| = 0.51\ m/s$.

3.2. Payload mass estimation with compliant joint arm

The possibility to estimate the weight of an object to be grasped results useful in aerial manipulation since it allows to regulate the thrust of the aerial platform on flight as well as to adjust the parameters of the attitude controller according to the variation of the mass and inertia. This was the first capability exploited in the first prototype of lightweight and compliant joint arm developed by the author, which is depicted in **Figure 3.3** (see also **Section 2.3.3**) along with its geometric model. The contact points of the linear servo in the upper arm and forearm links are $\boldsymbol{P_1}$ and $\boldsymbol{P_2}$ respectively, whose position are defined in a local frame attached to the upper arm link and given by:

$$\boldsymbol{P_1} = \begin{bmatrix} h_1 \\ l_1 \end{bmatrix} \quad \boldsymbol{P_2} = \begin{bmatrix} l_2 sin(\theta) + h_2 cos(\theta) \\ -l_2 cos(\theta) + h_2 sin(\theta) \end{bmatrix} \tag{3.6}$$

The distance from $\boldsymbol{P_1}$ to $\boldsymbol{P_2}$ is equal to the length of the linear actuator plus the length of the stroke and the extension spring:

$$\|\boldsymbol{P_2} - \boldsymbol{P_1}\| = D + d_{stroke} + d_{spring} \tag{3.7}$$

If d_0 and Δd represent the natural length and the elongation of the spring when a load is exerted over the forearm in the direction of gravity, then it remains that:

$$\Delta d = \|\boldsymbol{P_2} - \boldsymbol{P_1}\| - D - d_{stroke} - d_0 \tag{3.8}$$

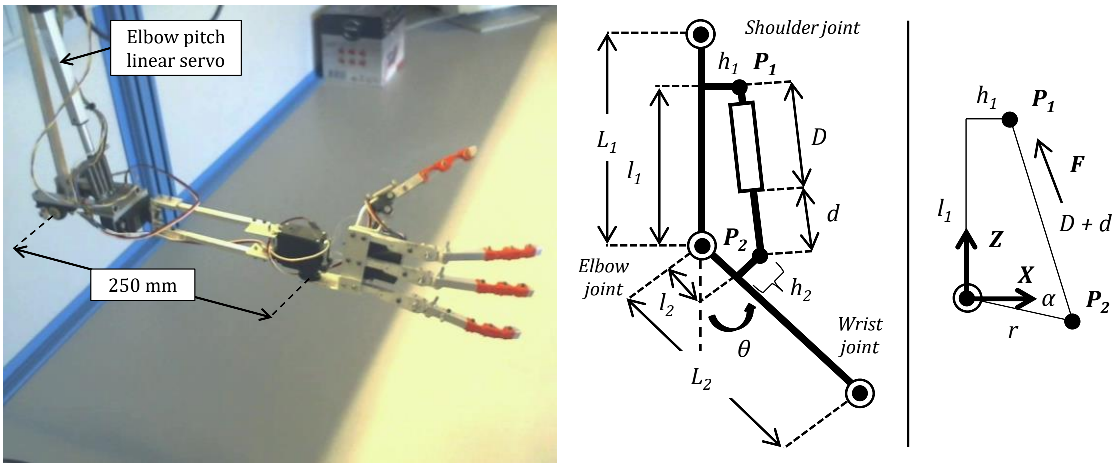

Figure 3.3. Lightweight arm with compliant elbow joint (left) and geometric model (right).

Whenever the arm is holding or lifting a load mass, the spring will be elongated. Spring elongation can be computed from Equation **(3.8)** known the elbow joint position and the displacement of the stroke, and it can be related with the payload mass in terms of equilibrium of torques. Assuming that measurement is done in static conditions, that is, inertias are negligible, then the torque exerted by the spring equals the torque due to gravity. Let denote by m_{PL} the payload mass and K the spring stiffness. Then taking into account the right side on **Figure 3.5**, the following expressions are derived:

$$\tau_{gravity} = m_{PL} \cdot g \cdot L_2 \cdot \sin(\theta) \tag{3.9}$$

$$\tau_{spring} = K \cdot \Delta d \cdot r \cdot sin(\alpha) \tag{3.10}$$

where $r = \sqrt{l_2^2 + h_2^2}$ and α can be obtained from vectors $\boldsymbol{P_1}$ and $\boldsymbol{P_2}$. Equaling both terms in Equation **(3.9)** and Equation **(3.10)** it results that:

$$m_{PL} = \frac{K \cdot \Delta d \cdot r \cdot sin(\alpha)}{g \cdot L_2 \cdot \sin(\theta)} \tag{3.7}$$

Note that there is a singularity associated to $\theta = 0$ that in practice will degrade the accuracy of the estimation for small joint angles. Therefore it is preferable to carry out the process of measurement with angles around 90 deg.

3.3. Passive/active compliance in compliant manipulators

The passive compliance is a mechanical property of the aerial manipulator associated to the joint and/or link flexibility that allows the robot to accommodate to forces acting over it without the need to generate movement with the actuators, but with the displacement caused by the deflection. Since the aerial manipulator is intended to operate in contact with the environment or close to obstacles, it is expected that the manipulator is affected by impacts and overloads due to unexpected or undesired deviations in the position of the aerial platform caused by sensors noise, wind disturbances, reaction wrenches generated by the arms or oscillations introduced by the controller. What is more, bimanual manipulation tasks like grasping require the coordination of both arms in order to prevent that the deviation in the position of one arm induces an overload in the other one, which is typical in closed kinematic chain configurations. These situations have been illustrated in **Figure 3.4**.

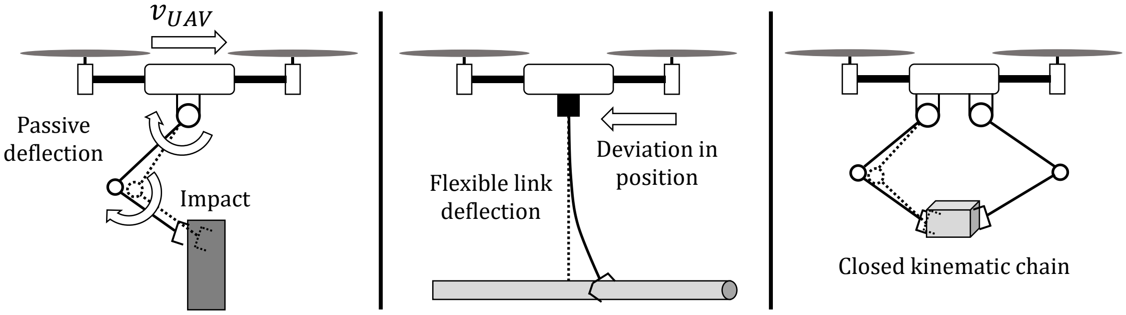

Figure 3.4. Three situations illustrating the passive compliance capability: unexpected impact against obstacle (left), flexible link deflection in grabbing situations (middle), and closed kinematic chain (right).

The level of mechanical tolerance against overloads can be characterized quantitatively in terms of maximum deflection and stiffness, and it is constrained by the positioning accuracy of the end effector, since lower stiffness typically involve higher positioning errors. This motivates the development of the active compliance methods, in which the deflection of the joints and links is monitored and controlled conveniently to extend the apparent deflection range and to prevent that the excess of energy stored in the elastic elements is released at high rates, what may cause acceleration peaks in the links. This last concept is illustrated in **Figure 3.5**. Consider the human-like arm with compliant elbow joint described in **Section 2.3.3**, which is rotating due to the contraction of the linear actuator. If an obstacle blocks the movement of the forearm link, the springs that act as tendons will suffer an elongation that can be measured in such a way that, in case it excess a certain threshold, the linear actuator reacts to reduce the deflection (elastic potential energy).

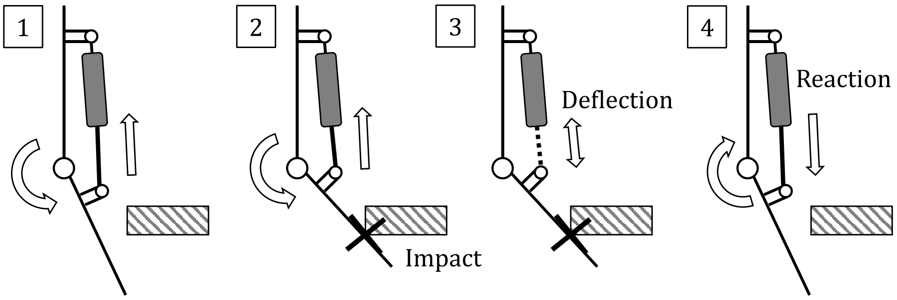

Figure 3.5. Active compliance applied to the detection and reaction against impacts.

3.4. Soft collision detection and contact-based obstacle localization

An aerial manipulation robot navigating in narrow spaces or operating close to obstacles has the potential risk to impact and crash if any of its parts (landing gear, propellers, arms) collides with the environment and the controller of the aerial platform is destabilized. In order to prevent undesired repairs, with the consequent cost and waste of time, it is highly desirable that the system is capable to detect and react against unexpected obstacles. In this sense, the manipulator can be exploited for this purpose, imitating the behaviour of a person which moves within a room at night without seeing (blind navigation). Intuitively, in these situations a person tends to extend the arms and fingers in the forward direction so any wall or obstacle is detected by contact by the fingers, protecting the body and head from impacts. What is more, once the obstacle is detected, it is possible to perform an active "scan" to determine its dimensions and find a way free to continue, simply following the surface of the obstacle while maintaining a slight contact force with it. The low mass and stiffness of the fingers reduces the energy of the impact and thus the influence over the body, whose speed should be low to avoid strong decelerations.

This principle can be applied in a compliant joint manipulator. Although the aerial platform may count with several navigation and positioning systems that can be used to determine the presence of obstacles, such as LIDAR, stereo cameras or ultrasonic devices, these may not be reliable for close ranges or in certain conditions, or well there are blind areas that cannot be covered. The contact-based obstacle detection method extends the functionalities of the aerial manipulator, based on the information provided by the encoders integrated in the servos actuators and the deflection sensors integrated in the joints of the compliant arms. The operation principle is simple. The compliant manipulator is stretched, but without reaching the kinematic singularity, while the aerial platform moves slowly through the obstacle. The deflection of the joints is continuously monitored, so any collision will cause a sudden deviation in the measurement of one or more joints of the arm and/or finger that can be easily detected, determining the distance to the obstacle from the forward kinematics. Just after that, the arms are retracted to avoid the contact, and the platform goes back to skip the collision. The manipulator can also perform a scan trajectory to cover a wider space, or well to determine more accurately the position of the obstacle previously detected.

This soft-collision detection and reaction capability is also useful in transportation operations. If the dual arm aerial manipulator depicted in **Figure 3.6** is carrying a long bar, and this collides against an unexpected obstacle in the environment, then the robot can react releasing the bar to prevent the crash. The impact is initially supported by the passive deflection of the compliant joints, storing the excess of energy as elastic potential energy. The collision can be detected simply observing a sudden change in the deflection, so the amplitude of the variation in a short period of observation may serve to decide if the bar has to be released for safety.

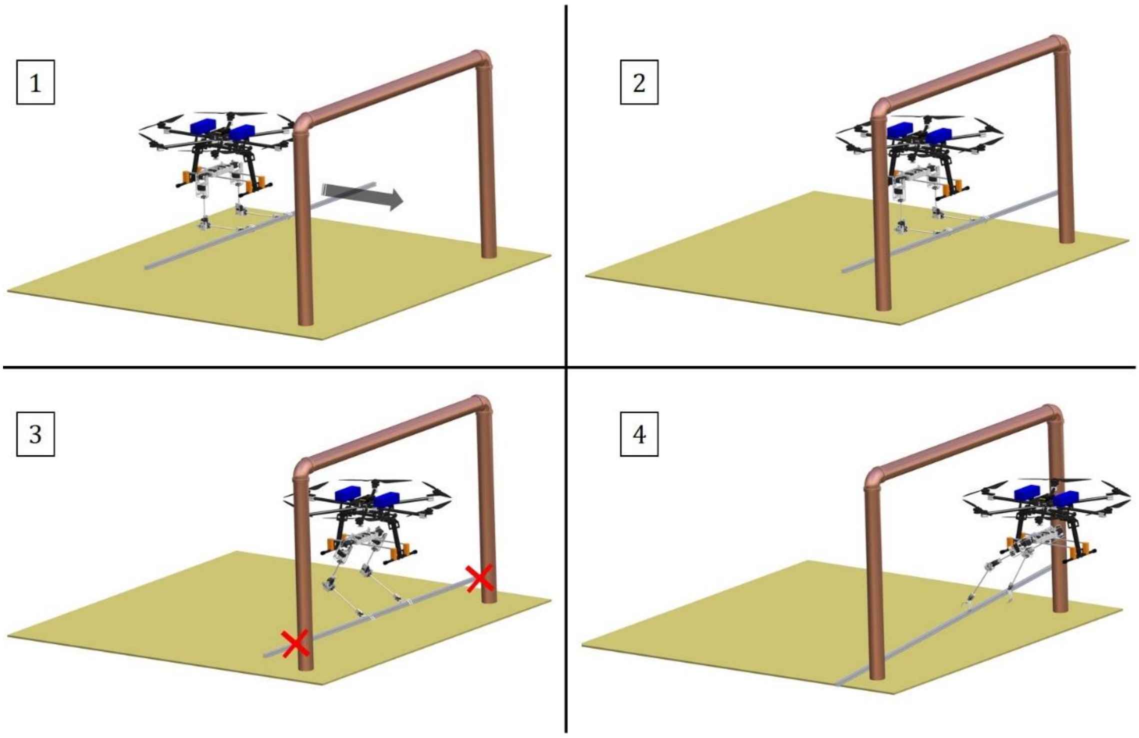

Figure 3.6. Dual arm aerial manipulator carrying a long bar (1) – (2). Unexpected collision with obstacle in the environment, which causes a deflection in the compliant arms (3), releasing the bar for safety (4).

3.5. Monitoring force/displacement in grabbing situations

The possibility to estimate and control the interactions forces exerted by the manipulator in terms of joint deflection improves safety in the realization of some operations on flight, taking into account that the physical interactions are supported by the aerial platform and that the thrust of the propellers is limited. Let us consider an illustrative example in which the aerial manipulator has to retrieve an inspection tool installed over a pipe (**Figure 3.7**), which involves grasping the tool by the handle and pulling upwards. If, for some reason, the tool is blocked at the pipe and it cannot be lifted, then the manipulator may be damaged due to overload and the stability of the aerial platform might be affected since the grabbing situation imposes a kinematic constraint and the propagation of external wrenches. Therefore, the aerial robot should be capable to determine if the object can be retrieved or not, what can be done applying a known pulling force and monitoring the displacement of the end effector, assuming that the aerial platform keeps its position fixed during the operation. The method is similar to the one employed by any person to determine if a door can be opened: a pushing/pulling force is applied while standing in front of it, observing the displacement of the hand/arm.

This method relies on the contact force control method based on joint deflection measurement. The magnitude of the force reference to apply during the monitoring period should be high enough to cause a significant displacement of the object in case it can be retrieved, which implies a prior knowledge about its weight. In any case, the torque limit of the servo actuators must not be exceeded, and the pose of the arms should be far from the kinematic singularities to prevent strange behaviours. In this sense, the L-shaped pose (90° elbow flexion) is preferable, so lifting forces in the vertical axis are due to the torque of the elbow joint servo, whereas pushing/pulling forces in the horizontal axis depend on the shoulder pitch joints. The direction of the applied force should be adapted according to the particular operation to perform. Considering again the example of the door, the manipulator hast to apply first a vertical pushing force downwards to rotate the handle, and then apply a horizontal pulling force to open the door.

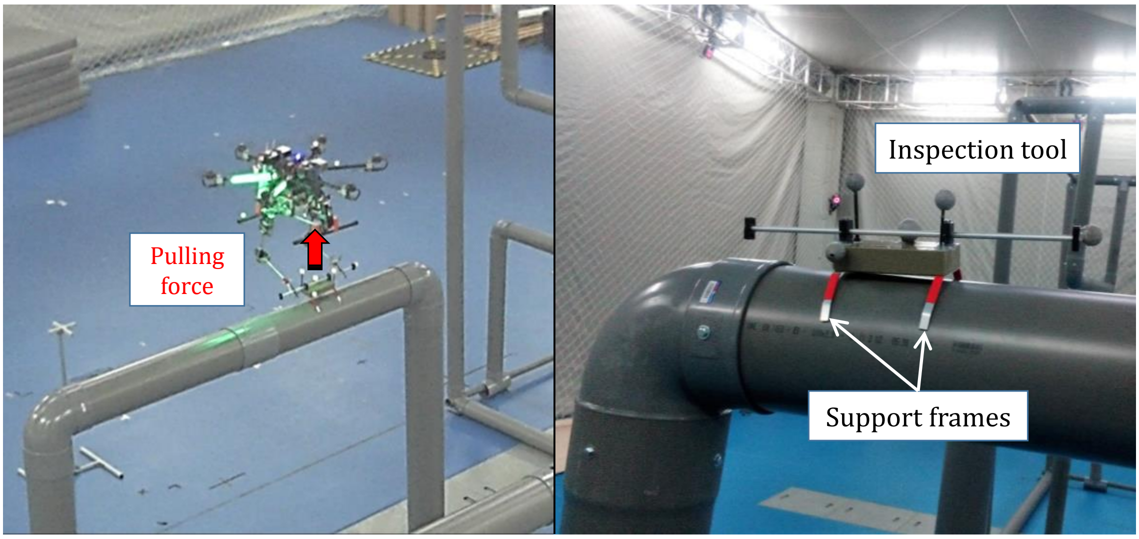

Figure 3.7. Retrieval on flight of inspection tool installed on a pipe. The compliant dual arm apply a pulling force in the vertical axis while monitoring the displacement of the end effector to detect if the tool is blocked.

3.6. Operations with dual arm aerial manipulator

3.6.1. Operating while grabbing on flight with compliant dual arm

Most aerial manipulation operations to be executed on flight require a high positioning accuracy. Since the effective reach of a human-size manipulator is around 20 cm, taking into account that the nominal operation position is usually the L-shaped configuration (90° elbow joint flexion), then it is necessary that the platform is capable to stay at a fixed position during the execution of the task with deviations below 5 cm. Otherwise the probability of success will be low. This strong requirement depends directly on the performance of the position sensors and the controller of the aerial platform. Furthermore, the problem is significantly more complex in outdoors than in indoors, where there is a wide variety of solutions that can be applied (Vicon or OptiTrack systems, time-of-flight sensors, or vision based SLAM). Outdoor environments however, where the aerial robots are aimed to work, are less favourable for cameras and laser sensors due to the variations in the illumination conditions and the interference of the sunlight. Additionally, the aerial platform is exposed to wind disturbances with the consequent risk of impact against obstacles in the workspace.

One interesting application of a compliant dual arm system consist of using one arm to execute the operation, while the other one is used as position sensor relative to a grasping point. The concept is illustrated in **Figure 3.8**. Let us consider that the aerial manipulator has to install a sensor device, using the left arm for this purpose. Both arms are initially retracted in a rest position. Once the aerial manipulator enters in the workspace, the right arm (sensor arm) is deployed and grasp the pipe at a point next to the installation point. Then, the torque control of this arm is enabled, specifying a zero torque reference in such a way that any deviation of the aerial platform will not generate a significant reaction torque in the arm. That is, the right arm accommodate to the motion of the aerial platform while it is grabbing the pipe. However, the position deviations should be monitored to prevent that the arm reaches the kinematic limit, releasing the pipe in that case for safety. Since the position of the end effector relative to the base of the multirotor is known from the forward kinematic model, then it is possible to define a Cartesian position error relative to the grabbing point, considering for example that the zero position error corresponds to the position of the end effector for the L-shaped configuration of the right arm. The multirotor controller introduces then this position estimation in the control loop during the operation of the left arm. Note that the accuracy of the estimation is high since it is computed from the measurements provided by the encoders integrated in the arm servos and the forward kinematic model.

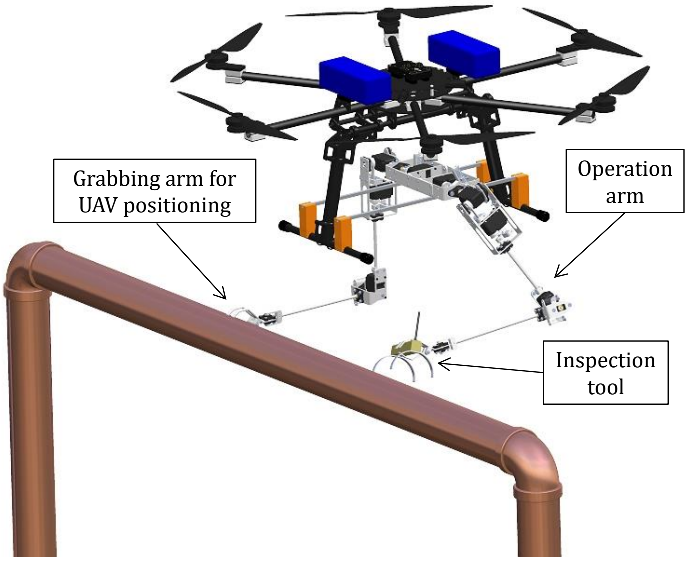

Figure 3.8. Compliant dual arm aerial manipulator installing a sensor device with the left arm (operation arm) while the right arm is grabbed at a fixed point in the workspace measuring the relative position.

3.6.2. Installation and retrieval of two sensor or devices

It is expected that the aerial manipulator has to operate in remote areas or in complex scenarios, requiring a significant amount of time for the navigation phase. Given the current limitations of the Lithium-Polymer batteries, the flight time for a human-size aerial manipulator carrying a dual arm system is around 20 minutes. Therefore, it is convenient to maximize the performance of the aerial robot once it is in the workspace, trying to reduce as much as possible the time devoted to reach this. Since some inspection and maintenance operations involve the use of different sensors (humidity, gas, temperature) or devices (drilling tools, cleaning tools, insulating materials), a dual arm system can be exploited in such a way that each of the arms takes care of a certain task. However, the maximum lift load provided by the arms imposes a constraint to the weight of the sensors or tools to carry.

3.6.3. Transportation of long bars or heavy objects

Although a single-arm aerial manipulator may be capable to execute a wide variety of tasks, a dual arm system results more adequate for some operations involving the grasping and transportation of long or heavy objects. Intuitively, the reliability in the realization of such operations depends on the stability of the grasping points. Since the conditions on flight are much less favourable than in a fixed base scenario, a dual arm manipulator results more adequate for object grasping, which contributes to increase the probability of success with respect to the single arm case. There are other tasks, such as disconnecting a plug from a cable, which involve the application of forces in opposite directions, requiring necessarily the participation of two robotic arms.

3.7. Functionalities of flexible link long reach aerial manipulators

This section covers the functionalities developed for the flexible link, long reach aerial manipulators presented in **Section 2.7**. The first three subsections (**3.7.1 – 3.7.3**) are focused on the horizontal configuration (**Figure 3.9**-left) in which the effect of gravity is ignored, considering only the lateral deflection of the flexible link due to interaction forces or non-compensated reaction wrenches, whereas **Subsection 3.7.4** is focused on the passive pendulum configuration (**Figure 3.9**-middle, right), exploiting the passivity properties of the joint at the base of the flexible link.

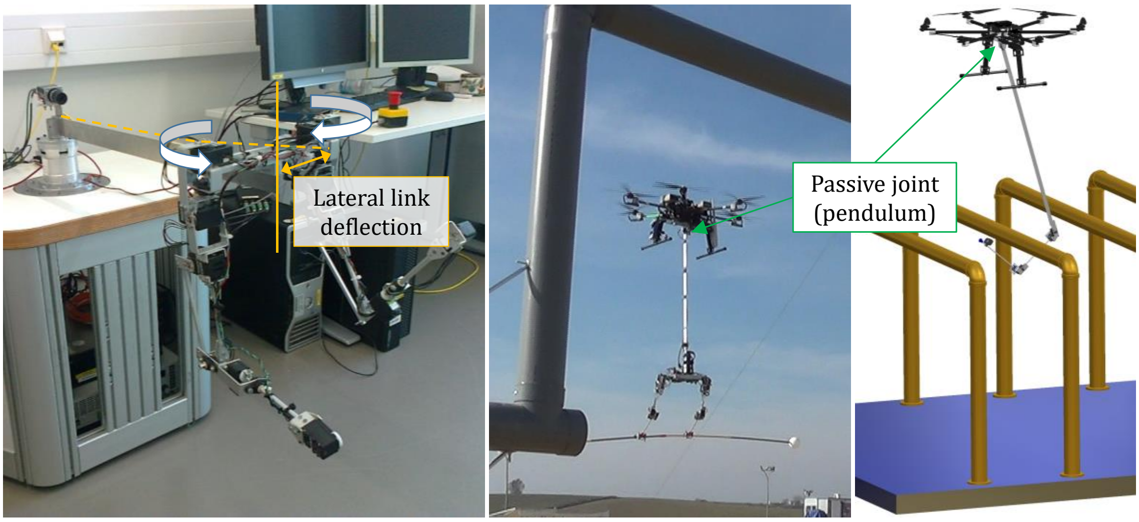

Figure 3.9. Flexible link long reach manipulator with lightweight dual arm in test bench (left), and passive pendulum aerial manipulators, single arm (right) and dual arm (middle).

3.7.1. Vibration suppression in flexible link based on zero-cross detection

Despite the evident benefit of extending the reach of a manipulator whose workspace is reduced when it is integrated in an aerial platform, the accuracy in the positioning of the end effector is severely affected by the intrinsic deflection of the flexible link (see **Figure 3.9**-left). Any impact [79], contact force or non-compensated reaction wrench caused by the motion of the arms [80][81] will induce an undesired oscillation in the flexible link that should be suppressed [82][83]. This can be done in two ways: 1) introducing an actuator at the base of the link so the torque transmitted at this point can be controlled, or 2) coordinating the motion of the manipulator attached at the tip in such a way that the oscillations are suppressed. The first method does not results convenient in aerial manipulation since it implies increasing the weight due to the additional actuator and because the non-minimum phase zeros associated to the transfer function which relates the torque with the deflection at the tip complicates the control [78]. Therefore, the second method is considered here.

The proposed method for vibration suppression makes use of a vision sensor for identifying online the maximum amplitude of the flexible link tip oscillation and the time instant in which the deflection crosses by zero. According to the dynamic model described in **Section 4.7.1** and to the identification experiments presented in **Section 5.6.1**, the deflection of the flexible link at the tip in free vibration conditions can be expressed in the following way:

$$w(t,L) = W_0 \cdot e^{-d_1 \cdot t} \cdot sin(\omega_1 \cdot t + \phi_0) \tag{3.8}$$

where W_0 is the initial amplitude of the oscillation, ω_1 is the natural frequency, d_1 is the damping coefficient, and ϕ_0 is the initial phase. The method for attenuating the oscillation of the link, described in **Table 3.1**, consists of an iterative process executed while the maximum amplitude of the deflection, W_{max}, is higher than a desired error W_ε. For each iteration, the program waits until a change in the sign of the deflection signal is detected. Meanwhile, the maximum amplitude of the oscillation is identified just evaluating the absolute value of the deflection signal. When the zero cross is detected, the shoulder yaw joint servos of the arms are commanded to a reference position $\theta_{1,ref}^{LR}$ which is proportional to the maximum deflection with constant K, and it is π radians out of phase with respect to $w(t,L)$. The play time of the servos is set to a quarter of the oscillation period, that is, the remaining time before the tip deflection reaches again its maximum value. Phase φ indicates the direction of the deflection, whose value is given by:

$$\begin{gathered} w(t_0^-,L) < w(t_0^+,L) \rightarrow \varphi = 0 \\ w(t_0^-,L) > w(t_0^+,L) \rightarrow \varphi = \pi \end{gathered} \tag{3.9}$$

where t_0^- and t_0^+ represent the time instants just before and just after the zero cross.

Table 3.1. Pseudocode implementing the vibration suppression method.

```
while $W_{max} < W_\varepsilon$
        $W_{max} = 0;$
        while $sign(w(t^-,L)) \neq sign(w(t,L))$
                if $|w(t,L)| \geq W_{max} \rightarrow W_{max} = |w(t,L)|$
        MoveServo($\theta_{1,ref}^{LR} = -K \cdot W_{max} \cdot \cos(\varphi)$,$play\ time = \frac{T_1}{4}$)
end
```

This method is model free [82] in the sense that gain K can be tuned empirically without requiring knowledge of the parameters of the dynamic model. The proof of stability is also simple and intuitive: as long as the energy injected by the arm(s) on each oscillation period, which depends on the adjustable parameter K, is lower than the mechanical energy of the oscillating mass within the same period, then the amplitude of the oscillation will tend to decrease.

3.7.2. Contact-based obstacle detection and localization

Consider the situation depicted in **Figure 3.12**, in which the long reach dual arm aerial manipulator is navigating in an area with close obstacles around that cannot be detected by the sensors onboard the aerial platform. Assuming that the only cause for flexible link tip deflection is the presence of an external force acting over any of the arms, then a simple collision detection method based on constant threshold can be applied for detecting the presence of an obstacle. During an initial scan phase, both arms move symmetrically so the reaction forces along the direction of the deflection are compensated. Following the criterion described in **Table 3.2**, it is even possible to infer in which side and in which arm the collision occurred taking into account the direction of rotation of the joint and the sign of the deflection. Here $w_{th}{\sim}10\ [mm]$ is the collision detection threshold. This value is low enough to prevent that high contact forces arise ("soft" collision detection), and high enough to reject false positives. In **Figure 3.10**, the collision in (2) causes a positive deflection while the right arm is rotating clock wise, inferring that the obstacle is on the right side. The assumption regarding the cause of the deflection requires that the motion of the arms do not cause any reaction force in the direction of the deflection, what can be achieved if the left and right arms move symmetrically around the plane of the link. **Figure 3.11** illustrates the obstacle detection process based on active arms scan and flexible link monitoring.

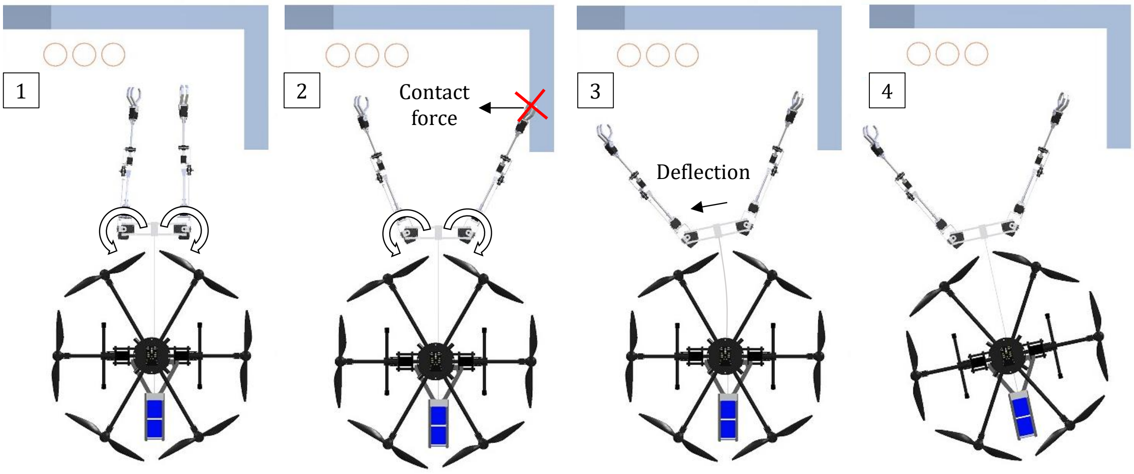

Figure 3.10. The dual arm system executes a scan for detecting obstacles, rotating the shoulder yaw joint until a collision occurs. The contact force causes a deflection in the flexible link and a reaction on the UAV.

Table 3.2. Criteria for identifying which arm and in which side a collision occurs based on flexible link tip deflection and the sign of the scan.

Left/Right arm rotation	Deflection	Affected arm/side
Counter clockwise/clockwise	$w(t,L) \leq -w_{th}$	Left arm, left side
	$w(t,L) \geq w_{th}$	Right arm, right side
Clockwise/counter clockwise	$w(t,L) \geq w_{th}$	Left arm, right side
	$w(t,L) \leq -w_{th}$	Right arm, left side

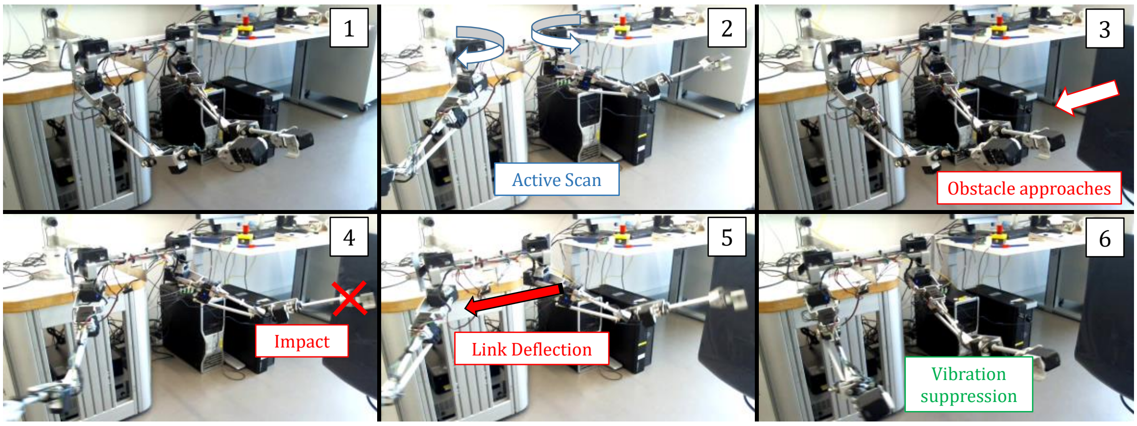

Figure 3.11. Evaluation in fixed test-bench of the obstacle detection function based on the flexible link deflection measurement provided by the vision system.

The obstacle detection function can be easily extended in such a way that, known the position of the arm affected by the contact, it is possible to determine the position of the obstacle. Although it is expected that the aerial robot is equipped with vision and range sensors for navigation in narrow spaces, it is possible that these sensors are not reliable in certain situations, for example due to the lack of texture in the environments, obstacles out of the field of view or out of the detectable range. In this sense, the compliant contact sensor increases reliability.

In order to accurately localize the contact point, a two-step process will be executed, taking into account that the contact may occur in any point along the upper arm or forearm. In the first step, both arms are fully stretched ($\theta_2^{LR} = \pi/2$, $\theta_3^{LR} = 0$) and perform a scan motion rotating the shoulder yaw joints from an initial value $\theta_1^{LR} = \pm\alpha_0$. This scan phase ends when the collision is detected, determining the scan angle $\theta_1^{LR} = \pm\beta$ for the second step. Starting now with the arms retracted, a new scan is performed around this angle with a certain amplitude $\Delta\beta{\sim}5\ [deg]$. The idea is to force that the first contact point is the end effector, stretching the arms on each iteration so the scan reach is increased until the second collision occurs. The method is illustrated in **Figure 3.12**.

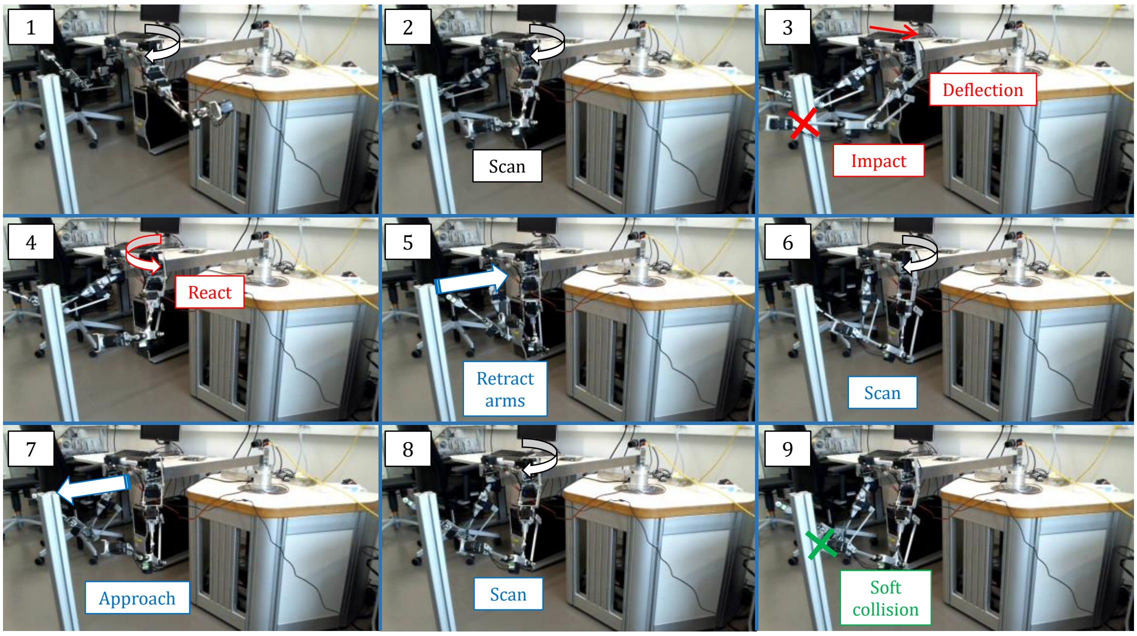

Figure 3.12. Sequence of images showing the obstacle localization method based on soft-collision detection.

3.7.3. Contact force control based on tip deflection measurement

The vision sensor can be employed as force sensor if the measurement of flexible link tip deflection is related to the corresponding force through a static characteristic. Let assume that the flexible link behaves as a linear spring in conditions of static contact, ignoring impact dynamics [79]. According to the model of flexible link described in **Section 4.7.1.1** (see Equation **(4.74)** and Equation **(4.75)**), it is possible to obtain a proportional relationship between tip deflection and the contact force, so a feedback control scheme as the one depicted in **Figure 3.13** can be implemented. Here the contact force, estimated from the flexible link tip deflection, is controlled by means of the shoulder yaw joint of the arm, which is in contact with the surface. The concept is illustrated in **Figure 3.14**.

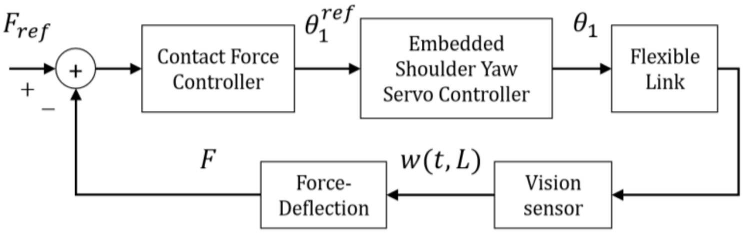
F_{ref}
+
+
−
Contact Force Controller
θ_1^{ref}
Embedded Shoulder Yaw Servo Controller
θ_1
Flexible Link
F
Force-Deflection
$w(t,L)$
Vision sensor

Figure 3.13. Contact force control scheme. The shoulder yaw joint determines the pushing force of the end effector against a surface in the direction of the flexible link tip deflection.

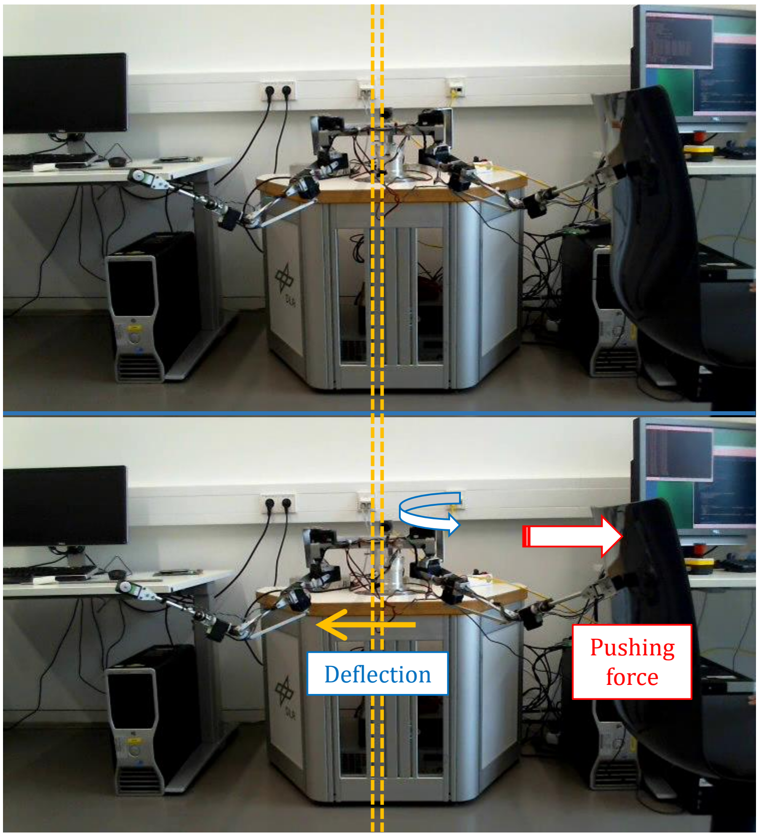
Deflection
Pushing force

Figure 3.14. Estimation and control of the contact force exerted by the left arm through the rotation around the shoulder yaw joint. The camera installed at the base of the link measures the deflection at the tip.

3.7.4. Long reach aerial manipulators in passive pendulum configuration

The main drawback of the long reach manipulator in horizontal configuration considered before is that it induces very high torques at the base of the manipulator due to the displacement of the mass and the effect of contact forces at the end effector. Therefore, its integration and application with an aerial platform may not be suitable, unless some kind of mechanism for load compensation (in pitch and yaw angles) is incorporated. This has motivated the development of the vertical – "or pendulum" – configuration with passive joint (see **Section 2.7.2** and **Section 2.7.3**). Introducing a non-actuated joint at the base of the long reach link that can rotate freely presents several benefits for the aerial platform. First of all, the interaction wrenches acting over the manipulator are transmitted to the base of the UAV as a force, not as a torque, which is more convenient to reduce the required thrust of the propellers. Note that the induced torque is proportional to the external force F_{ext} applied at the end effector and to the distance from the center of mass of the aerial manipulator to the contact point. This idea is illustrated in **Figure 3.15**. Secondly, the pendulum acts as an energy storage element, so in case the manipulator hits an obstacle while the UAV is moving at a certain speed (kinetic energy), the excess of energy released during the impact is transformed into potential energy in the pendulum, dissipating this by means of joint friction during the consequent oscillation. This feature contributes to improve safety during the operation of flight of the aerial manipulator, since the aerial platform will be less affected by unexpected physical interactions, reducing the probability of crashes. Another effect observed in the realization of the experiments is that both the passive joint and the flexible link tend to keep the center of mass of the manipulator aligned with the vertical axis. For example, if the manipulator attached at the tip moves in the forward direction to grasp an object, the passive joint will generate a reaction recoil motion in the opposite direction. This is convenient in terms of mass-load distribution for the aerial platform, but not in terms of kinematics and position control, since it reduces the positioning accuracy (see **Figure 3.16**-left and middle). Finally, it is interesting to realize that, measuring the rotation angle of the passive joint, it is possible to estimate the force exerted by the manipulator at the end effector based on the equilibrium of forces with gravity. This principle is represented in **Figure 3.16**-right. The pushing force in the forward direction depends on the mass of the manipulator and the rotation angle, and this can be controlled through the position of the aerial platform relative to the contact point.

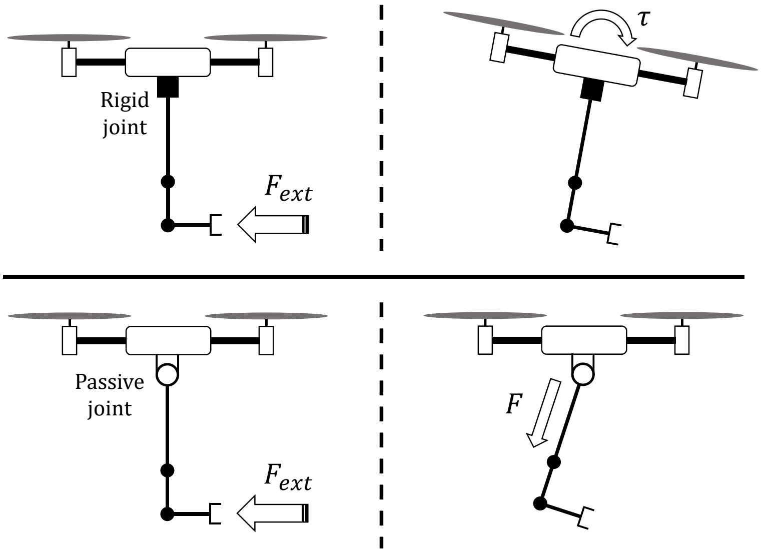

Figure 3.15. Two different behaviours of the long reach aerial manipulator to an external force acting at the end effector: propagation of torque through rigid joint (up), and reaction force with passive joint (bottom).

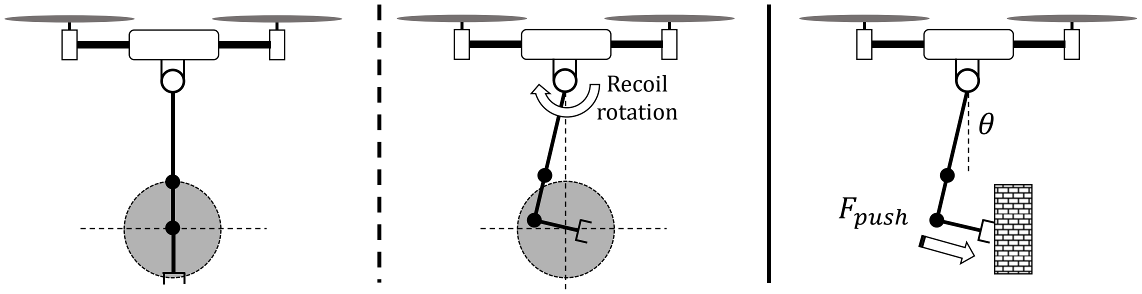

Figure 3.16. Recoil rotation in the passive joint caused by the motion of the manipulator attached at the tip of the long reach link (left, middle). Estimation and control of the pushing force applied at the end effector through the rotation angle of the passive joint exploiting the gravity force (right).

The passive pendulum aerial manipulator presents two main drawbacks. One the one hand, and as mentioned before, the positioning accuracy of the manipulator depends on the rotation angle of the passive joint, and this is affected by contact forces, accelerations in the aerial platform, or even by the motion of the manipulator itself. On the other hand, the undesired oscillations induced in the passive joint as consequence of the mentioned effects should be removed coordinating the motion of the aerial platform or generating an appropriate reaction motion with the manipulator attached at the tip. In this sense, the vibration suppression method described in **Section 3.7.1** can be applied for attenuating the amplitude of the oscillations.

Conclusion

This chapter explored the functionalities and potential applications of mechanical compliance in aerial manipulation, highlighting its benefits in particular situations involving physical interactions with the environment. This includes unexpected impacts during the realization of manipulation tasks, collisions in transportation operations, or the accommodation to joint overloads in bimanual grasping tasks. The possibility to detect, measure and control the contact forces in a safe way exploiting the passivity properties of the springs and the flexible links increases the robustness and reliability of the aerial robot, extending also the situational awareness of the environment. In this sense, the deflection measurement can be exploited for detecting and localizing close obstacles that cannot be perceived by other sensors due to limitations in the operation range. If the compliant joint manipulator is able to estimate the weight of grasped objects and monitor the interaction forces in grabbing situations from the deflection of the elastic element (springs or flexible links), then the aerial platform will be less exposed to risky situations, reducing the risk of impacts and crashes. The chapter also proposed some methods that exploit the manipulation capabilities of a dual arm system, for example using one arm as position sensor when grabbed to a fixed point while the other carries out the operation or the generation of reaction-less motions when the arms are attached at the tip of a flexible long reach link.

Chapter 4 – Modelling, estimation and control of compliant aerial manipulators

This chapter presents the kinematic and dynamic models of the different prototypes of lightweight and compliant aerial manipulators described in Chapter 2. Several control schemes are proposed for the arms, including position/trajectory, torque/force, and virtual variable impedance control. These are designed taking into account the control capabilities and the limitations of the servo actuators employed, and the deflection feedback provided by the sensors integrated in the joints.

The index followed throughout the chapter is indicated below:

4.1. Considerations and notation
4.2. Compliant joint dynamics and control
4.3. Position-force control in compliant joint arm
4.4. Position-force control in compliant finger module
4.5. Lightweight and human-size dual arm aerial manipulator
4.6. Anthropomorphic, compliant and lightweight dual arm
4.7. Flexible link, long reach aerial manipulators

4.1. Considerations and notation

4.1.1. Overview

It is expected that an aerial manipulation robot operating in outdoors is capable to execute certain inspection and maintenance operations or tasks involving physical interactions with the environment in a similar way a human operator or an industrial robot would do in fixed base. Some application examples include the installation and retrieval of sensor devices in polluted areas, the insulation of leaks in high altitude pipe structures, or the detection and repair of corrosion in the blades of wind turbines. The realization of these tasks can be divided into five phases: 1) the multirotor platform approaches to the workspace, so the point of interest is within the reach of the manipulator; 2) the manipulator is deployed, the position and orientation of the end effector is controlled to reach the desired pose; 3) the manipulation operation is carried out; 4) the manipulator is retracted; 5) the aerial platform gets out of the workspace. This section is focused on the control of the manipulator (phases 2 – 3), although several control schemes are proposed for the whole aerial manipulator.

4.1.2. Control capabilities and limitations of servo actuators

Unlike most industrial manipulators (KUKA, ABB, or Universal Robots), where accurate torque control is possible at rates above 1 kHz, the servo actuators typically employed in aerial manipulation (Herkulex, Dynamixel), do not provide any torque feedback or control capability, the update rate is below 100 Hz, and the embedded position controller has to be interfaced. Despite these limitations, these actuators are still the most suitable solution for building lightweight robotic arms intended to aerial manipulation due to their high torque to weight ratio (7 N·m / 145 g in case of the Herkulex DRS-0602), compact design, and easy assembly and integration.

Since the aerial manipulator is expected to perform different task involving physical interactions on flight with the environment, it is highly desirable to estimate and control the forces/torques acting over the robotic arms in order to prevent that the stability of the aerial platform is compromised and the manipulator is damaged. This motivated the introduction of a compliant spring-lever transmission mechanism, which allow the estimation and control of the forces/torque in terms of joint deflection. The main difference with respect to the industrial manipulators is that the joint stiffness and damping is 2 – 3 orders of magnitude lower in a compliant arm intended to aerial manipulation, so the effect of the deflection is much more evident. The compound servo actuator – compliant transmission is assimilated to a series elastic actuator, in which the position and force variables are related through the deflection of the elastic element.

4.1.3. Notation

The notation employed along the chapter is reproduced below. For the dual arm manipulators, superscript i will indicate the particular arm (left or right). In this way, $\boldsymbol{K}_C^1$ will represent the Cartesian stiffness matrix associated to the left arm. This index is omitted in the single arm case.

- i: superscript indicating the left/right arm, $i = \{1, 2\}$
- j: subscript indicating the joint, $j = \{1, 2, 3, 4\}$
- θ: the servo shaft angular position
- θ_{ref}: position reference sent to the embedded servo controller
- q: output link angular position
- $\Delta\theta$: deflection angle
- L_1: upper arm link length
- L_2: forearm link length
- D: separation between the left and right arms
- $\boldsymbol{FK}$: forward kinematics
- $\boldsymbol{IK}$: inverse kinematics
- $\Delta\boldsymbol{l}$: Cartesian deflection
- $\boldsymbol{\tau}$: joint torque vector
- $\boldsymbol{F}$: Cartesian force vector
- k_j^i: joint stiffness (equivalent torsion spring)
- d_j^i: joint damping
- $\boldsymbol{M}$: generalized mass matrix
- $\boldsymbol{C}$: Coriolis and centrifugal terms
- $\boldsymbol{G}$: force/torque components due to gravity
- $\boldsymbol{K}$: force/torque components due to elastic potential
- $\boldsymbol{D}$: force/torque components due to damping
- $\boldsymbol{K}_p$: physical stiffness matrix (diagonal)
- $\boldsymbol{D}_p$: physical damping matrix (diagonal)
- $\boldsymbol{K}_C$: Cartesian stiffness matrix (virtual)
- $\boldsymbol{D}_C$: Cartesian damping matrix (virtual)
- $\boldsymbol{J}$: Jacobian matrix of the manipulator
- $\boldsymbol{r}_{\boldsymbol{UAV}} = [x, y, z]^T$: UAV position
- $\boldsymbol{\eta} = [\phi, \theta, \psi]^T$: UAV orientation (roll, pitch, and yaw)

4.1.4. Kinematics, dynamics, and control

It was imposed by design that the axes of rotation in the developed manipulators intersect in a common point in order to simplify the analytical resolution of the inverse kinematics. Both the single compliant arm described in **Section 2.3.1** and the stiff-joint dual arm prototype presented in **Section 2.5** implement the classical kinematic configuration employed by the industrial manipulators with two joints at the shoulder and one at the elbow, whereas the anthropomorphic and compliant dual arm described in **Section 2.6** provides three joints at the shoulder and one at the elbow joint. The forward and inverse kinematic models of both configurations will be derived and exhaustively used by the position, trajectory and force controllers. The main reason to consider a control scheme based on inverse kinematics rather than in the Jacobian is that the servo actuators employed by the arms are designed for position control, although both schemes are equivalent.

The dynamic model of the different prototypes of compliant aerial manipulators presented here are derived following the Euler-Lagrange formulation based on the Lagrangian and the generalized equation for the forces and torques:

$$\frac{d}{dt}\left\{\frac{\partial L}{\partial \dot{\boldsymbol{\xi}}}\right\} - \frac{\partial L}{\partial \boldsymbol{\xi}} = \boldsymbol{\Gamma} \quad ; \quad L = K\left(\dot{\boldsymbol{\xi}}, \boldsymbol{\xi}\right) - V(\boldsymbol{\xi}) \tag{4.1}$$

where L is the Lagrangian, defined as the difference between the kienetic and the potential energy, K and V, respectively. The vector of generalized coordinates $\boldsymbol{\xi}$ typically includes the Cartesian position and orientation of the aerial platform, along with the joint variables of the manipulator, taking into account that the position of a compliant joint is determined by two variables: the servo shaft and the output link angular position (related through the deflection angle). Actually, the potential energy of the system will be the sum of the gravity potential and the elastic potential associated to the springs integrated in the joints. The model can be simplified taking into account that, in practice, most part of the kinetic energy of the manipulator is associated to the output link variables, whereas the kinetic energy of the servo shafts is almost negligible since its mass/inertia is relatively small. The vector of generalized forces $\boldsymbol{\Gamma}$ will include the forces and torques acting over the aerial platform, as well as the servo torque and the output link torque. The definition of these two vectors will be particularized for each of the prototypes presented here, expressing the dynamic model in the usual matrix form.

Finally, this chapter proposes different schemes for the control of the compound aerial platform – manipulator. Although the particular implementation will depend on the sensors available and the control capabilities of the autopilot, the scheme should be similar to the one depicted in **Figure 4.1**.

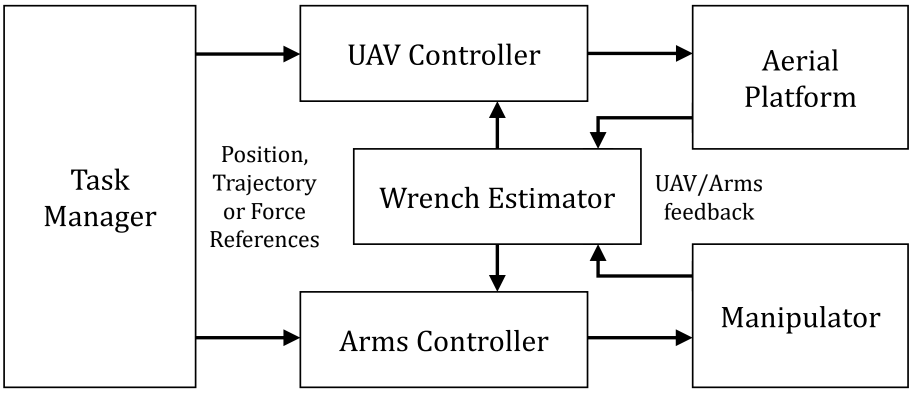

Figure 4.1. General control scheme of an aerial manipulation robot.

4.2. Compliant joint dynamics and control

4.2.1. Compliant joint dynamics

One of the main goals of this work is to demonstrate the functionalities of a compliant joint robotic arm, which requires a precise knowledge about this kind of actuators in the first place. Let us consider the compliant actuator depicted in **Figure 4.2** along with its model, assimilated to a series elastic actuator consisting of a Herkulex DRS-0101 and the spring-lever transmission mechanism. The servo accepts as reference the desired goal position/trajectory θ_{ref}, generating internally a trapezoidal velocity profile which ensures that the servo reaches the reference at the specified playtime. The feedback provided by the device is its current position θ and differential position (speed estimation) $\dot{\theta}$. A first order dynamics characterized by a time constant T_{servo}, and a delay T_{delay} associated to the serial communications are identified experimentally, so the servo can be modelled by the following first order transfer function:

$$G_{servo}(s) = \frac{\theta}{\theta_{ref}} = \frac{e^{-T_{delay} \cdot s}}{1 + T_{servo} \cdot s} \tag{4.2}$$

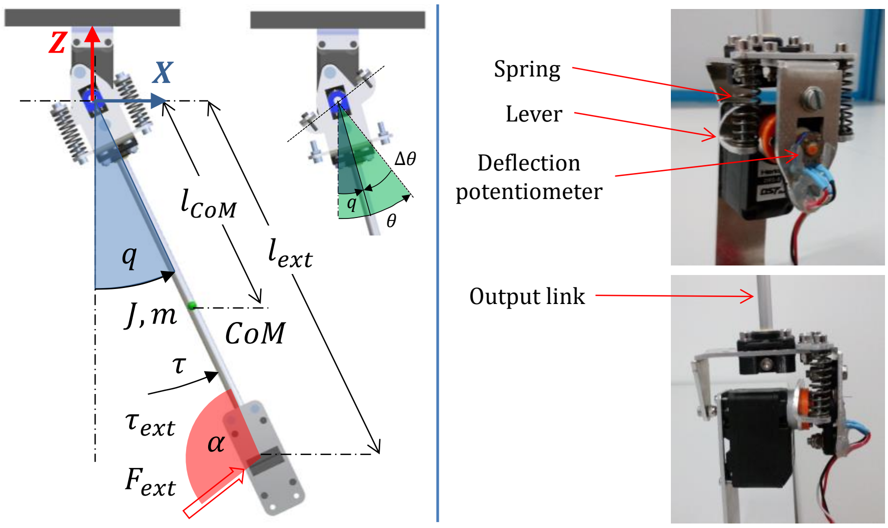

Figure 4.2. Model of the compliant actuator and mechanical construction.

The compliant transmission mechanism is represented by a spring-damper system characterized by its physical stiffness k_p and damping d_p. The torque transmitted by the spring-lever mechanism will depend on the deflection angle, defined as the difference between the servo shaft angular position and the output link angular position:

$$\tau = k_p(\theta - q) + d_p\left(\dot{\theta} - \dot{q}\right) = k_p\Delta\theta + d_p\Delta\dot{\theta} \tag{4.3}$$

The spring-lever mechanism can be assimilated to a linear torsional spring for small joint deflection angles, whose equivalent stiffness can be obtained from the stiffness of the compression spring and the lever length:

$$k_p = \frac{\Delta\tau}{\Delta\theta} \cong \frac{(K_s \cdot L_{lever} \cdot \Delta\theta) \cdot L_{lever}}{\Delta\theta} = K_s \cdot L_{lever}^2 \tag{4.4}$$

Here K_s is the stiffness of the compression spring, and L_{lever} is the length of the lever, that is, the distance from the rotation axis to the contact point of the spring. Next subsection describes in more detail the torque-deflection relationship, although the linear approximation is good enough for joint deflection angles below 30 degrees.

The torque delivered by the servo is dedicated to compensate its friction and inertia b, transmitting the torque τ to the output link:

$$\tau_m = b\ddot{\theta} + \tau_f + \tau \tag{4.5}$$

The torque transmitted by the spring-lever and the external torque accelerate the output link and compensate the gravity:

$$\tau + \tau_{ext} = J_p\ddot{q} + mgl_{COM}sin(q) \tag{4.6}$$

Here m and J_p are the mass and inertia of the output link, respectively, g is the gravity constant, and l_{COM} is the distance from the servo shaft to the center of mass. The parameters of the compliant joint under study (see **Figure 4.2**-right) are summarized in **Table 4.1**. The mass, inertia and distance to the CoM of the output link are obtained from the CAD model, whereas the servo time constants and d_p were determined experimentally from the Fast Fourier Transform of the deflection signal, exciting the servo with a sine chirp position reference. The matching between the measured deflection and the simulation model given by Equations **(4.2)** – **(4.6)** determines the value of this parameter.

Table 4.1. Parameters of the compliant joint actuator.

Servo Actuator		**Spring-Lever**		**Output Link**	
T_{servo}	$0.035\ s$	k_n	$1.2\ Nm/rad$	J	$0.0044\ kgm^2$
T_{delay}	$0.02\ s$	d_n	$0.02\ Nms$ $/rad$	m	$0.118\ kg$
$\tau_{m,stall}$	$1.17\ Nm$	$\Delta\theta_{ma}$	$30\ deg$	l_{CoM}	$0.132\quad m$

4.2.2. Torque-deflection relationships in a spring-lever mechanism

The torque estimation in a compliant joint actuator is based on the measurement of the deflection angle, defined as the difference between the servo shaft and the output link angular position:

$$\Delta\theta = \theta - q \tag{4.7}$$

This angle is directly measured by the deflection potentiometer or encoder integrated in the frame structure of the compliant joints (see **Section 2.2**), whereas the servo shaft position is given by the corresponding sensor embedded in the actuator. Consider now the diagram depicted in **Figure 4.3**, where the compliant joint is deflected clockwise so the spring is compressed with a force proportional to its elongation:

$$F_{spring} = K_S \cdot \Delta d = K_S \cdot [d(0) - d(\Delta\theta)] \tag{4.8}$$

Here K_S is the elastic constant of the compression springs, and $d(\Delta\theta) = \|\boldsymbol{P_1} - \boldsymbol{P_2}\|$ is the distance between the contact points of the compression spring:

$$\boldsymbol{P_1} = \begin{bmatrix} a \\ 0 \end{bmatrix} \quad \boldsymbol{P_2} = \begin{bmatrix} r \cdot sin(\Delta\theta + \varphi_0) \\ r \cdot cos(\Delta\theta + \varphi_0) \end{bmatrix} \tag{4.9}$$

The torque generated by the spring is then:

$$\tau_{spring} = F_{spring} \cdot r \cdot sin(\Delta\theta + \varphi_0) \tag{4.10}$$

where φ_0 is the separation angle of the spring, which depends on the lever length L_{lever} and on the spring length. The maximum deflection angle is determined by the minimum length of the spring when this is fully compressed.

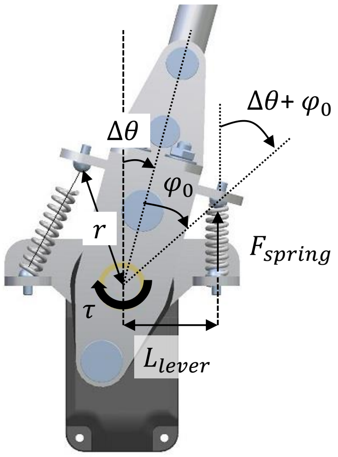

Figure 4.3. Geometric model considered in the derivation of the torque-deflection relationship.

4.2.3. Torque control

The spring-lever transmission mechanism introduced between the servo shaft and the output link allows, not only to estimate the torque in terms of deflection, but also to control it through the servo angular position. As stated in the introduction, one of the main benefits of considering series elastic actuators is that the force control problem is transformed into a position control problem, extending the control capabilities of most servo actuators that do not provide any torque control or estimation. The torque estimation provided by Equation **(4.3)** can be introduced in a feedback control scheme as the one depicted in **Figure 4.4**. The torque controller takes as input the torque error, defined as the difference between the torque reference and the torque transmitted to the output link by the compliant transmission mechanism:

$$\tau_e = \tau_{ref} - \tau = \tau_{ref} - \left(k_p \Delta\theta + d_p \Delta\dot{\theta}\right) \tag{4.11}$$

The torque controller gives as output an incremental control signal $\Delta\theta_c$ that represents the angular increment to be applied to the servo shaft so that the torque error tends to zero. That is, if at a certain time instant the torque error is greater than zero, the servo should increase the pushing force applied to the output link through the compression of the springs. The control signal is said to be incremental as the position reference of the servo is the sum of the correction term and its current position:

$$\theta_{ref} = \theta + \Delta\theta_c \tag{4.12}$$

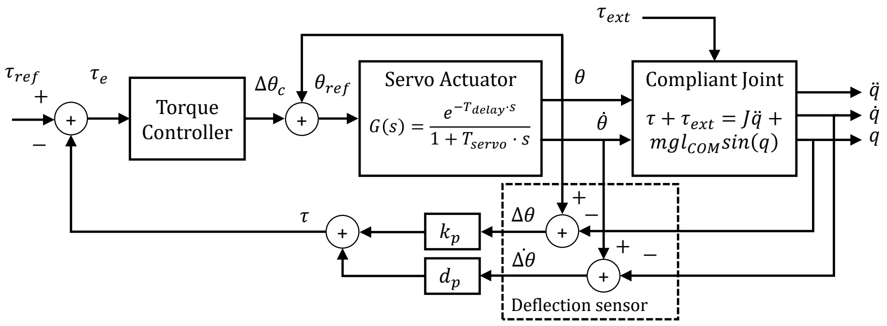
τ_{ref}
τ_e
Torque Controller
$\Delta\theta_c$
θ_{ref}
Servo Actuator
$G(s) = \frac{e^{-T_{delay} \cdot s}}{1 + T_{servo} \cdot s}$
θ
$\dot{\theta}$
τ_{ext}
Compliant Joint
$\tau + \tau_{ext} = J\ddot{q} + mgl_{COM}sin(q)$
$\ddot{q}$
$\dot{q}$
q
τ
k_p
d_p
$\Delta\theta$
$\Delta\dot{\theta}$
Deflection sensor

Figure 4.4. Torque control scheme in a compliant actuator with joint deflection feedback.

In order to achieve smooth operation of the servo, the position references should be sent to this at the midpoint of the trapezoidal velocity profile generated by the embedded controller, imposing that the playtime of the servo is two times the control period. The control rate should be around 50 Hz to prevent packet loss in the serial communications and duplicity in the measurements due to lack of time to update the internal registers of the actuator. Although the manufacturer of the Herkulex servos does not specify the internal control rate, the datasheet indicates that the period of the internal tick corresponds to 11.2 ms. Identification experiments performed over the DRS-0101 model reveal that the data packets returned by the servo contain repeated measurements when the read rate is around 70 – 100 Hz.

If the torque controller is implemented with a PID, the incremental servo position is given by:

$$\Delta\theta_c = K_p\tau_e + K_d\dot{\tau}_e + K_i\int_0^t \tau_e dx \tag{4.13}$$

where K_p, K_d, and K_i are the proportional, derivative and integral constants. An initial guess of the proportional constant can be obtained from the maximum deflection angle and the stall torque of the servo actuator:

$$K_p \sim \frac{\max\{\Delta\theta\}}{\tau_{stall}} \tag{4.14}$$

The value of the integral constant can be approximated in a similar way, imposing for example that the convergence time is around one second. The contribution of the derivative term depends on the noise associated to the deflection speed, obtained indirectly from the derivative in time of the deflection speed, or well directly from a gyroscope integrated in the compliant joint. However, the measurement of a gyroscope will be affected by the motion of other joints or by the rotation of the aerial platform.

The performance of the torque controller is limited by the delay and the first order dynamics of the servo, what can be experimentally evaluated applying a sine chirp signal as torque reference and comparing this with the torque estimation.

4.2.4. Virtual variable impedance control

According to the model detailed in **Section 4.2.1**, the compliant joint is characterized by its physical inertia J_p, damping d_p and stiffness k_p, in such a way that their particular values are associated to the corresponding "physical" realization of the joint. These parameters may have a significant influence in the behaviour of the aerial manipulator when impact and contact forces arise during its operations on flight. Then, it would result convenient to vary the apparent stiffness, dampening or inertia of the joints depending on the particular task, but without increasing the weight of the actuator (the variable stiffness actuators introduce a second motor to adjust the stiffness). Then, this work proposes the implementation of a virtual variable impedance behaviour at control level based on the feedback and control of the joint deflection. Let us define first the desired virtual stiffness to external load in the following way:

$$\tau_{ext} = J_v\ddot{q} + d_v\dot{q} + k_v(q - q_0) \tag{4.15}$$

Here J_v, d_v and k_v are the desired virtual inertia, dampening and stiffness, whereas q_0 is the virtual zero deflection angle. The torque τ_{ext} is associated to the external forces acting over the joint. Now, the torque that the physical compliant joint should transmit to the output link for providing the desired impedance to the external load is obtained combining Equations **(4.6)** and **(4.15)**:

$$\tau_{ref} = (J_p - J_v)\ddot{q} - d_v\dot{q} + mgl_{CoM}sin(q) - k_v(q - q_0) \tag{4.16}$$

The torque error defined in Equation **(4.11)** is controlled through the joint deflection, which can be indirectly controlled through the servo position, as described in Equation **(4.12)** and **(4.13)**. **Figure 4.5** represents the desired behaviour to external load, and the implementation with the compliant joint.

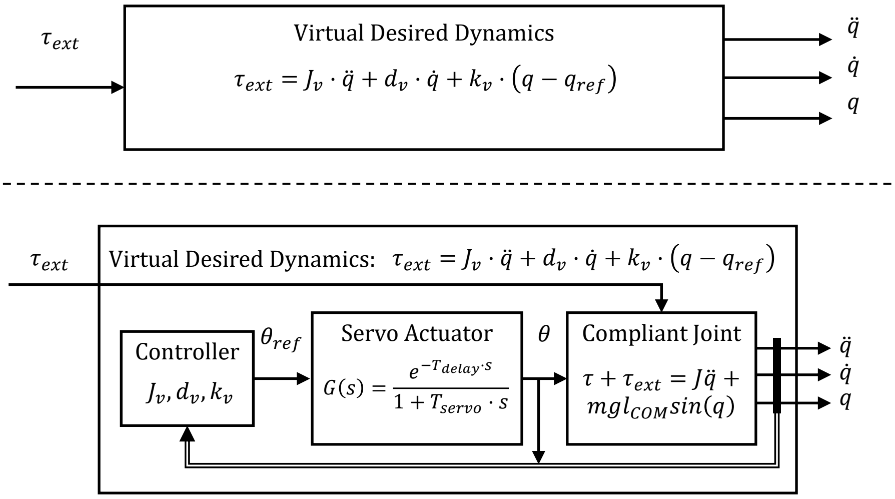
τ_{ext}
Virtual Desired Dynamics
$\tau_{ext} = J_v \cdot \ddot{q} + d_v \cdot \dot{q} + k_v \cdot (q - q_{ref})$
$\ddot{q}$
$\dot{q}$
q
τ_{ext}
Virtual Desired Dynamics: $\tau_{ext} = J_v \cdot \ddot{q} + d_v \cdot \dot{q} + k_v \cdot (q - q_{ref})$
Controller
J_v, d_v, k_v
θ_{ref}
Servo Actuator
$G(s) = \frac{e^{-T_{delay} \cdot s}}{1 + T_{servo} \cdot s}$
θ
Compliant Joint
$\tau + \tau_{ext} = J\ddot{q} + mgl_{CoM}sin(q)$
$\ddot{q}$
$\dot{q}$
q

Figure 4.5. Virtual variable impedance actuator. Response to external load (up) and implementation (down).

The performance of this virtual variable impedance control scheme is strongly affected by the noise in the discrete-time derivatives involved in Equation **(4.16)**. Although the deflection $\Delta\theta$ is measured with a potentiometer, the angular speed of the output link, $\dot{q}$, should be measured with a gyroscope, whereas the servo provides the angular position and differential position (speed estimation), θ and $\dot{\theta}$. The estimation of the output link angular acceleration $\ddot{q}$ can be avoided imposing that $J_v = J_p$, that is, if the desired virtual inertia is equal to the physical inertia.

4.3. Force/position control in 3-DOF compliant arm

4.3.1. Arm kinematics

Let us consider the 3-DOF robotic arm depicted in **Figure 4.6**, whose kinematic configuration is similar to the one employed in the industrial manipulators, where the shoulder yaw joint (base) is stiff, whereas the shoulder pitch and the elbow pitch joints are compliant. The angular position of the joints is denoted as q_1, q_2 and q_3. The upper arm link length (from shoulder to elbow) and the forearm link length (from elbow to wrist point) are L_1 and L_2, respectively. The position of the wrist point with respect to the reference frame attached to the base of the arm is obtained from the forward kinematic model that can be easily derived:

$$\begin{bmatrix} x \\ y \\ z \end{bmatrix} = \begin{bmatrix} r(q_2, q_3) \cdot cos(q_1) \\ r(q_2, q_3) \cdot sin(q_1) \\ L_1 \cdot cos(q_2) + L_2 \cdot cos(q_2 + q_3) \end{bmatrix} \tag{4.17}$$

where $r(q_2, q_3)$ is defined in the following way:

$$r(q_2, q_3) = L_1 \cdot sin(q_2) + L_2 \cdot sin(q_2 + q_3) \tag{4.18}$$

The proposed configuration has analytical solution for the inverse kinematics, so the joint variables can be obtained from the desired Cartesian position of the end effector as follows:

$$\begin{bmatrix} q_1 \\ q_2 \\ q_3 \end{bmatrix} = \begin{bmatrix} atan2(y, x) \\ \cos^{-1}\left(\dfrac{x^2 + y^2 + z^2 + L_1^2 - L_2^2}{2L_1\sqrt{x^2 + y^2}}\right) \\ \cos^{-1}\left(\dfrac{x^2 + y^2 + z^2 - L_1^2 - L_2^2}{2L_1 L_2}\right) \end{bmatrix} \tag{4.19}$$

The volume of operation of the arm is a hollow semi-sphere generated by the revolution of the upper arm/forearm links around the shoulder yaw joint, and whose outer and inner radius correspond to the fully stretched and fully retracted configurations.

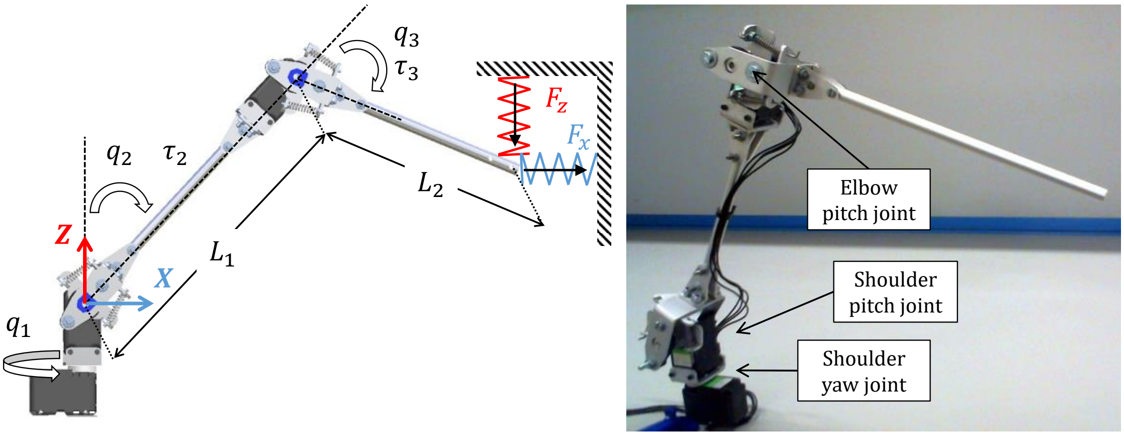

Figure 4.6. Geometric model considered in the kinematic model and in the derivation of the force-torque relationships (left). Developed prototype (right) with two compliant joints in elbow and shoulder.

4.3.2. Force-Torque relationships in 2D space

As the compliant arm is expected to operate in contact with the environment, it is necessary to relate the contact forces at the end effector or at the wrist point with torque estimated from the joint deflection. Taking into account that only the shoulder pitch and the elbow pitch joints are compliant, then the problem is reduced to a 2-DOF manipulator (**Figure 4.6**-left). The torque in these two joints is related with the XZ components of the force at the wrist point in the following way:

$$\begin{bmatrix} \tau_2 \\ \tau_3 \end{bmatrix} = \begin{bmatrix} a & b \\ c & d \end{bmatrix} \cdot \begin{bmatrix} F_x \\ F_y \end{bmatrix} \quad ; \quad \begin{bmatrix} F_x \\ F_z \end{bmatrix} = \frac{1}{\Delta} \begin{bmatrix} d & -b \\ -c & a \end{bmatrix} \cdot \begin{bmatrix} \tau_2 \\ \tau_3 \end{bmatrix} \tag{4.20}$$

where the variables a, b, c, d and Δ are defined as follows:

$$\begin{gathered} a = -L_1 \cdot cos(q_2) - L_2 \cdot cos(q_2 + q_3) \\ b = L_1 \cdot sin(q_2) + L_2 \cdot sin(q_2 + q_3) \\ c = -L_2 \cdot cos(q_2 + q_3) \\ d = L_2 \cdot sin(q_2 + q_3) \\ \Delta = -L_1 \cdot L_2 \cdot \sin(q_3) \end{gathered} \tag{4.21}$$

These relationships can be easily derived expressing the cross product between the position vector and the force vector in a matrix form, obtaining the torque, and inverting it for obtaining the force.

4.3.3. Dynamic model of compliant joint arm

The equations of the dynamic model for a robotic arm with compliant joints can be derived from the Lagrangian and the generalized equation of the forces and torques given by Equation **(4.1)**. The model is decomposed in two parts. One the one hand, the output link dynamics can be expressed in the usual matrix form:

$$\boldsymbol{M(q)\ddot{q} + C(q, \dot{q})\dot{q} + G(q) = \tau + \tau_{ext}} \tag{4.22}$$

$$\boldsymbol{\tau = \ K(\theta - q) + D(\dot{\theta} - \dot{q}) = K\,\Delta\theta + D\,\Delta\dot{\theta}} \tag{4.23}$$

where $\boldsymbol{M}$, $\boldsymbol{C}$ and $\boldsymbol{G}$ represent the link inertia, centrifugal and Coriolis term, and the gravity component, respectively, $\boldsymbol{\tau}$ is the torque introduced by the compliant joint with $\boldsymbol{K} = diag(k_i)$ and $\boldsymbol{D} = diag(d_i)$ being the elastic and friction constants for each joint, while $\boldsymbol{\tau_{ext}}$ is a torque generated from the action of external forces. This model assumes that the compliant joint behaves as a spring-damper system. On the other hand, the dynamics for the servos are described by:

$$\boldsymbol{B(\theta)\ddot{\theta} + \tau = \tau_m - \tau_f} \tag{4.24}$$

Here $\boldsymbol{B}$ is the inertia of servos' shaft, $\boldsymbol{\tau_m}$ is the torque generated by the motor and $\boldsymbol{\tau_f}$ is a friction term. As it can be seen, the common term in **(4.22)** and **(4.24)** is the torque supported by the compliant element, which transmit the torque generated by the motor to the output link. As this work is focused in the estimation and control of the contact force in static conditions, the inertial, Coriolis and centrifugal terms in this model have not been considered. However, it is necessary to remark that the position control of the arm may become unstable if joint deflection is introduced in the control loop without considering theses terms. What is more, it would be necessary to model the perturbation that the motion of the UAV introduces over the compliant joint. This will be done in **Section 4.6.3**.

4.3.4. Force-Position control in compliant arm

Section 4.2.3 presented a method to control the torque in a compliant joint in terms of deflection. This idea can be extended to control the contact force in a compliant joint manipulator, taking into account the force-torque relationships described above. In the realization of an aerial manipulation task involving contact forces, it is necessary to position the end effector close to the contact point, and then apply the force. This involves switching between two control modes: position (approaching), and force (interaction).

The proposed control scheme, illustrated in **Figure 4.7**, exploits the position controller embedded in all the Herkulex servos for the generation of joint trajectories with smooth variation of the velocity profiles. The controller of the servos takes as input the desired goal position θ_{ref} along with the play time, that is, the time desired to reach the reference position. According to the manual of these servos, the embedded controller generates a trapezoidal velocity profile divided into three zones: constant acceleration (25% play time), constant velocity (50% play time) and constant deceleration (25% play time). One of the most interesting features of these servos is the Velocity Over-Ride (VOR) operation mode. Consider that the servo is at the midpoint of the velocity profile, that is, at half the play time, and a new position reference is sent. With the VOR mode, the controller re-computes the velocity profile from the value in the time instant the new reference is received. The idea now is to send the sequence of joint position references at the midpoint of the play time, so the servos generate a trajectory with smooth variation of the velocity profile, which reduces the influence of the inertia term.

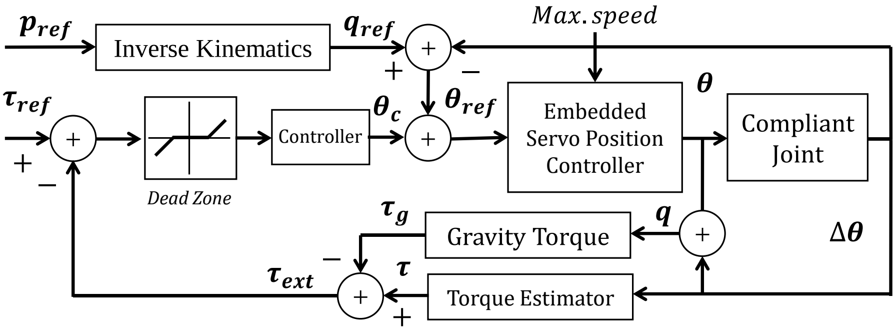

Figure 4.7. Position-torque control scheme in static (contact) conditions. The input references are the end effector position reference, the torque reference, and the maximum speed of the servos.

The proposed control scheme takes as input the desired Cartesian position of the end effector $\boldsymbol{p}_{ref}$, transformed into the joint position vector $\boldsymbol{q}_{ref}$ applying Equation **(4.19)**, and the force reference in the contact phase, transformed into the torque $\boldsymbol{\tau}_{ref}$ applying Equation **(4.20)**. The position reference sent to the servos, $\boldsymbol{\theta}_{ref}$, is the sum of two terms. The first one is obtained from $\boldsymbol{q}_{ref}$ and the deflection feedback, and determines the pose of the arm during the execution of the contact force control task. The second one is the correction term $\boldsymbol{\theta}_c$ that compensates deviations in the estimated torque due to the application of the contact force. A PI controller takes as input the difference between the torque reference $\boldsymbol{\tau}_{ref}$ and the external torque $\boldsymbol{\tau}_{ext}$ estimated from Equation **(4.22)**. The adjustable threshold Dead Zone block acts as rejection filter, preventing that small deviations in the compliant joint affects the position controller. In the extreme case, it can be used as a switch for enabling or disabling the force/torque control mode. The inertial and centrifugal term in Equation **(4.22)** can be neglected if the speed of the servo is slow enough so joint deflection is small. **Section 4.6.5.3** proposes another method to estimate and control the contact force based on the idea of Cartesian deflection, defined as the deviation in the position of the end effector with respect to an equivalent stiff joint arm.

4.4. Position-Force control in compliant finger module

This section presents a method to control the metacarpo-phalangeal (MCP) joint position, velocity and torque from the PWM signal that is taken as input by the H-bridge in the finger module described in **Section 2.4**, depicted in **Figure 4.8**. Two case studies should be distinguished: object grasping with motor stalled (force-torque control), and motor in free running mode (position-velocity control). In the following, θ_{MCP}, $\dot{\theta}_{MPC}$ and τ_{MCP} will represent joint position, speed and torque of the MCP joint, respectively, F_{tendon} and l_{tendon} will denote the tendon force and length, whereas r_{reel} is the radius of the reel that drives the tendon. The motor torque, speed and current will be denoted by T_m, ω_m and i_m, respectively. The proximal inter-phalange (PIP) and distal inter-phalange (DIP) joints are under-actuated and their positions are not measured, so they are not considered in the model. Inertia and friction terms will not be taken into account for simplicity and because they have not a significant influence in joint position controller. The analysis presented here only affects to the flexion motion. Finger extension is achieved with the elastic elements disposed at finger joints, providing a faster response than the tendon drive mechanism.

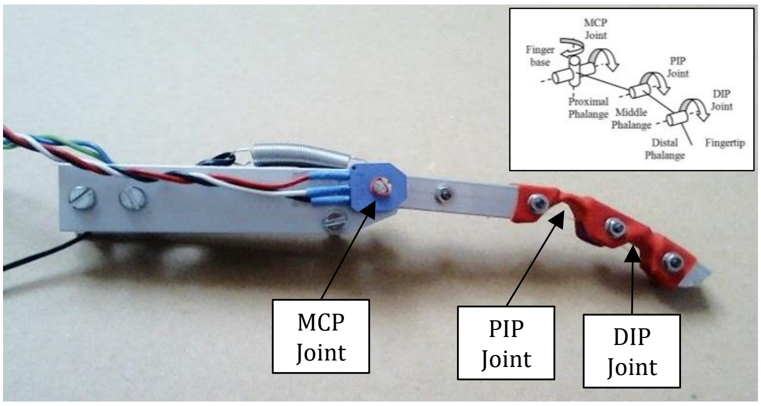

Figure 4.8. Anthropomorphic, compliant and lightweight finger module.

4.4.1. Force-torque relationships for object grasping

When the finger is grasping an object or it is completely flexed, the motor is stalled and the nylon tendon tensed. The torque generated by a brushed DC motor is proportional to the supplied current. However, the manufacturer usually provides the stall torque and current parameters, which correspond to a situation in which motor shaft is blocked and the current consumption is maximum. The H-bridge circuit controls the mean current injected to motor coil in terms of current pulses of variable duty cycle. If the PWM (Pulse Width Modulation) signal is in the range [0, 1], from no current to stall, then the motor torque can be controlled in the following way:

$$0 \leq T_m = k_t \cdot i_{stall} \cdot pwm \leq T_{stall} \tag{4.25}$$

where $k_t = T_{stall}/i_{stall}$ is torque constant. The tensile force of the tendon is obtained dividing the motor torque between radius of the reel:

$$F_{tendon} = \frac{T_m}{r_{reel}} = \frac{k_t \cdot i_{stall} \cdot pwm}{r_{reel}} \tag{4.26}$$

This expression shows that tendon tension can be directly controlled with the PWM signal in open loop. It is useful in the experimental identification of the torque constant, since it is relatively easy to measure the tensile force with extension springs. The computation of the torque at the MCP joint depends on the tendon pass points, P_1 and P_2 points in **Figure 4.9**, whose position relative to the XZ frame depends on three parameters, b, c and d. Note that P_1 will be a function of the MCP joint angle θ_{MCP}, whereas P_2 is fixed:

$$\boldsymbol{P_1} = \begin{bmatrix} d \cdot cos(\theta_{MCP}) \\ -d \cdot sin(\theta_{MCP}) \end{bmatrix} \quad ; \quad \boldsymbol{P_2} = \begin{bmatrix} -b \\ -c \end{bmatrix} \tag{4.27}$$

The joint torque is then:

$$T_{MCP} = F_{tendon} \cdot d \cdot sin(\alpha) \quad , \quad \alpha = \cos^{-1}\left(\frac{\boldsymbol{P_1} \cdot \boldsymbol{P_2^T}}{||\boldsymbol{P_1}|| \cdot ||\boldsymbol{P_2}||}\right) \tag{4.28}$$

where α is the separation angle between the tendon-pass points. The numerical values of these constants in the implemented mechanism are the following: $b = 9\ [mm]$, $c = 11\ [mm]$, $d = 14\ [mm]$, $T_{stall} = 0.49\ [Nm]$ and $i_{stall} = 1.6\ [A]$.

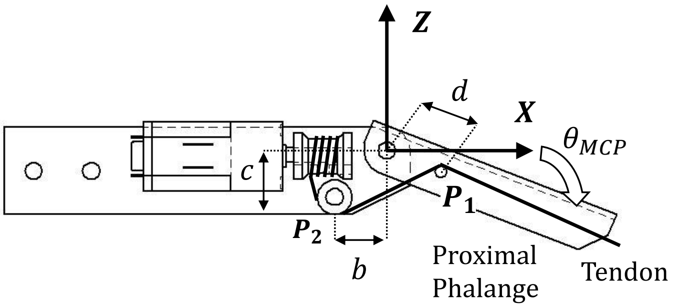

Figure 4.9. Model used in the computation of the MCP joint torque. The nylon tendon passes through P_1 and P_2 before it is rolled up on the reel.

4.4.2. Position-speed relationships for finger positioning

The developed finger module integrates a potentiometer to measure the MCP joint rotation, as it can be seen in **Figure 4.8**. The other alternative would consists of measuring the rotation of the motor shaft to obtain the displacement of the tendon, although this has two main drawbacks if more than one turn of the reel is needed to achieve finger flexion: the lack of an absolute position reference, and the necessity of counting turns. Since the position of the MCP joint is controlled trough the rotation of the reel attached to the motor, it is necessary to relate the position of the tendon, l, with the MCP joint angle. This can be done taking into account that l is the distance between the tendon pass points, obtained from Equation **(4.27)**:

$$l(\theta_{MCP}) = ||\boldsymbol{P_1} - \boldsymbol{P_2}|| = \sqrt{b^2 + c^2 + d^2 + 2 \cdot d \cdot [b \cdot cos(\theta_{MCP}) - c \cdot \sin(\theta_{MCP})]} \tag{4.29}$$

As it can be seen, it is not possible to express analytically joint angle θ_{MCP} as a function of tendon position, l, although a linear approximation could be obtained taking into account the particular values of the parameters and the rotation range of the joint ($\theta_{MCP} \in [0, 90]\ deg$). The same occurs with the joint speed, which is proportional with motor speed but depends on joint angle:

$$\dot{\theta}_{\mathrm{MCP}} = -\frac{l(\theta_{MCP}) \cdot r_{reel} \cdot \omega_m}{d \cdot [b \cdot sin(\theta_{MCP}) + c \cdot cos(\theta_{MCP})]} \tag{4.30}$$

The motor speed ω_m can be controlled in open loop with the PWM signal, and thus the angular speed of the MCP joint, $\dot{\theta}_{MCP}$.

4.4.3. Control scheme

The force-position control scheme implemented in the finger module is illustrated in **Figure 4.10**. The controller takes as input the joint reference θ_{MCP}^{ref} which is scaled to obtain the equivalent voltage at the potentiometer. The measurement provided by this sensor is subtracted for computing MCP joint error, whose sign determines the direction of motion and its amplitude the duty cycle of the PWM signal applied to the H-bridge. A simple proportional controller with constant K_p generates the required duty cycle signal from the absolute value of the joint error. Maximum tendon force and motor speed are regulated saturating the PWM signal in the range [0, 1], that is, from no current to the stall current. Finally, a dead zone is considered for preventing unnecessary changes in motor direction when joint error is low, which significantly reduces current consumption.

Note that the range of motion of the MCP joint is between zero and 90 degrees approximately. In the case θ_{MCP}^{ref} is above this value, the motor will continue exerting a force on the tendon, so the PIP and DIP joints will be flexed.

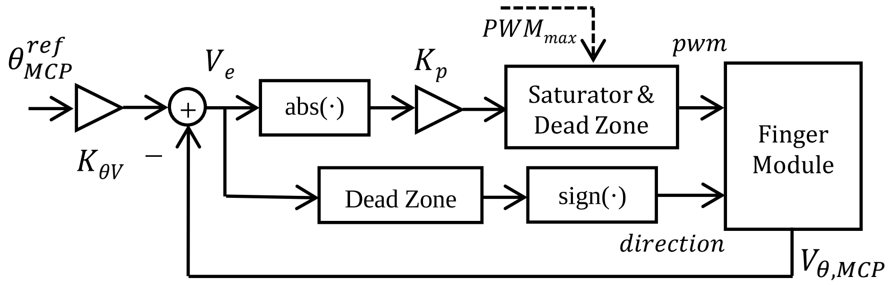

Figure 4.10. MCP joint position control.

4.5. Lightweight and human-size dual arm aerial manipulator

4.5.1. Dual arm kinematics

The lightweight and human-size dual arm manipulator described in **Section 2.5** provides 10-DOF in a kinematic configuration similar to the industrial manipulators, as it can be seen in **Figure 4.11**. Each arm includes three joints for end effector positioning (shoulder yaw at the base, shoulder pitch, and elbow pitch), and two additional joints for wrist orientation (roll and pitch joints). The wrist yaw actuator is not implemented in this prototype due to the necessity to reduce as much as possible the mass and inertia of the arm, especially when the actuator is close to the end effector, and because its range of rotation is quite limited in most bimanual operations. The angular position of the j-th joint of the i-th arm is denoted by q_j^i, where superscript $i = \{1, 2\}$ indicates the left/right arm, and subscript $j = \{1,2,3,4,5\}$ indicates the particular joint following the same order and sign criteria (right hand criteria) defined in **Figure 4.11**. Note that all the joints in this manipulator are stiff, and so $q_j^i = \theta_j^i$ and $\Delta\theta_j^i = 0 \; \forall i, j$.

Since the arms were designed following a bioinspired approach, it is possible to identify the three representative lengths corresponding to the upper arm and forearm links, L_1 and L_2, respectively, and the separation distance between both arms, denoted as D. The upper arm link length is defined as the distance between the shoulder pitch and the elbow pitch joint axes, whereas the forearm link length is the distance between the elbow pitch and the wrist pitch axes. The rotation axes of the two shoulder joints and the elbow joint intersect in a common point, which simplifies the resolution of the inverse kinematics. A representative diagram of the kinematic model of the dual arm is depicted in **Figure 4.12**. Three reference frames are defined: the manipulator base frame $\{\boldsymbol{X_0 Y_0 Z_0}\}$, and the left and right arm frames $\{\boldsymbol{X_0^1 Y_0^1 Z_0^1}\}$ and $\{\boldsymbol{X_0^2 Y_0^2 Z_0^2}\}$, whose origin is in the intersection point in the shoulder joint of the respective arm. These are parallel to the base frame, translated $\pm D/2$ along the $\boldsymbol{Y_0}$-axis.

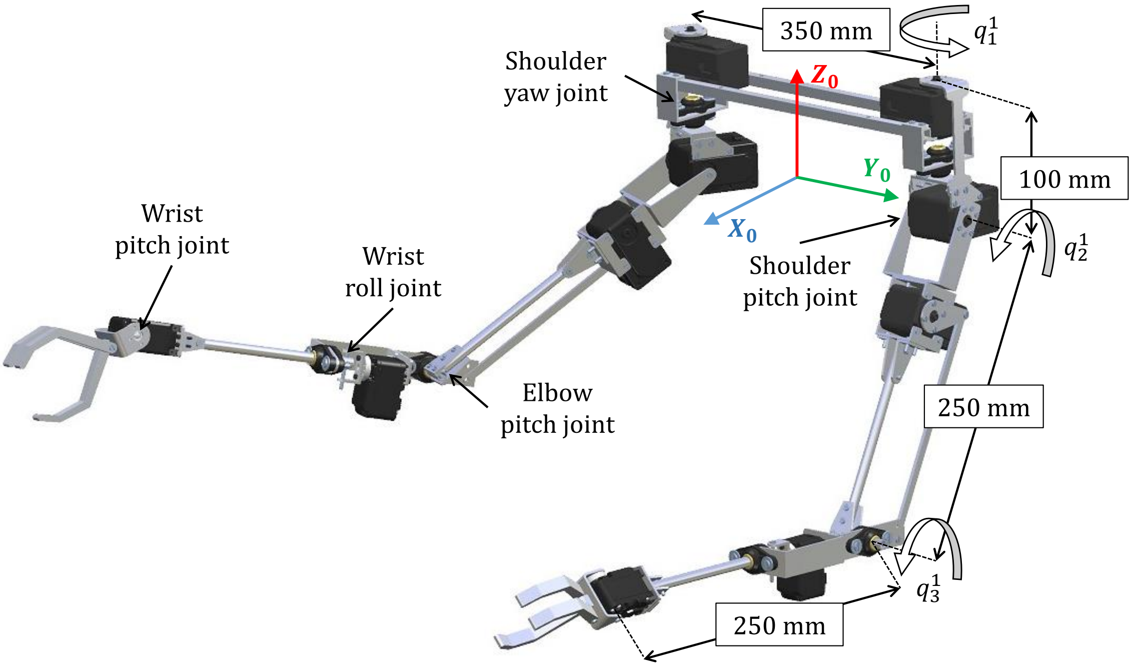

Figure 4.11. Reference frame, joint variables, sign criteria and link lengths in the human-size dual arm.

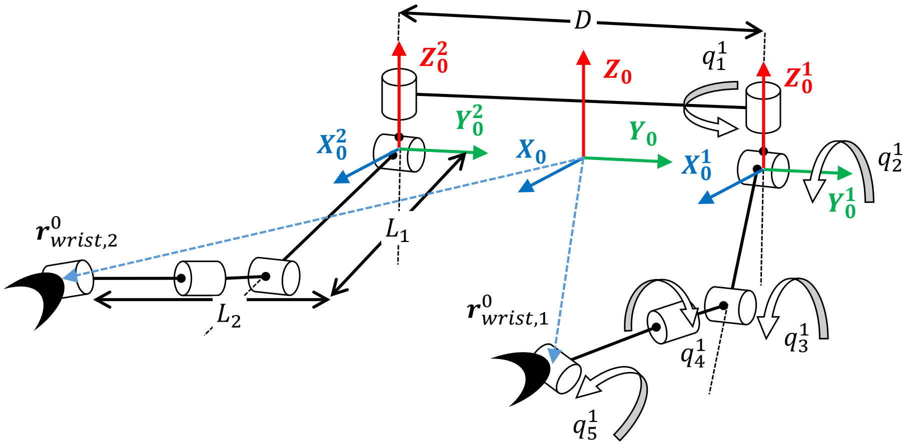

Figure 4.12. Kinematic model of the lightweight dual arm.

In order to simplify the resolution of the forward and inverse kinematics, this work considers the positioning of the wrist point, since the tool center point (TCP) position may vary with the rotation of the wrist pitch joint. On the one hand, the forward kinematic model of the i-th arm, $\boldsymbol{FK_i}: \boldsymbol{\Re^3} \rightarrow \boldsymbol{\Re^3}$, provides the Cartesian position of the wrist point of the arm with respect to the reference frame $\{\boldsymbol{X_0^i Y_0^i Z_0^i}\}$ for a particular value of the joint variables:

$$\boldsymbol{r_{wrist}^i} = \boldsymbol{FK_i}(\boldsymbol{q^i}) = \begin{bmatrix} x^i \\ y^i \\ z^i \end{bmatrix} = \begin{bmatrix} r(q_2^i, q_3) \cdot cos(q_1^i) \\ r(q_2^i, q_3^i) \cdot sin(q_1^i) \\ L_1 \cdot cos(q_2^i) + L_2 \cdot cos(q_2^i + q_3^i) \end{bmatrix} \tag{4.31}$$

where $r(q_2^i, q_3^i)$ is defined in the following way:

$$r(q_2^i, q_3^i) = L_1 \cdot sin(q_2^i) + L_2 \cdot sin(q_2^i + q_3^i) \tag{4.32}$$

The kinematics of the dual arm manipulator is the same as in the arm described in **Section 4.3.1**, and thus its analytical resolution. Note also that a certain point in the Cartesian space can be reached in two different ways, corresponding to the elbow-up and elbow-down configurations. However, the rigid bar transmission employed in the elbow joint imposes that only the elbow down configuration can be adopted.

The inverse kinematic model, $\boldsymbol{FK_i}: \boldsymbol{\Re^3} \rightarrow \boldsymbol{\Re^3}$, returns the joint variables of the shoulder and elbow joints for a given Cartesian position of the wrist point, that is:

$$\boldsymbol{q^i} = \boldsymbol{IK^i}(\boldsymbol{r_{wrist}^i}) = \begin{bmatrix} q_1^i \\ q_2^i \\ q_3^i \end{bmatrix} = \begin{bmatrix} atan2(y^i, x^i) \\ \cos^{-1}\left(\dfrac{(x^i)^2 + (y^i)^2 + (z^i)^2 + L_1^2 - L_2^2}{2L_1\sqrt{(x^i)^2 + (y^i)^2}}\right) \\ \cos^{-1}\left(\dfrac{(x^i)^2 + (x^i)^2 + (x^i)^2 - L_1^2 - L_2^2}{2L_1 L_2}\right) \end{bmatrix} \tag{4.33}$$

The inverse kinematic model is the base of the position/trajectory controller described below, as the servo actuators typically employed in aerial manipulation do not provide direct velocity control, which constraints the implementation of Jacobian-based controllers.

4.5.2. Dual arm aerial manipulator dynamics

The dynamic model of a dual arm aerial manipulator can be derived from the Lagrangian and the generalized equations of the forces given by Equation **(4.1)**. The reference frames and representative parameters of the dual arm aerial manipulator are represented in **Figure 4.13**. Here m_j^i and $\boldsymbol{I}_j^i$ are the mass and inertia of the j-th link of the i-th arm, whose center of mass relative to the Earth fixed frame $\{\boldsymbol{X_E Y_E Z_E}\}$ is denoted by $\boldsymbol{r}_j^i$. The mass, inertia, and the position vector of the center of mass of aerial platform are denoted by m_{UAV}, $\boldsymbol{I}_{UAV}$ and $\boldsymbol{r}_{UAV}$, respectively.

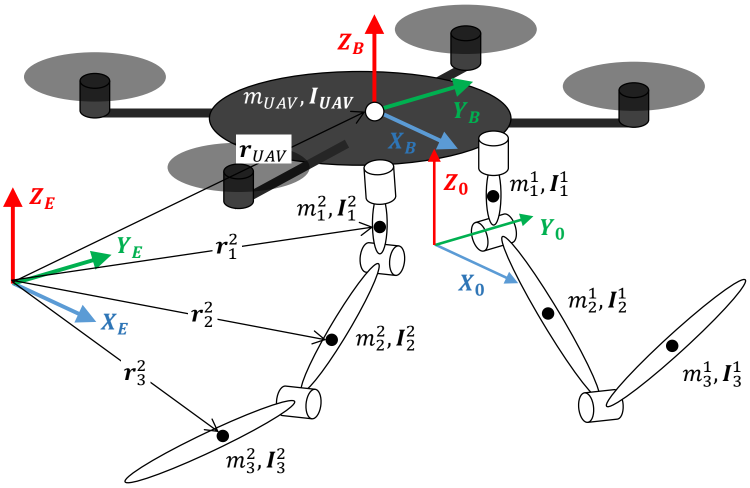
$\boldsymbol{Z_B}$
$m_{UAV}, \boldsymbol{I_{UAV}}$
$\boldsymbol{Y_B}$
$\boldsymbol{X_B}$
$\boldsymbol{r_{UAV}}$
$\boldsymbol{Z_0}$
$m_1^1, \boldsymbol{I}_1^1$
$\boldsymbol{Z_E}$
$m_1^2, \boldsymbol{I}_1^2$
$\boldsymbol{Y_E}$
$\boldsymbol{r}_1^2$
$\boldsymbol{Y_0}$
$\boldsymbol{X_0}$
$m_2^1, \boldsymbol{I}_2^1$
$\boldsymbol{X_E}$
$\boldsymbol{r}_2^2$
$m_2^2, \boldsymbol{I}_2^2$
$\boldsymbol{r}_3^2$
$m_3^1, \boldsymbol{I}_3^1$
$m_3^2, \boldsymbol{I}_3^2$

Figure 4.13. Reference frames, position vectors, mass and inertia parameters involved in the dynamic model of the dual arm aerial manipulator.

The vector of generalized coordinates will contain the position and orientation of the multirotor, $\boldsymbol{r}_{UAV} = [x, y, z]^T \in \Re^3$ and $\boldsymbol{\eta}_{UAV} = [\phi, \theta, \psi]^T \in \Re^3$, and the angular position vectors of both arms, $\boldsymbol{q^1} = [q_1^1, q_2^1, q_3^1]^T$ and $\boldsymbol{q^2} = [q_1^2, q_2^2, q_3^2]^T$. It is necessary to remark that the dynamic model considers only the shoulder and elbow joint variables since the dynamic terms associated to the wrist joints is very small compared to the positioning joints. Note also that the joints of the dual arm manipulator shown in **Figure 4.11** are stiff, so the vector of generalized coordinates only consider the output link angular positions. The vector is then defined as follows:

$$\boldsymbol{\xi} = [x \quad y \quad z \quad \phi \quad \theta \quad \psi \quad q_1^1 \quad q_2^1 \quad q_3^1 \quad q_1^2 \quad q_2^2 \quad q_3^2]^T \in \Re^{12} \tag{4.34}$$

The vector of generalized forces contains the forces and moments acting over the aerial platform, $\boldsymbol{F_{UAV}} = \left[F_x, F_y, F_z\right]^T$ and $\boldsymbol{\tau_{UAV}} = \left[\tau_x, \tau_y, \tau_z\right]^T$, and the torques associated to the joints, τ_j^i:

$$\boldsymbol{\Gamma} = \left[F_x \quad F_y \quad F_z \quad \tau_x \quad \tau_y \quad \tau_z \quad \tau_1^1 \quad \tau_2^1 \quad \tau_3^1 \quad \tau_1^2 \quad \tau_2^2 \quad \tau_3^2\right]^T \in \Re^{12} \tag{4.35}$$

The kinetic energy of the dual arm aerial manipulator is the sum of the kinetic energy of the aerial platform (UAV) and the kinetic energy of each link of the manipulator, considering the translational and rotational components:

$$K = \frac{1}{2}\begin{pmatrix}\dot{\boldsymbol{r}}_{UAV}\\ \dot{\boldsymbol{\eta}}_{UAV}\end{pmatrix}^T \begin{bmatrix} m_{UAV}\cdot \boldsymbol{I}_{3\times 3} & \boldsymbol{0}\\ \boldsymbol{0} & \boldsymbol{J}_{UAV}^T\end{bmatrix}\begin{pmatrix}\dot{\boldsymbol{r}}_{UAV}\\ \dot{\boldsymbol{\eta}}_{UAV}\end{pmatrix} + \frac{1}{2}\sum_{i=1}^{2}\sum_{j=1}^{3}\begin{pmatrix}\dot{\boldsymbol{r}}_j^i\\ \boldsymbol{\omega}_j^i\end{pmatrix}^T \begin{bmatrix} m_j^i\cdot \boldsymbol{I}_{3\times 3} & \boldsymbol{0}\\ \boldsymbol{0} & \boldsymbol{J}_j^{i,T}\end{bmatrix}\begin{pmatrix}\dot{\boldsymbol{r}}_j^i\\ \boldsymbol{\omega}_j^i\end{pmatrix} \tag{4.36}$$

Here $\boldsymbol{\omega}_j^i$ is the angular velocity of the j-th link of the i-th arm. The dynamic coupling between the aerial platform and the links of the arms is foreseen taking into account that the position of the center of mass of each link w.r.t. the inertial frame depends, not only on its corresponding joint angle, but also on the UAV position and orientation.

The potential energy of the aerial robot is due to gravity, and is given by:

$$V = g\cdot\left(m_{UAV}\cdot \boldsymbol{e}_z^T\cdot \boldsymbol{r}_{UAV} + \sum_{i=1}^{2}\sum_{j=1}^{3} m_j^i\cdot \boldsymbol{e}_z^T\cdot \boldsymbol{r}_j^i\right) \tag{4.37}$$

where g is the gravity constant and $\boldsymbol{e}_z^T = [0 \quad 0 \quad 1]$.

After the application of the Euler-Lagrange method, it is possible to represent the dynamics of the system in the usual matrix form:

$$\boldsymbol{M}(\boldsymbol{\xi})\ddot{\boldsymbol{\xi}} + \boldsymbol{C}(\boldsymbol{\xi},\dot{\boldsymbol{\xi}}) + \boldsymbol{G}(\boldsymbol{\xi}) = \boldsymbol{\Gamma} \tag{4.38}$$

where $\boldsymbol{M} \in \Re^{12\times 12}$ is the generalized mass matrix, $\boldsymbol{C} \in \Re^{12}$ represents the centrifugal and Coriolis terms, and $\boldsymbol{G} \in \Re^{12}$ is the gravity component.

4.5.3. Estimation and control

Most model-based controllers assume that joint torque control or feedback is possible. However, the servo actuators employed for building low weight robotic arms intended to aerial manipulation only provide position measurements at low rates (<100 Hz). What is more, the controller embedded in these devices only accepts motion commands specifying the desired goal position and playtime. These technological limitations have motivated the design of the control scheme described in this section.

4.5.3.1. Structure of the controller

Let us consider an aerial manipulation task in which the arms should execute a certain operation on flight while the aerial platform remains stable in hover. It is assumed that arms can move independently while the aerial platform remains in hover. In order to compensate positioning and orientation disturbances due to dynamic coupling, the controller will compensate the reaction torques that the arms exert over base of the UAV. This scheme is represented in **Figure 4.14**. The dual arm aerial manipulator consists of the aerial platform with the left and right arms. The task manager module generates the desired UAV and arms trajectories for accomplishing the specific task, keeping updated the current state of the robot. A torque estimator is developed, taking as input the joints position and speed of the arms, giving as output the estimated reaction torque of the arms computed from the dynamic model presented in **Section 4.5.2**. A Phase Lock Loop (PLL) provides smooth estimations of joint acceleration from the speed of each servo, avoiding errors associated to the differentiation of the speed signal. The UAV controller takes as input the data provided by the Inertial Measurement Unit (IMU) along with the arms torque estimation for the compensation (**see Section**

4.5.3.3), and the reference trajectory generated by the task manager, giving at its output the control signal $\boldsymbol{U} = \left[u_z, u_\phi, u_\theta, u_\psi\right]^T$ for the total thrust and the roll, pitch and yaw torque inputs of the UAV. The controller of the arms, detailed in **Section 4.5.3.2**, takes as input the desired Cartesian trajectory of the Tool Center Point (TCP) and the state of the servos, providing the references for each servo in the arms.

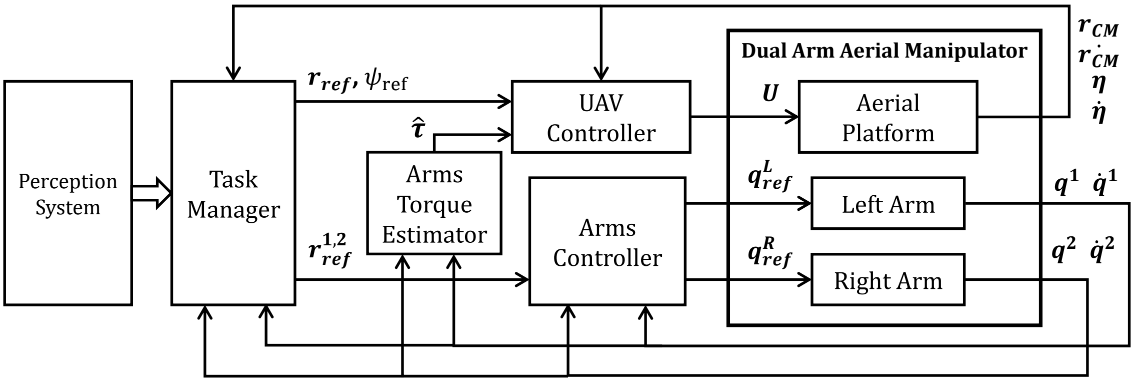

Figure 4.14. Control structure of the dual arm aerial manipulator with arms torque compensation.

Intuitively, the performance of the controller will be qualitatively improved if the arms torque estimation is accurate enough and the delay in the signal transmission and processing is at least five times lower than the lowest time constant of the system. Note that the natural frequency in the attitude control of a high inertia mechanical system as a multirotor is around 2 Hz, whereas the update rate of the torque estimator is 50 Hz.

4.5.3.2. Arms controller

A simple trajectory generation method that exploits the position controller embedded in the Herkulex servos is described here. The goal is that the end effector follows a sequence of way-points with smooth variations of the velocity profile, avoiding acceleration peaks. According to the manual of the servos, three working modes are defined: normal operation mode, Velocity Over-Ride (VOR) disabled, and VOR enabled. These have been illustrated in **Figure 4.15**. Each servo takes as input the desired goal position and the play time, that is, the desired time for reaching the goal position. The embedded servo controller generates then a trapezoidal velocity profile for satisfying the position and timing constraints.

The trajectory generation method described in **Figure 4.16** makes use of the VOR mode for achieving smooth motions with the manipulators. Let $\boldsymbol{P}^i_E$ be a continuous time trajectory in the Cartesian space for the end effector of the i-th manipulator, which is sampled each T seconds for obtaining the corresponding sequence of way-points. Applying the inverse kinematic model, the joint position references $q^i_{1,ref}$, $q^i_{2,ref}$ and $q^i_{3,ref}$ are obtained. Now, it is imposed that joint position references are sent to the servos at the midpoint of the velocity profile, that is, 50% of the elapsed play time, which implies that the play time is equal to $2 \cdot T$. This constraint ensures that the velocity profile is re-generated from the constant speed zone. The manual of the servos specifies that the velocity profile is symmetrical, with a default acceleration ratio of 25% of the play time. Experimental results show that the way-point sampling period T should be over 25 ms, as the internal control period for the servos is 11.3 ms. Note that this timing-based control scheme is not affected by error integration, as the error is only allow to grow during a play time period and it is reset with each new joint position reference.

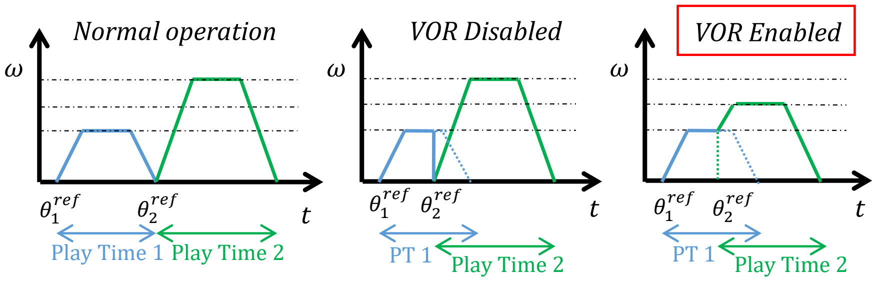

Figure 4.15. Velocity profiles for the three operation modes of the Herkulex servos. In the Velocity Over-Ride (VOR) mode, the new profile (green) is re-computed from the velocity in the time instant the new reference is received, preventing acceleration peaks.

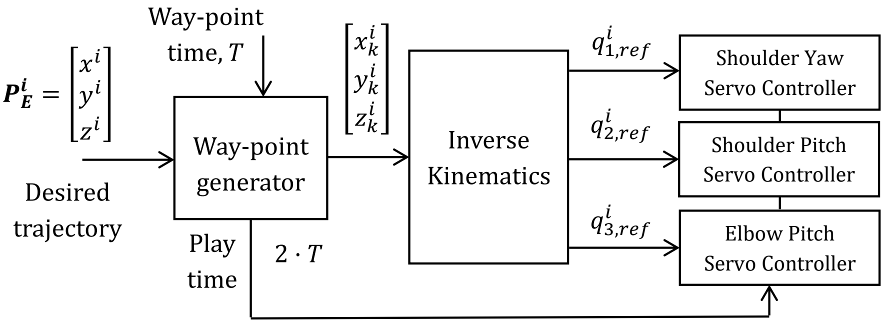
$P_E^i = \begin{bmatrix} x^i \\ y^i \\ z^i \end{bmatrix}$
Desired trajectory
Way-point time, T
Way-point generator
Play time
$2 \cdot T$
$\begin{bmatrix} x_k^i \\ y_k^i \\ z_k^i \end{bmatrix}$
Inverse Kinematics
$q_{1,ref}^i$
$q_{2,ref}^i$
$q_{3,ref}^i$
Shoulder Yaw Servo Controller
Shoulder Pitch Servo Controller
Elbow Pitch Servo Controller

Figure 4.16. Arms control structure based on inverse kinematics. Smooth trajectories are achieved sending the position references to the servos at the midpoint of the trapezoidal velocity profile, imposing that the play time is two times the way-point tracking time.

4.5.3.3. Arms torque estimator

The control method represented in **Figure 4.14** relies on the estimation of the reaction torques caused by the motion of the arms, which are introduced in the base of the aerial platform. This approach exploits the knowledge on the dynamics of the system (see **Section 4.5.2**), considering that the reaction of the arms over the multirotor can be computed and thus compensated by the attitude controller. Unlike the problem of estimating and controlling a multirotor vehicle affected by external wrenches like wind disturbances or unknown contact forces, the compensation of endogenous forces/torques is a more simple problem in the sense that its estimation is straightforward if the state of the servos is known and the dynamic model is available.

The structure of the Arms Torque Estimator block in **Figure 4.14** is detailed in **Figure 4.17**. The servo actuators provide joint position and speed measurements at 50 Hz, obtaining the acceleration signal at the output of a Phase Lock Loop (PLL). This method is preferred to the differentiation as it provides smoother estimations and attenuates the effect of noise and outliers in the velocity signal. The position, velocity and acceleration of the shoulder and elbow joint servos is then provided to the dynamic model, giving as output the gravity, centrifugal and Coriolis terms, and the inertia torque components referred to the system center of mass. These were identified in the experiment shown in **Figure 4.18**.

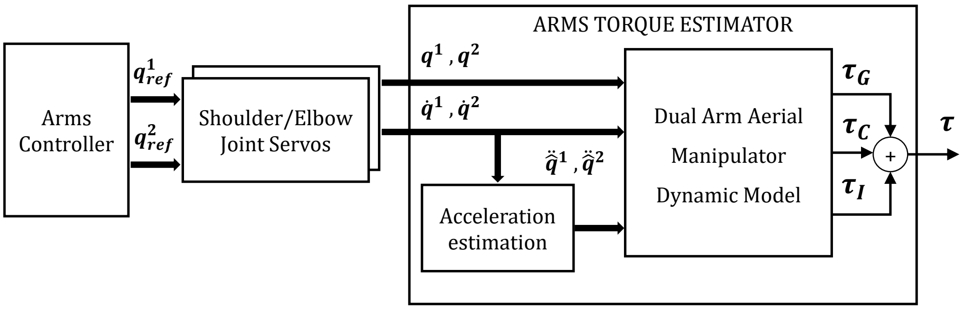
ARMS TORQUE ESTIMATOR
Arms Controller
q^1_{ref}
q^2_{ref}
Shoulder/Elbow Joint Servos
q^1, q^2
$\dot{q}^1, \dot{q}^2$
$\ddot{q}^1, \ddot{q}^2$
Acceleration estimation
Dual Arm Aerial Manipulator Dynamic Model
τ_G
τ_C
τ_I
+
τ

Figure 4.17. Structure of the arms torque estimator.

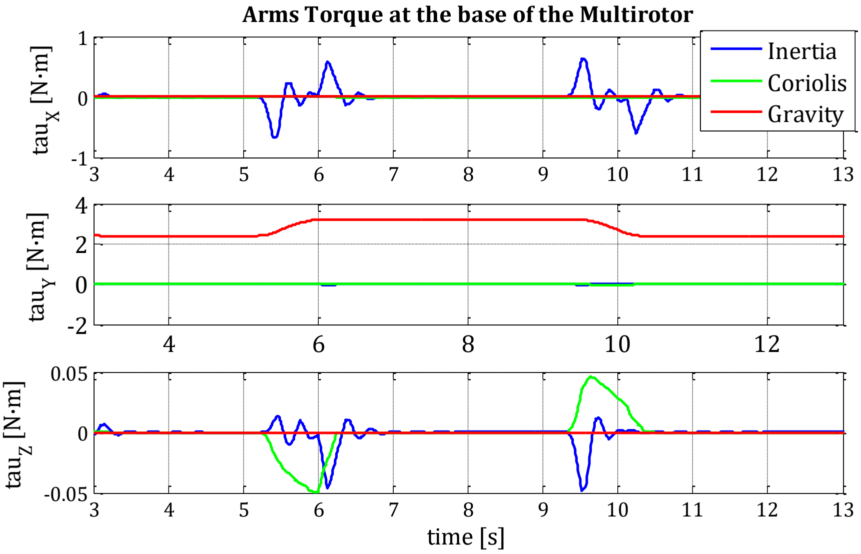

Figure 4.18. Inertia (blue), Coriolis and centrifugal (green) and gravity (red) terms in the XY axes for the 90° step in the shoulder pitch joint of the left arm. The components in the X-Z axes are due to the asymmetry in the motion of the arms.

4.6. Anthropomorphic, compliant and lightweight dual arm

4.6.1. Kinematics

The anthropomorphic dual arm provides 4 DOF's for end effector positioning in a human-like kinematic configuration with the shoulder pitch joint at the base, followed by the shoulder roll, shoulder yaw and the elbow pitch joint. The corresponding joint variables of the output links are denoted by q_1^i, q_2^i, q_3^i, and q_4^i, respectively, with $i = 1, 2$ for the left and right arms. The wrist orientation joints have not been implemented in this version. A rendered view of the arms with the parameters of the kinematic model is represented in **Figure 4.19**, including the forearm and upper arm lengths, the separation between the arms, and the joint angles with the positive direction of rotation given by the right-hand criteria. A reference frame $\{\boldsymbol{X_0^i Y_0^i Z_0^i}\}$ attached to the intersection point of the joints of the shoulder of each arm is defined, so the tool center point (TCP) or any point in the workspace will be referenced to this frame. Each arm provides one redundant DOF that can be exploited for collision avoidance, null space control, or for orienting the end effector. In this work the shoulder roll angle is considered as a parameter, $q_2^i = \varphi_i$, which can be tuned according to the task. For example, in the take-off or landing operations, the arms should be in a position such that the elbow and wrist points are above the landing gear, so $\varphi_i = \pm 90$ degrees, whereas in a visual servoing task, this angle will take values around $\varphi_i = \pm 10$ degrees.

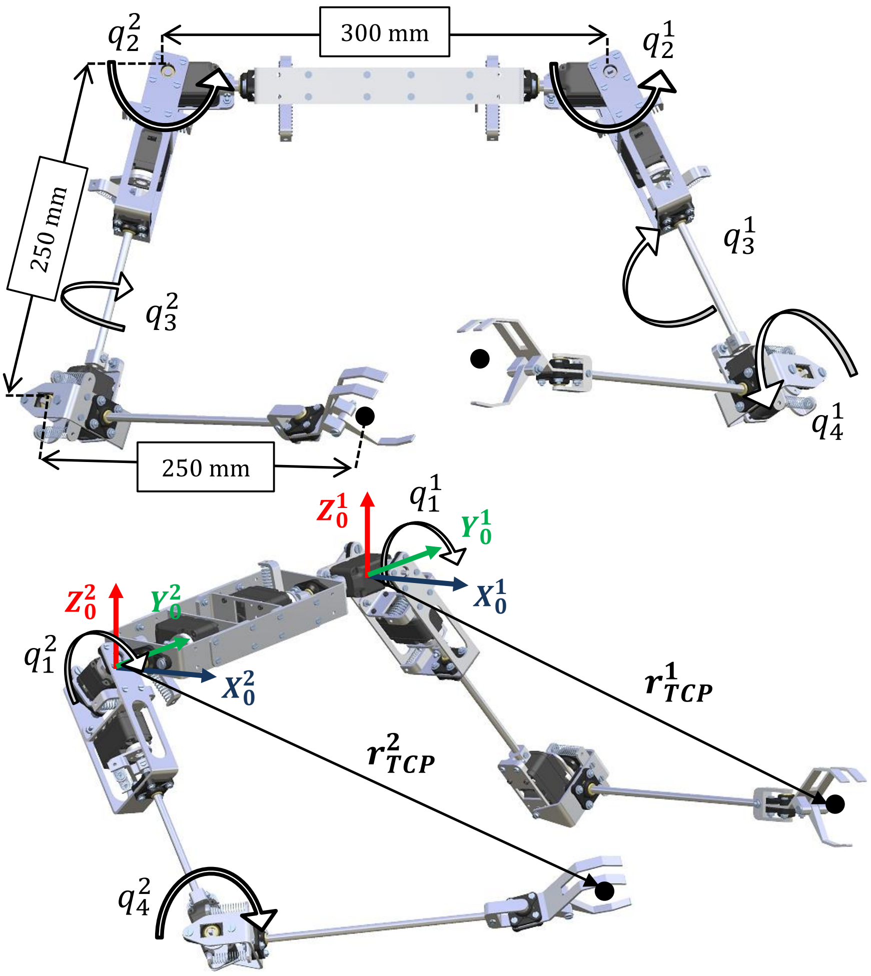

Figure 4.19. Kinematic configuration of the anthropomorphic dual arm and reference frames of both arms attached to the shoulder joint.

4.6.1.1. Forward kinematics

Let $\boldsymbol{FK_i}\colon \mathfrak{R}^4 \rightarrow \mathfrak{R}^3$ represents the forward kinematics of the i-th arm. The position of the TCP of each arm is obtained multiplying the transformation matrices associated to each joint:

$$
\begin{gathered}
{}^{0}_{1}\boldsymbol{T}_i\left(q_1^i\right) = \begin{bmatrix} c_1^i & 0 & s_1^i & 0 \\ 0 & 1 & 0 & 0 \\ -s_1^i & 0 & c_1^i & 0 \\ 0 & 0 & 0 & 1 \end{bmatrix} \quad {}^{1}_{2}\boldsymbol{T}_i\left(q_2^i\right) = \begin{bmatrix} 1 & 0 & 0 & 0 \\ 0 & c_2^i & -s_2^i & 0 \\ 0 & s_2^i & c_2^i & 0 \\ 0 & 0 & 0 & 1 \end{bmatrix} \\
{}^{2}_{3}\boldsymbol{T}_i\left(q_3^i\right) = \begin{bmatrix} c_3^i & -s_3^i & 0 & 0 \\ s_3^i & c_3^i & 0 & 0 \\ 0 & s_2^i & 1 & 0 \\ 0 & 0 & 0 & 1 \end{bmatrix} \quad {}^{3}_{4}\boldsymbol{T}_i\left(q_4^i\right) = \begin{bmatrix} c_4^i & 0 & s_4^i & 0 \\ 0 & 1 & -s_2^i & 0 \\ -s_4^i & 0 & c_4^i & -L_1 \\ 0 & 0 & 0 & 1 \end{bmatrix}
\end{gathered}
\tag{4.39}
$$

Here $c_j^i = \cos\left(q_j^i\right)$ and $s_j^i = \sin\left(q_j^i\right)$. The upper arm link length (from shoulder to elbow) and the forearm length (from elbow to TCP) are denoted by L_1 and L_2, respectively. The last transformation matrix is referred to the elbow joint, so it is displaced the upper arm link length L_1. The position of the TCP referred to each frame is computed as follows:

$$
\boldsymbol{r^i_{TCP}}\left(\boldsymbol{q^i}\right) = \begin{bmatrix} x_i \\ y_i \\ z_i \end{bmatrix} = \boldsymbol{FK_i}\left(\boldsymbol{q^i}\right) = \left(\prod_{j=1}^{4} {}^{j-1}_{j}\boldsymbol{T}\left(q_j^i\right)\right) \cdot \begin{bmatrix} 0 \\ 0 \\ -L_2 \\ 1 \end{bmatrix} \tag{4.40}
$$

where $\boldsymbol{q^i} = \left[q_1^i, q_2^i, q_3^i, q_4^i\right]^T$ is the angular position vector of the output link, denoting as $\boldsymbol{\theta^i} = \left[\theta_1^i, \theta_2^i, \theta_3^i, \theta_4^i\right]^T$ the servo position vector.

4.6.1.2. Inverse kinematics

In order to provide an analytical solution to the inverse kinematics, it was imposed by design that the rotation axis of all the joints intersect in a common point. The joint angles of the output links can be determined from the desired Cartesian position applying the inverse kinematics $\boldsymbol{IK_i}\colon \mathfrak{R}^3 \rightarrow \mathfrak{R}^4$:

$$
\boldsymbol{IK_i}\left(\boldsymbol{r^i_{TCP}}\right) = \boldsymbol{FK_i^{-1}}\left(\boldsymbol{r^i_{TCP}}\right) = \begin{bmatrix} q_1^i \\ q_2^i \\ q_3^i \\ q_4^i \end{bmatrix} \tag{4.41}
$$

As mentioned before, it is imposed for simplicity that $q_2^i = \varphi_i$, considering the angle φ_i as a parameter. The elbow pitch angle only depends on the position of the TCP and on the forearm and upper arm links lengths:

$$
q_4^i = -\cos^{-1}\left(\sqrt{\frac{x_i^2 + y_i^2 + z_i^2 - L_1^2 - L_2^2}{2 \cdot L_1 \cdot L_2}}\right) \tag{4.42}
$$

It can be demonstrated that the shoulder pitch joint satisfies the following trigonometric equation whose analytical solution is omitted for space reasons:

$$x^i \cdot sin(q_1^i) + z^i \cdot \cos(q_1^i) = w_i \tag{4.43}$$

$$w_i = \frac{L_2^2 - (L_1^2 + x_i^2 + z_i^2) + 2 \cdot L_1 \cdot y_i \cdot \sin(q_2^i)}{2 \cdot L_1 \cdot \cos(q_2^i)} \tag{4.44}$$

Note however that the resulting quadratic equation may have two solutions, corresponding to the elbow-up/down poses. The shoulder yaw angle is finally obtained:

$$q_3^i = atan2(a^i, b^i) \tag{4.45}$$

$$a^i = x_i \cdot s_1^i \cdot s_2^i + y_i \cdot c_2^i + z_i \cdot c_1^i \cdot s_2^i \tag{4.46}$$

$$b^i = x_i \cdot c_1^i - z_i \cdot s_1^i \tag{4.47}$$

4.6.2. Arms position/trajectory control based on inverse kinematics

The position/velocity control scheme implemented in the dual arm system is illustrated in **Figure 4.20**. In this case, the Cartesian position of the end effector of both arms is controlled using a 6-DOF mouse that provides the velocity reference, although this scheme has been also applied to the visual servoing task described below. The inverse kinematics block generates the joint references taken as input by the low level arms controller, giving as output the reference position and play time (PT) sent to the servos. This scheme exploits the controller embedded in the Herkulex servos, which generates a trapezoidal velocity profile for reaching the goal position in the desired time. Smooth trajectories are achieved imposing that the position references are sent at the midpoint of the velocity profile

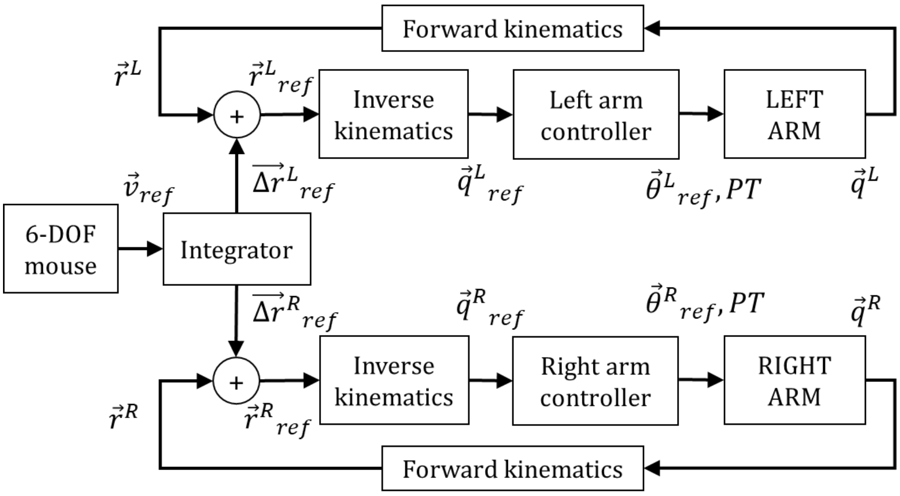
Forward kinematics
$\vec{r}^L$
$\vec{r}^L{}_{ref}$
+
Inverse kinematics
Left arm controller
LEFT ARM
$\vec{v}_{ref}$
$\overrightarrow{\Delta r}^L{}_{ref}$
$\vec{q}^L{}_{ref}$
$\vec{\theta}^L{}_{ref}, PT$
$\vec{q}^L$
6-DOF mouse
Integrator
$\overrightarrow{\Delta r}^R{}_{ref}$
$\vec{q}^R{}_{ref}$
$\vec{\theta}^R{}_{ref}, PT$
$\vec{q}^R$
+
Inverse kinematics
Right arm controller
RIGHT ARM
$\vec{r}^R$
$\vec{r}^R{}_{ref}$
Forward kinematics

Figure 4.20. Cartesian position/velocity controller based on inverse kinematics.

Let us consider now a bimanual grasping task as the one represented in **Figure 4.21**. The Cartesian positioning error for the i-th arm is defined as the difference between the grasping point given by a vision system and the TCP position that is obtained applying the direct kinematic model over the joints position provided by the servos, $\boldsymbol{e^i} = \boldsymbol{r^i_{ref}} - \boldsymbol{r^i}$. Let call v to the desired Cartesian speed of the TCP, and T to the control period. The idea is that, in each iteration of the control loop, the TCP moves a step towards the grasping point, that is, in the direction of the normalized error vector:

$$\boldsymbol{r}_{goal}^{\boldsymbol{i}} = \boldsymbol{r}^{\boldsymbol{i}} + v \cdot T \cdot \frac{\boldsymbol{e}^{\boldsymbol{i}}}{\|\boldsymbol{e}^{\boldsymbol{i}}\|} + \Delta\boldsymbol{r}_{\boldsymbol{G}}^{\boldsymbol{i}} \tag{4.48}$$

The terms in the right side of Equation (**4.48**) are the current position of the TCP, the increment to apply for approaching to the grasping point, and the estimated Cartesian deflection due to gravity. It is imposed that the TCP approaches to the grasping point at constant speed until the error threshold e_{th}^{i} is reached, decreasing then proportionally with the error:

$$v = \begin{cases} 0.2\ [m/s]\ \ if\ \ \|\boldsymbol{e}^{\boldsymbol{i}}\| \geq e_{th}^{i} = 0.04\ [m] \\ 0.2 \cdot \dfrac{\|\boldsymbol{e}^{\boldsymbol{i}}\|}{e_{th}^{i}}\ \left[\dfrac{m}{s}\right]\ \ if\ \ \|\boldsymbol{e}^{\boldsymbol{i}}\| < e_{th}^{i} = 0.04\ [m] \end{cases} \tag{4.49}$$

The reference position for each servo is finally obtained applying the inverse kinematic model:

$$\boldsymbol{\theta}_{ref}^{\boldsymbol{i}} = \boldsymbol{IK}^{\boldsymbol{i}}(\boldsymbol{r}_{goal}^{\boldsymbol{i}}, \phi^{i}) \tag{4.50}$$

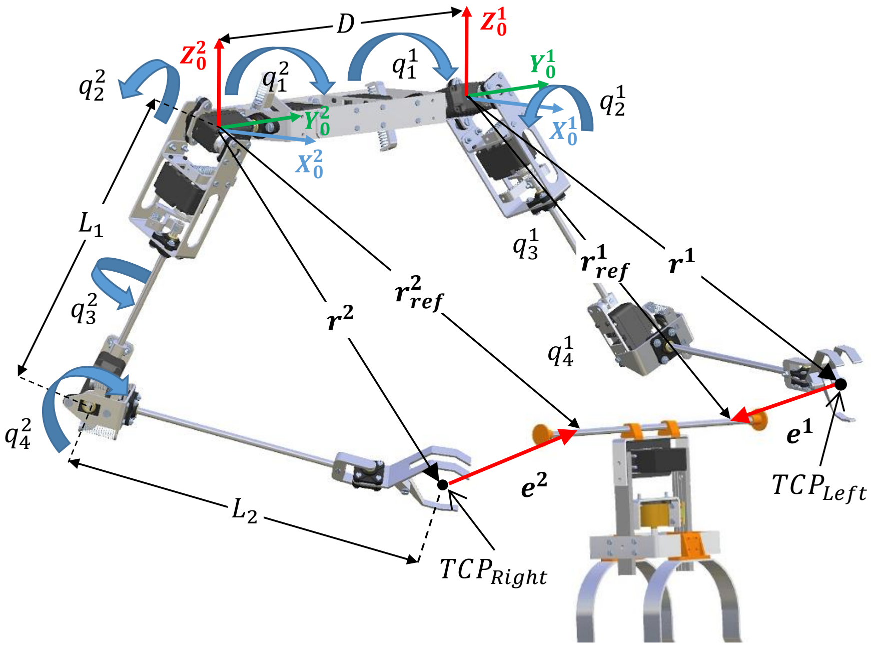

Figure 4.21. Geometric model considered in the bimanual grasping task with visual servoing.

4.6.3. Dynamics

The dynamic model of a compliant joint manipulator can be expressed in the usual matrix form, obtaining the equations of motion from the Euler-Lagrange method based on the Lagrangian and the generalized equation of the forces and torques.

As in the single joint case, the equations of the dynamic model of a compliant joint arm can be divided into two parts. Firstly, the servo-side dynamics includes the torque of the motor, the friction of the gearbox, the torque transmitted by the spring-lever mechanism, and the inertia of the rotor:

$$\boldsymbol{\tau}_{\boldsymbol{m}}^{\boldsymbol{i}} = \boldsymbol{B}_{\boldsymbol{i}}(\boldsymbol{\theta}^{\boldsymbol{i}})\ddot{\boldsymbol{\theta}}^{\boldsymbol{i}} + \boldsymbol{\tau}_{\boldsymbol{f}}^{\boldsymbol{i}} + \boldsymbol{\tau}^{\boldsymbol{i}} \tag{4.51}$$

Here $\boldsymbol{B_i} \in \mathbb{R}^{4\times4}$is the servo inertia matrix, and $\boldsymbol{\tau_m^i}$, $\boldsymbol{\tau_f^i}$, and $\boldsymbol{\tau^i} \in \mathbb{R}^4$ are the motor, friction and transmitted torques of the i-th arm. Now, the output link dynamics includes the inertia, Coriolis and centrifugal terms, and the gravity component:

$$\boldsymbol{M_i}(\boldsymbol{q^i})\boldsymbol{\ddot{q}^i} + \boldsymbol{C_i}(\boldsymbol{q^i}, \boldsymbol{\dot{q}^i}) + \boldsymbol{G_i}(\boldsymbol{q^i}) = \boldsymbol{\tau^i} + \boldsymbol{\tau_{ext}^i} \tag{4.52}$$

where $\boldsymbol{M_i}\epsilon\mathbb{R}^{4\times4}$ is the output link inertia matrix, $\boldsymbol{C_i}$ and $\boldsymbol{G_i} \in \mathbb{R}^4$ are the Coriolis and gravity terms, respectively, and $\boldsymbol{\tau_{ext}^i} \in \mathbb{R}^4$ is the torque due to external forces exerted over the i-th arm. The common term in **Equations (4.51)** and **(4.52)** is the torque $\boldsymbol{\tau^i}$ which can be estimated from the joint deflection:

$$\boldsymbol{\tau^i} = \boldsymbol{K^i}(\boldsymbol{\theta^i} - \boldsymbol{q^i}) + \boldsymbol{D^i}(\boldsymbol{\dot{\theta}^i} - \boldsymbol{\dot{q}^i}) = \boldsymbol{K^i}\Delta\boldsymbol{\theta^i} + \boldsymbol{D^i}\Delta\boldsymbol{\dot{\theta}^\iota} \tag{4.53}$$

where $\boldsymbol{K^i} = diag(k_j^i)$ and $\boldsymbol{D^i} = diag(d_j^i) \in \mathbb{R}^{4\times4}$ are the joint stiffness and damping matrices.

4.6.4. Aerial manipulator dynamics

Section 4.5 covered the dynamic model of a dual arm aerial manipulator with stiff joints, following the Euler-Lagrange formulation. In the case of the compliant manipulator described in **Section 2.6**, the vector of generalized coordinates $\boldsymbol{\xi} \in \mathbb{R}^{22}$ includes both the servo and output link angular position vectors, as well as the UAV position and attitude vectors, $\boldsymbol{r}$ and $\boldsymbol{\eta} \in \mathbb{R}^3$, respectively:

$$\boldsymbol{\xi} = \begin{bmatrix}\boldsymbol{r}^{\boldsymbol{T}} & \boldsymbol{\eta}^{\boldsymbol{T}} & \boldsymbol{\theta}^{\boldsymbol{1,T}} & \boldsymbol{q}^{\boldsymbol{1,T}} & \boldsymbol{\theta}^{\boldsymbol{2,T}} & \boldsymbol{q}^{\boldsymbol{2,T}}\end{bmatrix}^{\boldsymbol{T}} \tag{4.54}$$

The vector of generalized forces $\boldsymbol{\Gamma} \in \mathbb{R}^{22}$ will include the forces and torques acting over the aerial platform, $\boldsymbol{F_{UAV}}$ and $\boldsymbol{\tau_{UAV}} \in \mathbb{R}^3$, the torque $\boldsymbol{\tau^i}$ transmitted by the motors, and the external torque $\boldsymbol{\tau_{ext}^i}$ acting over the output links:

$$\boldsymbol{\Gamma} = \begin{bmatrix}\boldsymbol{F_{UAV}}^{\boldsymbol{T}} & \boldsymbol{\tau_{UAV}}^{\boldsymbol{T}} & \boldsymbol{\tau}^{\boldsymbol{1,T}} & \boldsymbol{\tau}_{\boldsymbol{ext}}^{\boldsymbol{1,T}} & \boldsymbol{\tau}^{\boldsymbol{2,T}} & \boldsymbol{\tau}_{\boldsymbol{ext}}^{\boldsymbol{2,T}}\end{bmatrix}^{\boldsymbol{T}} \tag{4.55}$$

The equations of the dynamic model can be derived following the Euler-Lagrange approach based on the Lagrangian and the generalized equation of the forces given by Equation **(1)**. The kinetic energy of the aerial manipulator is the sum of the contributions of the platform and each link of the arms:

$$T = \frac{1}{2}\begin{pmatrix}\boldsymbol{\dot{r}_{CoM}} \\ \boldsymbol{\dot{\eta}}\end{pmatrix}^T \begin{bmatrix}m_T \cdot \boldsymbol{I}_{3\times3} & \boldsymbol{0} \\ \boldsymbol{0} & \boldsymbol{J}\end{bmatrix}\begin{pmatrix}\boldsymbol{\dot{r}_{CoM}} \\ \boldsymbol{\dot{\eta}}\end{pmatrix} + \frac{1}{2}\sum_{i=1}^{2}\sum_{j=1}^{4}\begin{pmatrix}\boldsymbol{\dot{r}_j^i} \\ \boldsymbol{\omega_j^i}\end{pmatrix}^T \begin{bmatrix}m_j^i \cdot \boldsymbol{I}_{3\times3} & \boldsymbol{0} \\ \boldsymbol{0} & \boldsymbol{J_j^i}\end{bmatrix}\begin{pmatrix}\boldsymbol{\dot{r}_j^i} \\ \boldsymbol{\omega_j^i}\end{pmatrix} \tag{4.56}$$

where m_T and $\boldsymbol{J_T}$ are the total mass and inertia of the robot, m_j^i and $\boldsymbol{J_j^i}$ are the mass and inertia of the j-th link of the i-th arm, whose translational and angular speed are represented as $\boldsymbol{\dot{r}_j^i}$ and $\boldsymbol{\omega_j^i}$. Unlike the stiff joint case, the potential energy includes two terms, the gravitational potential and the elastic potential energy associated to the flexible joints, which depends on the joint stiffness and the deflection angle. The potential energy is then computed as follows:

$$V = m_T g \boldsymbol{r_{CoM}}\begin{pmatrix}0 \\ 0 \\ 1\end{pmatrix} + \frac{1}{2}\sum_{i=1}^{2}(\boldsymbol{\theta^i} - \boldsymbol{q^i})^T\boldsymbol{K^i}(\boldsymbol{\theta^i} - \boldsymbol{q^i}) \tag{4.57}$$

where g is the gravity constant, and $\boldsymbol{K^i} = diag(k_j^i)$ is the stiffness diagonal matrix of the i-th arm. After some work, it is possible to express the model in the following matrix form:

$$\boldsymbol{M}(\xi)\ddot{\xi} + \boldsymbol{C}(\xi, \dot{\xi}) + \boldsymbol{G}(\xi) + \boldsymbol{K}(\xi) + \boldsymbol{D}(\xi, \dot{\xi}) = \boldsymbol{\Gamma} \tag{4.58}$$

where $\boldsymbol{M} \in \mathbb{R}^{22\times22}$ is the generalized inertia matrix, $\boldsymbol{C} \in \mathbb{R}^{22}$ represents the centrifugal and Coriolis terms, $\boldsymbol{G} \in \mathbb{R}^{22}$ is the gravity component of the wrenches, whereas $\boldsymbol{K}$ and $\boldsymbol{D} \in \mathbb{R}^{22}$ are the components associated to the deflection and the friction of the compliant joints. According to the notation, all these terms depend on the generalized coordinate vector, or well on a specific group of coordinates. The position of the manipulator relative to the base of the aerial platform and the angular position of the links modifies the value of the inertia matrix and the thrust that the propellers should deliver to compensate the torque due to gravity when the center of mass is displaced. In general, it is convenient that the manipulator is as close as possible to the geometric center of the UAV, maintaining the symmetry in the mass distribution, although from the theoretical point of view, the particular location of the arms does not affect the model.

4.6.5. Force-torque relationships

4.6.5.1. Geometric interpretation

In many manipulation operations it is necessary to estimate and control the contact forces at the end effector. This can be done measuring the deflection of the joints and applying the force-torque relations. These can be obtained in two steps: 1) compute the torque vector $\boldsymbol{\tau_j^i} = \boldsymbol{F_j^i} \times \boldsymbol{r_j^i}$ for all the joints, that is, the cross product between the force acting over the link of the joint and its position, and 2) project the torque on the corresponding joint axis. The matrix representation is then obtained. Let consider the diagram shown in **Figure 4.22**, where S, E and W are the shoulder, elbow and wrist points referred to frame $\{\boldsymbol{0^i}\}$ attached to the shoulder joint. These points, whose position vectors are $\boldsymbol{r_s} = \boldsymbol{0}$, $\boldsymbol{r_e}$ and $\boldsymbol{r_w}$, define the SEW plane and the normal vector $\boldsymbol{n_{sew}}$. The elbow and wrist points are obtained from the forward kinematic model. From now on, superscript $\boldsymbol{i}$ is omitted for clarity in the notation. The normalized position vectors shoulder-elbow and elbow-wrist are denoted by $\boldsymbol{u_{se}}$ and $\boldsymbol{u_{ew}}$, and are defined as follows:

$$\boldsymbol{u_{se}} = \frac{\boldsymbol{r_e}}{\|\boldsymbol{r_e}\|} \tag{4.59}$$

$$\boldsymbol{u_{ew}} = \frac{\boldsymbol{r_w} - \boldsymbol{r_e}}{\|\boldsymbol{r_w} - \boldsymbol{r_e}\|} \tag{4.60}$$

The normal vector to the SEW plane can be computed as:

$$\boldsymbol{n_{sew}} = \frac{\boldsymbol{u_{se}} \times \boldsymbol{u_{ew}}}{\|\boldsymbol{u_{se}} \times \boldsymbol{u_{ew}}\|} \tag{4.61}$$

It will be assumed that the contact force $\boldsymbol{F}$ is applied at the wrist point. The torque supported by the elbow pitch and the shoulder yaw joints is firstly obtained from the vector:

$$\boldsymbol{\tau_{ew}} = \boldsymbol{F} \times (\boldsymbol{r_w} - \boldsymbol{r_e}) \tag{4.62}$$

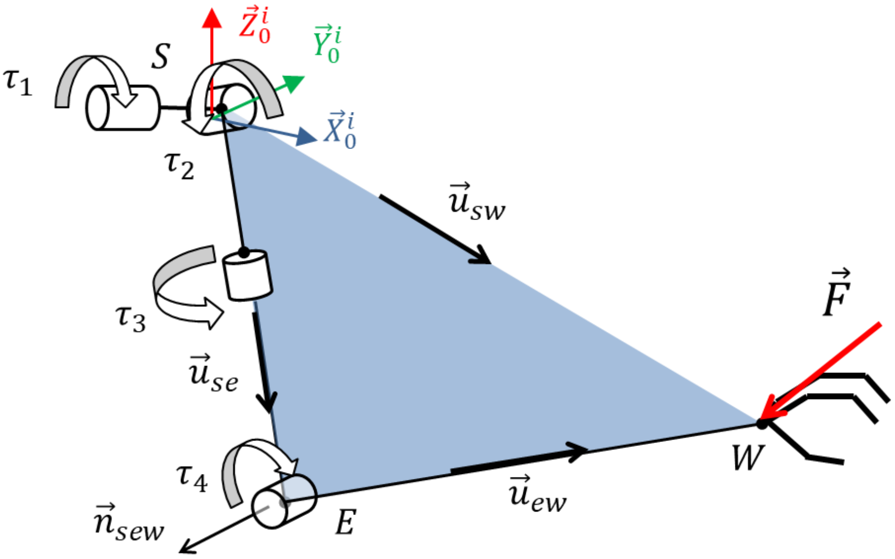

Figure 4.22. Geometric model considered for deriving the force-torque relationships.

Now, the projection of this torque vector in the direction of the rotation axis of each joint provides the corresponding joint torque. In the case of the elbow joint, the direction of rotation is parallel to $\boldsymbol{n_{sew}}$ and thus:

$$\tau_4 = \boldsymbol{n}_{\boldsymbol{sew}}^{\boldsymbol{T}} \cdot \boldsymbol{\tau}_{\boldsymbol{ew}} \tag{4.63}$$

The axis of rotation of the shoulder yaw joint is $\boldsymbol{u_{se}}$, so:

$$\tau_3 = \boldsymbol{u}_{\boldsymbol{se}}^{\boldsymbol{T}} \cdot \boldsymbol{\tau}_{\boldsymbol{ew}} \tag{4.64}$$

The torque in the shoulder roll and pitch joints is obtained in a similar way, considering the shoulder-to-wrist vector and the direction of rotation of these joints:

$$\boldsymbol{\tau}_{\boldsymbol{sw}} = \boldsymbol{F} \times \boldsymbol{r}_{\boldsymbol{w}} \tag{4.65}$$

$$\tau_2 = [\cos q_1, 0, \sin q_1] \cdot \boldsymbol{\tau}_{\boldsymbol{sw}} \tag{4.66}$$

$$\tau_1 = [0, 1, s0] \cdot \boldsymbol{\tau}_{\boldsymbol{sw}} \tag{4.67}$$

Equations **(4.63)** – **(4.67)** can be rewritten in matrix form, in such a way that the torque-force relation is linear. This is done expressing the cross product as matrix multiplication using a skew-symmetric matrix defined as follows:

$$\boldsymbol{F} \times \boldsymbol{r} = \boldsymbol{F} \times \begin{bmatrix} r_x \\ r_y \\ r_z \end{bmatrix} = \begin{bmatrix} 0 & -r_z & r_y \\ r_z & 0 & -r_x \\ -r_y & r_x & 0 \end{bmatrix} \cdot \boldsymbol{F} = \boldsymbol{A} \cdot \boldsymbol{F} \tag{4.68}$$

4.6.5.2. Jacobian based interpretation

The force at the end effector can be computed from the joint torque and the Jacobian of the manipulator. Assuming that the contact force control task is executed in static or close to static conditions, the torque can be computed easily from the joint deflection and the joint stiffness matrix (neglecting the damping), so the force vector in task space will be given by:

$$\boldsymbol{F^i} = \left(\boldsymbol{J^{i,T}}\right)^{-1}\boldsymbol{\tau^i} = \left(\boldsymbol{J^{i,T}}\right)^{-1}\boldsymbol{K^i}\Delta\boldsymbol{\theta^i} \tag{4.69}$$

Here $\boldsymbol{J^i} \in \Re^{3\times4}$ is the Jacobian of the $\boldsymbol{i}$-th manipulator, whereas $\boldsymbol{K^i} = diag\{k_j^i\} \in \Re^{4\times4}$ is the corresponding joint stiffness matrix.

4.6.5.3. Cartesian deflection and contact force control

It is interesting to note that, if $\boldsymbol{q^i}$ is replaced by $\boldsymbol{\theta^i}$ in Equation **(4.40)**, then $\boldsymbol{FK_i}(\boldsymbol{\theta^i})$ represents the forward kinematics of an equivalent stiff joint manipulator. The difference between the position of the TCP in this virtual manipulator and in the compliant arm is called the Cartesian deflection, $\Delta\boldsymbol{l^i}$:

$$\Delta\boldsymbol{l^i} = \boldsymbol{FK_i}(\boldsymbol{\theta^i}) - \boldsymbol{FK_i}\left(\boldsymbol{q^i}\right) \tag{4.70}$$

The Cartesian deflection represents the deviation in the position of the TCP due to the deflection of the compliant joints. This concept is useful if, for example, a camera head gives the 3D position of a marker attached at the end effector, as it would allow the estimation and control of contact forces directly in the task space, increasing at the same time the positioning accuracy. This has been represented in **Figure 4.23**. In static conditions, the contact force will be proportional to the Cartesian deflection:

$$\boldsymbol{F^i} = \boldsymbol{K_C^i} \cdot \Delta\boldsymbol{l^i} \tag{4.71}$$

where the Cartesian stiffness matrix $\boldsymbol{K_C^i} \in \Re^{3\times3}$ is obtained from the joint stiffness matrix and the Jacobian:

$$\boldsymbol{K_C^i} = \left(\boldsymbol{J^{i,T}}\right)^{-1}\boldsymbol{K_s^i}\left(\boldsymbol{J^i}\right)^{-1} \tag{4.72}$$

According to this equation, the Cartesian stiffness will vary with the position of the joints. In particular, infinite stiffness is associated to the kinematic singularities of the arms.

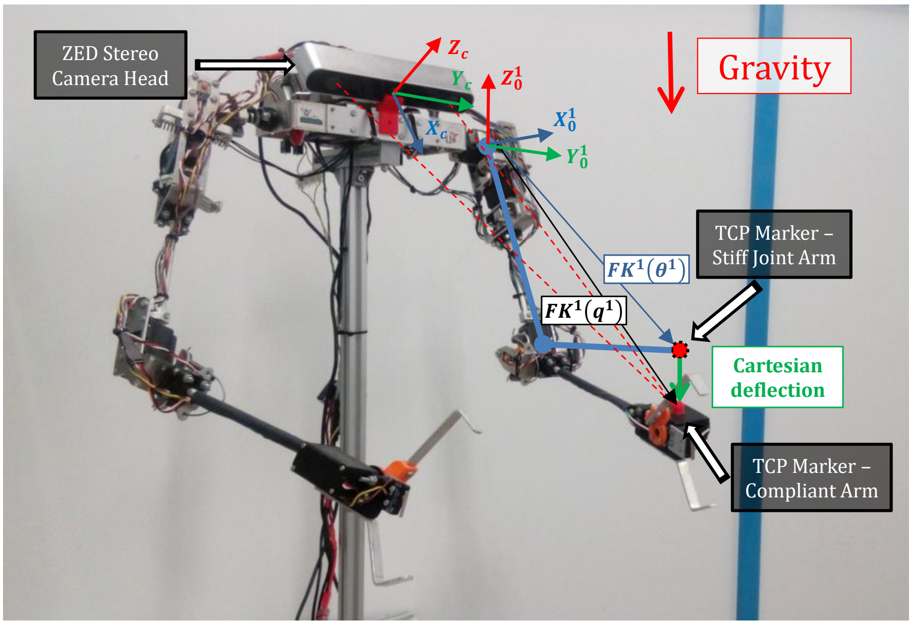

Figure 4.23. Cartesian deflection measured at the TCP of the left arm using the stereo camera head and.

The Cartesian deflection is the basis of the contact force control scheme depicted in **Figure 4.24**, which has been implemented and tested on flight with the compliant dual arm aerial manipulator (see **Section 5.8.3**). The variables involved here are the angular position of the servos, the joint deflection signal measured by the encoders integrated in the joints, and the output link angular position vector. The output link angular position is computed indirectly from the servo shaft angular position and the deflection measurement, whereas the Cartesian deflection is obtained from the forward kinematic model of the manipulator. The contact force is obtained multiplying this vector by the Cartesian stiffness matrix given by Equation **(4.72)**, which depends on the physical joint stiffness and on the Jacobian of the manipulator. It is necessary to remark that, due to the inverse of the Jacobian, the torque required to maintain a certain contact force tends to increase rapidly as the manipulator is closer to the kinematic singularities (arm fully stretched). The experimental results conducted in test bench evidence that the L-shaped configuration (90° elbow flexible) is more suitable for this purpose.

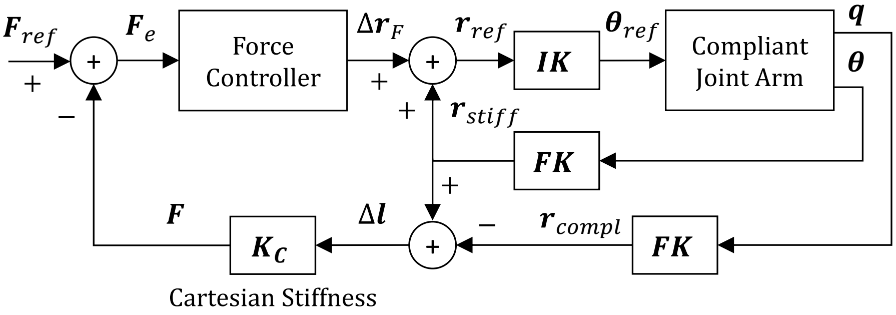

Figure 4.24. Contact force control scheme based on Cartesian deflection.

4.6.6. Vision-based deflection estimation in compliant arm

This section proposes the application of a stereo vision system for estimating and controlling the deflection in a compliant manipulator. A color marker attached at the end effector is visually tracked by a camera head, obtaining its position and velocity through an Extended Kalman Filter (EKF). The Cartesian deflection of the manipulator is defined as the difference between the real position of the marker given by the EKF, and the position in the equivalent stiff joint manipulator obtained from the encoders of the servos. The proposed method avoids the integration of a deflection sensor in the joints, which facilitates the development of tasks requiring contact force control.

4.6.6.1. Structure of the estimator

The block diagram of the developed deflection estimator is depicted in **Figure 4.25**, and it is based on the kinematic model described in Section 3.1. The estimator takes as input the angular position of the servo actuators, $\boldsymbol{\theta}^i$, along with the centroid of the i-th marker projected over the k-th camera given by the tracking algorithm, giving as output the estimated Cartesian and joint deflection, $\Delta \boldsymbol{l}_{M,i}^i$ and $\Delta\boldsymbol{\theta}^i$, respectively. The EKF integrates the measurements provided by the tracking algorithm, obtaining the XYZ position and velocity of the markers, $\boldsymbol{r}_{M,i}^i$ and $\boldsymbol{v}_{M,i}^i$. The Cartesian deflection is computed subtracting the position of the marker in the equivalent stiff-joint manipulator to the position given by the EKF. The joint deflection is computed in a similar way, applying the inverse kinematic model.

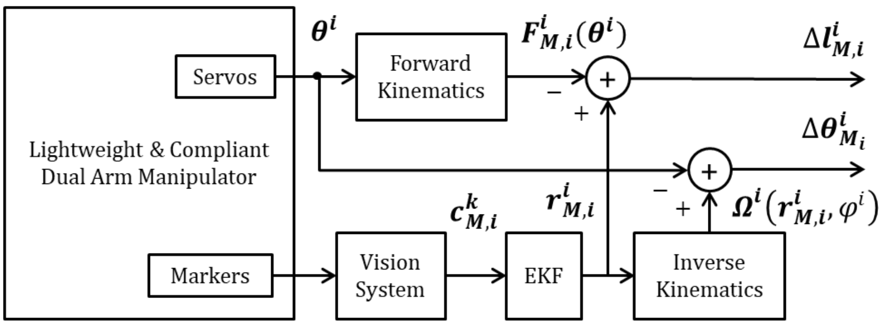
$\boldsymbol{\theta}^i$
$\boldsymbol{F}^i_{M,i}(\boldsymbol{\theta}^i)$
$\Delta \boldsymbol{l}^i_{M,i}$
Servos
Forward Kinematics
−
+
Lightweight & Compliant Dual Arm Manipulator
$\Delta \boldsymbol{\theta}^i_{M_i}$
−
+
$\boldsymbol{c}^k_{M,i}$
$\boldsymbol{r}^i_{M,i}$
$\boldsymbol{\Omega}^i(\boldsymbol{r}^i_{M,i}, \varphi^i)$
Markers
Vision System
EKF
Inverse Kinematics

Figure 4.25. Structure of the deflection estimation system.

4.6.6.2. Vision system

The vision system consists of a ZED stereo camera focused on the color markers attached at the wrist point of both arms, and a program developed in C++ that implements a modified version of the CAMShift which allows the tracking loss detection and object re-detection using color and geometric information. The CAMShift algorithm is a well suited solution for tracking color objects due to its simplicity, low computational requirements in time and memory, robustness to blurring and to changes in the illumination conditions. However, its main drawback is the necessity of a marker whose color is in high contrast with respect to the background. The shape of the marker should be spherical so its projection of the image plane of the stereo pair is independent from the point of view or pose of the arms.

A calibration process is carried out in an offline phase for determining the focal length, principal point as well as the distortion coefficients of the ZED camera. The hue, saturation and value (HSV) rejection thresholds used for isolating the markers on the back-projection image were tuned experimentally from a picture of the markers at the nominal observation distance.

4.6.6.3. Extended Kalman Filter

Although the position of the markers can be estimated geometrically from the pair of projection centroids given by the CAMShift algorithm, the Kalman filter is preferred as it also provides an estimation of the velocity of the marker, which can be exploited for estimating the rate of energy exchange during the impact of the manipulator. The nonlinearity associated to the pin-hole camera model requires the application of the extended version of this algorithm. A simple constant velocity model is assumed for describing the motion of the marker, so the state vector is defined as follows:

$$\boldsymbol{x} = \begin{bmatrix} x & y & z & v_x & v_y & v_z \end{bmatrix}^T \tag{4.73}$$

The measurement vector taken as input by the EKF is the centroid of the marker projected on each camera, $\boldsymbol{c}^k_{M,i}$, along with the elapsed time since last update, Δt. The accuracy in the position-velocity estimations has been tuned through the process noise and measurement noise covariance matrices $\boldsymbol{Q} \in \boldsymbol{\Re}^{6\times 6}$ and $\boldsymbol{R} \in \boldsymbol{\Re}^{2\times 2}$, respectively.

$$\boldsymbol{Q} = \begin{bmatrix} diag_{3\times 3}(\sigma_p^2) & \boldsymbol{0}_{3\times 3} \\ \boldsymbol{0}_{3\times 3} & diag_{3\times 3}(\sigma_v^2) \end{bmatrix} \quad ; \quad \boldsymbol{R} = \begin{bmatrix} \sigma_c^2 & 0 \\ 0 & \sigma_c^2 \end{bmatrix} \tag{4.74}$$

where $\sigma_p^2 = 2.5\ [m]$, $\sigma_v^2 = 100\ [m/s]$ and $\sigma_c^2 = 25\ [pixels]$.

4.7. Flexible link, long reach aerial manipulators

This section covers the dynamic models of the long reach manipulators described in **Section 2.7**. Before its integration in an aerial platform, a first prototype consisting of the lightweight and human size dual arm and a flexible link was developed and tested in fixed base test-bench, so the dynamic behaviour of the compound can be identified more clearly. In particular, the oscillation of the flexible link and the dynamic coupling with the arms are modelled and identified experimentally (see **Section 5.7**). In the integration with the aerial platform, the long reach manipulator is supported by a passive joint at the base of the multirotor that allows the free rotation of the flexible link in one axis, similarly to a pendulum. This is done so to facilitate the take-off and landing manoeuvres, and to prevent that the manipulator induces a torque at the base of the aerial platform.

4.7.1. Flexible long reach link with lightweight dual arm

4.7.1.1. Flexible link dynamics

The dynamic behavior of a flexible link is derived from the Lagrangian and the Euler-Bernouilli beam theory. According to the assumed-modes method, the deflection of the flexible link can be expressed as the sum of an infinite number of vibration modes in the following way:

$$w(t,x) = \sum_{i=1}^{\infty} \varphi_i(x) \cdot \delta_i(t) \tag{4.75}$$

Here $\varphi_i(x)$ is the modal shape function and $\delta_i(t)$ is the generalized coordinate of the i-th vibration mode. **Figure 4.26** represents the geometric model typically considered. The parameters of the flexible link are its mass, length, Young's modulus of elasticity and the cross-sectional moment of inertia (m, L, E and I), whereas J_0 is the rotor inertia, and m_p is the payload mass at the tip. The torque and rotation angle of the base joint (not used in this work) are denoted by τ and θ, and α is the link tip angle. The deflection at the tip of the link is $w(t,L)$, and $f_{ext}(t)$ is the external force acting at this point.

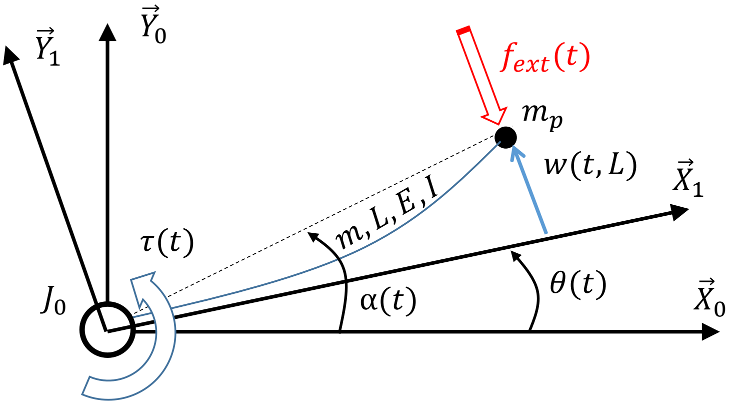

Figure 4.26. Geometric model and parameters in the flexible link manipulator.

Each vibration mode has associated a frequency that depends on the mechanical parameters of the link and the tip. Therefore, the deflection of the tip will be approximated by:

$$w(t, L) \approx \varphi_1(L) \cdot \delta_1(t) \tag{4.76}$$

The deflection of flexible link tip caused by an external force $f_{ext}(t)$ can be modeled as mass-spring-damper system in the following form:

$$m_1 \ddot{\delta}_1(t) + d_1 \dot{\delta}_1(t) + k_1 \delta_1(t) = f_{ext}(t) \tag{4.77}$$

The friction d_1 and elastic constant k_1 parameters can be obtained experimentally from the impulsive response, and the generalized mass m_1 from the CAD model. As most part of the mass of the dual arm system is placed close to the shoulder frame, the variation of these parameters due to changes in joint position is not significant. The dynamic coupling between the dual arm and the flexible link is described in next subsection.

4.7.1.2. Kinematics

In an aerial manipulation system, three reference frames are usually defined: the Earth fixed frame $\{\boldsymbol{E}\}$, the UAV base frame $\{\boldsymbol{B}\}$, and the manipulator frame $\{\boldsymbol{M}\}$, denoting as $\boldsymbol{T}_{\boldsymbol{M}}^{\boldsymbol{B}}$ and $\boldsymbol{T}_{\boldsymbol{B}}^{\boldsymbol{E}} \in \Re^{4\times4}$ to the respective transformation matrices. For convenience, the points of interest for the manipulation task will be defined in the reference frame of the manipulator. If $\boldsymbol{p}^{\boldsymbol{M}} = [x, y, z, 1]^T$ represents a certain target point in $\{\boldsymbol{M}\}$, then the same point can be expressed in the inertial frame $\{\boldsymbol{E}\}$ in the following way, more suitable during the approaching phase:

$$\boldsymbol{p}^{\boldsymbol{E}} = \boldsymbol{T}_{\boldsymbol{B}}^{\boldsymbol{E}} \cdot \boldsymbol{p}^{\boldsymbol{B}} = \boldsymbol{T}_{\boldsymbol{B}}^{\boldsymbol{E}} \cdot \left(\boldsymbol{T}_{\boldsymbol{M}}^{\boldsymbol{B}} \cdot \boldsymbol{p}^{\boldsymbol{M}}\right) \tag{4.78}$$

The kinematic model of the flexible LRM with the dual arm prototype at the tip is represented in **Figure 4.27**. As it can be seen, the dual arm system suffers a translation and a slight rotation due to the deflection of the flexible link, so $\boldsymbol{T}_{\boldsymbol{M}}^{\boldsymbol{B}}$ will depend on the flexible link tip deflection $w(t, L)$, where L is the flexible link length. The forward and inverse kinematics referred to the manipulator frame were described in **Section 4.5.1**.

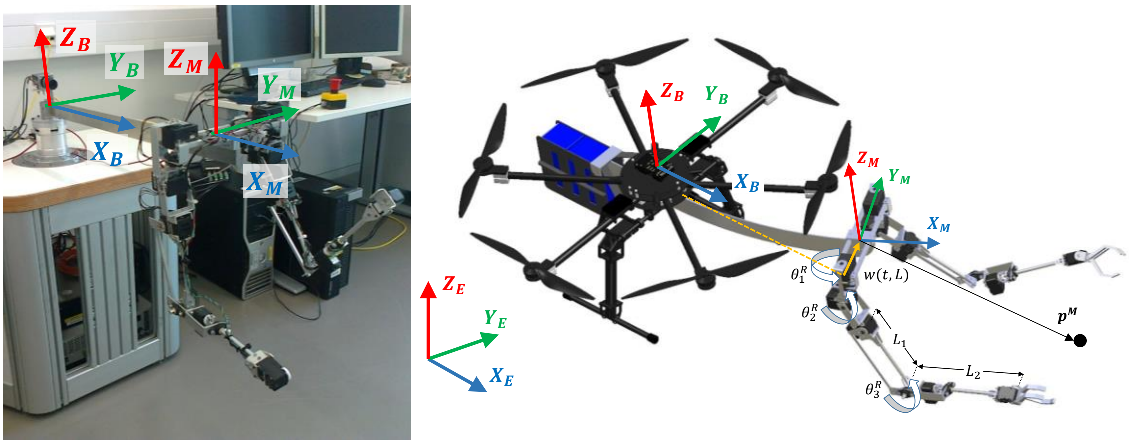

Figure 4.27. Reference frames and kinematic model of the flexible link dual arm manipulator.

4.7.1.3. Dynamic coupling between dual arm and flexible link

The dynamic model of the compound flexible link-dual arm can be written in the following form:

$$\begin{bmatrix} m_1 & \boldsymbol{H_{bm}} \\ \boldsymbol{H_{bm}^T} & \boldsymbol{H_m} \end{bmatrix} \begin{bmatrix} \ddot{\delta}_1 \\ \ddot{\boldsymbol{\theta}} \end{bmatrix} + \begin{bmatrix} d_1\dot{\delta}_1 \\ \boldsymbol{0} \end{bmatrix} + \begin{bmatrix} k_1\delta_1 \\ \boldsymbol{\tau_g} \end{bmatrix} + \begin{bmatrix} c_b \\ \boldsymbol{c_m} \end{bmatrix} = \begin{bmatrix} f \\ \boldsymbol{\tau} \end{bmatrix} \tag{4.79}$$

Here $\boldsymbol{\theta}$ and $\boldsymbol{\tau} \in \Re^6$ are the generalized coordinates and the joint torque of the dual arm system, respectively, while $\boldsymbol{\tau_g} \in \Re^6$ is the gravity term affecting the shoulder pitch and elbow pitch joints. Note from **Figure 4.27** that gravity does not affect to the flexible link as long as $\boldsymbol{Z_B}$ and the gravity vector are parallel. Matrices $\boldsymbol{H_m} \in \Re^{6\times6}$ and $\boldsymbol{H_{bm}} \in \Re^{1\times6}$ represent the inertia of the dual arm and the coupling inertia matrix between the dual arm and the flexible link. Finally, c_b and $\boldsymbol{c_m} \in \Re^6$ are nonlinear terms that depend on deflection and joint speed.

4.7.2. Long reach aerial manipulator with passive joint: single arm

4.7.2.1. Kinematics

The reference frames, position vectors, joint variables and link lengths of the developed long reach aerial manipulator are represented in **Figure 4.28**. Here, $\{\boldsymbol{E}\}$, $\{\boldsymbol{B}\}$ and $\{\boldsymbol{0}\}$ are the Earth fixed frame, the UAV based frame, and the manipulator base frame, respectively. The position and orientation of the UAV are denoted by $\boldsymbol{r} = [x, y, z]^T$ and $\boldsymbol{\eta} = [\varphi, \theta, \psi]^T$. The rotation angle of the pendulum is represented by q_0, whereas q_1 and q_2 are the shoulder pitch and elbow pitch joints of the compliant arm, whose position and orientation relative to the UAV base frame is given by the transformation matrix:

$$^{B}\boldsymbol{T}_0 = \begin{bmatrix} c(q_0) & 0 & s(q_0) & -L_0 s(q_0) \\ 0 & 1 & 0 & 0 \\ -s(q_0) & 0 & c(q_0) & -L_0 c(q_0) \\ 0 & 0 & 0 & 1 \end{bmatrix} \tag{4.80}$$

The position of the tool center point (TCP) in the Earth frame (assuming hovering conditions, $\varphi = \theta = 0$) depends on the three joint angles and on the heading of the aerial vehicle:

$$^{E}\boldsymbol{r}_{TCP} = \begin{bmatrix} -cos(\psi)\cdot\rho \\ -sin(\psi)\cdot\rho \\ -\gamma \end{bmatrix} \tag{4.81}$$

$$\rho = L_0 s(q_0) + L_1 s(q_0 + q_1) + L_2 s(q_0 + q_1 + q_2) \tag{4.82}$$

$$\gamma = L_0 c(q_0) + L_1 c(q_0 + q_1) + L_2 c(q_0 + q_1 + q_2) \tag{4.83}$$

This work considers the rotation in the yaw angle of the aerial platform instead of using a third joint for this purpose.

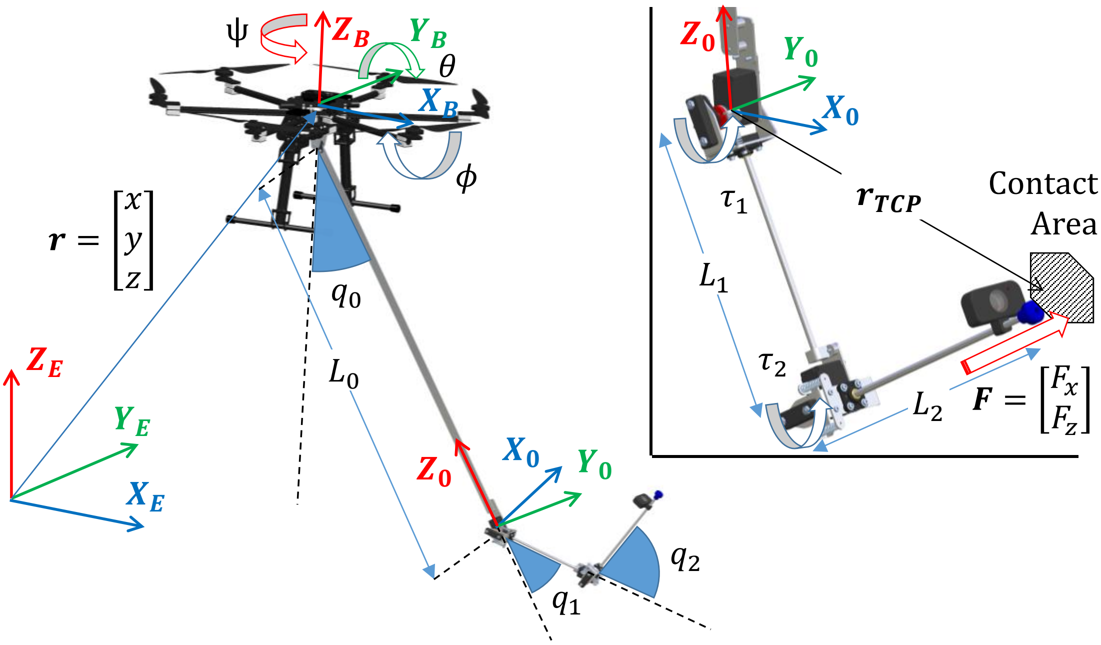

Figure 4.28. Kinematic model of the long reach aerial manipulator with single arm.

4.7.2.2. Dynamics

The dynamic model of the developed complaint joint, long reach aerial manipulator can be derived from the Lagrangian and the generalized equation of the forces and torques:

$$\frac{d}{dt}\left\{\frac{\partial L}{\partial \dot{\boldsymbol{\xi}}}\right\} - \frac{\partial L}{\partial \boldsymbol{\xi}} = \boldsymbol{\Gamma}\ ;\ L = K_{UAV} + K_{LRM} - (V_{UAV} + V_{LRM}) \tag{4.84}$$

Here L is the Larangian, defined as the difference between the kinetic and the potential energy of the system, which is the sum of the energy of the aerial platform and the long reach manipulator. The vector of generalized coordinates $\boldsymbol{\xi}$ includes the position and attitude of the aerial platform and the joint variables, and the generalized force vector $\boldsymbol{\Gamma}$ contains the wrenches acting over the platform along with the arm torques:

$$\boldsymbol{\xi} = [\boldsymbol{r}^T \quad \boldsymbol{\eta}^T \quad q_0 \quad q_1 \quad q_2 \quad \theta_1 \quad \theta_2]^T \in \Re^{11} \tag{4.85}$$

$$\boldsymbol{\Gamma} = [\boldsymbol{F}^T \quad \boldsymbol{\tau}^T \quad \tau_0 \quad \tau_1 \quad \tau_2 \quad \tau_{1,m} \quad \tau_{2,m}]^T \in \Re^{11} \tag{4.86}$$

Here q_0 is the rotation angle of the passive joint, θ_1 and θ_2 are the angular position of the arm servos, whereas q_1 and q_2 area the angular position of the output links. Both variables are related through the joint deflection angle $\Delta\theta_i$:

$$\Delta\theta_i = \theta_i - q_i \quad ; \quad \tau_{i,m} = k_i \Delta\theta_i + d_i \Delta\dot{\theta}_i \quad ; \quad i = \{1,2\} \tag{4.87}$$

where k_i and d_i are the stiffness and damping of the i-th joint. The external wrenches acting over the manipulator can be estimated from the torque delivered by the motor, $\tau_{i,m}$, and the output link torque, τ_i. Since the joint of the pendulum is passive, and its rotation axis is close to the center of mass of the multirotor, it can be assumed that $\tau_0 \cong \mathbf{0}$. This means that the long reach manipulator does not exert a force over the base of the aerial platform, but a force, similarly to a tethered load. It is necessary to remark that this features contributes to increase safety during the operation on flight, as the passive joints of the pendulum prevents that the physical interactions on flight may destabilize the aerial platform.

The kinetic and potential energy of the UAV are obtained from its mass m_{UAV} and inertia $\boldsymbol{I}_{UAV}$ in the following way:

$$K_{UAV} = \frac{1}{2} m_{UAV} \dot{\boldsymbol{r}}^T \dot{\boldsymbol{r}} + \frac{1}{2} \boldsymbol{\omega}^T \boldsymbol{I}_{UAV}^T \boldsymbol{\omega} \, ; V_{UAV} = m_{UAV} g z \tag{4.88}$$

The kinetic energy of the long reach manipulator depends on the mass and inertia of each of its links, m_i and $\boldsymbol{I}_i$, with $i = \{0, 1, 2\}$, whereas the potential energy is the sum of the gravity term and the elastic potential of the compliant joints:

$$K_{LRM} = \frac{1}{2} \sum_{i=0}^{2} \left\{ m_i \left({}^{E}\dot{\boldsymbol{r}}_i \right)^T \left({}^{E}\dot{\boldsymbol{r}}_i \right) + \left({}^{E}\boldsymbol{\omega}_i \right)^T \boldsymbol{I}_i^T \left({}^{E}\boldsymbol{\omega}_i \right) \right\} \tag{4.89}$$

$$V_{LRM} = g \sum_{i=0}^{2} m_i z_i + \sum_{i=1}^{2} k_i (\Delta\theta_i)^2 \tag{4.90}$$

The dynamic model of the long reach aerial manipulator can be expressed in the usual matrix form:

$$\boldsymbol{M}(\boldsymbol{\xi})\ddot{\boldsymbol{\xi}} + \boldsymbol{C}(\boldsymbol{\xi}, \dot{\boldsymbol{\xi}}) + \boldsymbol{G}(\boldsymbol{\xi}) + \boldsymbol{K}(\boldsymbol{\xi}) + \boldsymbol{D}(\dot{\boldsymbol{\xi}}) = \boldsymbol{\Gamma} \tag{4.91}$$

where $\boldsymbol{M}$ is are the generalized inertia matrix, $\boldsymbol{G}$ represents the centrifugal and Coriolis terms, $\boldsymbol{G}$ is the gravity component, whereas $\boldsymbol{K}$ and $\boldsymbol{D}$ are the elastic and damping terms of the compliant joint, long reach manipulator. The dynamic model defined by Equation **(4.91)** will be used by the UAV controller described in next subsection for compensating the oscillations of the passive pendulum and the motion of the compliant arm.

4.7.2.3. Coordinated UAV-Manipulator control scheme

The proposed long-reach aerial manipulator is intended to perform inspection operations and tasks requiring accurate position and force control of the end effector. The particular implementation will depend on the positioning system (GPS, laser tracking system, visual odometry, SLAM…) and on the way the operator specifies the desired inspection point. However, control scheme should follow a scheme similar to the one represented in **Figure 4.29**, where the UAV position, heading and thrust ($\boldsymbol{r}_{ref}$, ψ_{ref} and $\boldsymbol{U}$ in the diagram) are commanded in such a way that the manipulator is able to reach and exert the desired position and force.

The application of contact forces has associated two main effects over the robot. On the one hand, the component of the force in the forward direction will cause a recoil displacement in the passive joint until the equilibrium of forces is reached, that is, when the applied force $F_{x,ref}$ equals the projection in the X-axis of the gravity force:

$$F_{x,ref} = m_{LRM} \cdot g \cdot sin(q_0) \tag{4.92}$$

where m_{LRM} is the mass of the long reach manipulator, g is the gravity constant, and q_0 is the rotation of the pendulum joint. Note that the pushing or pulling force in this axis can be controlled indirectly through the relative position of the aerial platform w.r.t. the contact point, which determines the rotation angle q_0. On the other hand, the Z-axis component of the contact force should be compensated by the propellers, being possible to define an impedance behavior.

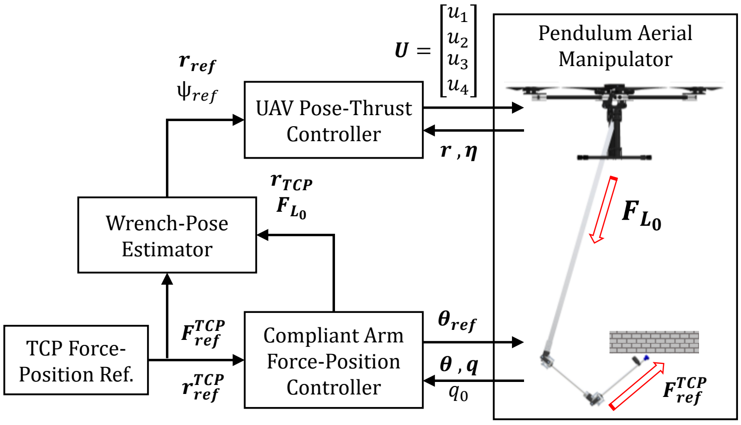
$\boldsymbol{r_{ref}}$
ψ_{ref}
$\boldsymbol{U} = \begin{bmatrix} u_1 \\ u_2 \\ u_3 \\ u_4 \end{bmatrix}$
Pendulum Aerial Manipulator
UAV Pose-Thrust Controller
$\boldsymbol{r}, \boldsymbol{\eta}$
$\boldsymbol{r_{TCP}}$
$\boldsymbol{F_{L_0}}$
Wrench-Pose Estimator
$\boldsymbol{F_{L_0}}$
$\boldsymbol{F^{TCP}_{ref}}$
TCP Force-Position Ref.
$\boldsymbol{r^{TCP}_{ref}}$
Compliant Arm Force-Position Controller
$\boldsymbol{\theta_{ref}}$
$\boldsymbol{\theta}, \boldsymbol{q}$
q_0
$\boldsymbol{F^{TCP}_{ref}}$

Figure 4.29. Coordinated UAV-long reach manipulator control scheme. The goal is to control the position and force of the TCP of the arm. The pose and thrust of the UAV is adapted to achieve this reference.

The undesired oscillations introduced in the passive joint due to impacts or accelerations can be cancelled coordinating the motion of the robotic arm with the aerial platform, or well using any of these separately. However, the capacity of the compliant arm to attenuate the oscillations in the pendulum is limited since the mass and inertia of the arm is much lower than the mass/inertia of the long reach manipulator. This can be also derived comparing the kinetic and potential energy of the aerial platform and the manipulator given by Equations **(4.89)** and **(4.90)**.

4.7.2.4. Force-Position control scheme

The force/position control scheme implemented in the arm is depicted in **Figure 4.30**, and it is a modified version of the force controller described in **Section 4.6.5.3** which also allows to control the position of the end effector to the contact point. The force error, that is, the difference between the reference and the force estimation given by Equation **(4.71)** is taken as input by the feedback force controller, giving as output the displacement of the TCP for correcting the force error. The joint position reference sent to the servos is obtained from the inverse kinematics, applied over the position vector $\boldsymbol{r_{ref}}$, which is the sum of the force and position corrections, and the current TCP position obtained from the forward kinematics.

$$\boldsymbol{\theta_{ref}} = \boldsymbol{IK}(\boldsymbol{r_{ref}}) = \boldsymbol{IK}(\Delta \boldsymbol{r_F} + \Delta \boldsymbol{r_P} + \boldsymbol{FK}(\boldsymbol{\theta})) \tag{4.93}$$

The position correction term $\Delta \boldsymbol{r_P} \in \Re^2$ is obtained integrating the velocity references provided by a joystick controlled by the operator of the arms. The force/position control modes can be switched simply enabling or disabling the force/position terms in Equation **(4.93)**.

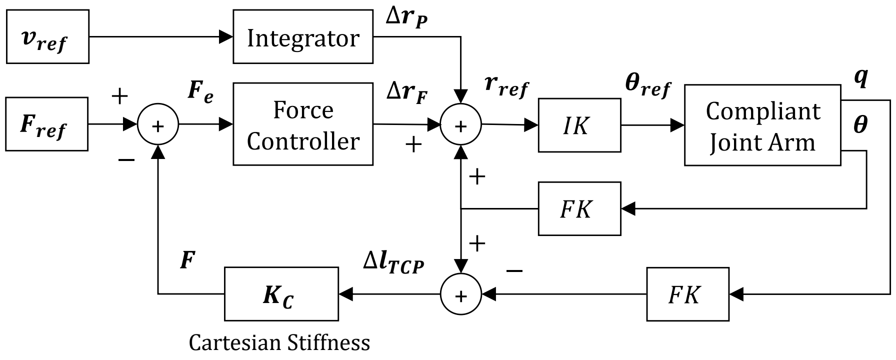
v_{ref}
Integrator
Δr_P
F_{ref}
+
−
F_e
Force Controller
Δr_F
+
r_{ref}
IK
θ_{ref}
Compliant Joint Arm
q
θ
+
FK
+
−
F
Δl_{TCP}
K_C
FK
Cartesian Stiffness

Figure 4.30. Force-position control scheme implemented in the compliant arm. The force is estimated from the Cartesian deflection $\Delta \boldsymbol{l}_{TCP}$ and stiffness $\boldsymbol{K}_C$.

4.7.3. Long reach aerial manipulator with passive joint: dual arm

The kinematics, dynamics and control of the single arm long reach aerial manipulator described in **Section 4.7.2** can be extended to the dual arm case. **Figure 4.31** represents the kinematic model of this system. The vector of generalized coordinates and generalized forces given in Equation **(4.85)** and Equation **(4.86)** is extended with the sixteen joint variables of the two arms, corresponding to the servo shaft and output link angular position. The model should incorporate the dynamic coupling with the flexible link, since the rotation of the shoulder roll and yaw joints, or well the acceleration of the aerial platform along the $\boldsymbol{Y}_B$ axis, may induce lateral deflections and excite the vibration modes.

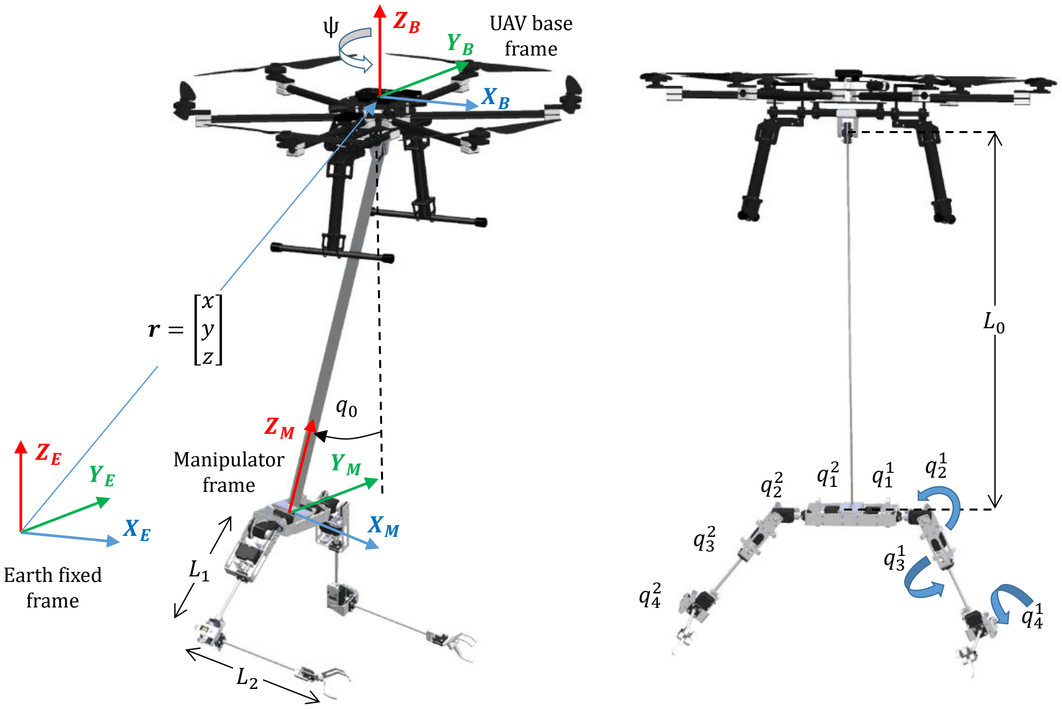
ψ
Z_B
Y_B
UAV base frame
X_B
$r = \begin{bmatrix} x \\ y \\ z \end{bmatrix}$
q_0
Z_M
Manipulator frame
Y_M
X_M
Z_E
Y_E
X_E
Earth fixed frame
L_1
L_2
L_0
q_2^2
q_1^2
q_1^1
q_2^1
q_3^2
q_3^1
q_4^2
q_4^1

Figure 4.31. Reference frames, joint variables and position vectors of the long reach aerial manipulator with compliant dual arm in pendulum configuration.

Conclusion

This chapter described the kinematics, dynamics and control schemes of the different prototypes of lightweight and compliant manipulators developed by the author, highlighting the possibility to estimate and control the forces and torques measuring the deflection of the spring-lever transmission mechanism introduced between the servo actuators and the output links. The dynamic model of the single compliant joint is firstly analysed, showing that the actuator may vary its apparent stiffness and damping controlling properly the deflection angle through the servo position. The forward/inverse kinematics and the force-torque relationships in a 3-DOF compliant joint arm are then presented, proposing a force/position control scheme which exploits the embedded servo position controller. This arm was equipped with an anthropomorphic, compliant and lightweight finger module which provides three under-actuated joints driven by a single actuator, controlling the angular position of the first joint and the grasping force through the PWM signal applied directly to the motor.

Two prototypes of dual arm aerial manipulators were analysed: the lightweight and human-size dual arm (stiff joints), and the anthropomorphic, compliant and lightweight dual arm. The equations of the forward and inverse kinematics are described, showing the derivation of the dynamic model of the dual arm aerial manipulator following the Euler-Lagrange formulation. Position, trajectory and contact force control schemes are designed based on the inverse kinematic model and on the deflection feedback. The development of a vision system for measuring the deviation in the position of the end effector due to the joint deflection leads to the definition of the Cartesian deflection and the design of force controllers based on this signal, considering a virtually equivalent Cartesian robotic manipulator.

The kinematic and dynamic models of the flexible link long reach manipulator (fixed base) and the passive pendulum aerial manipulators (single and dual arm) were also analysed, where the main difference with respect to the conventional configuration, where the arms are attached at the base of the aerial platform, is the introduction of a flexible link dynamics and the passive joint that prevents the transmission of torques to the multirotor base in the pitch angle. A general control scheme for the compound is proposed, including a force-position controller based on Cartesian deflection which is applied to the compliant arm installed at the tip of the long reach link.

Chapter 5 – Experimental results with compliant joint manipulators (single arm)

This chapter evaluates the single arm manipulators described in Chapter 2, presenting experimental results that validate the models, functionalities and control methods detailed in Chapters 3 and 4. The dynamic behaviour of the single compliant joint and the 2-DOF compliant arm is analysed through frequency characterization and impact response, evidencing the underdamped second order dynamics associated to the spring-lever transmission mechanism and the dynamic coupling between the joints at the resonance frequencies. Passive-active compliance, force/torque/impedance control, contact-based obstacle detection and localization experiments are conducted in test-bench, so these concepts can be illustrated more clearly. The design of the anthropomorphic and compliant finger module is validated through different force-position control and grasping experiments. Finally, the performance of the flexible link, long reach aerial manipulator in passive pendulum configuration is evaluated in test-bench and in outdoor flight tests, showing the take-off and landing manoeuvers, its application to contact-based inspection operations with visual feedback, and the attenuation of oscillations in the passive joint using the compliant arm installed at the tip.

The experimental results presented here are organized in the following way:

5.1. Compliant joint: identification, estimation and control
5.2. Compliant joint arm with compliant finger module
5.3. Passive/active compliance and payload mass estimation
5.4. Control, grasping, and impact detection of finger module
5.5. Long reach aerial manipulator in passive pendulum configuration

5.1. Compliant joint: identification, estimation and control

5.1.1. Frequency characterization

The goal of this experiment is to validate the dynamic model of the compliant joint described in **Section 4.2.1**, generating a sine chirp signal in the range 0 – 8 Hz as position reference for the servo. The frequency response, obtained applying the FFT (Fast Fourier Transform) over the servo position and the deflection signal, is represented in **Figure 5.1**. As it can be seen, the deflection is almost zero for frequencies below the resonance peak at $f = 2.82$ Hz, when the amplitude of the output link oscillation is maximal, reaching the mechanical limits of the deflection. Note also that the angular position of the servo drops abruptly at this frequency, decreasing from the pole given by Equation **(4.2)**, whose bandwidth is $f = 1/(2\pi T_{servo}) = 4.5$ Hz.

The parameters of the compliant joint depicted on the right side of **Figure 5.1** are summarized in **Table 5.1**. The mass, inertia and distance to the CoM of the output link are obtained from the CAD model, whereas the time constants of the servo and the physical joint damping d_p were determined experimentally. The matching between the measured deflection (red line) and the simulation model (green line) given by Equations **(4.2)** – **(4.6)** determines the value of the damping parameter.

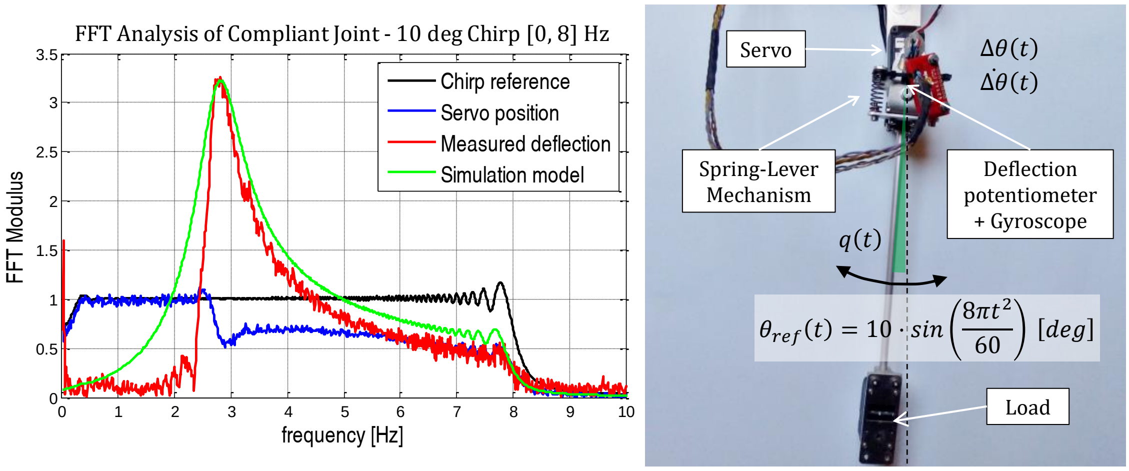

Figure 5.1. Frequency response of the compliant joint actuator to sine chirp signal generated by the servo. Validation of the mass-spring-damper model.

Table 5.1. Parameters of the compliant joint actuator depicted in **Figure 5.1**.

Servo Actuator		Spring-Lever		Output Link	
T_{servo}	$0.035\ s$	k_p	$1.2\ Nm/rad$	J	$0.0044\ kgm^2$
T_{delay}	$0.02\ s$	d_p	$0.02\ Nms/rad$	m	$0.118\ kg$
$\tau_{m,stall}$	$1.17\ Nm$	$\Delta\theta_{max}$	$30\ deg$	l_{CoM}	$0.132\ m$

5.1.2. Virtual variable impedance control

The control method described in **Section 4.2.4** is evaluated here, comparing the desired simulation response with respect to the virtual variable impedance actuator. No torque source is used, instead, the response to the initial condition $q(0) = 90°$ is considered for simplicity in the realization of the experiments. **Figure 5.2** represents the evolution of the output link position, q, for different values of virtual joint damping, d_v, and stiffness, k_v. The gains of the controller in Equation **(4.13)** were tuned experimentally for both use cases, with the values indicated in **Table 5.2**.

Table 5.2. Proportional, integral and derivative constants used in the virtual variable impedance controller.

Experiment	$K_p\ [rad/Nm]$	$K_i\ \ [rad/Nms]$	$K_d\ \ [rads/Nm]$
Variable damping	2.4	278.6	0.24
Variable stiffness	0.4	15.9	0.08

The control rate was set to 50 Hz, which is in practice the recommended value for preventing packet loss without exceeding the maximum read rate of the servo. A gyroscope attached to the output link was essential for obtaining these results, as it compensates the noise of the deflection signal. As can be seen in **Figure 5.2**, the results of the experiments with the virtual variable impedance actuator are similar to the simulation, with very close values of overshoot and slightly larger rise times.

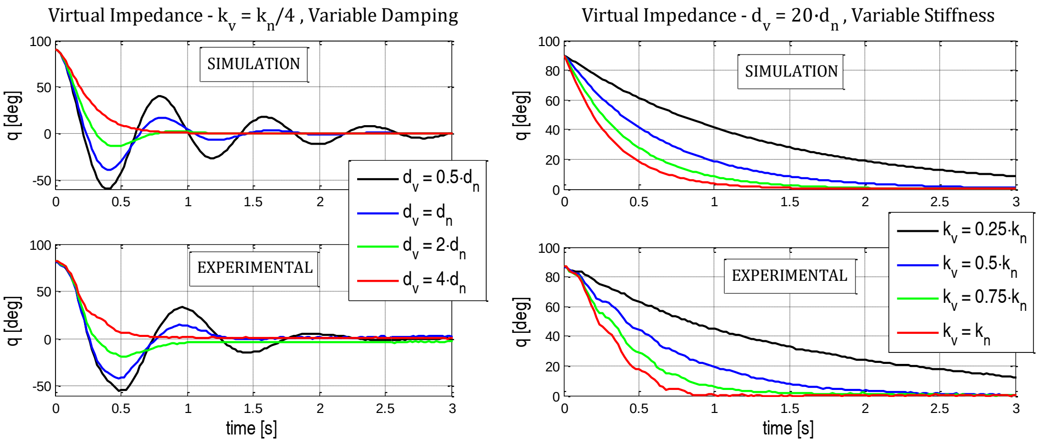

Figure 5.2. Output link angular position for initial condition $q(0) = 90$ deg: variable damping for $k_v = k_n/4$ (left), and variable stiffness for $d_v = 20 \cdot d_n$ (right). Simulated desired response (up) and experimental (down).

5.2. Compliant joint arm with compliant finger module

5.2.1. Frequency characterization of 2-DOF compliant joint arm

The frequency behaviour of a 2-DOF compliant joint arm with joint stiffness $k_1 = 0.94$ Nm/rad and $k_2 = 1.3$ Nm/rad, and 250 mm forearm/upper arm link lengths was evaluated experimentally. **Figure 5.3** shows the arm employed along with the FFT of the deflection measurement of the elbow (green) and shoulder (blue) joints when the corresponding servos are excited separately. The most relevant effect is the dynamic coupling between the compliant joints. In the left side, the elbow servo is excited with a 10° amplitude sine chirp signal in the range 0 – 10 Hz, inducing an oscillation in the shoulder at the resonance frequency f = 1.66 Hz. The same effect can be observed when the shoulder joint is excited. The resonance frequency of each joint is determined by its stiffness and the inertia of the output link. As expected, the first peak corresponds to the shoulder joint since its mass is higher.

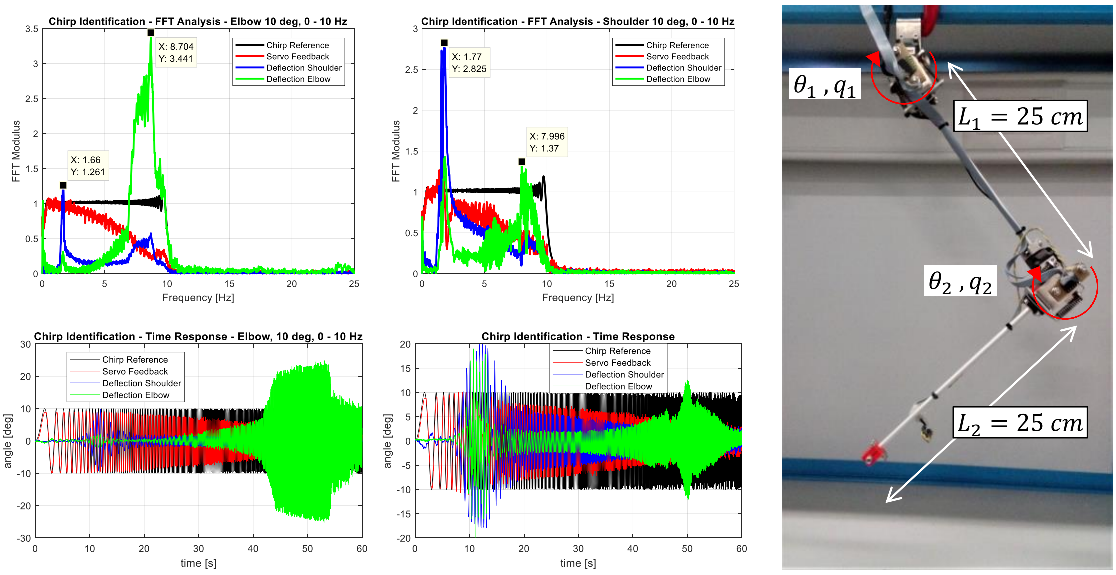

Figure 5.3. Frequency (up) and time (down) response of the shoulder and elbow compliant joints to a 10° amplitude sine chirp signal in the range 0 – 10 Hz. Excitation of the elbow (left) and shoulder (right) joints.

5.2.2. Step response

The dynamic behaviour of the 3-DOF compliant arm depicted on the right side of **Figure 5.4** (see **Section 2.3**) has been also analysed in the time domain through the step signal. In this experiment the servo actuator of the should pitch joint, θ_2, is excited with a 30 deg amplitude step reference, specifying different playtimes, from 0.6 up to 1 s, which correspond to a mean joint speed between 50 deg/s and 30 deg/s. These tests were conducted with the arm fully stretched ($q_3 = 0$), so the mass of the output frame corresponds to the upper arm and forearm links. The embedded servo controller generates a trapezoidal velocity profile (25% acceleration, 50% constant speed, 25% deceleration), ensuring that the reference position is reach in the indicated playtime. The position reference of the servo, its current position, and the deflection angle (measured with a potentiometer integrated in the output frame) are represented on the left side of **Figure 5.4**. As it can be seen, the amplitude of the oscillations in the deflection angle increases with the joint speed due to the inertial terms of the output link.

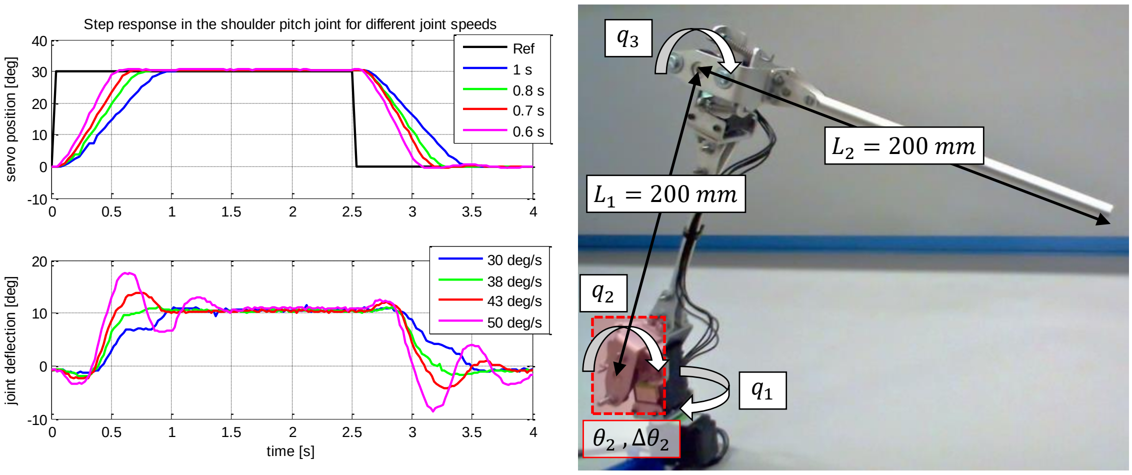

Figure 5.4. Shoulder pitch joint position reference, feedback and deflection angle for different playtimes. The amplitude of the overshoot in the deflection increases as the speed of the servo is higher.

The deflection offset in steady state is caused by the effect of gravity over the output link, and it may be useful for estimating the joint stiffness in the following way:

$$\tau_g = m_{eq} g l_{CoM} sin(\theta_{ref} + \Delta\theta) = k \cdot \Delta\theta \rightarrow k = \frac{m_{eq} g l_{Com} sin(\theta_{ref} + \Delta\theta)}{\Delta\theta} \tag{5.1}$$

Here τ_g is the torque due to gravity acting over the joint, m_{eq} and l_{CoM} are the equivalent punctual mass and its distance to the rotation axis, $\Delta\theta$ is the deflection of the compliant joint with stiffness k, θ_{ref} is the servo position reference, and g is the gravity constant. The parameters corresponding to **Figure 5.4** are $m_{eq} = 0.2$ kg, $l_{CoM} = 0.185$ m, $\theta_{ref} = 30$ deg, and $\Delta\theta = 10$ deg, obtaining finally that $k = 1.34$ Nm/rad.

5.2.3. Contact force control in fixed base test-bench

The control scheme proposed in **Section 4.3.4** is applied here to control the contact force at the wrist point of the 3-DOF compliant arm described in **Section 2.3.1**, introducing a vertical contact surface at 18 cm from the base of the arm, which is initially stretched ($q_1 = q_2 = q_3 = 0$). The experimental setup is depicted in the right side of **Figure 5.5**. The collision with the surface occurs when the elbow pitch servo moves from $\theta_3 = 0$ to $\theta_3 = 90$ deg and $q_3 \approx 90$ deg. The desired contact force in the X-axis varies from 0.5 N up to 1.5 N, while the force in the Z-axis is set to zero. **Figure 5.5**-left shows the reference and the estimated force in both axes along with the deflection angles in the elbow pitch and in the shoulder pitch joints.

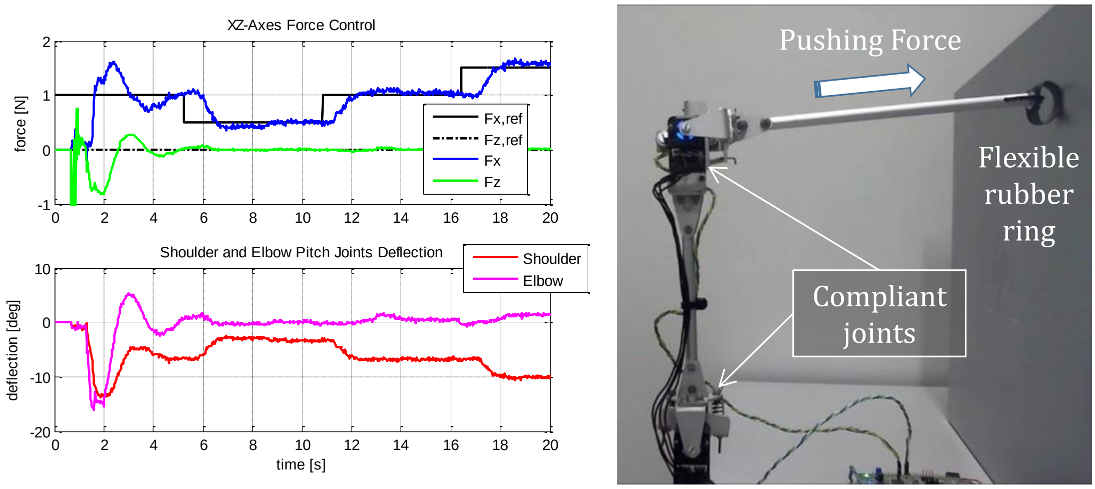

Figure 5.5. XZ-axes force reference and estimation (up, left) and joints deflection (bottom, left) when the wrist point is in contact with the surface. The collision occurs at t = 0.7 s with $q_2 \approx 0$ and $q_3 \approx 90$ [deg].

The compliant arm prototype shown in **Figure 5.5** employed the Murata SV01A potentiometers to measure the joint deflection. However, these devices were affected by clearance, alignment errors, and noise in the voltage signal (the sensitivity was 10 mV/deg) that limited the performance of the force controller. This motivated the use of magnetic encoders in the prototype depicted in **Figure 5.3**, as these sensors do not require mechanical contact to measure the deflection angle between the servo shaft and the output link, and because they provide high resolution measurements (14-bit) at high update rates (up to 1 kHz). **Figure 5.6** shows the estimated force/torque when the reference force is ±1 N in the XZ axes, evidencing the improvement with respect to the results presented in **Figure 5.5**.

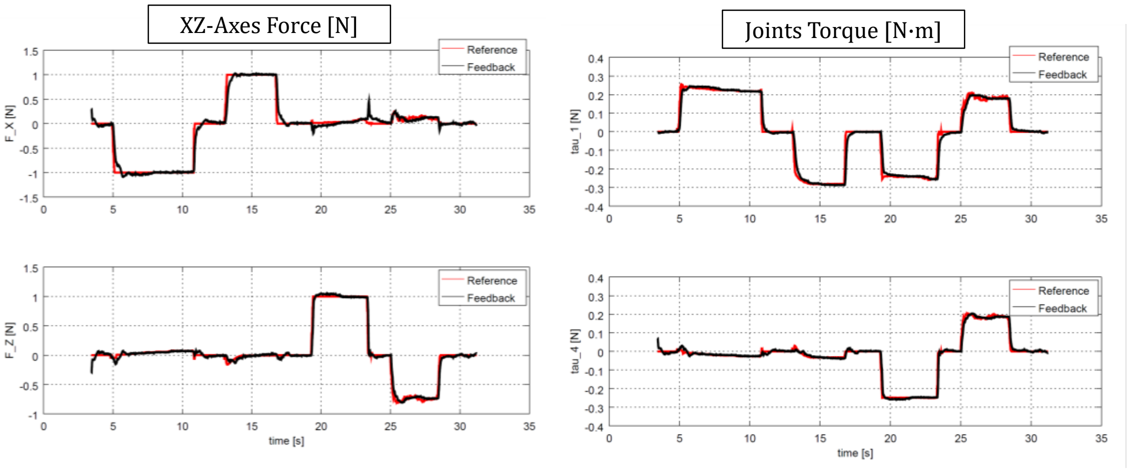

Figure 5.6. Force (left) and torque (right) reference and feedback estimated from the joint deflection measured with the magnetic encoders.

5.2.4. Obstacle localization based on soft-collision detection with compliant finger module

In this experiment, the compliant finger module described in **Section 2.4** was attached at the tip of the forearm link of the 3-DOF compliant arm (see **Section 2.3.2**), so the distance from the elbow joint to the MCP joint is 20 cm. The arm, at fixed base, executed a 180 deg scan around the shoulder yaw joint, increasing the scan radius from 20 cm up to 35 cm in the XY plane. The collision detection threshold for the compliant MCP joint was set to 15 deg. The position of the tool center point (the MCP joint) during the scan has been represented in **Figure 5.7**, where the black marks correspond to those points in which finger deflection exceeds the detection threshold.

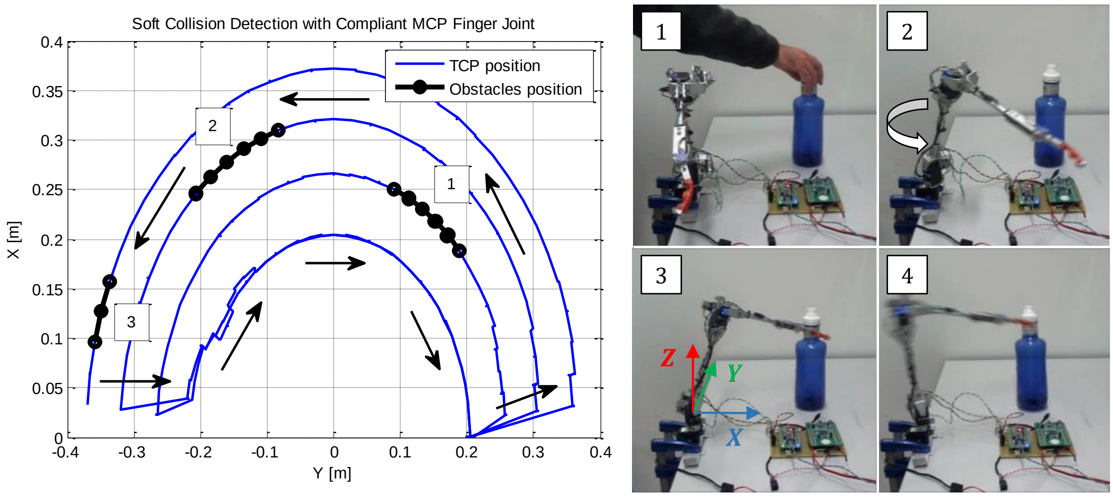

Figure 5.7. Tool Center Point (TCP) position w.r.t. arm base (blue), and collision points (black) on the XY-plane. The position of the obstacle was moved from position 1 to position 3 during the experiment. In 4, the arm retracts once the collision is detected by the finger module.

5.3. Passive/active compliance and payload mass estimation

This section shows the functionalities of the first prototype of lightweight and compliant arm developed by the author, designed following a bioinspired approach with the intention to replicate the size, kinematics, mass distribution, and features of the human arm in an aerial manipulation robot.

5.3.1. Kinematics and rotation range

As detailed in **Section 2.3.3**, this prototype employs a linear actuator as biceps to lift the forearm link around the elbow joint, introducing a pair of extension springs as elastic tendons. The hand (non-actuated) can be oriented in two axis, roll and pitch. The first one corresponds to the direction along the forearm link, as in the human arm. The motion of the joints can be identified in **Figure 5.8**. The rotation range of the elbow joint is between 0 and 135 degree, approximately, although the upper limit decreases with the payload mass (see next subsection), whereas the range of both wrist joints is ±90 degrees.

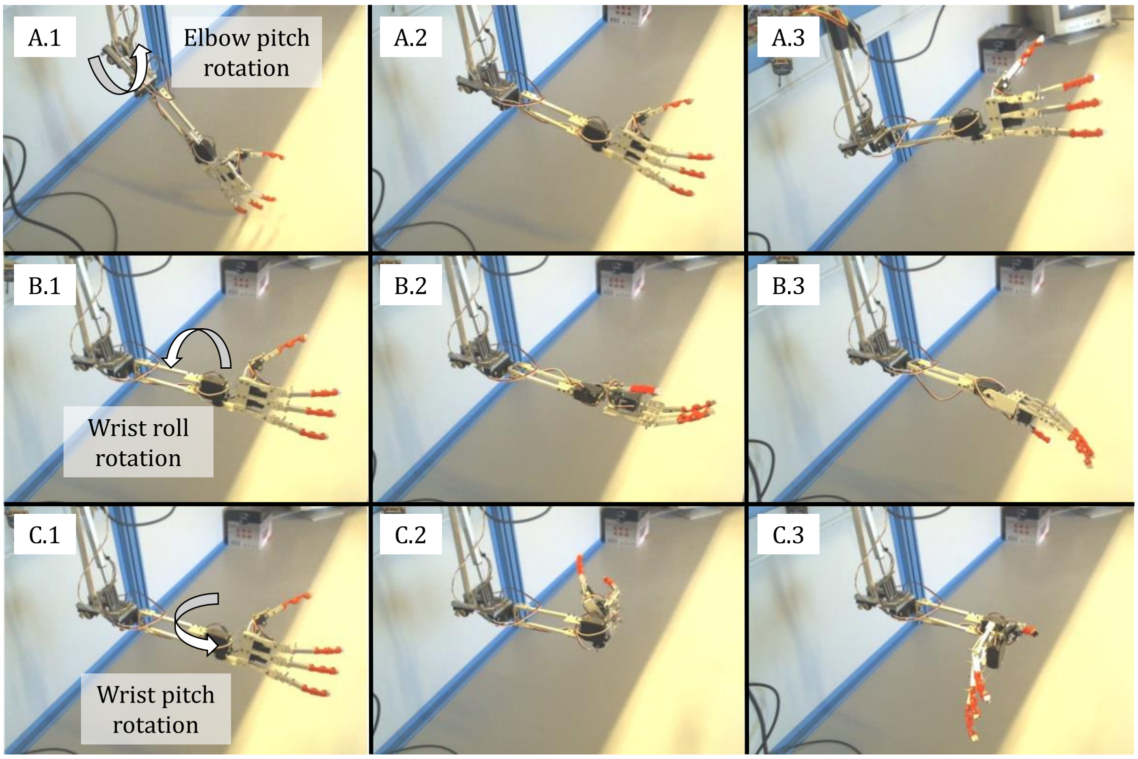

Figure 5.8. Rotation of the compliant arm in its three joints: elbow (compliant, A.1 – A.3), wrist roll (stiff, B.1 – B.3), and wrist pitch (stiff, C.1 – C.3).

5.3.2. Influence of payload mass over compliant elbow joint

The maximum rotation angle for the elbow joint when there is no payload is around 135 degrees. However, as the payload mass increases, the elongation of the extension springs connecting the linear actuator with the forearm also increases, reducing the reachable joint position. This is evidenced in **Figure 5.9**, where it has been represented the linear servo position along with the corresponding joint position for different payload masses. Although it results convenient for the extension springs to have a low stiffness constant in order to obtain a higher accuracy in the mass estimation, it is also desirable that the elongation of the spring remains as low as possible to maximize the rotation range.

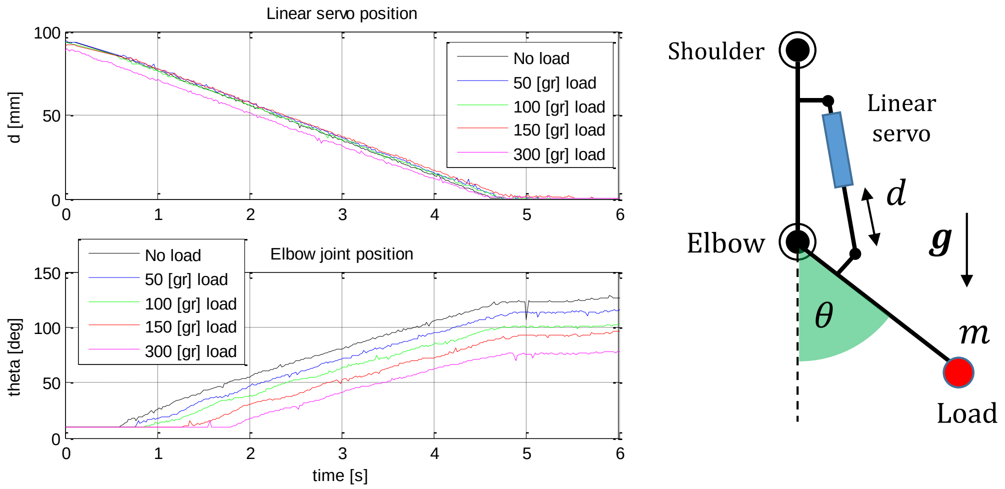

Figure 5.9. Evolution of linear servo position and elbow joint position for different payloads.

The dead zone in the elbow joint is due to the effect of gravity over the elastic tendons (springs), being more evident for higher values of the payload. Although the linear servo is acting, the elbow joint will not start to move until the equilibrium of forces between gravity and the tensile force of the extension spring is reached. It is also interesting to note that the speed of the Firgelli linear servo, ~2 $cm \cdot s^{-1}$, is not significantly affected by the payload mass attached at the wrist point, as deduced from the upper part of **Figure 5.9**, so the payload to weight ratio of the arm is above 1. In relation with this, it is possible to vary in an easy way the maximum payload or well the maximum rotation range/speed of the arm simply displacing the support point of the springs in the forearm, that is, the lever length ratio.

5.3.3. Static and dynamic payload mass estimation

The experiments for payload mass estimation have been carried out in both static and dynamic conditions, that is, with the elbow joint staying at fixed position and moving during the measurement process. **Table 5.3** summarizes the results for the first case for different payloads and joint positions. The value obtained when there is no load (offset) corresponds to the estimation of the load associated to the forearm itself, which is taken as offset and subtracted from the rest of estimations. The content of the table has been graphically represented in **Figure 5.10**, which represents the estimated values with respect the real one. There is a singularity in the estimation for joint angles close to zero. When the 300 grams mass is attached at the wrist point with a reference elbow joint angle of 45 deg (blue line in **Figure 5.10**), the elongation of the springs makes the joint angle drop below 20 deg, so the estimation error is significantly high. This problem could be solved with an additional mass estimator in the forearm or in wrist. **Figure 5.11** shows the evolution of the estimated payload mass when the elbow joint is moving. A 120 g offset corresponding to forearm weight is subtracted. The estimation becomes almost constant when joint position is above 45 degrees. For angles close to zero (extended arm), the accuracy of the results is significantly affected by the singularity mentioned before.

Table 5.3. Static payload mass estimation for different elbow joint angles.

Payload mass [gr]	**Elbow Joint Angle**		
	45 [deg]	**90 [deg]**	**135 [deg]**
Offset	120	73	59
50	33	66	28
100	97	118	89
150	143	172	135
300	494	302	290

5.3.4. Passive compliance vs active compliance

In the following experiment, it is assumed that the arm is free of load and the elbow joint rotates from 0 (completely stretched) to 135 degrees (completely retracted). At a certain instant, the forearm is blocked, but the linear servo keeps contracting, which causes the elongation of the springs. If the forearm is suddenly released, the springs will try to reduce the excess of elastic potential energy at a high rate, inducing high accelerations in the elbow joint and, possibly, a hard impact of the forearm against the actuator itself. This situation has been experimentally verified, showing the results in **Figure 5.12**. As seen in the lower part of the figure, the elongation of the springs increases as soon as the forearm is blocked, and it takes around 0.4 s to recovery its normal position once the forearm is released. What is more, there is an interval when the estimated spring elongation is negative, which means that the tendon became slack.

The idea of active compliance is applied here to reduce the energy stored in the springs at a lower rate, preventing high accelerations in the forearm. This can be achieved increasing the stroke of the linear actuator until spring elongation becomes zero. The control method described in **Section 3.3** was tested, with the results shown in **Figure 5.13**. An elongation threshold of 25 mm was specified for the collision detection. The elbow joint is blocked at $t = 1.25$ s, which is detected at $t = 1.7$ s. At $t = 1.9$ s the linear actuator reacts, extending the stroke until $t = 3$ s, when spring elongation returns to its nominal value. The elongation threshold was empirically determined as midpoint between the maximum spring elongation and the offset value due to the weight of the forearm.

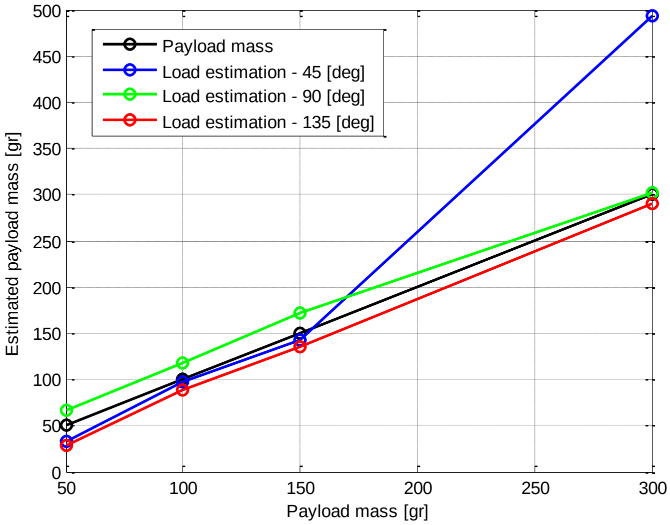

Figure 5.10. Estimated payload mass for different elbow joint angles in static conditions.

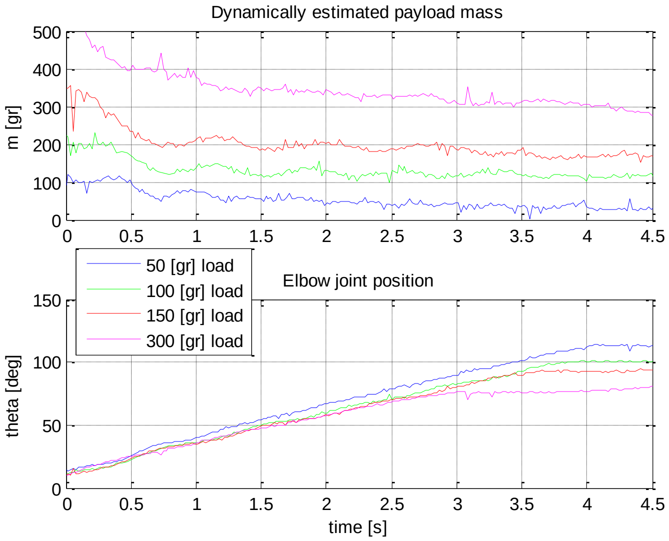

Figure 5.11. Influence of elbow joint position over payload estimation for different payloads. The accuracy in the estimation is lower for joint angles close to zero, remaining almost constant for angles above 45 deg.

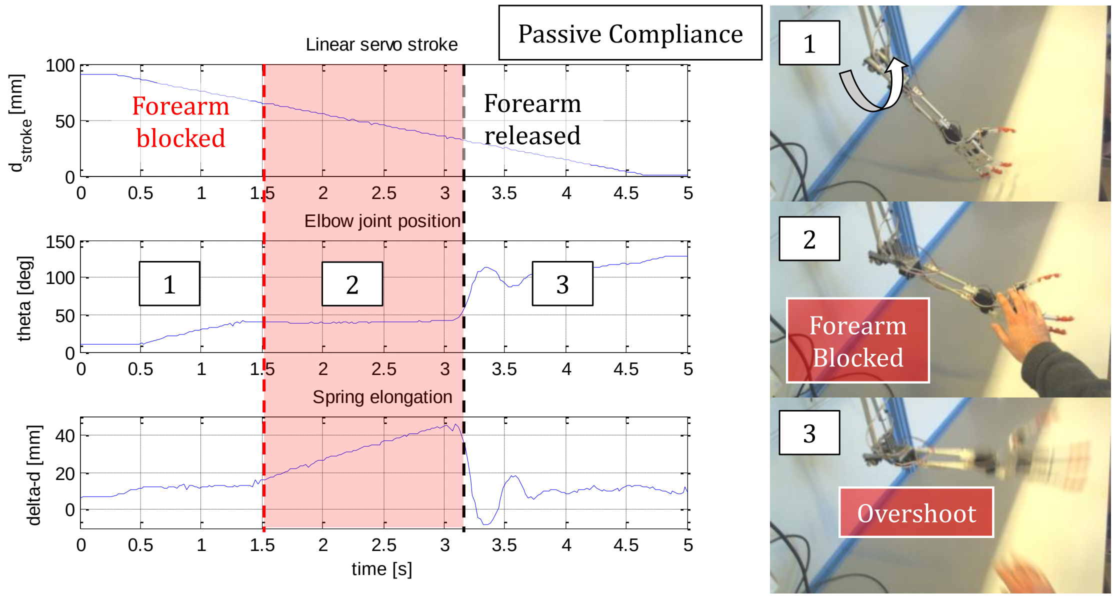

Figure 5.12. Response of elbow joint without active compliance. The forearm is blocked at t = 1.5 s while the linear servo keeps moving, being released at 3.1 s. The extension springs recover their normal elongation at t = 3.7 s.

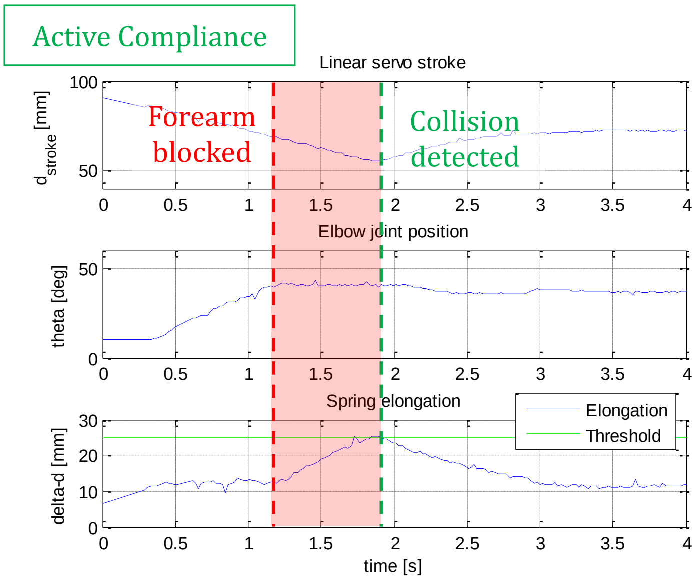

Figure 5.13. Response of the elbow joint with active compliance. The forearm is blocked at t = 1.2 s while the linear servo keeps moving. The collision is detected at t = 1.9 s when the springs elongation exceeds the 25 mm threshold. The springs have released the excess of energy at t = 3 s.

5.4. Control, grasping, and detection with compliant finger module

This section validates the position-force control, grasping, and collision detection capabilities of the anthropomorphic, compliant and lightweight finger module described in **Section 2.4**.

5.4.1. Position and force control

The control scheme described in **Section 4.4.3** is applied here to control the flexion and extension motion of the finger, rolling-up the nylon wire in the reel attached to the motor. **Figure 5.14** represents the reference and feedback position of the MCP joint along with the duty cycle of the PWM signal that is taken as input by the H-bridge. The proportional gain of the controller is set to $K_p = 2.5$ V^{-1}, saturating the PWM signal to the 80%, with a dead zone of 1%. Finger flexion is achieved generating a tensile force with the motor, whereas the extension motion is produced by the flexible element of the joints (the extension spring in the MCP joint, and the heat shrink tube in the PIP and DIP joints). At $t = 17$ s, the reference is set to 200 deg, which is an unreachable position as the proximal phalange is mechanically blocked at 90 deg. This causes the rotation of the PIP and DIP joints, whose stiffness is higher. The motion sequence in full finger flexion can be seen in **Figure 5.15**.

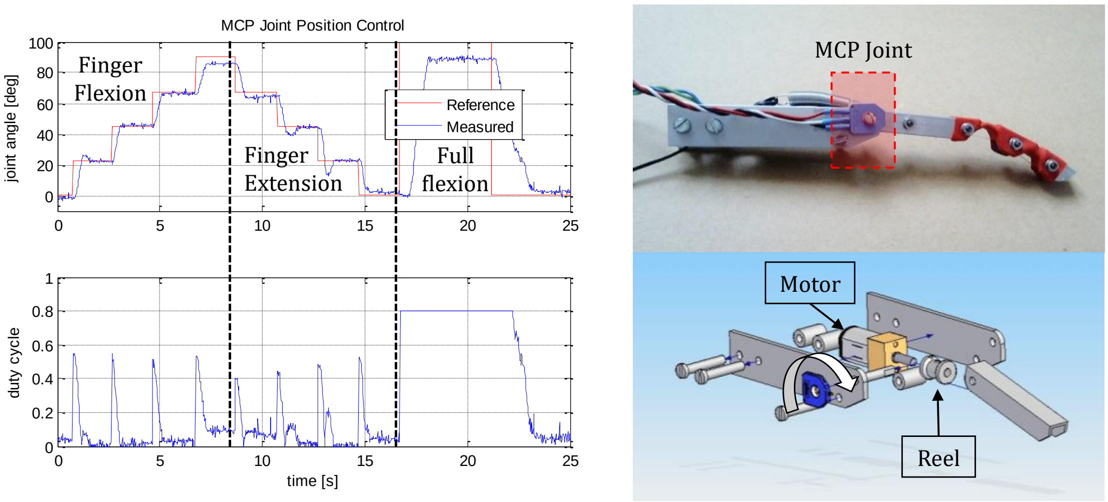

Figure 5.14. MCP joint position control and PWM signal. Stair reference for flexion and extension. The proportional gain of the controller is set to $K_p = 2.5$, and the PWM signal is saturated to 80%.

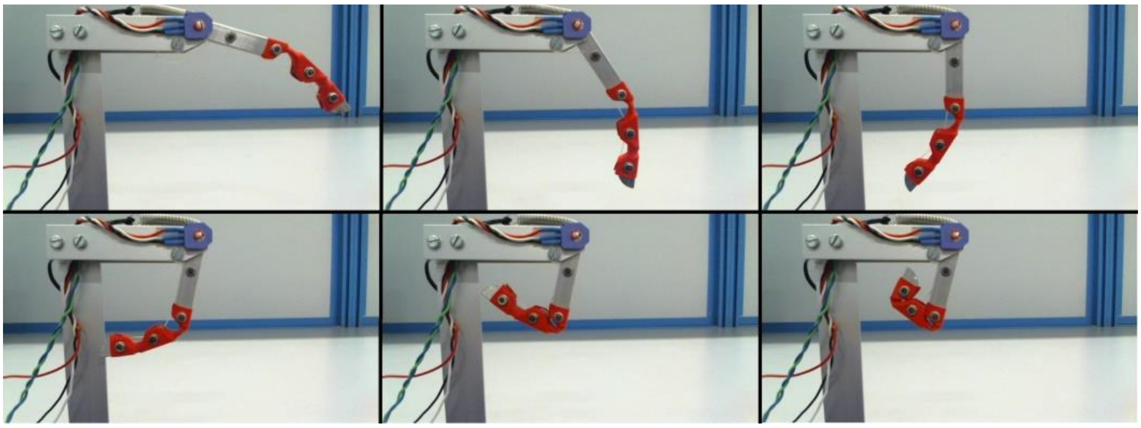

Figure 5.15. Finger flexion motion performed by the three joints driven by the single DOF.

Section 4.4.1 showed that the tensile force in the tendon is proportional to the duty cycle in the H-bridge, which is related with the torque in the MCP joint through Equation **(4.26)**. The position controller described in **Section 4.4.3** introduces a saturation block after the proportional gain with a tuneable parameter PWM_{max} that regulates the grasping force of the finger. **Figure 5.16** represents the joint position and torque when the finger is grasping a flexible rubber cup for an unreachable goal position of 200 deg. Different saturation thresholds from 30% up to 80% are considered. **Figure 5.17** shows how the rubber cup is deformed as the threshold increases.

5.4.2. Object grasping

The finger module is capable of grasping objects of different shapes and forms in a stable way by itself, without requiring any other fingers. **Figure 5.18** shows four examples in which the finger module is grasping a bottle, a screw driver, a plier and a ball. This is so thanks to its three compliant and underactuated joints that adapt the finger bones to the contour of the object, exerting a constant torque on the three joints when the motor is stalled.

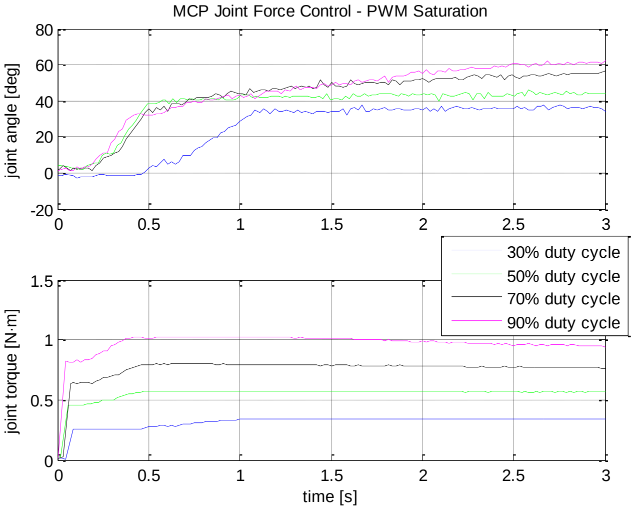

Figure 5.16. MCP joint position and torque in force control mode for different PWM saturation values.

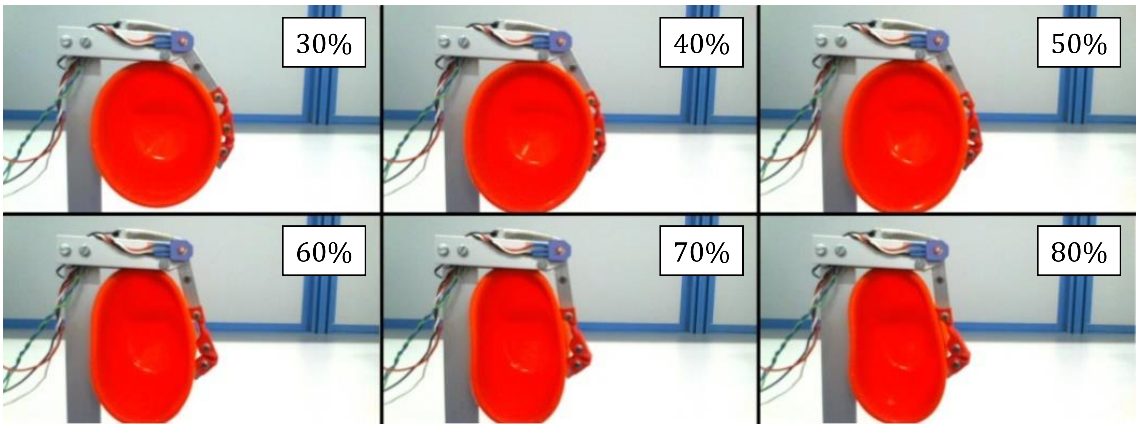

Figure 5.17. Regulation of grasping force adjusting the saturation of the PWM signal. The finger module is grasping a deformable rubber cup.

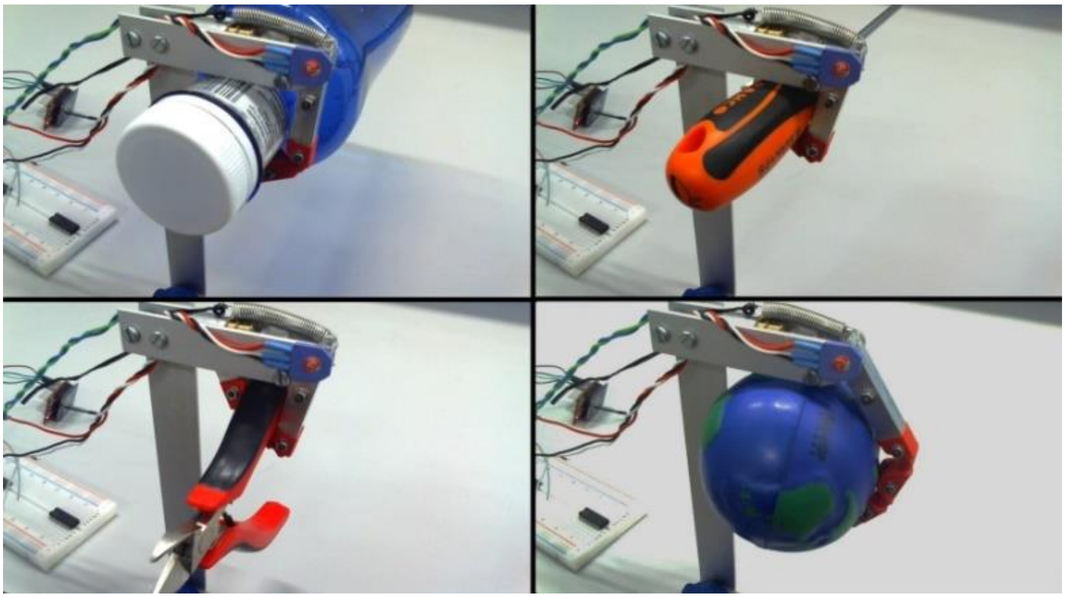

Figure 5.18. Stable grasping of different objects: bottle, screwdriver, pliers and ball.

5.4.3. Impact and collision detection

The low stiffness of the MCP joint can be exploited for detecting and reacting against collisions in the manipulator, in a similar way humans do when they move around in a dark room. This may be especially useful when the aerial robot is navigating in narrow scenarios with close obstacles that cannot be detected with vision or range sensors. For this purpose, the compliant finger module would remain extended and the MCP joint position controller disabled. Any impact over the finger will cause a deviation in joint position measured by the potentiometer that can be easily detected defining a constant threshold. **Figure 5.19** shows the response of the MCP joint when the finger is hit with a hammer (between $t = 0$ and $t = 5$ s), and when it is flexed due to a frontal collision (from $t = 6$ s). Two thresholds, ±20 deg amplitude, are considered in such a way that when the measured joint angle exceeds any of them, a collision is detected. This feature was used in the soft-collision detection experiment described in **Section 5.2.4**

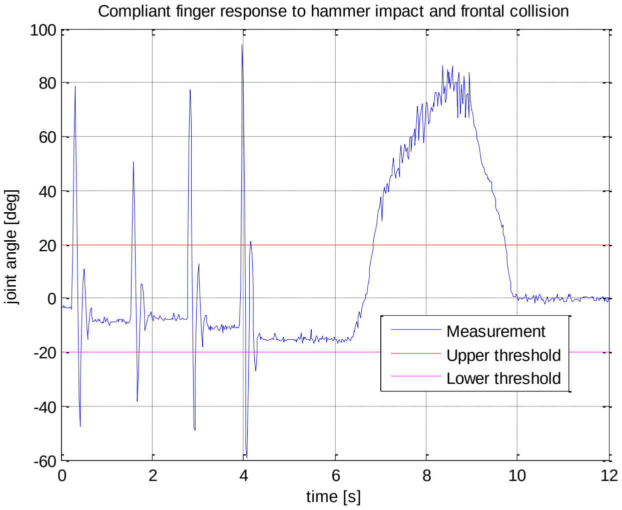

Figure 5.19. MCP joint response to hammer impact and to frontal collision, detected when the measured joint angle exceeds the upper or lower threshold.

5.5. Long reach aerial manipulator in passive pendulum configuration

This section evaluates in outdoor flight tests the long reach aerial manipulator prototype described in **Section 2.7**. This is intended to perform contact-based inspection operations, being equipped with deflection potentiometers for accurate force estimation and control, an eye-in-hand camera for visual inspection, and a range sensor for determining the distance to the contact point. Unlike the flexible link, long reach manipulator with lightweight dual arm described in **Section 2.7.1**, this prototype introduces a passive joint that allows the free rotation of the long reach link with respect to the base of the aerial platform (pendulum configuration).

5.5.1. Take-off and landing manoeuvres

The aim of this experiment is to demonstrate that the long reach aerial manipulator is capable to perform the take-off and landing operations without the need of a platform. **Figure 5.20** shows a sequence of images corresponding to the landing operation taken from the video. A C-shaped aluminium frame structure is attached at the back of the compliant arm for preventing that the servos or the joints are damaged during the manoeuvre. The evolution of the UAV position, velocity, attitude, and the rotation of the passive joint can be followed in **Figure 5.21**. The LRM lays initially in the floor almost horizontally, until the multirotor takes-off at t = 14 s. At t = 19 s it is on flight at two meters height. The take-off operation causes a 20 amplitude oscillation in the passive joint until the tip of the LRM hits the floor at t = 40, when the UAV is going to land. It was observed that the deflection of the flexible link provides a certain level of compliance in the vertical axis.

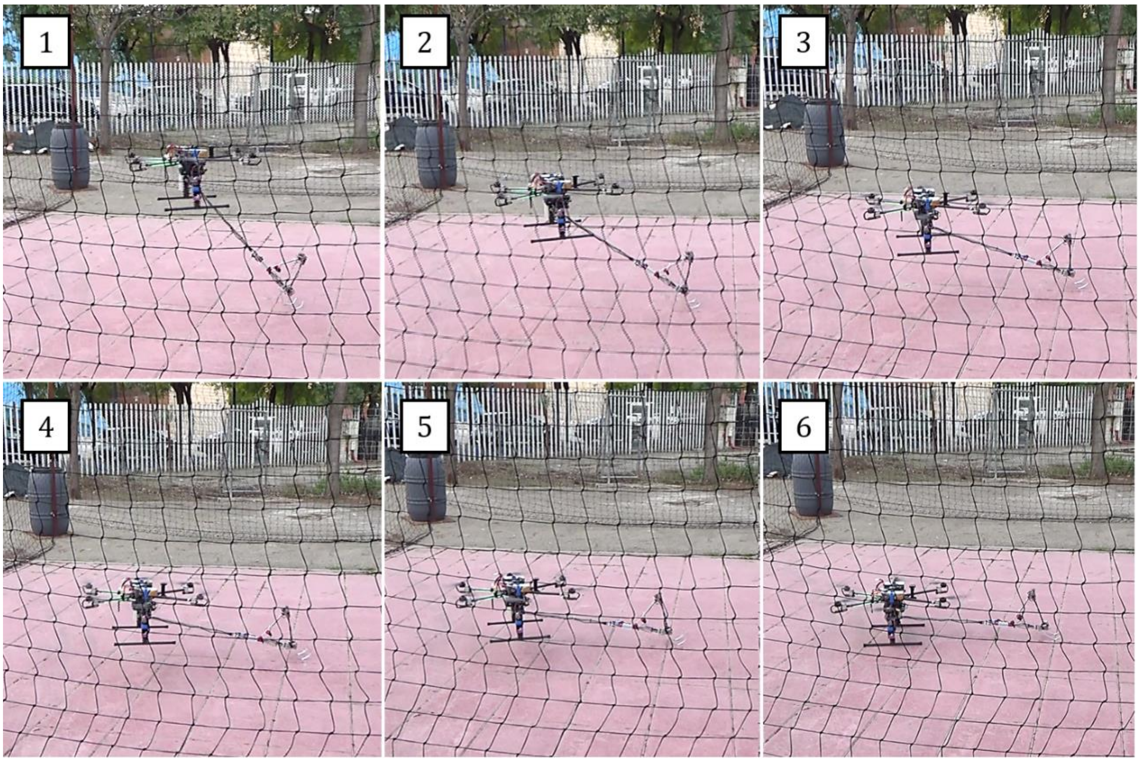

Figure 5.20. Sequence of images corresponding to the landing operation.

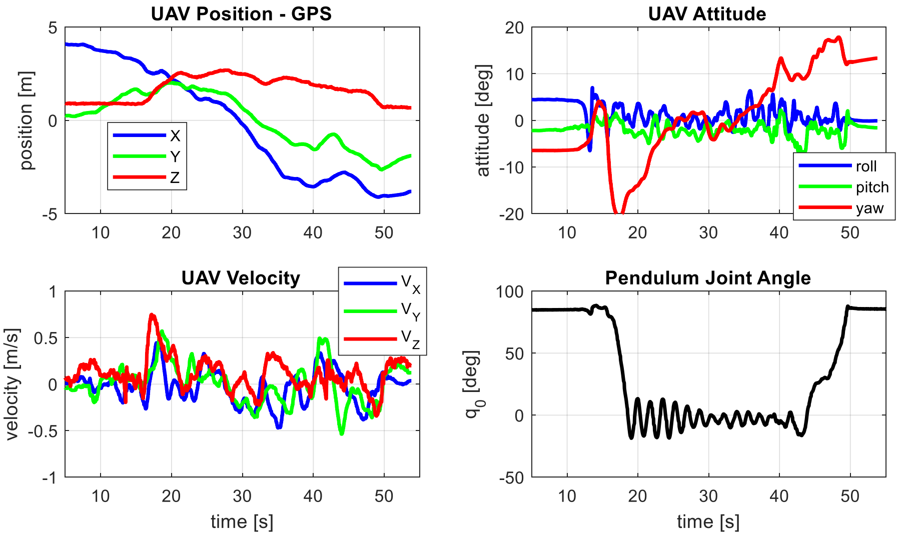

Figure 5.21. Multirotor position, velocity, attitude, and pendulum joint angle during the take-off and landing.

5.5.2. Impact response

The goal of this experiment is to demonstrate that the long reach aerial manipulator is tolerant to impacts thanks to the passive joint of the pendulum. This simple mechanism brings two benefits. On the one hand, the external wrenches exerted over the manipulator are not introduced as a torque to the base of the aerial platform, but as a force, so the propellers are less exposed to overloads. The pendulum acts as energy storage component (see Equations **(4.89)** – **(4.90)**), in such a way that the energy associated to an impact in the aerial manipulator will be stored initially as potential energy by the manipulator through the rotation of the passive joint and the deflection of the compliant joints, transformed later into kinetic energy through the acceleration of the links, and finally dissipated by means of heat in the bearings. **Figure 5.22** represents the position, velocity and orientation of the long reach aerial manipulator along with the rotation angle of the pendulum when this hits an obstacle at t = 160 s, while the aerial platform is moving at 2 m/s.

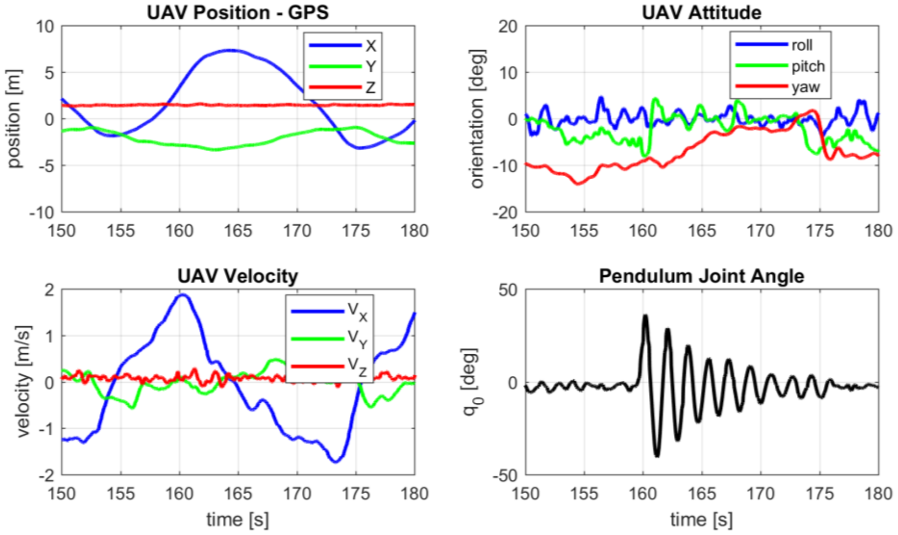

Figure 5.22. Multirotor position, velocity, attitude, and pendulum rotation when the tip of the long reach link hits an obstacle at t = 160 s while the hexarotor moves at 2 m/s, causing a 10° oscillation in the pitch angle.

The impact causes an oscillation of 36 degrees amplitude in the passive joint, which corresponds to a gravity potential energy of 1.3 J, known the mass of the system. The oscillation remains 15 s, until it almost disappears. It is interesting to observe that the inertia of the aerial platform and the damping of the airflow tend to attenuate faster this oscillation than in the test-bench (**Figure 5.25**). The effect of the impact over the attitude controller can be seen in the **Figure 5.22** as 10° jump in the pitch angle at t = 160 s. Note also that the pilot reduces the velocity of the aerial platform just after the impact.

5.5.3. Visual inspection with arm teleoperation

In this experiment, the compliant arm is tele-operated using the wearable exoskeleton interface described in **Section 2.7.2.2** and the visual display shown in **Figure 5.23**. In this task, the operator has to approach and touch the bottom of a PVC pipe. The display shows a model of the long reach manipulator, including the joint angles and the distance measured with the range sensor. **Figure 5.24** represents the evolution of the signals during the operation. The difference between the reference and the feedback of the compliant arm is due to the deflection of the compliant joints. The maximum distance measured by the range sensor is around 50 cm, forcing its measurement to zero if the target object is out of range.

It was found during the realization of the experiment that the visual representation of the LRM in the interface depicted in **Figure 5.23** contributes to improve the situational awareness of the operator during the execution of the task, since it does not result intuitive to guide the motion of the TCP using only the feedback provided by the eye-in-hand camera. The use of the exoskeleton interface also allows to replicate the motions of the operator in a more intuitive and comfortable way.

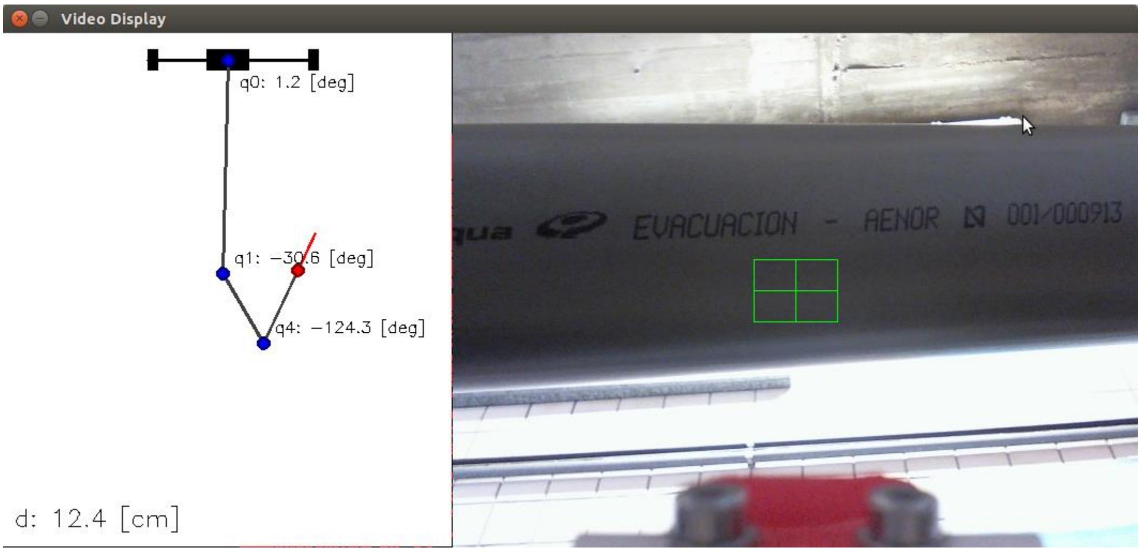

Figure 5.23. Visual display shown to the operator during the inspection task. The red line at the tip of the manipulator represents the distance to the pipe.

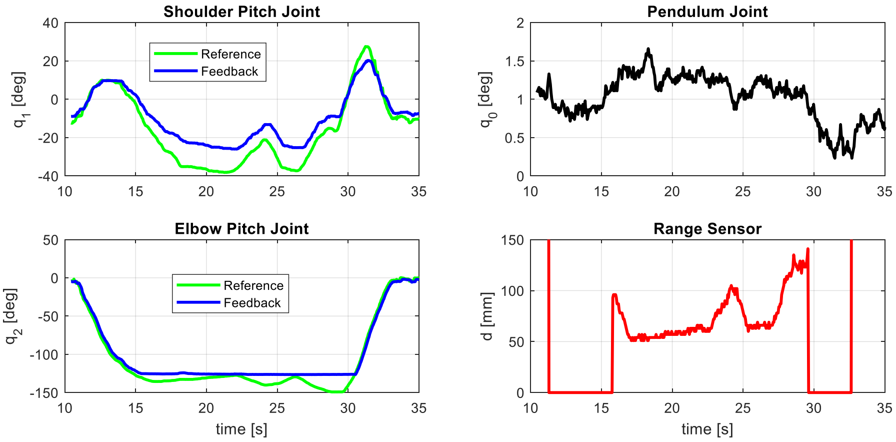

Figure 5.24. Joint position reference and feedback of the compliant arm (left), pendulum rotation (right, up) and range sensor (right, down) during the visual inspection of a pipe using the exoskeleton interface in test-bench.

5.5.4. Contact force control

This experiment considers the contact force control method described in **Section 4.7.2.4** based on Cartesian stiffness, employing magnetic encoders to measure the deflection of the compliant joints and estimating the Cartesian deflection from the forward kinematic model (Equation **(4.70)**) instead of using a vision sensor. In this test, the manipulator applies a 1 N pushing force in the X and Z axes consecutively, keeping the base of the pendulum fixed. **Figure 5.25** shows the force reference and estimation along with the joint variables and the evolution of the Cartesian stiffness matrix defined in Equation **(4.92)**. Two effects can be also observed: 1) the variation of the Cartesian stiffness matrix the servo angular position, as $\boldsymbol{K_C}$ depends on the Jacobian, and 2) the recoil of the pendulum when the arm applies the pushing force. The force controller block in **Figure 4.30** is a PID with $K_p = 25\ mm/N$, $K_d = 0.2\ mms/N$, and $K_i = 30\ mm/Ns$.

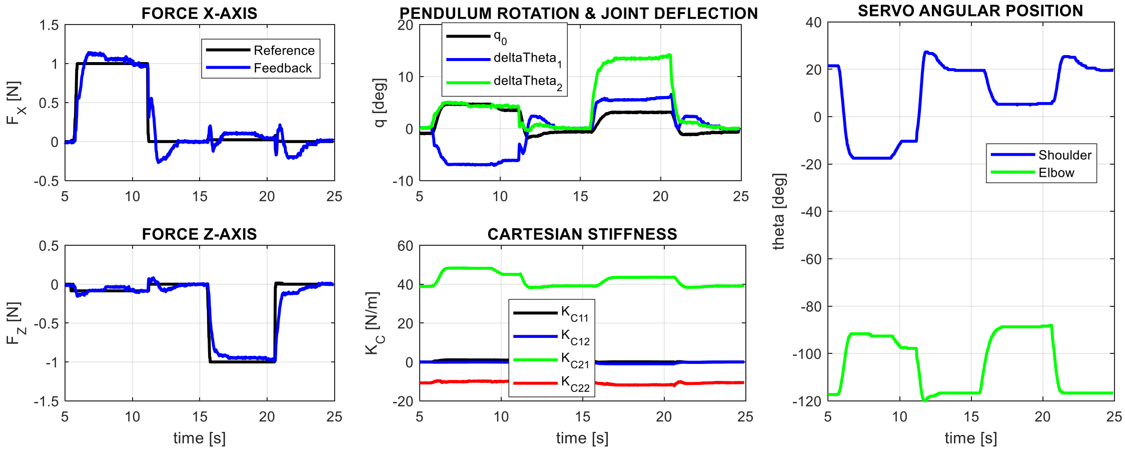

Figure 5.25 Contact force (left), joint deflection and servo angular position (middle) and Cartesian stiffness (right).

5.5.5. Attenuation of oscillations in passive joint pendulum

The arm attached at the tip of the long reach link can contribute to attenuate the oscillations in the passive joint of pendulum, caused by impacts or accelerations of the aerial platform. Since the mass/inertia of the LRM is much higher than the mass/inertia of the compliant arm, it is expected that the arm requires more than one period to completely cancel the oscillation of the pendulum. This can be also interpreted in terms of kinetic and potential energy obtained from Equations **(4.89) (4.90)**, evaluating its energy within a period.

The vibration suppression method described in **Section 3.7.1** is applied here to attenuate the oscillations in the pendulum. The method consists of determining the maximum amplitude of the oscillation within a semi-period, q_0^{max}, detect the zero cross (that is, the time instant in which the phase of q_0 is zero or π rad), and generate a reaction motion with the shoulder joint with the same phase, in such a way that the reaction force associated to the rotation of q_1 tends to cancel the oscillation of q_0. The amplitude of the reaction motion with the shoulder joint is proportional to the maximum amplitude of q_0, so the reaction tends to decrease. As it can be seen in **Figure 5.26**, the free oscillation of the passive joint corresponds to a sinusoidal of period $T_0 = 2.1\ s$, damping $d_0 = 0.05\ s^{-1}$, and initial amplitude $q_0 = 30\ [deg]$. **Figure 5.26** also evidences that the oscillation is attenuated faster for higher values of this constant, determined empirically. The reaction motion of the servo starts when the zero cross is detected, and it ends when the amplitude of the oscillation is maximum, that is, $T_0/4$ seconds later.

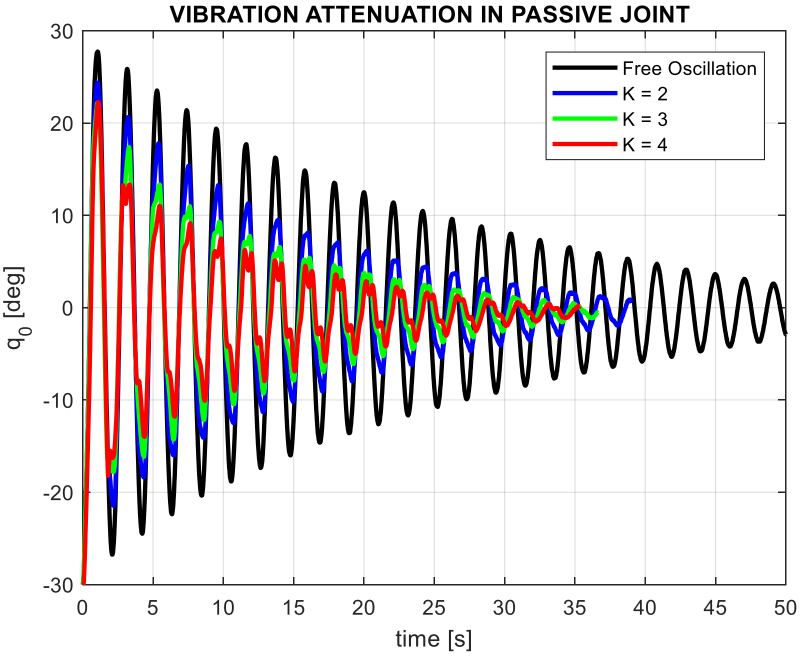

Figure 5.26. Rotation of the passive pendulum: free oscillation (black) and vibration attenuation using the arm with different compensation gains.

5.6. Conclusion

This chapter has presented experimental results that demonstrate the performance of the single arm, lightweight and compliant manipulators developed by the author. The dynamic behaviour of a single compliant joint was firstly evaluated in the frequency domain, identifying a resonance peak in the deflection signal, typical of mass-damper-spring systems. The analysis is extended to a two degree of freedom compliant arm, observing now the dynamic coupling between the joints and the excitation of the respective resonance frequencies. A contact force controller based on joint deflection feedback has been implemented and tested, comparing the results obtained with potentiometers and magnetic encoders. It was also demonstrated that it is possible to control the deflection of a compliant joint arm through the servo position in such a way that the joint shows a desired virtual variable impedance without the need of additional actuators. The 3-DOF compliant arm was equipped with a compliant and lightweight anthropomorphic finger module which extends its functionalities, allowing object grasping, soft-collision detection and contact-based obstacle localization. The differences between passive and active compliance features are evidenced in a human-like arm with compliant elbow joint, evaluating the estimation of the weight of grasped objects from the deflection of the springs. Several test-bench and outdoor flight tests have been carried out with the long reach aerial manipulator in passive pendulum configuration. The take-off and landing manoeuvres were firstly evaluated through a sequence of images from the video, representing the evolution of the position and attitude of the aerial platform along with the rotation angle of the passive joint. The response to impact evidences the dissipation of the energy absorbed by the pendulum due to the joint friction without affecting significantly the attitude controller. The compliant joint arm installed at the tip of the long reach link has been applied in inspection operations with visual feedback and contact force control, validating the method for attenuating the undesired oscillations in the passive joint.

Chapter 6 – Experimental results with dual arm aerial manipulators

This chapter is focused on the experimental evaluation of the lightweight and compliant dual arm prototypes described in Section 2.5 and 2.6, which have been integrated in three different commercial hexarotor platforms and tested in both indoors and outdoors. This includes the usual configuration with the arms attached at the base of the multirotor, as well as the flexible long reach link and the passive pendulum configurations. The performance of the position-force controller of the dual arm system is evaluated in test bench in terms of accuracy and repeatability, identifying also the dynamic behaviour of the compliant arms through frequency and impact response. The low weight and inertia features are validated analysing the influence of arms motion over the stability of the aerial platform, demonstrating bimanual grasping and contact force control on flight. These two functionalities are applied later in two inspection tasks: grasping and installation of pipe inspection tool, and installation of sensor device on pipe. A camera head is employed for visual servoing tasks and for the estimation and control of the contact forces in the Cartesian space. Several test-bench experiments have been conducted with the long reach manipulators, including vibration suppression, contact force control, and obstacle detection and localization, showing later their application on flight in two tasks.

The experimental results presented here are organized as follows:

6.1. Lightweight and human size dual arm aerial manipulator
6.2. Flexible long reach link with lightweight dual arm
6.3. Anthropomorphic, compliant and lightweight dual arm
6.4. Long reach aerial manipulator with compliant dual arm

6.1. Lightweight and human size dual arm aerial manipulator

Three types of experiments have been conducted for evaluating the performance of the human size and lightweight dual arm manipulator described in **Section 2.5**. The trajectory generation method presented on **Section 4.5.3.2** is applied for tracking a circular trajectory and for visual servoing. The possibility of compensating the reaction torques in the roll and yaw angles coordinating the motion of the left and right arms is evaluated in test-bench with the arms integrated in a hexarotor platform. Finally, the low weight and inertia features are validated in outdoor flight tests, generating different trajectories with the arms while the UAV is hovering, evaluating qualitatively the effect of the reaction wrenches caused by the arms over the attitude controller.

6.1.1. Trajectory tracking: accuracy and repeatability

The main purpose of this experiment is evaluating the repeatability and accuracy in the positioning of the end effector of both arms using the control method described in **Section 4.5.3.2**. Both arms executed a 30 cm amplitude circular trajectory in the YZ plane, maintaining constant the position in the X-axis. The motion of both arms is coordinated and given by the following discrete trajectory:

$$\begin{aligned} x(k) &= 0.2 \\ y(k) &= \pm 0.05 + 0.15 \cdot \sin(10 \cdot \pi \cdot k/N) \\ z(k) &= -0.25 + 0.15 \cdot \cos(10 \cdot \pi \cdot k/N) \end{aligned} \tag{6.1}$$

Here k denotes the way-point index and $N = 100$ is the number of way-points, which corresponds to five turns. A ±0.05 [m] offset term has been introduced in the Y-axis representing the separation of left and right wrist points with respect to the reference trajectory. The play time of the servos was set to 0.25 s, with a jump time between way points of 0.125 s (50% of the velocity profile). **Figure 6.1** represents the Cartesian trajectory followed by the wrist point of both arms, computed from the forward kinematic model applied over the joint position measurements. As it can be seen on the right side of the figure, the deviation in the X-axis is below 1 cm. A modified version of the CAMShift color-based tracking algorithm has been employed for determining the position on the image plane of a color marker attached to the wrist point of both arms. **Figure 6.2** shows two frames captured in frontal (left) and lateral (right) view points, along with the trajectory followed by the color markers during the execution of the experiment. Note that the visual tracking of the color marker introduces a certain error in the projection of the trajectory.

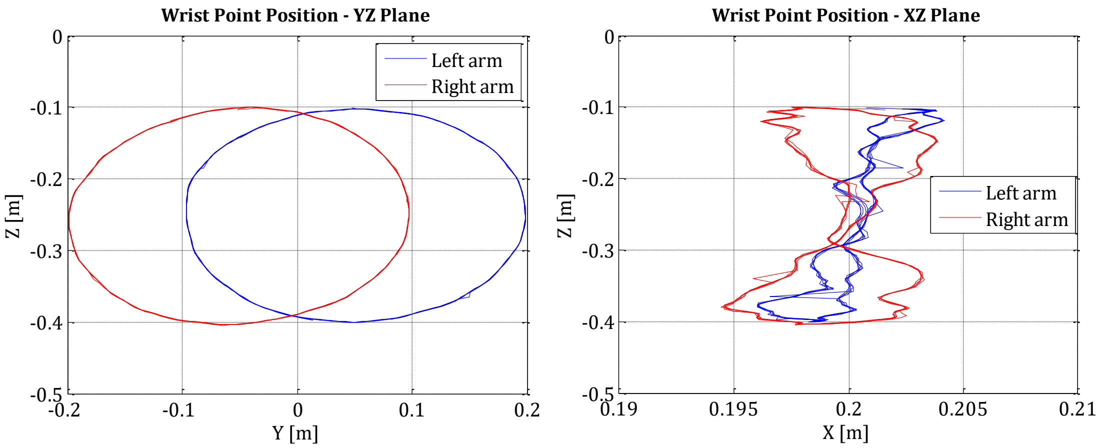

Figure 6.1. Circular trajectory at the wrist point of both arms in the YZ plane (left) and XZ plane (right). The arms performed five complete turns for evaluating repeatability and accuracy. Note the scale of the X-axis on the right figure.

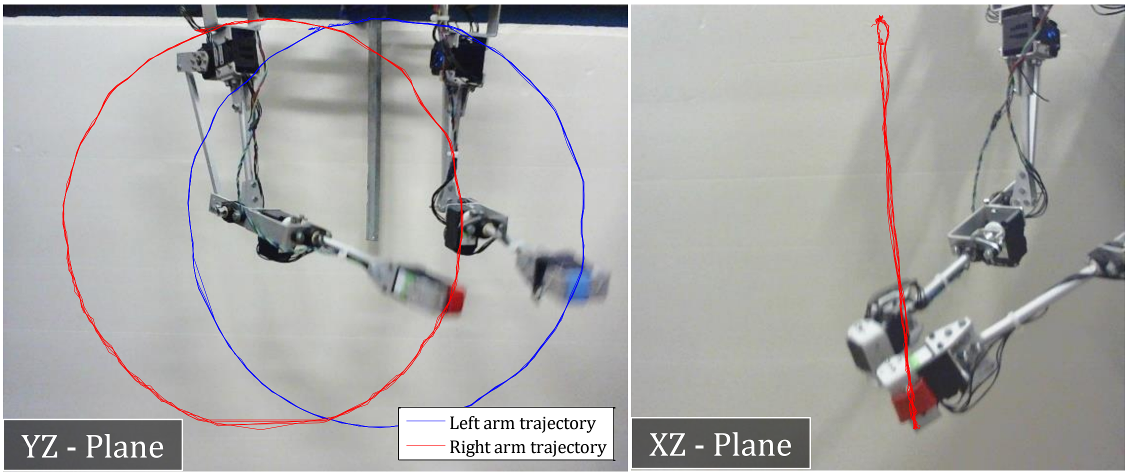

Figure 6.2. Tracking points given by the CAMShift algorithm in the frontal and side planes corresponding to the circular trajectory.

6.1.2. Visual servoing

In this experiment, a ZED camera was attached over the shoulder structure of the arms, looking 45 deg downwards so its field of view covered most part of the workspace of the manipulator. Two ARUCO tags attached to an aluminium bar and separated 25 cm visually tracked by the camera (see **Figure 6.3**), providing the position of each tag (relative to the arms frame) to the trajectory controller described in **Section 4.5.3.2**. The trajectory of the markers (red), the reference Cartesian position (black) and the current position of the arms (blue) are represented in **Figure 6.4**. The aluminium bar was rotated and translated manually in different axes. An offset distance of 10 cm between the end effector and the marker was imposed in order to prevent that the arms occluded the tags.

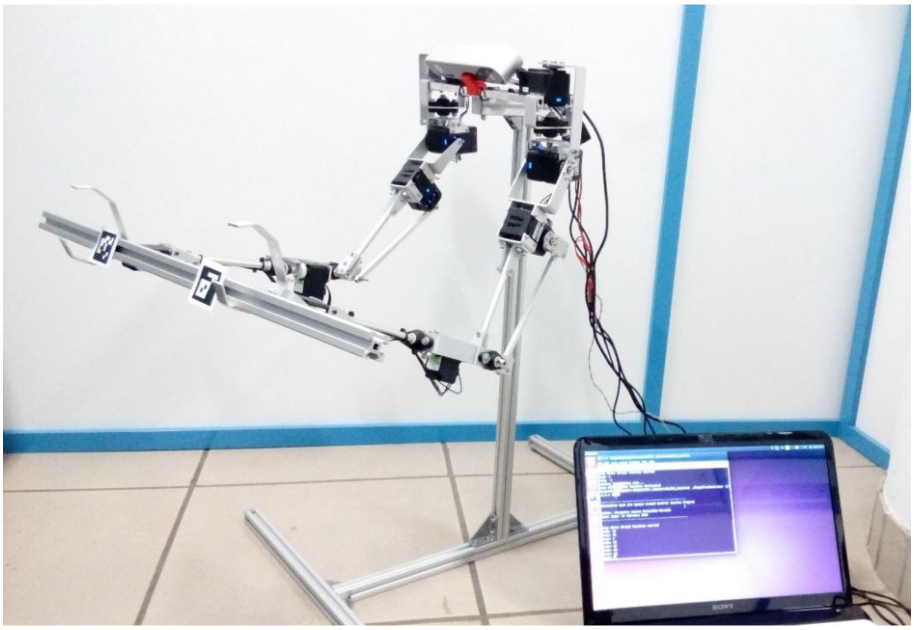

Figure 6.3. Experimental setup considered in the visual servoing experiment.

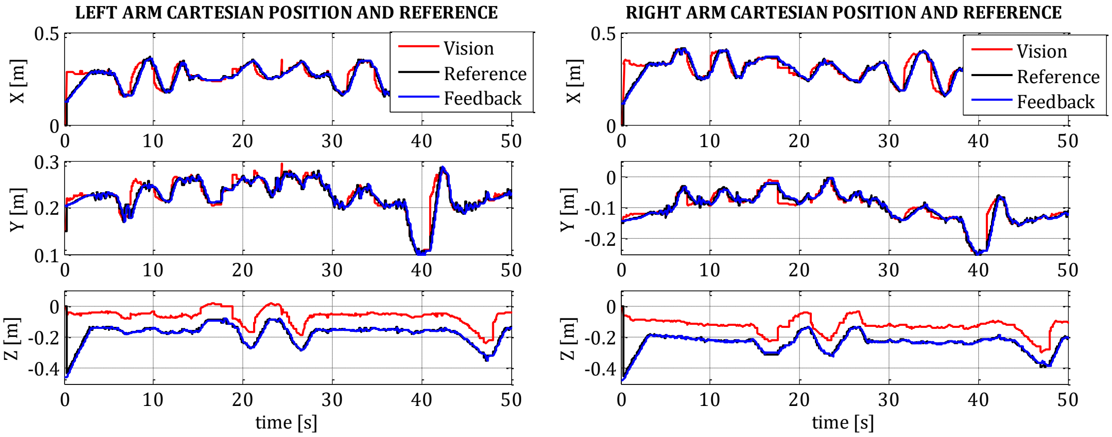

Figure 6.4. Cartesian position of the left and right arms in the visual servoing experiment where each arm tracks an ARUCO tag. An offset distance of 10 cm in the Z-axis was introduced for avoiding occlusions.

6.1.3. Step response: identification of joints state

In this experiment the arms generate a sequence of rotations, 90 deg amplitude, around their joints in the following order: shoulder pitch, shoulder yaw, and elbow pitch. The complete sequence is represented in **Figure 6.5** along with the joint speed and acceleration, measured at 50 Hz. The sign criteria is the one defined in **Figure 4.11**. Each rotation requires one second time, waiting another second until the next movement starts. From t = 5 s to t = 15 s the arms execute a symmetric motion around the XZ plane, so the torque in the roll and yaw angles is cancelled. From t = 22 to t = 32 s only the left arm moves, generating an uncompensated reaction torque at the base of the arms.

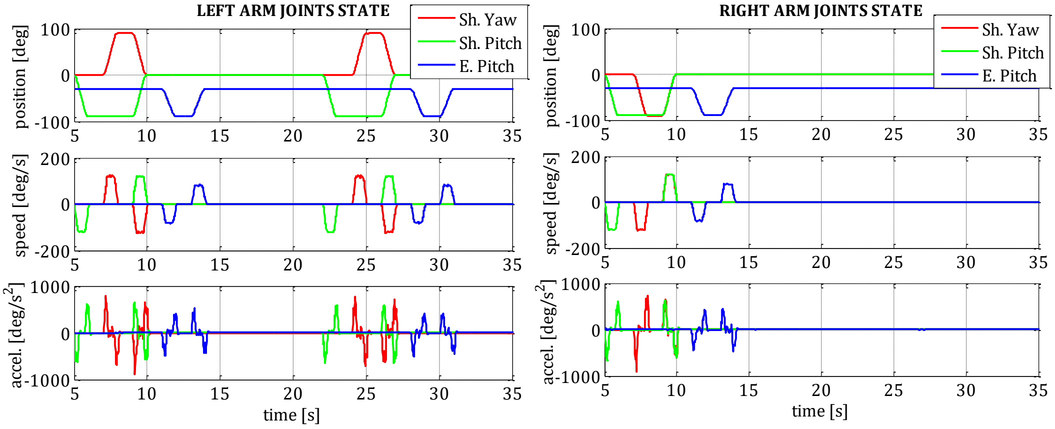

Figure 6.5. Position, speed and acceleration of the shoulder yaw (red), pitch (green) and elbow pitch (blue) joints of the left and right arms.

6.1.4. Dual arm – platform interactions in test-bench

The physical interaction between the dual arm manipulator and the aerial platform is verified experimentally here in a test bench, hanging the aerial platform from four wires attached to the central hub so that the reaction torques caused by the motion of the arms can be appreciated more clearly. The idea was to emulate hovering conditions without the action of the autopilot, allowing the free rotation of the platform at expenses of constraining its translation. The acceleration, angular speed and magnetic field at the base of the DJI Matrice 600 platform were measured with a STM32F3 Discovery board, used as external IMU connected to the Odroid U3 computer. The arms executed a simple sequence of four rotations (0 → 90 deg in q_2 | 0 → ±90 deg in q_1 | ±90 → 0 deg in q_1 | 90 → 0 deg in q_2) with two different play times (1 s and 0.5 s). Two use cases are also considered: symmetric motion of the left/right arms w.r.t. the XZ plane, and asymmetric motion moving only the left arm. **Figure 6.6** represents the servo position, speed, PWM, and the angular rate of the UAV in three use cases. The data provided by the gyroscope confirms two intuitive effects:

1) The amplitude of the oscillation of the hexarotor in the Y-axis caused by the rotation of the shoulder pitch joints is almost duplicated when the joint speed is two times higher (1st – 2nd cols)

2) The asymmetry in the motion of the arms induces a reaction in the roll and yaw angles (3rd col) which is compensated if the trajectory of the right arm is symmetric w.r.t. the XZ plane (1st, 2nd col).

However, the partial torque compensation in these two axes is achieved at expenses of increasing the reaction induced in the third axis. These effects are not so evident when the aerial manipulator is on flight due to sensor noise, wind perturbations, but especially due to the action of the autopilot, as the derivative term of the controller tends to compensate errors in angular rate.

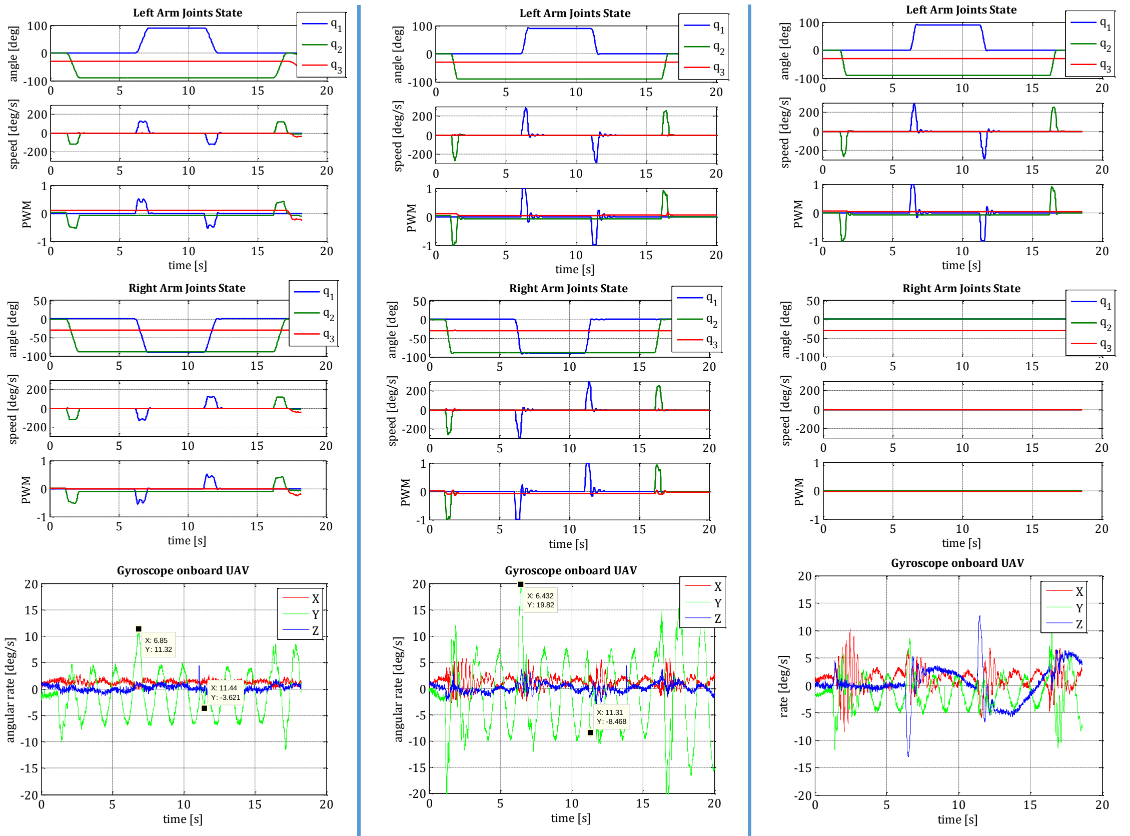

Symmetric L/R Arms Motion – PT = 1 s

Symmetric L/R Arms Motion – PT = 0.5 s

Asymmetric Left Arm Motion – PT = 0.5 s

Figure 6.6. Servo position, speed and PWM in the left (first row) and right (second row) arms during a sequence of rotations around the shoulder pitch and yaw joints. Oscillations in the platform are measured with a three axis gyroscope (third row). The amplitude and axes involved in the reaction of the platform depend on the joints speed and symmetry of the arms trajectory (cols 1 – 2 vs col 3).

6.1.5. Outdoor flight tests

An extensive set of flight tests were conducted in outdoors with the lightweight and human size dual arm prototype integrated in the DJI Matrice 600 and in a customized Drone Tools hexarotors, using in both cases the DJI A3 autopilot. A sequence of captures taken from the video are depicted in **Figure 6.7** and **Figure 6.8**. The tests were conducted within a 5×5×3 meters area covered by a safety net, counting with an expert human pilot for correcting eventual height/position deviations of the platform. The autopilot was configured in both cases in Attitude control mode in order to evaluate more clearly the influence of arms motion over the stability of the aerial platform on flight. The main purpose of these experiments was to evaluate qualitatively the interactions on flight between the manipulator and the aerial platform when a standard autopilot is employed and there is no feedback from the arms. That is, when the Arms Torque Estimator block in **Section 4.5.3.3** is not available. Note that this corresponds to the worst case in terms of control, since the endogenous reactions generated by the arms will be treated by the autopilot as an external perturbation in attitude. However, this use case is useful for validating the low weight and inertia features of the dual arm compared to the multirotor platform, whose weight is four times higher. The inspection of the video evidences small deviations in the position of the platform (<0.25 m) when high joint speed motions (250 deg/s) are generated at the shoulder joints, although it is difficult to distinguish the influence of wind perturbations from the displacement associated to the motion of the arms.

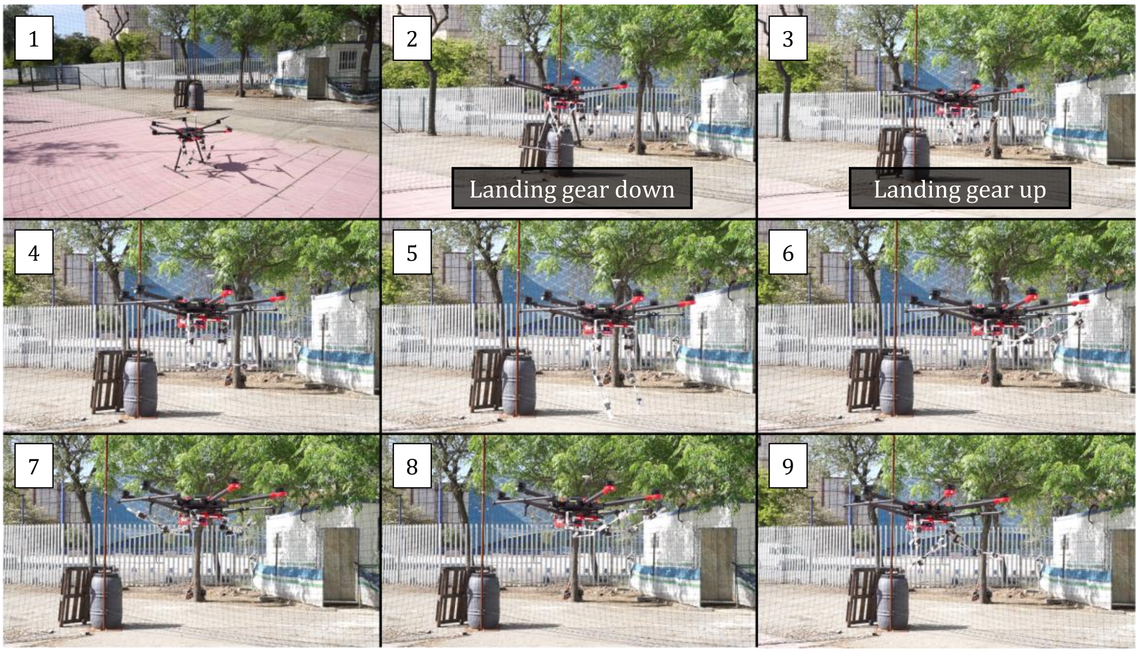

Figure 6.7. Sequence of images corresponding to the outdoor flight tests with the arms integrated in the DJI Matrice 600 platform. Platform landed (1), landing gear down – up transition (2 – 3), arms in operation position (4), rotation around the shoulder pitch joint (5 – 6), rotation around the shoulder yaw joint (7 – 8), and left arm fully stretched (9).

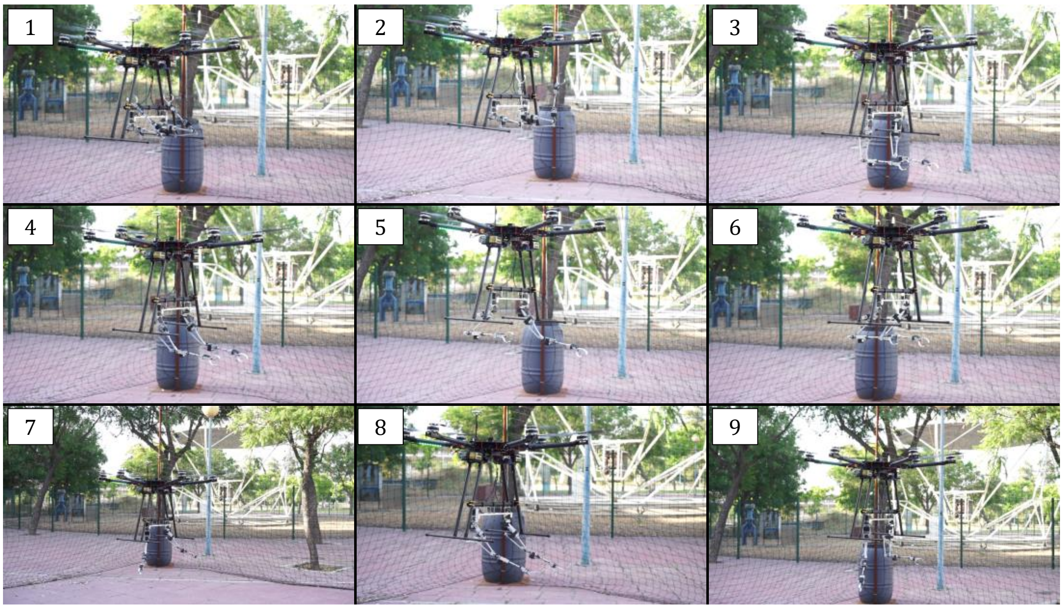

Figure 6.8. Sequence of images of the outdoor flight tests with the customized hexarotor manufactured by Drone Tools. Arms in take-off position (1), transition to operation position (2 – 3), execution of different trajectories (4 – 9).

Two relevant conclusions are derived from the analysis of the experiments. Firstly, the proposed low weight and inertia dual arm design has been successfully validated on flight since the video shows that the arms can perform high amplitude (50 cm reach) and high speed motions (up to 300 deg/s) without causing significant displacements of the aerial platform, taking into account that no feedback from the arms was provided to the attitude controller and that no position sensor was employed. The second point to remark is the performance of a standard industrial autopilot properly tuned, as it is capable to keep the platform stable in contactless situations despite the variation of the center of mass and the reaction wrenches associated to the manipulator.

6.1.6. Bimanual bar grasping on flight

This experiment evaluates the possibility to perform grasping tasks controlling the arms manually with a 6-DOF Space Navigator mouse while the aerial platform (DJI Matrice 600) is controlled by a human pilot in attitude control mode. A sequence of images taken from the video is shown in **Figure 6.9**. The experiment was conducted in the same area as in previous flight tests, introducing a 2×2×40 cm aluminium bar supported by a structure that facilitates its retrieval using both arms. The operator of the arms was placed 5 m far away from the bar structure, in a point of view similar to the camera, so the grasping operation could be done by direct sight. The main difficulty in the realization of the experiment was maintaining the hexarotor platform stable without oscillations in such a way that the bar is within the reach of both left and right arms. Although the DJI A3 autopilot employed by the Matrice 600 is well tuned from factory, the drift error in the GPS signal makes this sensor unsuitable for the manipulation phase, since the position error should be below 5 cm, taking into account that the effective reach of the manipulator is around 30 cm. One conclusion derived from the experiment is the need of a highly accurate positioning system which provides the position of the aerial platform relative to the point of interest within the workspace with an accuracy around 1 cm. The use of FPV (First Person View) camera-displays is also essential in teleoperation tasks like sensor installation and retrieval when the operator is far away from the workspace.

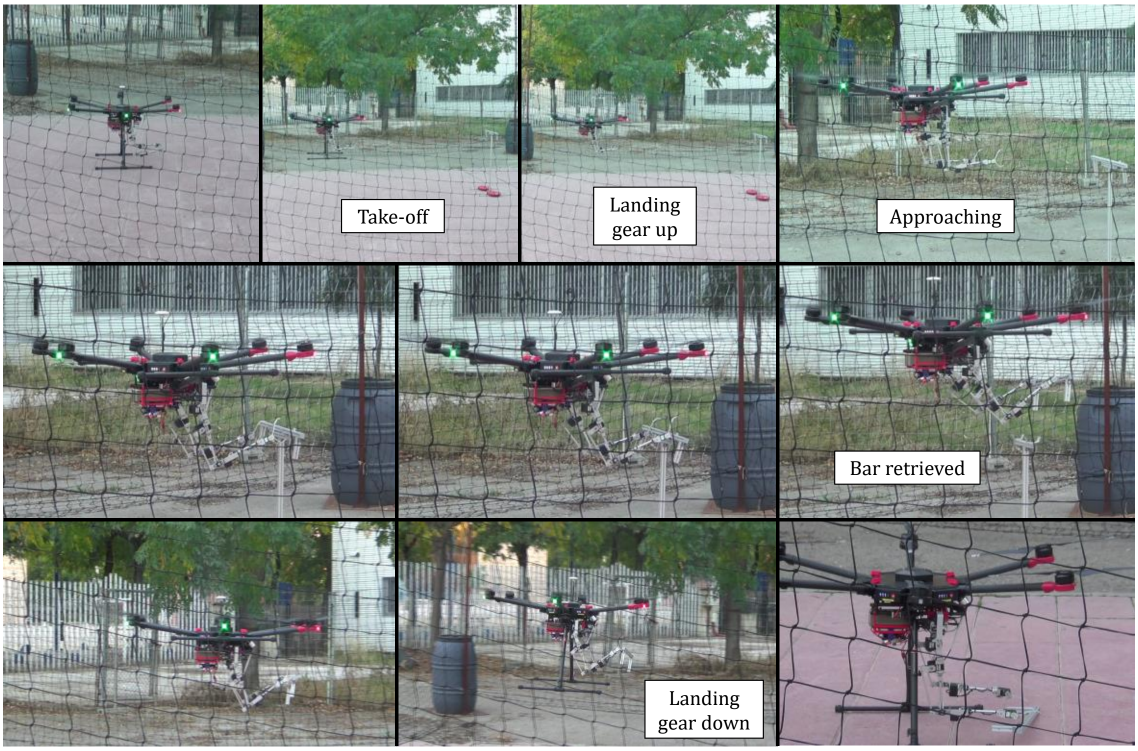

Figure 6.9. Outdoor flight tests for bar retrieval. Both arms were teleoperated using a single 6-DOF joystick

6.2. Flexible long reach link with lightweight dual arm

This section presents experimental results conducted in test-bench that demonstrate three basic functionalities of the long reach manipulator detailed in **Section 2.7.1**: vibration suppression, contact force control, and obstacle localization. The performance of the vision system employed to measure the deflection of the flexible link at the tip is evaluated in the first place, analysing later the natural response of the flexible link in free vibration conditions.

6.2.1. Characterization of flexible link

As explained in **Section 4.7.1.1**, the resonance frequencies associated to the vibration modes of a flexible link, determined by the roots of the transcendental equation, vary with the mass attached at the tip. **Figure 6.10** compares the deflection at this point measured with the vision system in two cases, with no load and with a 0.15 kg load, for the initial condition $w(0, L) = 100$ pixels. The natural response is a sinusoidal signal whose oscillation period increases with the mass at the tip, and whose attenuation rate decreases with it, since the kinetic energy to be dissipated is higher. A detailed view of the samples provided by the vision system within a 1 s period is depicted in **Figure 6.11** along with a sequence of images obtained from the marker detector. Note that the deflection measurement is the deviation of the marker with respect to the rest position along the horizontal axis. However, due to misalignment errors between the camera axis and the flexible link axis, a small oscillation in the vertical axis are identified. It is interesting to realize that the vision sensor can be also used to measure the torsion of the flexible link due to the dynamic coupling or the physical interaction between the dual arm manipulator and the flexible link.

The frequency spectrum of the deflection signal, obtained applying the Fast Fourier Transform (FFT) in the two cases (no load and with payload) is represented in left side of **Figure 6.12**, whereas the time performance of the vision system during the execution of the experiment is depicted in the right side. Since the update rate of the vision sensor is 100 Hz, the maximum bandwidth of the FFT is limited to 50 Hz, so any vibration mode whose frequency is within this range can be identified.

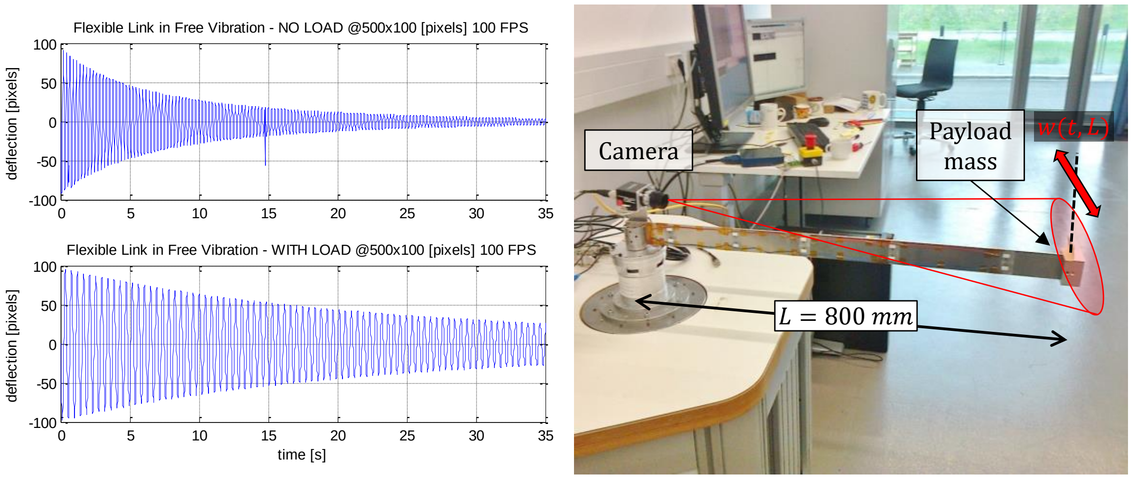

Figure 6.10. Flexible link tip deflection measured with the vision system. Response to initial condition $w(0, L) = 100\ pixels$ with no load and with load at the tip (left). Experimental setup (right).

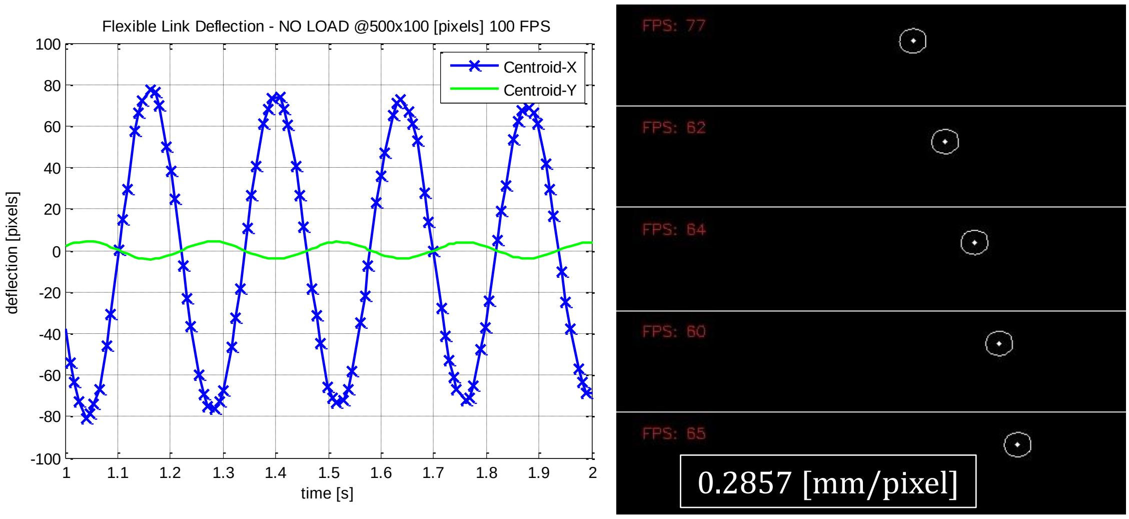

Figure 6.11. Detailed view of the flexible link tip deflection in 1 second interval (left). Sequence of images showing the displacement of the market attached at the tip of the flexible link (right). Saving the images as JPEG files reduced the frame rate.

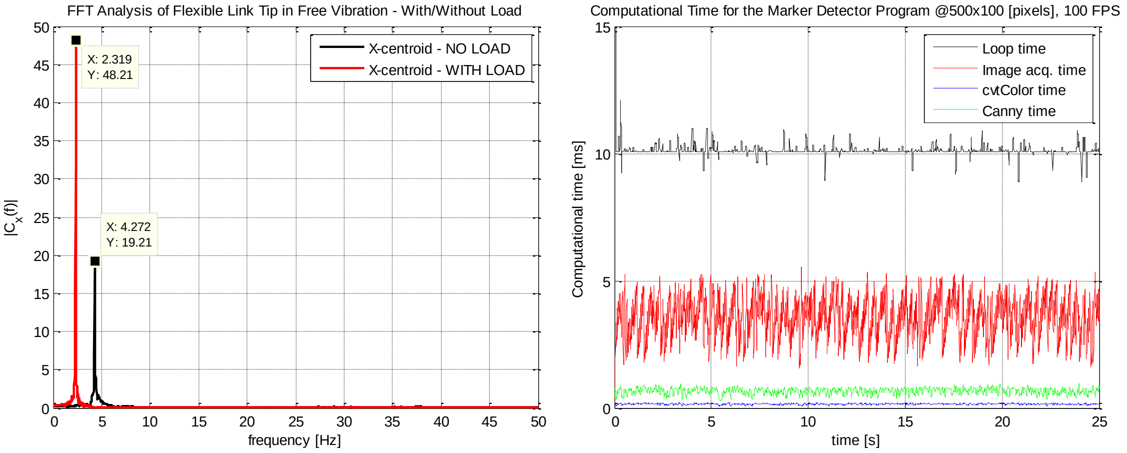

Figure 6.12. FFT of the flexible link tip deflection signal (left). Execution time of the vision system (right).

6.2.2. Vibration suppression

In this experiment, the control method described in **Section 3.7.1** is applied for removing the oscillations in the flexible link tip. **Figure 6.13** represents the tip deflection and the shoulder yaw joint speed for different compensation amplitudes of $\theta_{1,ref}^{LR}$. The execution of the experiment is as follows. The system is initially in a rest state, with the arms stretched and parallel to the floor ($\theta_1 = 0$, $\theta_2 = 90$, $\theta_3 = 0$ deg). At $t = 0$ the left arm generates a rotation motion around the shoulder yaw joint to inject energy into the flexible link, rotating from 0 to 45 deg in one second, going back to $\theta_1 = 0$ at $t = 2.2$ seconds. The excitation of the first vibration mode causes a 50 mm amplitude oscillation, with $1.58\ s$ period. Both parameters are measured online while the flexible link tip oscillates freely. Then, at $t = 5$, the vibration suppression mode is enabled. In this moment, the deflection signal changes its sign (zero cross), so its phase is determined (0 deg in this case). Immediately the shoulder yaw actuators of both arms move in the same direction for generating a reaction force that partially cancels the oscillation. As it can be derived from **Figure 6.13**, smaller amplitudes of the compensation oscillation require a higher number of iterations for removing the oscillation.

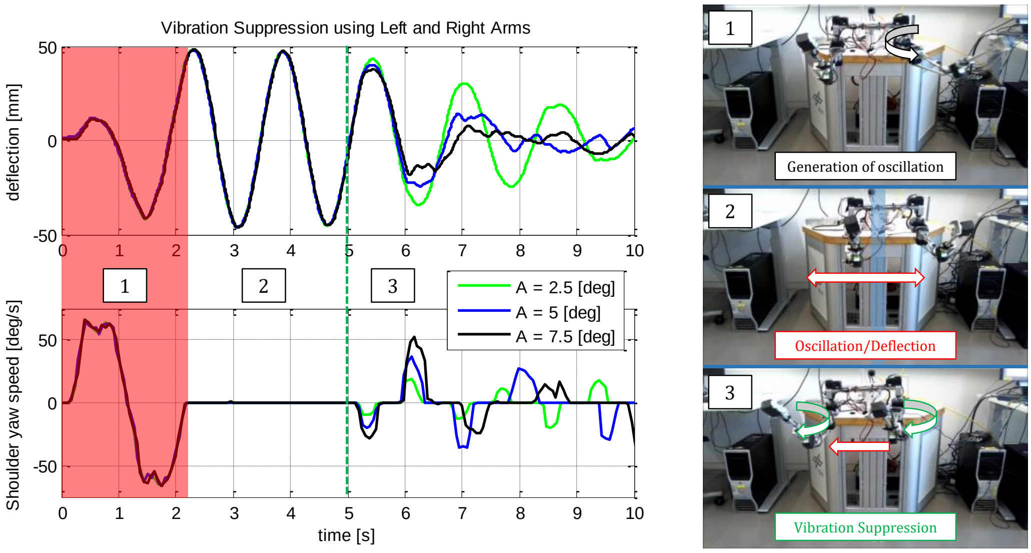

Figure 6.13. Flexible link tip deflection (top) and shoulder yaw joint speed (bottom) in the vibration suppression experiment for different compensation amplitudes. The left arm generates a disturbance between t = 0 and t = 2.2 seconds (red area). Vibration suppression is enabled at t = 5 s (green line).

6.2.3. Collision detection and contact force control

The methods described in **Section 3.7.2** and **3.7.3** for detecting obstacles close to the manipulator and controlling the contact force in terms of flexible link tip deflection are applied here. The dual arm system is initially in a rest state with both arms stretched and parallel to the floor ($\theta_1 = \mp 10$, $\theta_2 = 90$, $\theta_3 = 0$), with zero deflection. **Figure 6.14** shows the evolution of this signal along with the shoulder yaw joint angle of the left arm, and the two flags for enabling vibration suppression and force control. At $t = 5$ both arms start a scan motion rotating the shoulder yaw joint from $\theta_1 = -10$ to $\theta_1 = 60$ deg, going back to $\theta_1 = -10$ deg. At $t = 11.2$ s, during the second scan, the left arm impacts against a moving obstacle that appeared in its left side. The collision causes an immediate deflection of the flexible link which is detected when the $w_{th} = 10\,mm$ threshold is exceeded. In that moment, both arms go to a collision-free position, and the vibration suppression mode is enabled at $t = 13.1$. Then, the left arm approaches slowly to the contact point, and the contact force control mode is enabled for reaching the desired deflection at $t = 32$. When the left arm stops pushing the obstacle and goes back to $\theta_1 = 0$, the disturbance associated to the transition from the contact to the contactless state causes again the oscillation of the tip, which is removed enabling the vibration suppression mode again.

6.2.4. Obstacle localization based on soft collision detection

The method described in **Section 3.7.2.** for obstacle localization was implemented and evaluated experimentally. The positions of the end effector of both left and right arms in the XY plane has been represented in **Figure 6.15** along with the scan line (dashed) and the position of the obstacle (black dot). The arrows represent the direction of motion from the initial scan point, followed by the first scan that ends once the first contact point is detected, moment in which the scan line is determined. The second scan starts with the arms retracted, increasing the distance from the end effector to the base of the arms in 100 mm steps until the obstacle is located. The evolution of the flexible link tip deflection signal can be seen in **Figure 6.16**. The events marked in red correspond to the impact of the left arm against the obstacle during the first and second scans, respectively.

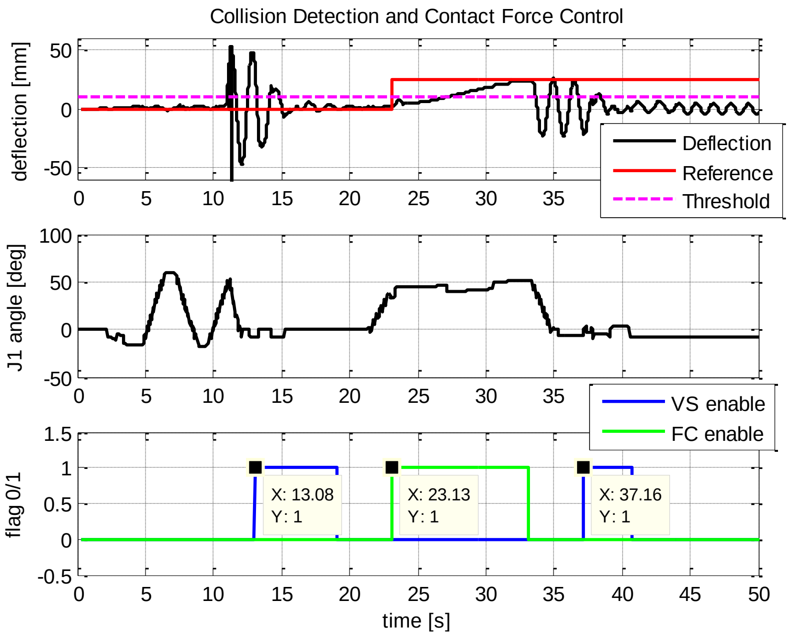

Figure 6.14. Flexible link tip deflection measurement and reference (top), shoulder yaw joint angle (middle), and control flags (bottom) corresponding to the collision detection experiment with contact force control.

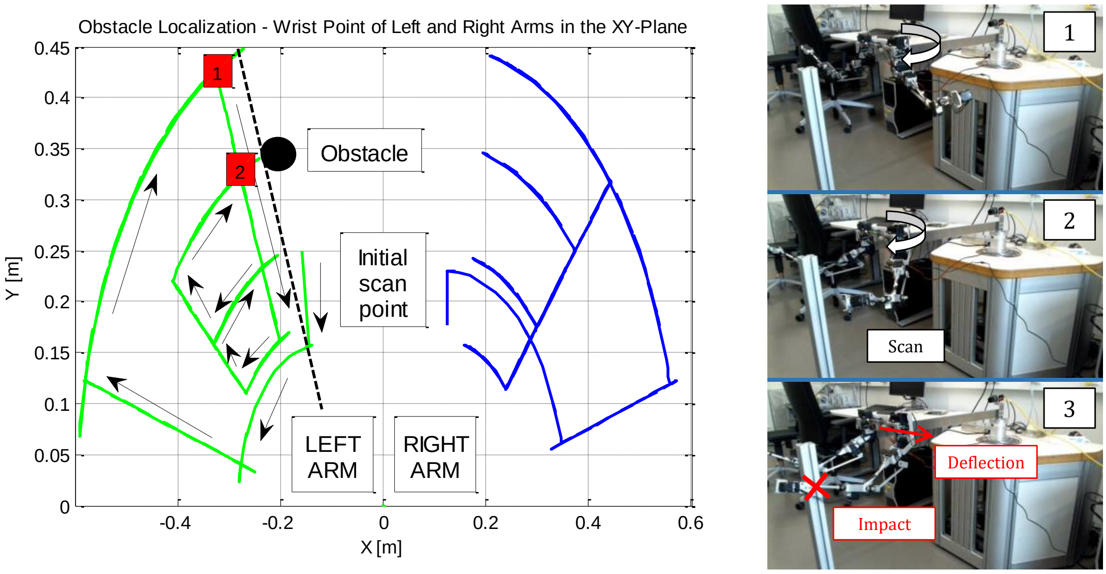

Figure 6.15. Trajectory followed by the wrist point of left and right arms for the obstacle localization experiment. The obstacle firstly impacts in the forearm of the left arm (1). Then both arms are retracted and an inner to outer scan phase is executed until the collision at the wrist point (2).

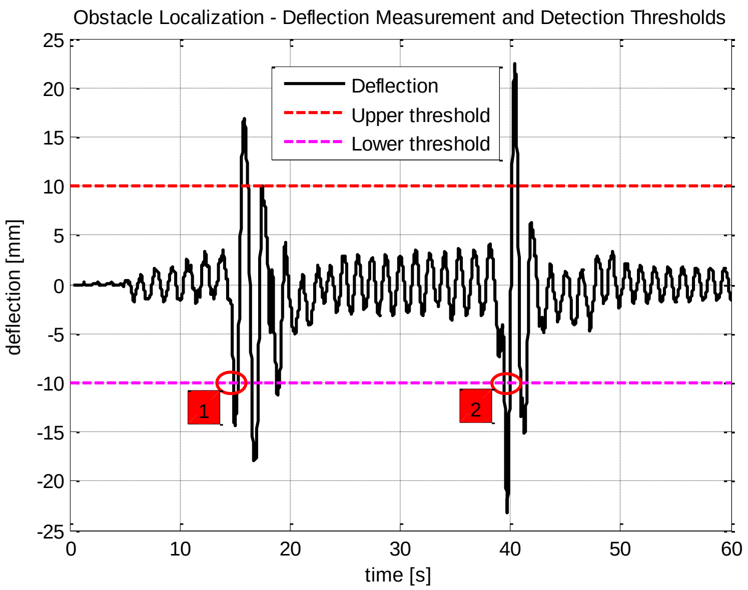

Figure 6.16. Flexible link tip deflection and thresholds for collision detection. Two impacts of the left arm against the obstacle are marked. Vibration suppression is executed after an impact for removing oscillations.

6.3. Anthropomorphic, compliant and lightweight dual arm

The experimental results presented here were obtained with the compliant joint dual arm system described in **Section 2.6**. Frequency characterization, impact response, bimanual grasping on flight and contact force control experiments have been conducted for evaluating its performance.

6.3.1. Frequency characterization

Each individual compliant joint can be assimilated to a mass-spring-damper system characterized by its natural frequency. In a compliant joint manipulator, the distribution of the mass will vary with the position of the joints, and so the resonance frequencies. Furthermore, the deflection of one joint may excite another joints due to dynamic coupling. The goal of this experiment is to identify these behaviours in the dual arm manipulator, introducing a sine chirp (sweep) signal in the elbow joint for this purpose. The elbow servo will generate a 15 deg amplitude oscillation, increasing the frequency linearly with the time from 0 up to 8 Hz in 60 seconds:

$$\theta_{4,ref}^{1,2}(t) = \theta_{4,offset}^{1,2} + 15 \cdot sin\left(\frac{8 \cdot \pi \cdot t^2}{60}\right) \tag{6.2}$$

Two representative configurations for the dual arm are considered depending on the offset angle of the elbow: arms fully stretched ($\theta_{4,offset}^{1,2} = 0$), and L-shaped elbow flexion ($\theta_{4,offset}^{1,2} = -90\ deg$). **Figure 6.17** shows the evolution of the elbow pitch servo position along with the elbow pitch and the shoulder pitch deflection. No filter was applied to these signals. As it can be seen, two resonance modes are identified at $t = 12\ s$ and at $t = 45\ s$. The first one is coupled to the shoulder pitch joint, whereas the second one mainly affects to the elbow joint. It is interesting to note that, at the resonance frequency of the first mode, the relative phase of the elbow pitch deflection signal drops 180 deg w.r.t. the servo position. This can be appreciated more clearly in **Figure 6.18**. Since the amplitude of the servo rotation is similar to the joint deflection but with different sign, the apparent effect is that the forearm link is not oscillating, which is confirmed by visual inspection of the experiment.

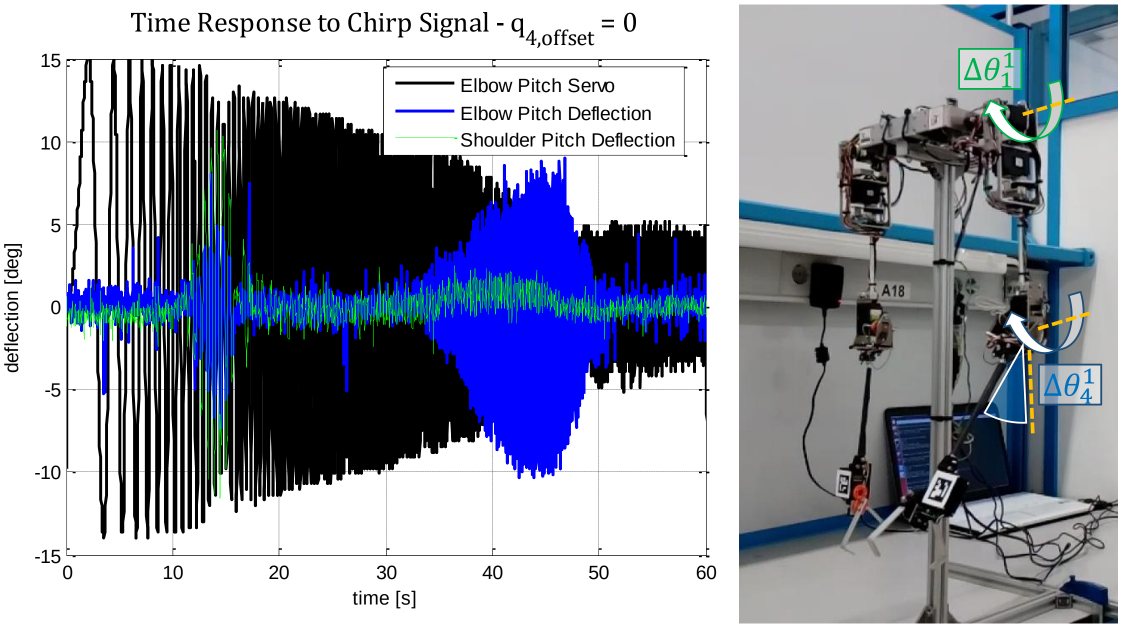

Figure 6.17. Elbow pitch (blue) and shoulder pitch (green) joint deflection for a 15 deg chirp signal generated by the elbow pitch servo (black).

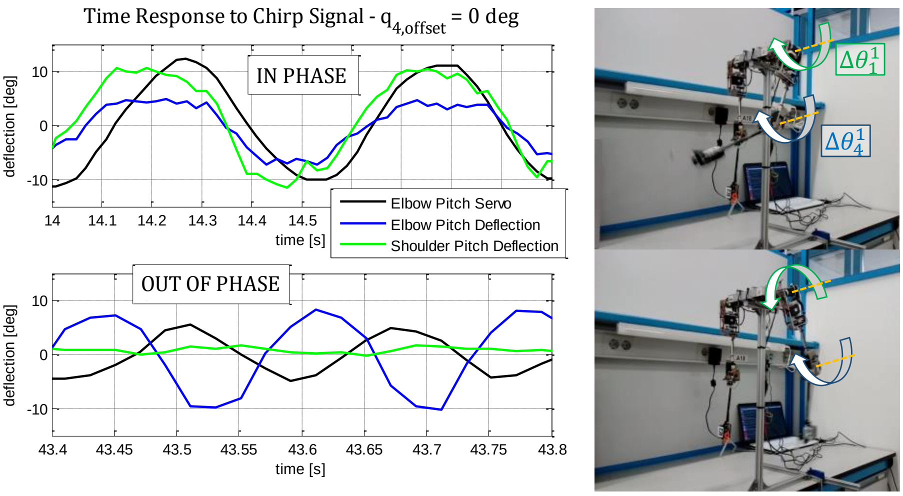

Figure 6.18. Detailed view of the servo position and the joints deflection. Before the first resonance peak the deflection is in phase with the servo (up), dropping 180 deg in the second resonance peak (down).

The Fast Fourier Transform (FFT) algorithm was applied to the signals depicted in **Figure 6.17** for obtaining a frequency representation of the servo bandwidth and the resonance peaks of the compliant joints. These can be identified clearly in **Figure 6.19**. The first resonance mode at $f_1 = 1.624\ Hz$ is associated to the elbow pitch and shoulder pitch joints, whereas the second mode at $f_2 = 5.92\ Hz$ only affects to the elbow joint and it has a wider bandwidth than the first one. The servo actuator is not able to follow the chirp reference from $f = 1.5\ Hz$ due to its limitations in speed and torque.

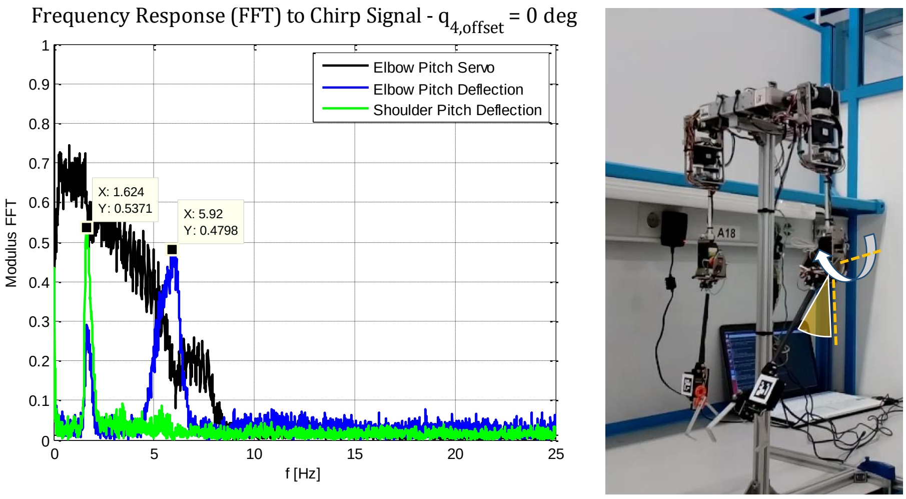

Figure 6.19. FFT applied to the elbow pitch servo (black) and to the elbow pitch (blue) and shoulder pitch (green) joint deflection. The resonance frequencies are identified at $f_1 = 1.6\ Hz$ and $f_2 = 5.9\ Hz$.

The variation in the frequency response of the compliant arm due to the rotation of the elbow joint is evidenced in **Figure 6.20**. In this case (90 deg elbow flexion), as the distance from the center of mass of the arm to the shoulder joint is lower, the resonance frequency increases, varying from $f_1 = 1.624\ Hz$ to $f_1 = 2.075\ Hz$. The amplitude of the second resonance mode is also higher due to the effect of gravity over the forearm link mass.

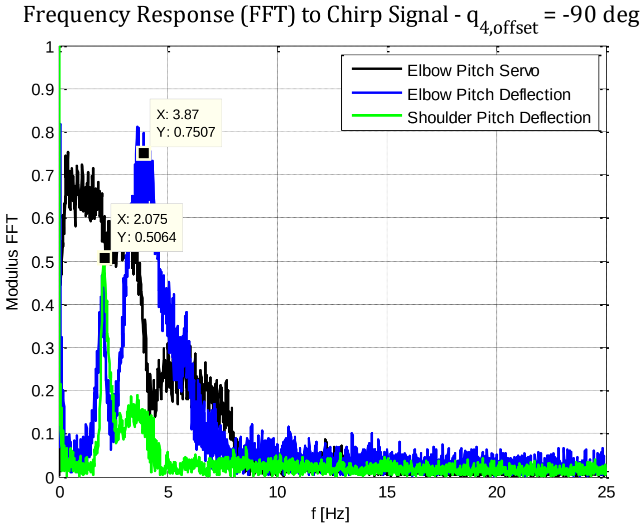

Figure 6.20. FFT applied to the elbow pitch servo (black), the elbow pitch (blue) and shoulder pitch (green) joint deflection. The spectrum and resonance frequencies have changed along with the mass of the arm.

6.3.2. Impact response: Cartesian deflection and velocity

In aerial manipulation, the transition from contactless to contact situations can be assimilated to an impact between the end effector and the environment. The vision system described in **Section 4.6.6** can be exploited for detecting this event, but also for controlling the contact force through the Cartesian deflection of the compliant manipulator. In this experiment, the gripper servo of the left arm is impact by a 62 g weight object thrown from a 0.5 m height, which corresponds to a potential energy of 0.3 J, while the arm rests in L-position (elbow flexion). A color marker was attached over the servo case, with the stereo camera head focused on it. The position and velocity of the marker is estimated by an Extended Kalman Filter (EKF) and the CAMShift algorithm, representing the result in **Figure 6.21**. The acceleration of the impact point and joint deflection are also represented. The underdamped behaviour of the Cartesian deflection validates mass-spring-damper model of the arm.

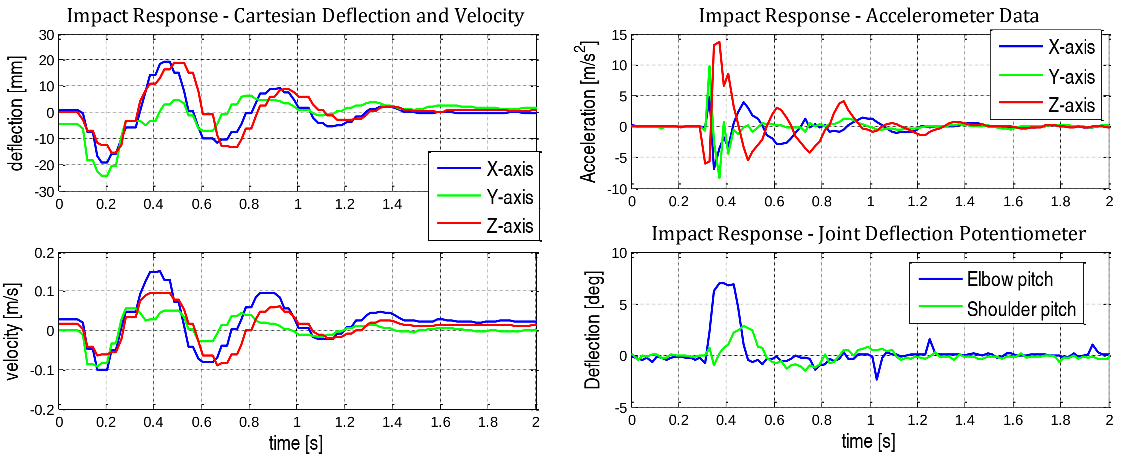

Figure 6.21. Impact response. Cartesian deflection and velocity measured with the vision system (left). Representation in the frequency domain (right).

6.3.3. Contact force control in hovering conditions

The control method described in **Section 4.6.5.3** is tested in an experiment in which the mobile manipulator approaches to a wall and exerts a 3 N pushing force with the left arm in the X-axis, maintaining a zero force reference in the other axes. The evolution of the experiment can be followed in **Figure 6.22** and **Figure 6.23**. The position of the platform is referred to the ARUCO tag placed in the wall, using two additional markers disposed over the gripper servos for measuring the position of the wrist. As seen on the right side of **Figure 6.22**, the joints involved in this task are mainly the shoulder and elbow pitch ones. It is interesting to observe how the Cartesian stiffness slightly varies with the angular position on the joints, as these depend on the Jacobian. The control period of the position controller was set to 0.1 s to prevent undesired effects of the derivative term in the controller.

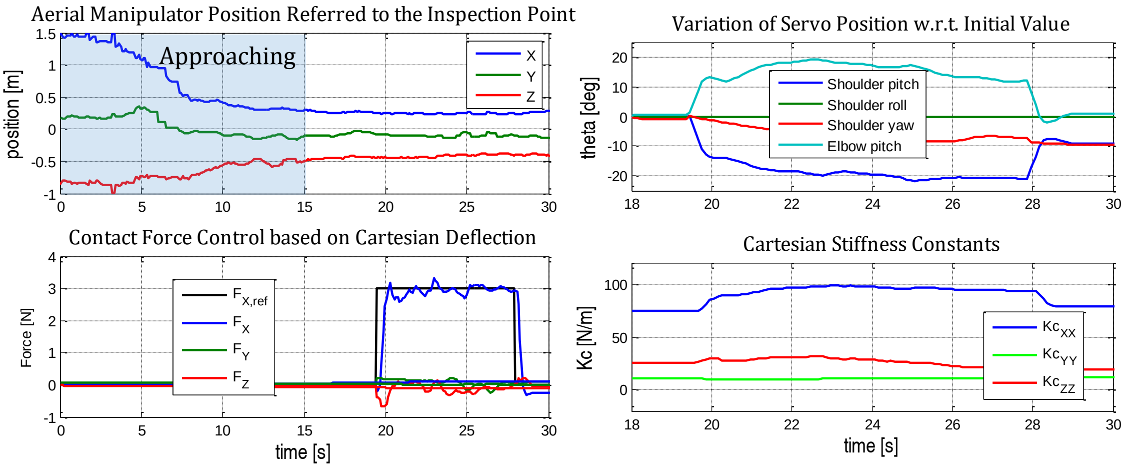

Figure 6.22. Signals involved in the contact force test: position of the platform (up, left), left arm force and reference (down, left), variation of the servos position (up, right), and Cartesian stiffness (down, right).

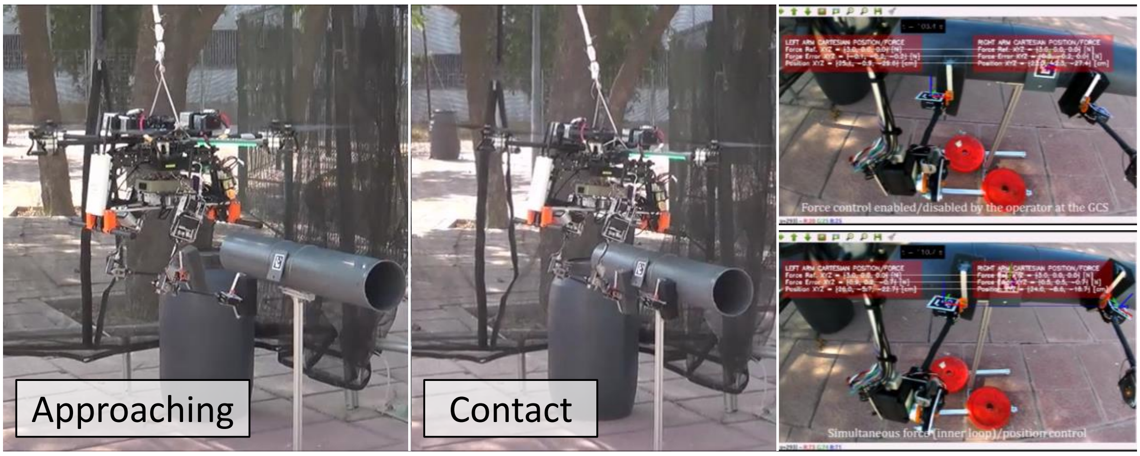
Approaching
Contact
Force control enabled/disabled by the operator at the GCS
Simultaneous force (inner loop)/position control

Figure 6.23. Approaching (left) and contact force control (middle) phases and images from onboard camera (right). The position of the left/right arms and the target contact point are measured with ARUCO tags.

6.3.4. Bimanual object grasping: force/displacement monitoring

During the realization of certain aerial manipulation tasks, it may occur that the robot try to grasp and retrieve an object whose mass exceeds the payload of the multirotor, or well it cannot be lifted because it is attached to a structure. A method for determining if an object can be retrieved consists of applying a pulling force and measuring the displacement of the manipulator. In **Figure 6.24**, a 35 cm length, 0.2 kg weight bar is grasped with both arms, applying a 1 N pulling force in the Z-axis at t = 2.3 s, which causes a significant displacement of the markers. The experiment is repeated, but holding the bar so it cannot be moved. As it can be seen in **Figure 6.25**, during the 2 s monitoring period, the displacement is below the 1 cm threshold, so the force ceases and the object is released.

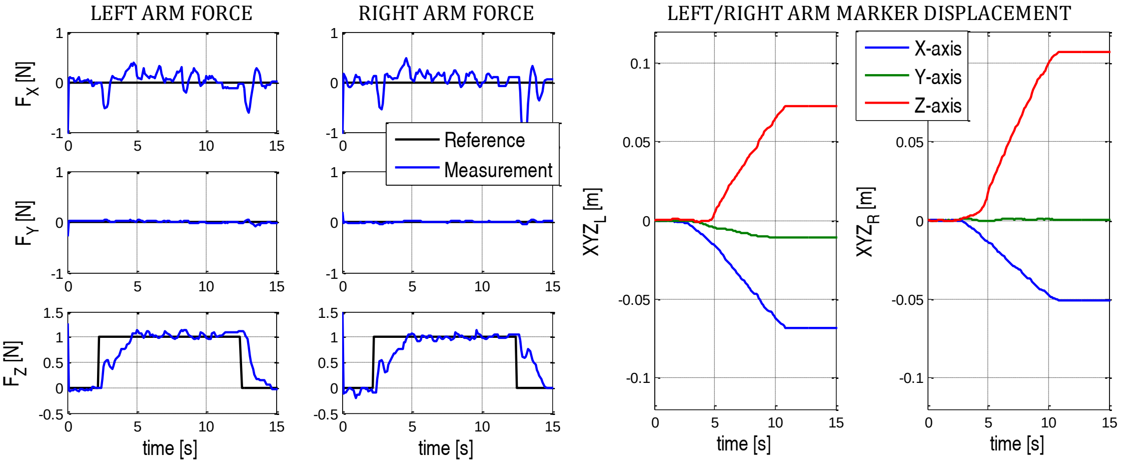

Figure 6.24. Force (left) and displacement (right) of the left/right arm markers when the grasped object is pulled in the Z-axis and this is lifted.

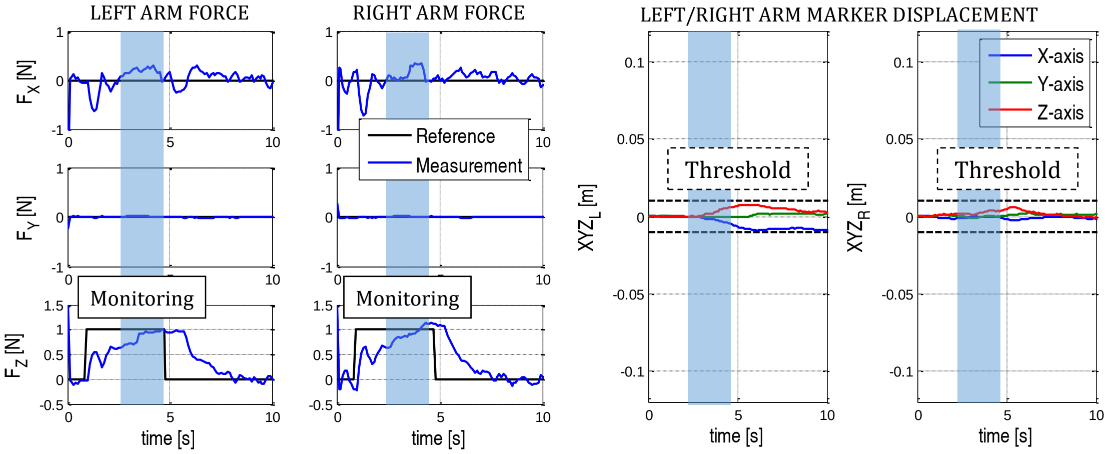

Figure 6.25. Pulling force and displacement when the object cannot be lifted. The displacement is monitored (blue area) since $F_Z \geq 0.75 \cdot F_{Z,ref}$.

6.3.5. Bimanual object grasping on flight

Outdoor flight tests were conducted for validating the dual arm design, demonstrating bimanual grasping based on visual servoing. The arms were integrated in a DJI Matrice 600 hexarotor for this purpose along with an Intel NUC computer board, a ZED stereo camera for visual servoing, a 5.8 GHz wireless link, and the batteries. The experiment consisted of six phases: 1) take off, 2) approach to the inspection tool installed on a PVC pipe, 3) move the arms to the operation position, 4) activate visual servoing, 5) retrieve the inspection tool, and 6) release the tool. The setup and the execution of the experiment are represented in **Figure 6.26** and **Figure 6.27**. The UAV was radio-controlled in position by an expert human pilot while an operator took care of the arms from a ground control station (GCS). The tests were conducted in a 6 × 6 × 4 meters area covered by a safety net. The purpose of the developed scenario was to illustrate the application of dual arm aerial manipulators to the installation and retrieval of inspection tools deployed in areas of difficult access such like high altitude pipes in chemical plants.

The grasping method consisted of guiding the TCP of the left and right arms from their initial position to the grasping points applying the control method described in **Section 4.6.2**, closing the grippers when the goal point is reached. The grasping points provided to the arms controller are obtained from a vision algorithm which recognizes the tags in the front part of the tool. A ZED stereo camera attached to the shoulder structure was employed due to its wide field of view and high image quality. **Figure 6.28** shows the trajectory of the TCP of left and right arms along with the grasping points given by the vision module during the flight experiment. Positioning errors are mainly due to non-compensated joint deflections and to misalignment errors between the arms frame and the camera frame. The control period and velocity were set to $T = 0.1\ s$, and the reference velocity of the arms was set to $v = 0.2\ m/s$.

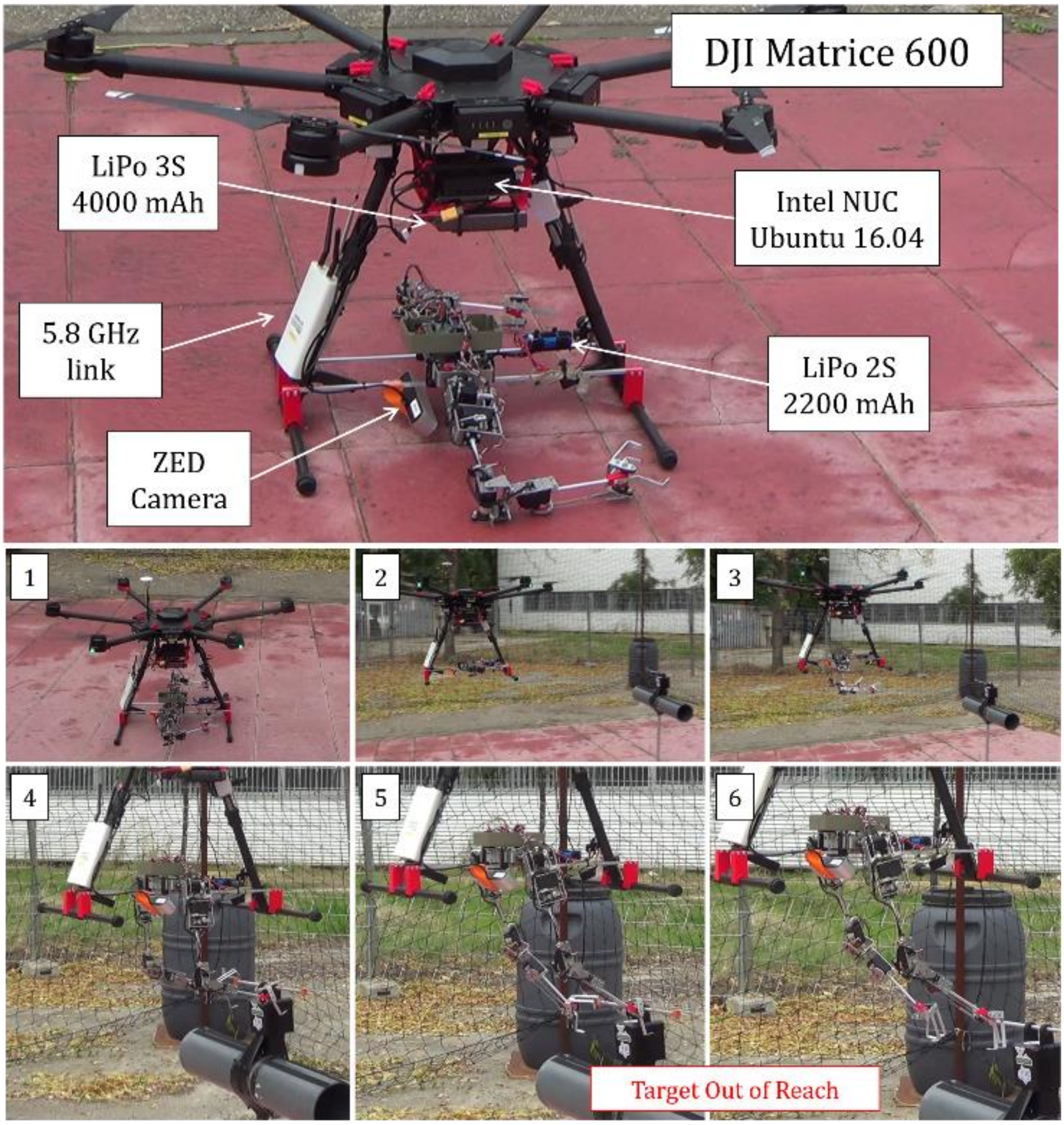
DJI Matrice 600
LiPo 3S 4000 mAh
Intel NUC Ubuntu 16.04
5.8 GHz link
LiPo 2S 2200 mAh
ZED Camera
1
2
3
4
5
6
Target Out of Reach

Figure 6.26. Compliant dual arm integrated in DJI Matrice 600 hexarotor. Take-off (1), approaching to inspection tool installed on pipe (2 – 3), and visual servoing (4 – 6). The target points are out of the reach of the arms due to the displacement of the aerial platform (5 – 6).

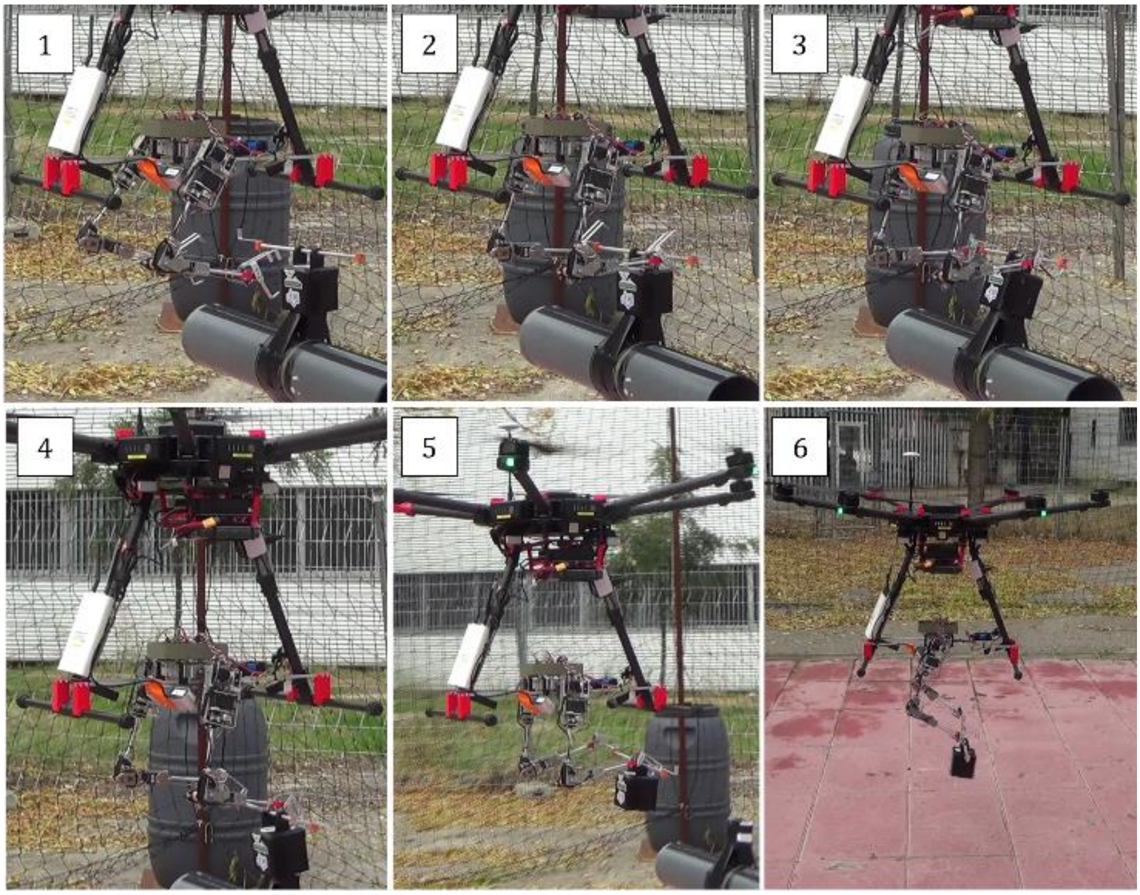

Figure 6.27 Bimanual object grasping on flight. The arms grasp the inspection tool installed over a pipe by a 50 cm length handle.

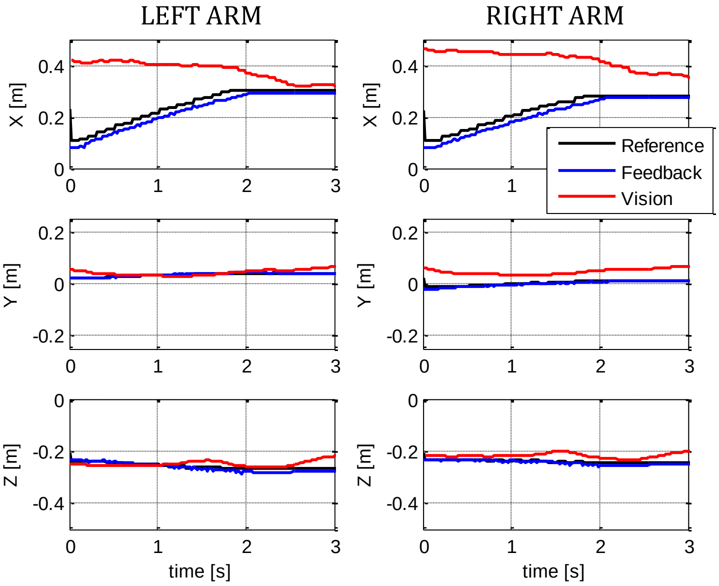

Figure 6.28. TCP Cartesian position of left/right arms. Grasping points given by the vision (red), reference (black) and servo feedback (blue).

6.3.6. Payload mass estimation

The accuracy in the force estimation was evaluated in test bench using a KERN FKB 8K0.1A bench scale (0.1 grams resolution). Five calibration masses were attached at the tip of the forearm link of the left arm, measuring the Cartesian deflection with the camera head, and estimating their weight from the Cartesian deflection (Equation **(4.71)**). **Figure 6.29** shows the payload estimation and the ground truth along with the view of the camera for four different masses.

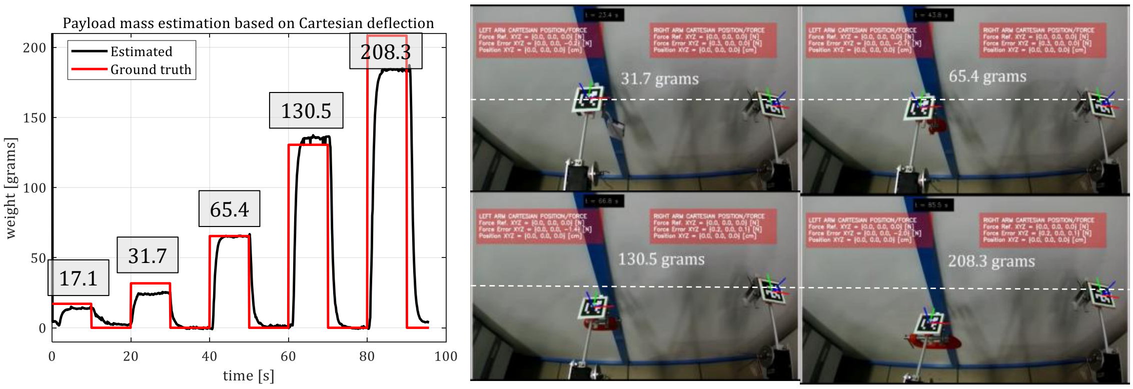

Figure 6.29. Evaluation of the accuracy in the vision-based force estimation. Different payload masses were attached at the wrist point of the left arm.

6.3.7. Grasping, installation and retrieval of inspection tool on pipe

This section demonstrates the application of the anthropomorphic, compliant and lightweight dual arm aerial manipulator in a pipe inspection task consisting of grasping, installing and retrieving an inspection tool stored in a tool bench, which involves an accurate position control of the UAV and the arms. The experiments were conducted in the CATEC indoor testbed, which is equipped with a highly accurate Vicon positioning system. A picture of the scenario and the aerial robot can be seen in **Figure 6.30**. The aerial robot consists of a hexarotor equipped with a PixHawk autopilot running the PX4 flight stack, an Intel NUC computer board where the control program is executed, an Ubiquiti wireless link, and the dual arm system. The inspection tool consists of a plastic box containing the sensor device, two C-shaped aluminium frames attached at its base so they adapt to the contour of the pipe where the tool will be installed, and a 45 cm length aluminium bar used as handle. Both the aerial platform and the tool are endowed with small infrared reflecting balls use by the Vicon system to measure the position and orientation of the objects.

The execution of the experiment consists of the following steps:

1. Take-off with the arms lifted above the floor
2. Approach above the tool bench where the tool is stored
3. Grasp the tool with the arms
4. Move close to the workspace (pipe structure)
5. Approach to the inspection point
6. Install the inspection tool over the pipe
7. Wait until the inspection operation is complete
8. Retrieve the inspection tool
9. Go back to the tool bench
10. Release the tool in the tool bench

11. Go back to the landing point
12. Lift the arms above the landing gear and land

A sequence of images taken from the on-board camera can be followed in **Figure 6.31**. The UAV position controller takes care of following the sequence of way-points associated to the phases listed before, whose positions are determined previously. The trajectory followed by the multirotor is mainly contained in the YZ plane of the reference frames associated to the testbed, maintaining almost constant the position in the X axis. The multirotor is commanded to hover at a fixed position so that the arms can operate in the workspace within their reach during the grasping and installation phases. The evolution of the trajectory is represented in **Figure 6.32**, indicating the different phases, whereas **Figure 6.33** shows the convergence of the end effector of both arms to the grasping point during phase 3, considering the local frame associated to each arm, located at the intersection of the shoulder joints. The tool center point (TCP) of both arms are guided automatically to the grasping points located over the tool handle using the position given by Vicon. The tool is retrieved once the grasping position error is below a pre-defined threshold (~1 cm). This event is reported to the UAV controller in order to continue with phase 4.

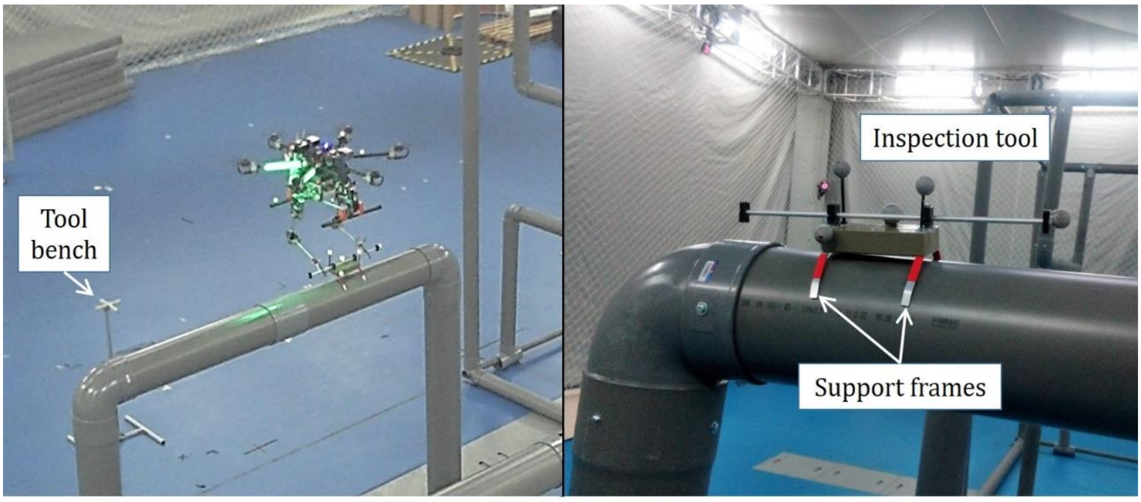

Figure 6.30. Application of dual arm aerial manipulator to pipe inspection with customized tool.

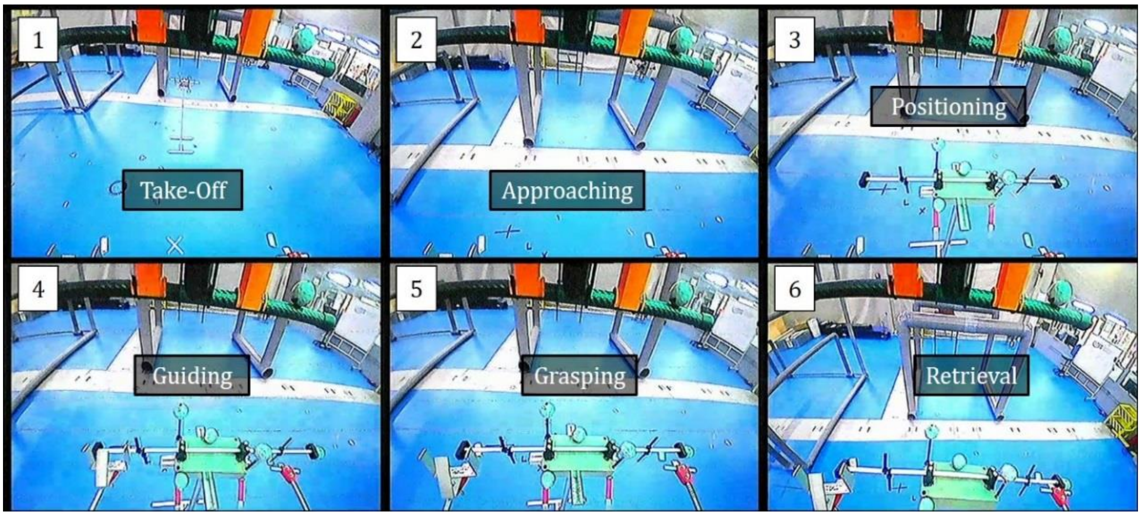

Figure 6.31. Sequence of images taken from the on-board camera representing the bimanual grasping of the inspection tool stored at the tool bench. The arms are guided to the grasping points using the Vicon system.

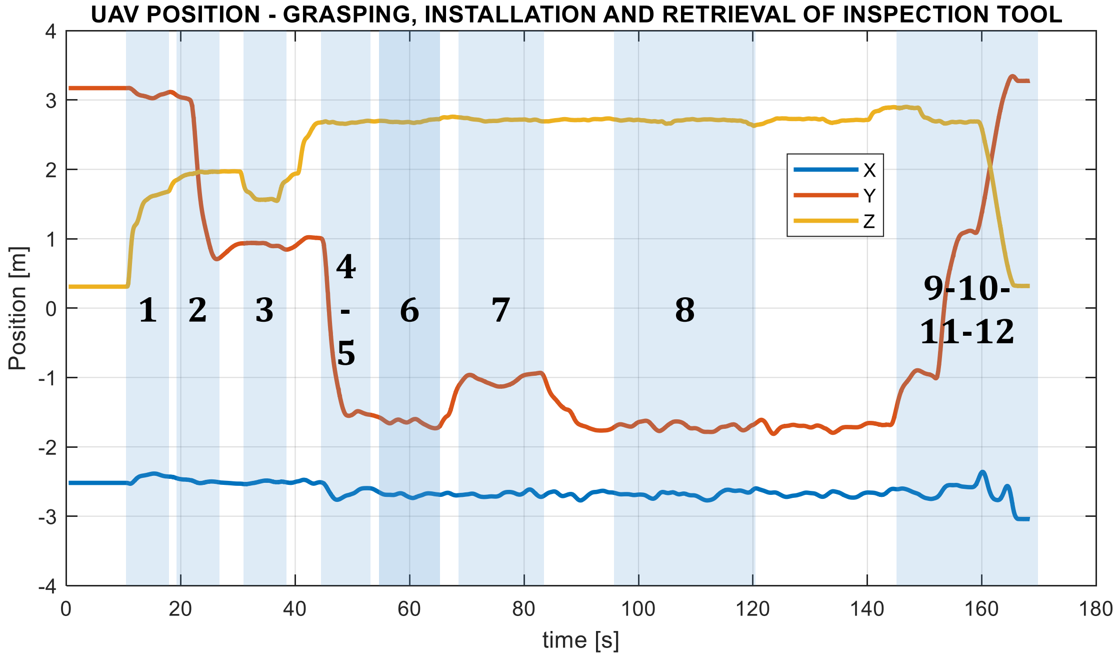

Figure 6.32. Trajectory followed by the aerial manipulator during the execution of the tool installation task. The numbers indicate the phase of the experiment according to the list indicated before.

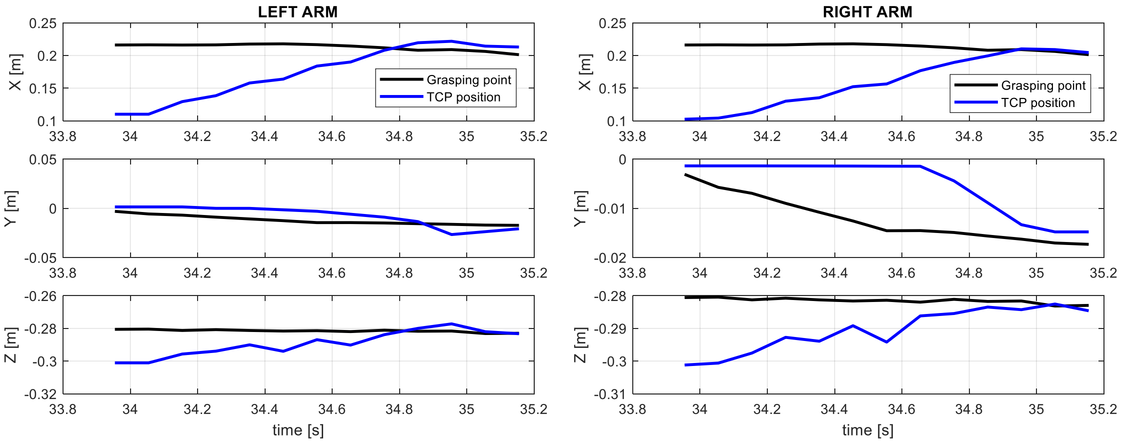

Figure 6.33. XYZ grasping points references (black) and current end effector position (blue) of the left and right arms. The grasping points are obtained from the position of the inspection tool, given b Vicon.

The grasping method consisted of guiding the end effector of the arms, whose position is obtained from the forward kinematic model, to the desired grasping points over the inspection tool, whose position is given by Vicon. On each iteration of the control loop (50 Hz rate), the position error vector is computed and normalized, so, in the next step, the arms will move in the appropriated direction with a displacement determined by the desired motion speed. The gripper can be closed automatically once the position error is below the threshold mentioned before. The performance of the arms controller has been evaluated in a 50 seconds experiment in which the platform stays in a fixed position while the end effector of both arms is tracking the grasping points. **Figure 6.34** and **Figure 6.35** represent the evolution of the grasping points and the end effector position, as well as the tracking error and the deviation of the multirotor position, caused by aerodynamic effects raised in the indoor testbed.

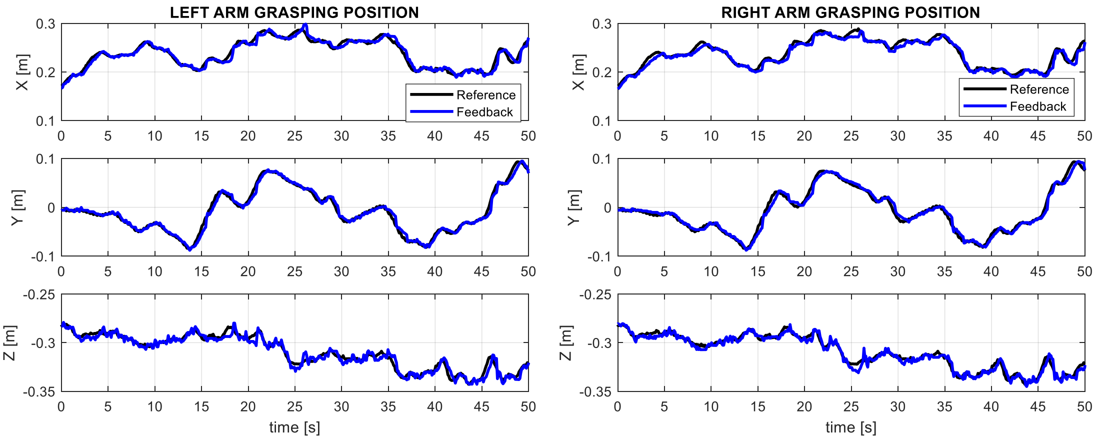

Figure 6.34. Grasping points obtained from Vicon (black) and current end effector position (blue) of both left and right arms in a 50 seconds evaluation period.

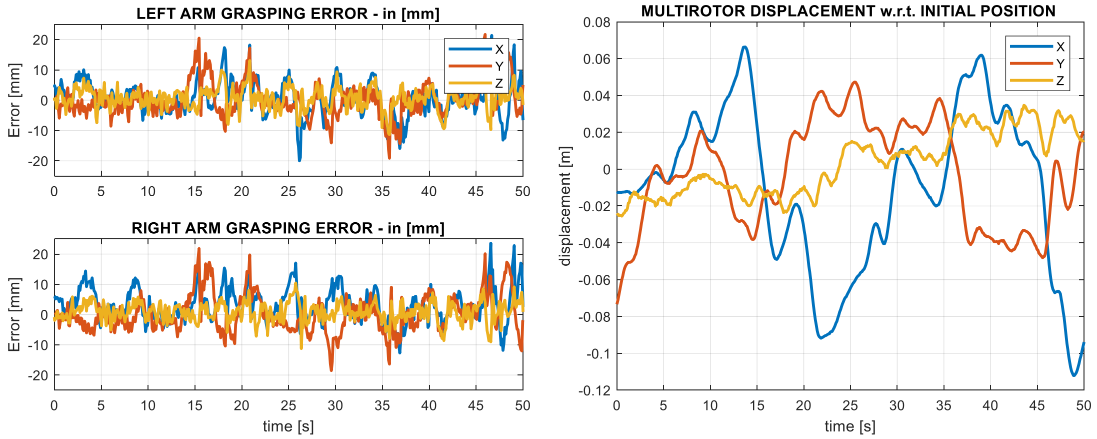

Figure 6.35. Tracking error in mm of the left and right arms during the long term grasping experiment (left). Displacement of the multirotor in hovering state (right).

The tool installation operation was conducted by a human operator using a 3DConnexion 6-DOF mouse as joystick for controlling the velocity at the end effector of both arms simultaneously. The control method is the same as the one used in the automatic grasping phase, replacing the position measurement given by Vicon by the position increment obtained from the joystick. A sequence of images from the on-board camera corresponding to the installation phase can be seen in **Figure 6.36**.

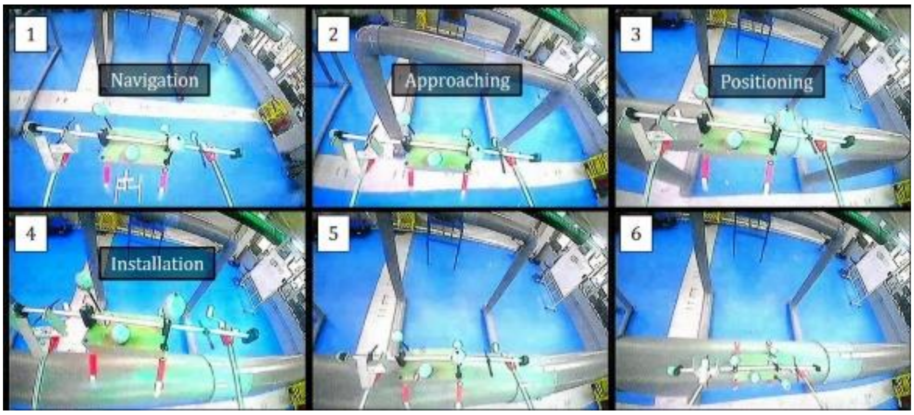

Figure 6.36. Sequence of images from the on-board camera corresponding to the tool installation phase.

6.4. Long reach aerial manipulators

This section evaluates through indoor and outdoor flight tests the long reach aerial manipulator with compliant dual arm described in **Section 2.7**. The main difference with respect to the flexible long reach manipulator with lightweight dual arm evaluated in **Section 6.2** is the introduction of a passive joint that allows the free rotation of the flexible link w.r.t. the base of the aerial platform in the so called pendulum configuration. Two application examples are presented below: transportation of bars and sensor installation on pipe with contact force control.

6.4.1. Transportation of long bars

The long reach dual arm aerial manipulator described in **Section 2.7.3** is intended to perform a transportation operation in an outdoor scenario that includes pipe structures, considered as obstacles. A sequence of images from the experiment can be followed in **Figure 6.37** and **Figure 6.38**. The transported object is a 2 m length bar grasped by both arms around the midpoint. Two white balls are placed at the tip of the bar so it can be identified more easily. The aerial manipulator follows a pre-computed trajectory that ensures a 0.5 m safety distance from the pipes, taking also into account the dynamics of the long reach manipulator. The lateral deflection of the flexible link is not taken into account since the hexarotor follows a forward trajectory without inducing lateral accelerations.

Unlike the long reach aerial manipulator evaluated in **Section 5.5**, this prototype made use of a take-off and landing platform consisting of a 1.8 m height table with a central slot for introducing the flexible link, leaving the dual arm below the table while the multirotor is supported over it. The take-off and landing manoeuvres were executed by a skilled pilot in attitude control mode.

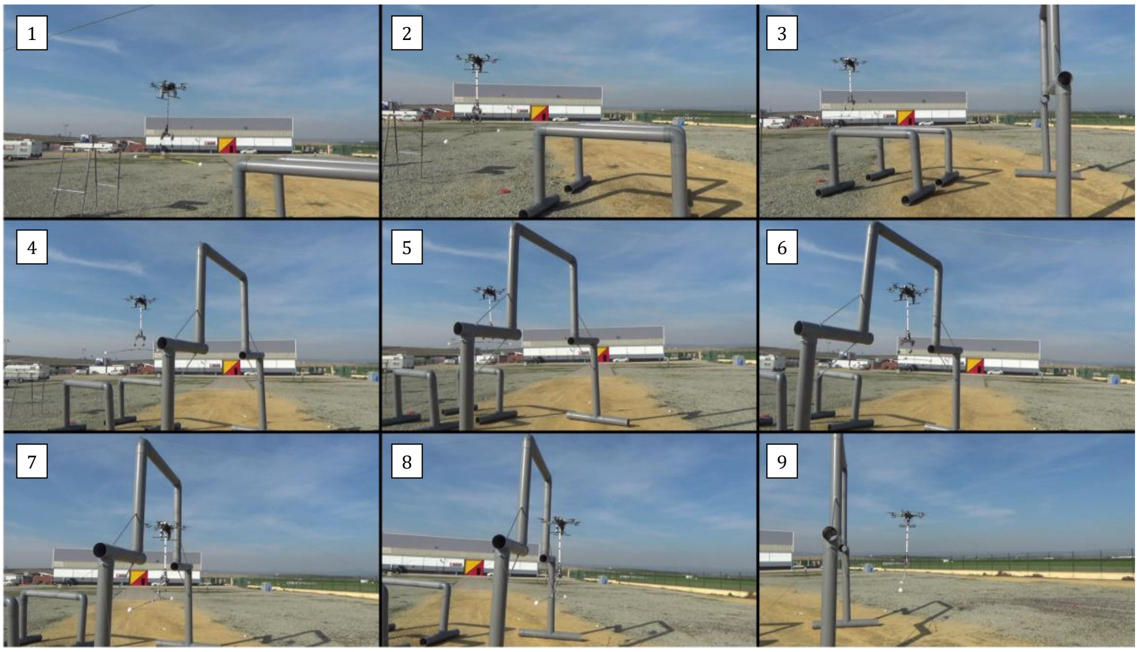

Figure 6.37. Transportation operation performed by the long reach aerial manipulator with compliant dual arm. Sequence of images taken from the ground camera.

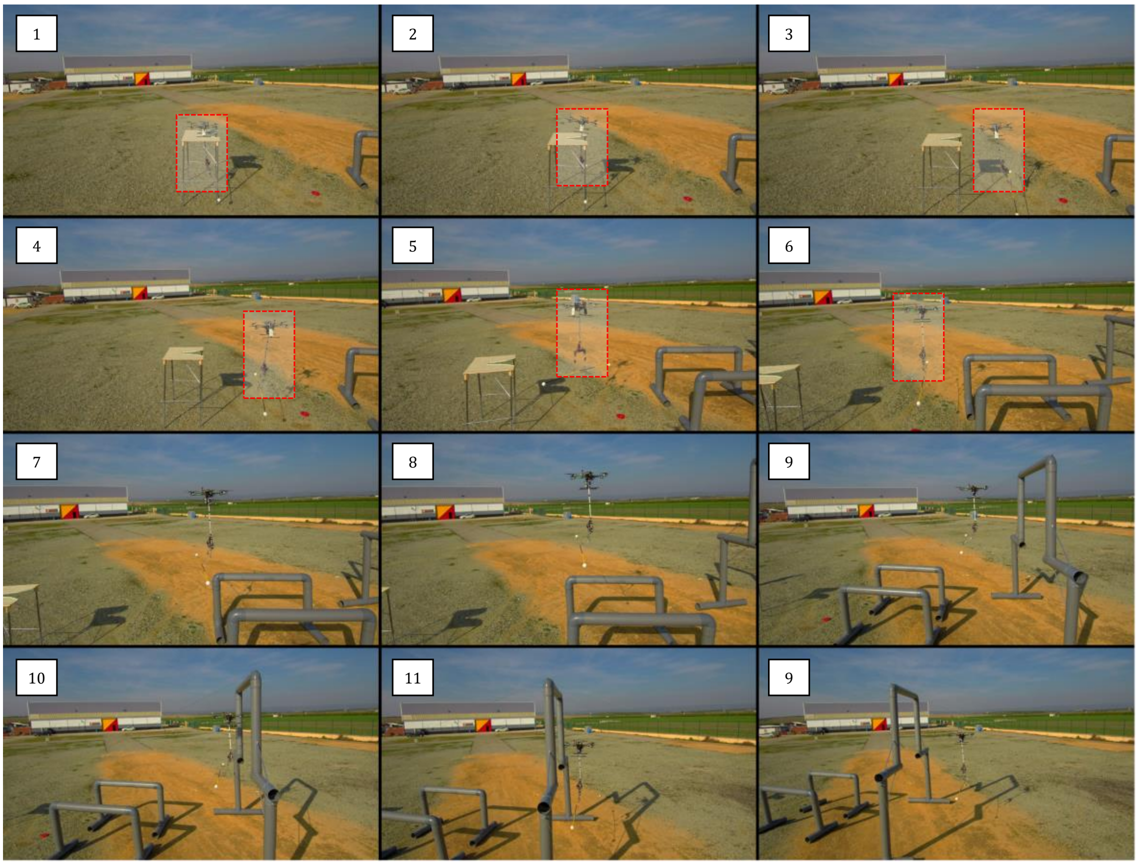

Figure 6.38. Sequence of images of the long reach aerial manipulator taken from the DJI Phantom 3 camera.

6.4.2. Sensor installation based on contact force control with long reach, dual arm aerial manipulator

This section demonstrates the application of the contact force control scheme based on Cartesian deflection described in **Section 4.7.2.4** in a sensor installation task carried out by the compliant joint aerial manipulator depicted in **Figure 6.39**. In this setup, denoted as passive pendulum configuration, the dual arm system is attached at the tip of a pair of long reach aluminium links (0.5 m length) supported by four igus® flange bearings, allowing the free rotation of the links with respect to the multirotor base. With this, the effective workspace of the manipulator, usually constrained by the landing gear, is extended, improving also safety during the physical interactions on flight. In fact, the contact forces exerted at the manipulator are transmitted to the aerial platform as a force in the XZ local axes, not as a torque, thanks to the passive joint located at the base of the pendulum (in the Y-axis), similarly to a load suspended from a wire attached at the UAV base. Note that the application of a pushing force in the forward direction will cause a recoil motion in the passive joint, reaching the equilibrium of forces when the force generated by the arm compensates the torque due to gravity in the passive joint. The lateral deflection of the flexible long reach links (Y-axis) also contributes to maintain the center of mass aligned in a passive way. In any case, experimental results evidence that the performance of the manipulator is not significantly affected by the passive joint during the manipulation phases. Also the separation distance between the blades of the multirotor and the obstacles in the workspace is higher, and thus the reaction time to prevent collision. The flight tests also reveal that the natural damping of the system tends to attenuate quickly the oscillation generated during the take-off phase or due to translational accelerations in the aerial platform.

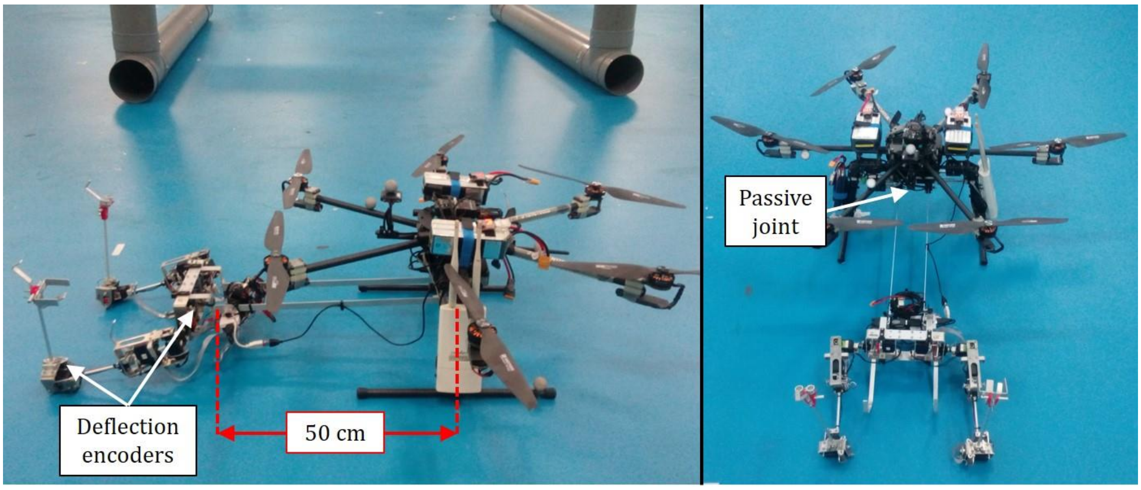

Figure 6.39. Dual arm aerial manipulator in passive pendulum configuration used in the sensor installation task. The left arm integrates magnetic encoders for estimating the contact forces in terms of joint deflection.

The anthropomorphic, compliant and lightweight dual arm employed in the experiments provides four joints per arm for end effector positioning (three at the shoulder and one at the elbow). In this experiment the shoulder pitch and elbow pitch joints integrate the magnetic encoders for measuring the joint deflection. The angular position reference of the shoulder roll and yaw joints was set to zero, although the deflection of these contributed to maintain the contact despite the displacement of the aerial platform around the operation position.

The execution of the experiment can be followed in **Figure 6.40**, **Figure 6.41**, and **Figure 6.42**. The take-off, approaching, positioning and landing operations were conducted by an expert human pilot in coordination with the operator of the arms, since the long reach manipulator requires special care in some phases. The contact force control task starts at t = 110 s and it ends at t = 135 s. The force reference is controlled by the operator through the 6-DOF mouse, imposing a maximum force of 2N on each axis to prevent that the servos exceed their maximum torque. The evolution of the contact force exerted by the left arm, the joint variables and the Cartesian stiffness can be observed in **Figure 6.40**. A 2N pushing force is applied in the X-axis to paste the sensor device into the pipe, maintaining a zero force reference in the Z axis. The joints involved are the shoulder pitch and elbow pitch, although the passive deflection of the shoulder roll and yaw joints contributes to compensate the deviations in the position of the UAV during the contact phase.

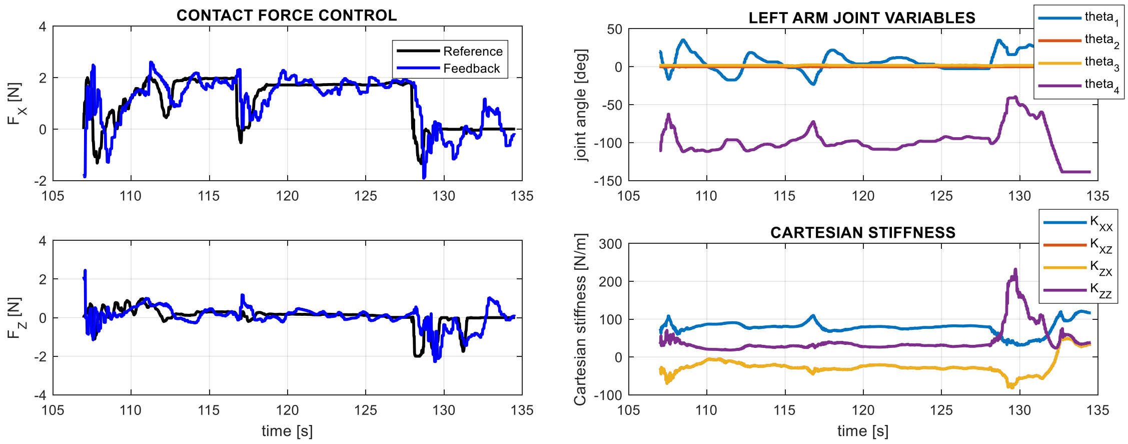

Figure 6.40. Force reference and feedback (left), and joint angles and Cartesian stiffness on the left arm (right) during the application of the contact force.

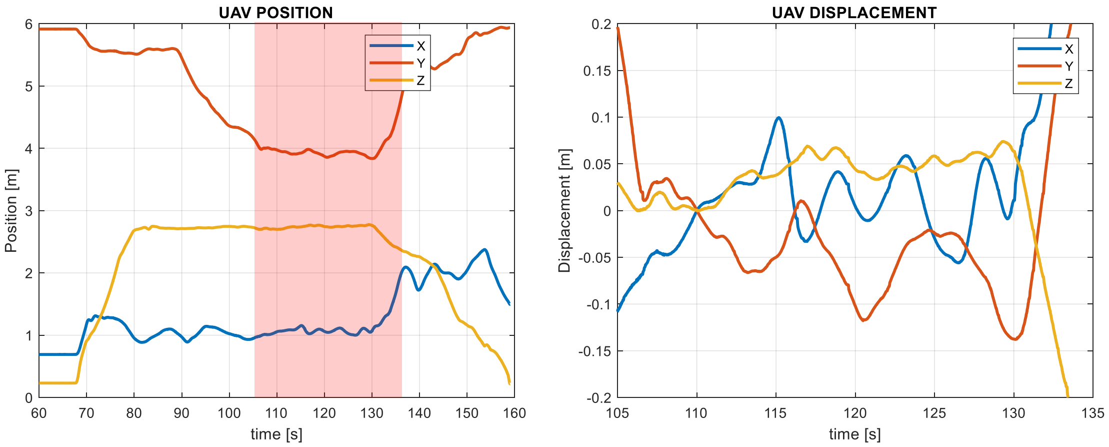

Figure 6.41. Hexarotor position (left) and displacement during the sensor installation operation (right).

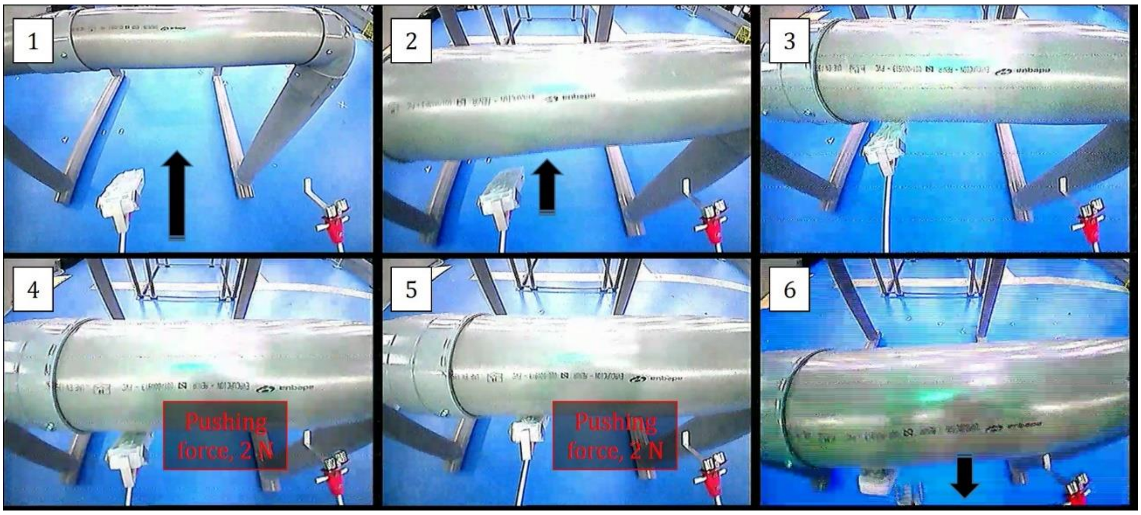

Figure 6.42. Installation of sensor on pipe applying a 2 N pushing force with the left arm. An adhesive tape located on the cage of the sensor maintains the device attached to the pipe. The pose of the arm (L-shaped configuration) results more favourable for the force controller since it is far from the kinematic singularities.

The ability to apply forces in Cartesian space depends on the angular position of the joints through the Jacobian matrix that relates joint torques with Cartesian forces and torques at the end effector. This is especially relevant in aerial manipulation, since the need of minimizing the weight of the arms leads to the use of lightweight servomotors with limited maximum torque. Thus, when the pose of the arm approaches to kinematic singularities (as for example close to the limits of the workspace) the maximum Cartesian forces that it can apply are reduced significantly. Furthermore, according to Equation **(4.72)**, the Cartesian stiffness matrix also depends on the Jacobian matrix of the arm. Then, the apparent stiffness of the compliant arm tends to infinity when the arm tends to reach the kinematic limit. Therefore, when working close to singularities, it is not possible to reach the desired force reference, as the servos are not capable to deliver enough torque, and the control of the forces gets more difficult as the stiffness increases. **Figure 6.43** shows another contact force control experiment, but this time the displacement of the aerial platform with respect to the contact point forced the left arm to adopt a pose close to the kinematic singularity, almost fully stretched. This can be seen clearly in **Figure 6.43**-3. The evolution of the Cartesian actual contact force and the reference are shown in **Figure 6.44** where it can be seen that the 2N reference force is not tracked.

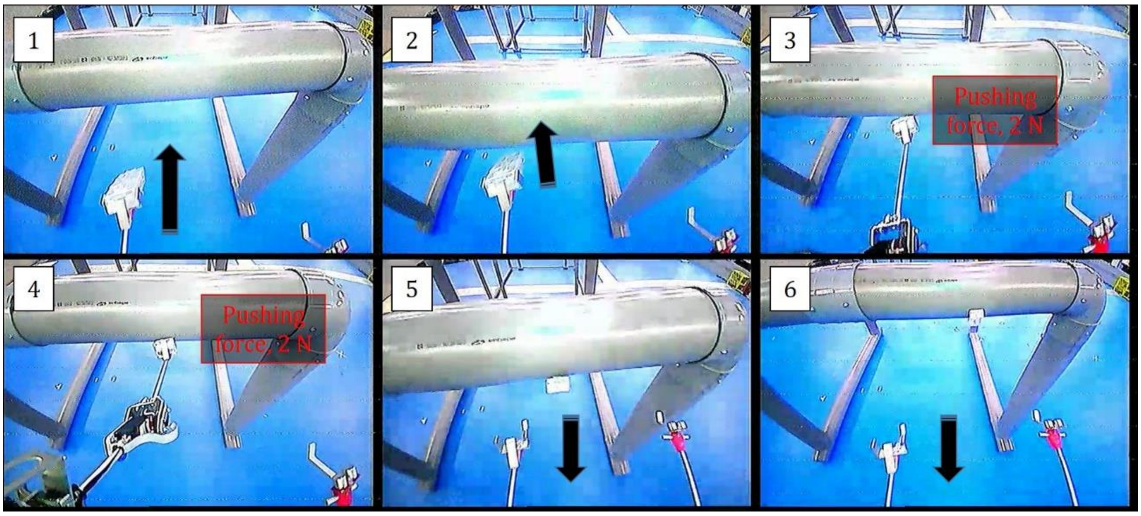

Figure 6.43. Sequence of images from the on-board camera corresponding to the second experiment of contact force control. As it can be seen in (3) and (4), the arm is almost fully stretched in the contact phase, so it is not possible to control accurately the force.

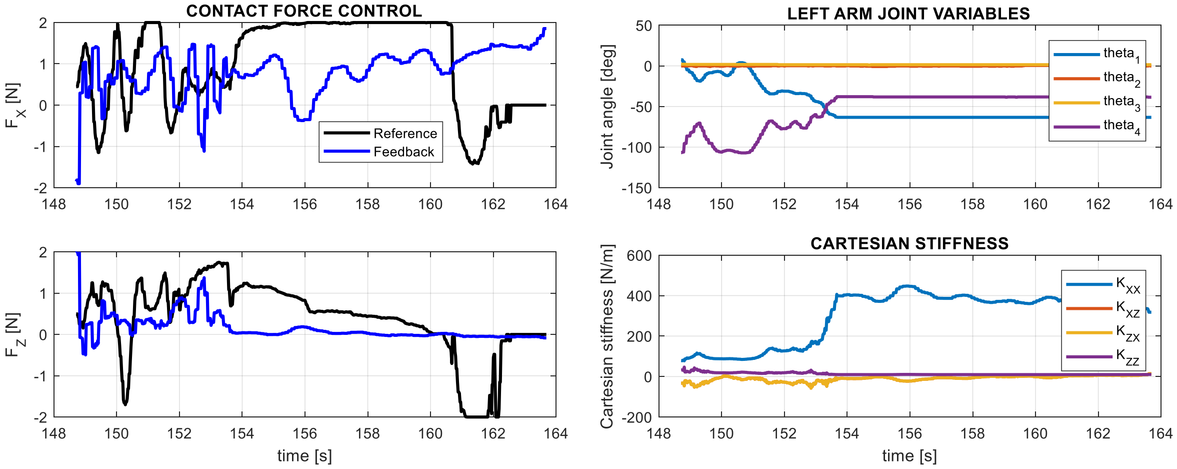

Figure 6.44. Force reference and feedback (left), joint variables and Cartesian stiffness (right) during the second contact force control experiment. Due to the displacement of the aerial platform w.r.t. the contact point, the left arm adopts a stretched pose close to the kinematic singularity, characterized by a high stiffness, so the servos are not capable to deliver the required torque.

6.5. Conclusion

This chapter has presented experimental results that validate the developed prototypes of dual arm aerial manipulators: stiff joint, anthropomorphic and compliant joint, and long reach manipulator in passive pendulum configuration. The performance of the manipulators has been evaluated in test-bench through different experiments, including trajectory tracking, visual servoing, identification of reaction wrenches over multirotor base, estimation and control of forces/torques, collision detection, obstacle localization, and frequency characterization. Indoor and outdoor flight tests were conducted with different hexarotor platforms, demonstrating bimanual object grasping, the installation of sensor devices with contact force control, and the transportation of long bars in scenarios with obstacles.

Chapter 7 – Conclusion and future work

7.1. Conclusion

The aerial manipulation technology proposes the integration of one or multiple robotic arms in aerial platforms, typically multirotors or autonomous helicopters, allowing the realization of several operations and tasks in high altitude areas or in difficult access workspaces. The main motivation for its development is the reduction of the time, cost and resources typically involved in several industrial inspection and maintenance operations in different scenarios, such as chemical plants, wind turbines, power lines, or polluted areas. However, the limitations in the payload and flight time of the aerial platform, the dynamic coupling with the manipulator, the effect of the interaction forces on flight, and the operational requirements in terms of dexterity, accuracy and mechanical robustness are some of the current challenges that make this topic of interest in the robotics research field.

This thesis has presented the design, development and experimental validation of several prototypes of lightweight and compliant manipulators integrated in different multirotor platforms, showing their capabilities and functionalities in test bench and in flight tests, in both indoors and outdoors. The prototypes described in Chapter 2 include compliant grippers, compliant joint arms, stiff-joint dual arms, anthropomorphic and compliant dual arms, and long reach manipulators, either single or dual arm. Since most commercially available robotic manipulators are not suitable for their integration in multirotor platforms, this thesis proposed a new design and manufacturing methodology based on three main features: lightweight and robust aluminium frame structure, mechanical servo protection implemented with polymer flange bearings that isolate the actuators from overloads or impacts, and mechanical joint compliance, introducing a simple spring-lever transmission mechanism between the servo shaft and the output link. These features have contributed significantly to reduce the time and cost associated to repairs in both the manipulator and the aerial platform as consequence of impacts during the operation on flight (contactless to contact transitions), or in case of strong crashes due to some failure. It is interesting to highlight that no servo had to be replaced in the last three years of operation of the dual arm systems developed by the author (~200 flight experiments). The mean repair time for the strong crashes with the aerial manipulator (5 m height falls) was around 3 hours, affecting only to a few aluminium frame parts that could be replaced or repaired easily.

One of the main contributions of this work is the introduction of mechanical compliance in aerial manipulation, either at joint level with the spring-level transmission mechanism placed between the servo shaft and the output link, exploiting the flexibility of the link, or considering a passive joint as in the long reach aerial manipulator in pendulum configuration. Since it is expected that the aerial manipulator operates in contact with the environment, it is necessary to reduce the influence of the interaction forces and the motion constraints raised during the operation on flight over the multirotor platform, preventing also that the manipulator is damaged. Note that the transition from contactless to contact in a grasping task can be assimilated to an impact whose energy depends on the kinetic and potential energy of the whole system, whereas the lack of coordination in bimanual operations in closed kinematic chain may generate overloads in the actuators. Thus, mechanical compliance provides a certain level of tolerance to peak forces and overloads in a passive way and at higher rates than the actuators may provide, increasing safety and robustness during the operation on flight. What is more, despite the evident limitations of the servos employed for building the arms (only position control, no torque feedback or control), the capabilities of these actuators are extended introducing a compliant transmission mechanism and measuring its deflection, that is, the deviation in its position due to the action of external forces or the acceleration of the links. By doing this, it is possible to estimate and control the torques and forces acting over the manipulator, estimate the weight of the grasped objects, monitor the interaction forces exerted in grabbing situations to prevent overloads, detect impacts by contact in a safe way, or even localize obstacles.

A compliant joint manipulator presents two main drawbacks compared to a stiff-joint arm. Firstly, the positioning accuracy at the end effector is typically lower if the joint deflection is not measured and compensated properly. It was found that, not only the gravity but also the airflow generated by the propellers causes a certain deviation in the position of the tool center point that should be taken into account. This effect complicates in practice the execution of certain tasks like grasping, requiring the integration of accurate deflection sensors in the joints or well the use of vision sensors that measure directly the position of the end effector as well as the grasping points. Actually the concept of Cartesian deflection/stiffness raised from the idea of measuring the deviation in the position of the end effector with respect to an equivalent stiff-joint manipulator, allowing the definition of the contact force control task directly in the Cartesian space. It was found during the realization of the multiple grasping experiments on flight that the positioning accuracy is probably the most difficult requirement to achieve, since it depends on the accuracy of the position sensor used by the aerial platform, the performance of its controller, and on the accuracy of each of the joints of the arms, which is affected by unavoidable manufacturing/assembly errors and by the deflection of the joints. Secondly, the dynamic behaviour of a compliant joint manipulator is more complex as the state of the joint is characterized by two variables (the servo shaft angular position and the output link angular position), and due to the underdamped second order dynamics that characterizes the deflection angle, which may cause undesired oscillations due to dynamic coupling with other joints or with the aerial platform. Therefore, the dynamic modelling and control is more complex. Note for example that the vector of generalized coordinates in the anthropomorphic and compliant dual arm aerial manipulator has dimension twenty two. In any case, the benefits of the mechanical joint-link compliance in aerial manipulation have been evidenced in different flight tests involving physical interactions.

Different control schemes have been proposed for the compliant aerial manipulators presented in this thesis. The general scheme considers three functional blocks (the aerial platform controller, the manipulator controller, and the wrench estimator) and two operation modes (position/force control) associated to contactless/contact situations involved during the realization of an aerial manipulation task. The transition between these two states can be easily detected monitoring the deflection of the joints or flexible links. According to the approach adopted in this work, the multirotor is considered as a mobile platform that must ensure the accurate positioning of the manipulator with respect to the workspace, compensating the reaction wrenches caused by the motion of the arms or the contact forces exerted at the end effector so the manipulation operation is not significantly affected. The idea is that the arms can operate as if they were in fixed base.

7.2. Future work

The motivation in the development of the aerial manipulation technology is clearly practical, since it is expected that in a near future these robots are capable to execute inspection and maintenance tasks in high altitude or difficult access workspaces in different industrial and civil scenarios. However this involves a level of integration, accuracy, reliability, robustness and safety in all the components of the system, including the manipulator, the aerial platform, the perception and the control system, which has not been achieved yet. Although the use of drones nowadays is quite extended due to their application in aerial photography and filming and due to the raise of manufacturers providing a wide variety of commercial platforms with different payloads and features, these have to be customized to integrate a robotic manipulator, and in most cases the control system is closed, so both components have to operate independently. Therefore, it is desirable that the manufacturers provide normalized interfaces for assembling and connecting the manipulator with the drone, allowing for example the estimation and compensation of the reaction wrenches. One of the main technological problems in aerial manipulation is the accurate position control of the robot during manipulation phase when this is operating close to obstacles and the risk of crashes is high, especially in outdoors, where the aerial vehicle may be affected by wind perturbations and there is not a position sensor suitable in all the cases. In this sense, the accurate position estimation and control of the aerial platform is essential in the realization of any manipulation operation on flight.

The current limitations of the servo actuators typically employed in most lightweight manipulators to be integrated in multirotor platforms motivates the development of new actuators whose features are similar to the industrial manipulators (control rates above 1 kHz, accurate torque/impedance and position control, high robustness and reliability), but with a very lightweight and high torque. These actuators should provide maximum dynamic torques around 10 N·m at angular speeds around 60 RPM, with a weight below 250 grams. The introduction of elastic elements between the actuator and the output link is still convenient since the experience derived from the realization of multiple flight tests evidences the benefits of mechanical compliance in aerial manipulation. The refinement of the manufacturing methodology of lightweight and compliant manipulators designed for their integration in aerial platforms is the next step towards the application of this technology in real scenarios.

References

[1] S. Kim, S. Choi and H. J. Kim. Aerial manipulation using a quadrotor with a two DOF robotic arm, *2013 IEEE/RSJ International Conference on Intelligent Robots and Systems*, Tokyo, 2013, pp. 4990-4995.

[2] C. D. Bellicoso, L. R. Buonocore, V. Lippiello and B. Siciliano. Design, modeling and control of a 5-DoF light-weight robot arm for aerial manipulation, *2015 23rd Mediterranean Conference on Control and Automation (MED)*, Torremolinos, 2015, pp. 853-858.

[3] A. E. Jimenez-Cano, J. Martin, G. Heredia, A. Ollero and R. Cano. Control of an aerial robot with multi-link arm for assembly tasks, *2013 IEEE International Conference on Robotics and Automation*, Karlsruhe, 2013, pp. 4916-4921.

[4] M. Kamel, K. Alexis, and R. Siegwart. Design and modelling of dexterous aerial manipulator. In IEEE/RSJ International Conferene on Intelligent Robots and Systems, 2016, pp. 4870-4876.

[5] M. Orsag, C. Korpela, S. Bogdan and P. Oh. Valve turning using a dual-arm aerial manipulator, *2014 International Conference on Unmanned Aircraft Systems (ICUAS)*, Orlando, FL, 2014, pp. 836-841.

[6] ProDrone Webpage: https://www.prodrone.jp/en/archives/1420/

[7] A. Suarez, A. E. Jimenez-Cano, V. M. Vega, G. Heredia, A. Rodriguez-Castaño, and A. Ollero. Design of a lightweight dual arm system for aerial manipulation. In Mechatronics, Vol. 50, 2018, pp. 30-44.

[8] A. Suarez, G. Heredia and A. Ollero, Design of an Anthropomorphic, Compliant and Lightweight Dual Arm for Aerial Manipulation, in *IEEE Access*. doi: 10.1109/ACCESS.2018.2833160

[9] A. Suarez, A. M. Giordano, K. Kondak, G. Heredia, and A. Ollero. Flexible link long reach manipulator with lightweight dual arm: soft-collision detection, reaction, and obstacle localization. In IEEE-RAS International Conference on Soft Robotics, 2018.

[10] A. Suarez, P. Sanchez-Cuevas, M. Fernandez, M. Perez, G. Heredia, and A. Ollero. Lightweight and compliant long reach aerial manipulator for contact-based inspection. In *2018 IEEE/RSJ International Conference on Intelligent Robots and Systems (IROS)*.

[11] V. Ghadiok, J. Goldin and W. Ren. Autonomous indoor aerial gripping using a quadrotor, *2011 IEEE/RSJ International Conference on Intelligent Robots and Systems*, San Francisco, CA, 2011, pp. 4645-4651.

[12] D. Mellinger, Q. Lindsey, M. Shomin, and V. Kumar. Design, modelling, estimation and control for aerial grasping and manipulation. In *2011 IEEE/RSJ International Conference on Intelligent Robots and Systems (IROS)*, pp. 2668-2673.

[13] P. E. Pounds, D. E. Bersak, A. M. Dollar. The yale aerial manipulator: grasping in flight. In IEEE International Conference on Robotics and Automation, 2011, pp. 2974-2975.

[14] M. Fumagalli, R. Naldi, A. Macchelli, F. Forte, A. Q. Keemink, S. Stramigioli, L. Marconi. Developing an aerial manipulator prototype: physical interaction with the environment. IEEE robotics & automation magazine, 2014, 21(3), 41-50.

[15] K. Steich, M. Kamel, P. Beardsley, M. K. Obrist, R. Siegwart, and T. Lachat. Tree cavity inspection using aerial robots. In IEEE/RSJ International Conference on Intelligent Robots and Systems, 2016, pp. 4856-4862.

[16] H. N. Nguyen, S. Park, and D. Lee. Aerial tool operation system using quadrotors and rotation thrust generators. In IEEE/RSJ Intelligent Robots and Systems (IROS), 2015, pp. 1285-1291.

[17] M. Zhao, K. Kawasaki, K. Okada, and M. Inaba. Transformable multirotor with two-dimensional multilinks: modelling, control and motion planning for aerial transformation. In Advanced Robotics, 2016, 30(13), 825-845.

[18] A. Suarez, P. Ramon-Soria, G. Heredia, G., B. C. Arrue, and A. Ollero. Anthropomorphic, compliant and lightweight dual arm system for aerial manipulation, *2017 IEEE/RSJ International Conference on Intelligent Robots and Systems (IROS)*, Vancouver, 2017.

[19] S. Rajappa, M. Ryll, H. H. Bülthoff and A. Franchi, "Modeling, control and design optimization for a fully-actuated hexarotor aerial vehicle with tilted propellers," *2015 IEEE International Conference on Robotics and Automation (ICRA)*, Seattle, WA, 2015, pp. 4006-4013.

[20] M. Ryll, D. Bicego and A. Franchi, "Modeling and control of FAST-Hex: A fully-actuated by synchronized-tilting hexarotor," *2016 IEEE/RSJ International Conference on Intelligent Robots and Systems (IROS)*, Daejeon, 2016, pp. 1689-1694.

[21] M. Ryll *et al*., "6D physical interaction with a fully actuated aerial robot," *2017 IEEE International Conference on Robotics and Automation (ICRA)*, Singapore, 2017, pp. 5190-5195.

[22] K. Kondak *et al*., "Aerial manipulation robot composed of an autonomous helicopter and a 7 degrees of freedom industrial manipulator," *2014 IEEE International Conference on Robotics and Automation (ICRA)*, Hong Kong, 2014, pp. 2107-2112.

[23] G. Heredia *et al*., "Control of a multirotor outdoor aerial manipulator," *2014 IEEE/RSJ International Conference on Intelligent Robots and Systems*, Chicago, IL, 2014, pp. 3417-3422.

[24] A. Briod, P. Kornatowski, J. C. Zufferey, and D. Floreano, "A Collision-resilient Flying Robot," in *Journal of Field Robotics*, vol. *31*, no 4, pp. 496-509, 2014.

[25] P. E. I. Pounds and W. Deer, "The Safety Rotor—An Electromechanical Rotor Safety System for Drones," in *IEEE Robotics and Automation Letters*, vol. 3, no. 3, pp. 2561-2568, July 2018.

[26] B. Yüksel, S. Mahboubi, C. Secchi, H. H. Bülthoff and A. Franchi, "Design, identification and experimental testing of a light-weight flexible-joint arm for aerial physical interaction," *2015 IEEE International Conference on Robotics and Automation (ICRA)*, Seattle, WA, 2015, pp. 870-87.

[27] A. Suarez, G. Heredia and A. Ollero, "Lightweight compliant arm with compliant finger for aerial manipulation and inspection," *2016 IEEE/RSJ International Conference on Intelligent Robots and Systems (IROS)*, Daejeon, 2016, pp. 4449-4454.

[28] R. Cano, C. Pérez, F. Pruano, A. Ollero, and G. Heredia, "Mechanical design of a 6-DOF aerial manipulator for assembling structures using UAVs", in 2nd RED-UAS 2013 workshop on research, education and development of unmanned aerial systems.

[29] S. Siebert and J. Teizer, Mobile 3D mapping for surveying earthwork projects using an Unmanned Aerial Vehicle (UAV) system, in Automation in Construction, vol. 41, 2014, pp. 1-14.

[30] J. M. Daly, M. Yan, and L. W. Steven, "Coordinated landing of a quadrotor on a skid-steered ground vehicle in the presence of time delays," in Autonomous Robots, vol. 38 (2), 2015, pp. 179-191.

[31] M. Blösch, S. Weiss, D. Scaramuzza and R. Siegwart, "Vision based MAV navigation in unknown and unstructured environments," *2010 IEEE International Conference on Robotics and Automation*, Anchorage, AK, 2010, pp. 21-28.

[32] M. Faessler, F. Fontana, C. Forster, E. Mueggler, M. Pizzoli, and D. Scaramuzza, "Autonomous, Vision-based Flight and Live Dense 3D Mapping with a Quadrotor Micro Aerial Vehicle," in *Journal of Field Robotics*, 2016, vol. *33*(4), pp. 431-450.

[33] F. Fraundorfer *et al*., "Vision-based autonomous mapping and exploration using a quadrotor MAV," *2012 IEEE/RSJ International Conference on Intelligent Robots and Systems*, Vilamoura, 2012, pp. 4557-4564.

[34] K. Schmid, T. Tomic, F. Ruess, H. Hirschmüller and M. Suppa, "Stereo vision based indoor/outdoor navigation for flying robots," *2013 IEEE/RSJ International Conference on Intelligent Robots and Systems*, Tokyo, 2013, pp. 3955-3962.

[35] A. Torres-González, J. R. Martinez-de Dios and A. Ollero, "Accurate fast-mapping Range-Only SLAM for UAS applications," *2015 International Conference on Unmanned Aircraft Systems (ICUAS)*, Denver, CO, 2015, pp. 543-550.

[36] F. R. Fabresse, F. Caballero and A. Ollero, "Decentralized simultaneous localization and mapping for multiple aerial vehicles using range-only sensors," *2015 IEEE International Conference on Robotics and Automation (ICRA)*, Seattle, WA, 2015, pp. 6408-6414.

[37] D. Honegger, L. Meier, P. Tanskanen and M. Pollefeys, "An open source and open hardware embedded metric optical flow CMOS camera for indoor and outdoor applications," *2013 IEEE International Conference on Robotics and Automation*, Karlsruhe, 2013, pp. 1736-1741.

[38] M. B. Rhudy, H. Chao and Y. Gu, "Wide-field optical flow aided inertial navigation for unmanned aerial vehicles," *2014 IEEE/RSJ International Conference on Intelligent Robots and Systems*, Chicago, IL, 2014, pp. 674-679.

[39] V. Grabe, H. H. Bülthoff and P. R. Giordano, "On-board velocity estimation and closed-loop control of a quadrotor UAV based on optical flow," *2012 IEEE International Conference on Robotics and Automation*, Saint Paul, MN, 2012, pp. 491-497.

[40] M. Achtelik, A. Bachrach, R. He, S. Prentice, and N. Roy, "Stereo vision and laser odometry for autonomous helicopters in GPS-denied indoor environments," in *Unmanned Systems Technology XI* (Vol. 7332, p. 733219), 2009. International Society for Optics and Photonics.

[41] S. Huh, D. H. Shim and J. Kim, "Integrated navigation system using camera and gimbaled laser scanner for indoor and outdoor autonomous flight of UAVs," *2013 IEEE/RSJ International Conference on Intelligent Robots and Systems*, Tokyo, 2013, pp. 3158-3163.

[42] Y. Song, B. Xian, Y. Zhang, X. Jiang, and X. Zhang, "Towards autonomous control of quadrotor unmanned aerial vehicles in a GPS-denied urban area via laser ranger finder," in *Optik-International Journal for Light and Electron Optics*, 2015, vol. *126* (23), pp. 3877-3882.

[43] F. Ruggiero, J. Cacace, H. Sadeghian and V. Lippiello. Impedance control of VToL UAVs with a momentum-based external generalized forces estimator, *2014 IEEE International Conference on Robotics and Automation (ICRA)*, Hong Kong, 2014, pp. 2093-2099.

[44] T. Tomić and S. Haddadin. A unified framework for external wrench estimation, interaction control and collision reflexes for flying robots, *2014 IEEE/RSJ International Conference on Intelligent Robots and Systems*, Chicago, IL, 2014, pp. 4197-4204.

[45] S. Waslander, and C. Wang, "Wind disturbance estimation and rejection for quadrotor position control," in *AIAA Infotech@ Aerospace Conference and AIAA Unmanned, 2009... Unlimited Conference* (p. 1983).

[46] J. Escareño, S. Salazar, H. Romero, and R. Lozano, "Trajectory control of a quadrotor subject to 2D wind disturbances," in *Journal of Intelligent & Robotic Systems*, 2013, vol. *70*(1-4), pp. 51-63.

[47] N. Sydney, B. Smyth and D. A. Paley, "Dynamic control of autonomous quadrotor flight in an estimated wind field," *52nd IEEE Conference on Decision and Control*, Firenze, 2013, pp. 3609-3616.

[48] G. Arleo, F. Caccavale, G. Muscio and F. Pierri, "Control of quadrotor aerial vehicles equipped with a robotic arm," *21st Mediterranean Conference on Control and Automation*, Chania, 2013, pp. 1174-1180.

[49] K. Kondak et al, "Closed-loop behavior of an autonomous helicopter equipped with a robotic arm for aerial manipulation tasks," in *International Journal of Advanced Robotic Systems*, 2013, vol. 10(2), 145.

[50] H. Yang and D. Lee, "Dynamics and control of quadrotor with robotic manipulator," *2014 IEEE International Conference on Robotics and Automation (ICRA)*, Hong Kong, 2014, pp. 5544-5549.

[51] P. E. I. Pounds and A. M. Dollar. Stability of Helicopters in Compliant Contact Under PD-PID Control, in *IEEE Transactions on Robotics*, vol. 30, no. 6, pp. 1472-1486, Dec. 2014.

[52] G. Giglio and F. Pierri. Selective compliance control for an unmanned aerial vehicle with a robotic arm, *22nd Mediterranean Conference on Control and Automation*, Palermo, 2014, pp. 1190-1195.

[53] M. Fumagalli *et al*., "Developing an Aerial Manipulator Prototype: Physical Interaction with the Environment," in *IEEE Robotics & Automation Magazine*, vol. 21, no. 3, pp. 41-50, Sept. 2014.

[54] E. Cataldi *et al*., "Impedance Control of an aerial-manipulator: Preliminary results," *2016 IEEE/RSJ International Conference on Intelligent Robots and Systems (IROS)*, Daejeon, 2016, pp. 3848-3853.

[55] F. Forte, R. Naldi, A. Macchelli and L. Marconi, "Impedance control of an aerial manipulator," *2012 American Control Conference (ACC)*, Montreal, QC, 2012, pp. 3839-3844.

[56] T. Bartelds, A. Capra, S. Hamaza, S. Stramigioli and M. Fumagalli, "Compliant Aerial Manipulators: Toward a New Generation of Aerial Robotic Workers," in *IEEE Robotics and Automation Letters*, vol. 1, no. 1, pp. 477-483, Jan. 2016.

[57] A. Suarez, G. Heredia and A. Ollero, "Physical-Virtual Impedance Control in Ultralightweight and Compliant Dual-Arm Aerial Manipulators," in *IEEE Robotics and Automation Letters*, vol. 3, no. 3, pp. 2553-2560, July 2018.

[58] D. W. Robinson, J. E. Pratt, D. J. Paluska and G. A. Pratt, "Series elastic actuator development for a biomimetic walking robot," *1999 IEEE/ASME International Conference on Advanced Intelligent Mechatronics (Cat. No.99TH8399)*, Atlanta, GA, USA, 1999, pp. 561-568. doi: 10.1109/AIM.1999.803231.

[59] J. Pratt, B. Krupp, and C. Morse, "Series elastic actuators for high fidelity force control," 2002 Industrial Robot: An International Journal, 29(3), 234-241.

[60] B. Vanderborght, A. Albu-Schäffer, A. Bicchi, E. Burdet, D. G. Caldwell, R. Carloni, R., ... and M. Garabini, "Variable impedance actuators: A review," in *Robotics and autonomous systems*, 2013, vol. *61*(12), pp. 1601-1614.

[61] R. Schiavi, G. Grioli, S. Sen and A. Bicchi, "VSA-II: a novel prototype of variable stiffness actuator for safe and performing robots interacting with humans," *2008 IEEE International Conference on Robotics and Automation*, Pasadena, CA, 2008, pp. 2171-2176.

[62] G. Tonietti, R. Schiavi and A. Bicchi, "Design and Control of a Variable Stiffness Actuator for Safe and Fast Physical Human/Robot Interaction," *Proceedings of the 2005 IEEE International Conference on Robotics and Automation*, 2005, pp. 526-531.

[63] F. Petit, M. Chalon, W. Friedl, M. Grebenstein, A. Albu-Schäffer and G. Hirzinger, "Bidirectional antagonistic variable stiffness actuation: Analysis, design & Implementation," *2010 IEEE International Conference on Robotics and Automation*, Anchorage, AK, 2010, pp. 4189-4196.

[64] S. Wolf and G. Hirzinger, "A new variable stiffness design: Matching requirements of the next robot generation," *2008 IEEE International Conference on Robotics and Automation*, Pasadena, CA, 2008, pp. 1741-1746.

[65] N. G. Tsagarakis, I. Sardellitti and D. G. Caldwell, "A new variable stiffness actuator (CompAct-VSA): Design and modelling," *2011 IEEE/RSJ International Conference on Intelligent Robots and Systems*, San Francisco, CA, 2011, pp. 378-383.

[66] B. S. Kim and J. B. Song, "Hybrid dual actuator unit: A design of a variable stiffness actuator based on an adjustable moment arm mechanism," *2010 IEEE International Conference on Robotics and Automation*, Anchorage, AK, 2010, pp. 1655-1660.

[67] K. Yoshida, R. Kurazume and Y. Umetani. Dual arm coordination in space free-flying robot, *Proceedings. 1991 IEEE International Conference on Robotics and Automation*, Sacramento, CA, 1991, pp. 2516-2521 vol.3.

[68] K. Yoshida, R. Kurazume and Y. Umetani. Torque optimization control in space robots with a redundant arm, *Intelligent Robots and Systems '91. 'Intelligence for Mechanical Systems, Proceedings IROS '91. IEEE/RSJ International Workshop on*, Osaka, 1991, pp. 1647-1652 vol.3.

[69] X. U. Wen-Fu, W. A. N. G. Xue-Qian, X. U. E. Qiang, and B. Liang. Study on trajectory planning of dual-arm space robot keeping the base stabilized. 2013, Acta Automatica Sinica, 39(1), 69-80.

[70] M. Yamano, J. S. Kim, A. Konno, and M. Uchiyama. Cooperative control of a 3d dual-flexible-arm robot. Journal of Intelligent and Robotic Systems, 39(1), 1-15, 2004.

[71] C. Ott, O. Eiberger, W. Friedl, B. Bäuml, U. Hillenbrand, C. Borst, C., ... and R. Konietschke. A Humanoid Two-Arm System for Dexterous Manipulation, *2006 6th IEEE-RAS International Conference on Humanoid Robots*, Genova, 2006, pp. 276-283.

[72] F. Caccavale, P. Chiacchio, A. Marino and L. Villani. Six-DOF Impedance Control of Dual-Arm Cooperative Manipulators, in *IEEE/ASME Transactions on Mechatronics*, vol. 13, no. 5, pp. 576-586, Oct. 2008.

[73] R. C. Luo, B. H. Shih and T. W. Lin. Real time human motion imitation of anthropomorphic dual arm robot based on Cartesian impedance control, *2013 IEEE International Symposium on Robotic and Sensors Environments (ROSE)*, Washington, DC, 2013, pp. 25-30.

[74] C. Smith, Y. Karayiannidis, L. Nalpantidis, X. Gratal, P. Qi, D. v. Dimarogonas, and D. Kragic. Dual arm manipulation—A survey. Robotics and Autonomous systems, 60(10), 1340-1353, 2012.

[75] A. Gouo, D. N. Nenchev, K. Yoshida, and M. Uchiyama, “Motion control of dual-arm long-reach manipulators,” in Advanced Robotics, 1998, vol. 13(6), pp. 617-631.

[76] X. Yu, and L. Chen, “Dynamic modeling and control of a free-flying space robot with flexible-link and flexible-joints,” in IEEE 2014 Inter. Conference on Robotics and Automation (ICRA) (pp. 6625-6630).

[77] C. Mavroidis, S. Dubowsky, and V. Raju, “End-point control of long reach manipulator systems,” in Proc. 9th World Congr. IFToMM, pp. 1740-1744, 1995.

[78] D. W. Gu, P. Petkov, and M. M. Konstantinov, “Robust control design with MATLAB®,” in Springer Science & Business Media, 2005.

[79] K. Yoshida, C. Mavroidis, and S. Dubowsky, “Impact dynamics of space long reach manipulators,” in Robotics and Automation, 1996. Proceedings, IEEE Int. Conf. on (Vol. 2, pp. 1909-1916).

[80] A. Gouo, D. N. Nenchev, K. Yoshida, and M. Uchiyama, “Dual-arm long-reach manipulators: Noncontact motion control strategies,” inn Intelligent Robots and Systems, 1998. Proceedings., 1998 IEEE/RSJ Int. Conf. on (Vol. 1, pp. 449-454).

[81] J. Malzahn, A. S. Phung, F. Hoffmann, and T. Bertram, “Vibration control of a multi-flexible-link robot arm under gravity,” in Robotics and Biomimetics (ROBIO), 2011 IEEE International Conference on (pp. 1249-1254).

[82] F. Petit, C. Ott, and A. Albu-Schaeffer, “A model-free approach to vibration suppression for intrinsically elastic robots,” in 2014 IEEE Int. Conference on Robotics and Automation (ICRA) (pp. 2176-2182).

[83] P. C. Tang, H. C. Wang, and S. S. Lu, “A vision-based position control system for a one link flexible arm,” in Journal of the Chinese Institute of Engineers, 1995, vol. 18(4), pp. 565-573.

[84] X. Jiang, A. Konno, and M. Uchiyama, “A vision-based endpoint trajectory and vibration control for flexible manipulators,” in Proc. 2007 IEEE Int. Conf. on Robotics and Automation (pp. 3427-3432).

[85] M. Manubens, D. Devaurs, L. Ros and J. Cortés, “Motion planning for 6-D manipulation with aerial towed-cable systems,” in *Robotics: Science and Systems (RSS)*, Berlin, Germany, 2013

[86] H-N. Nguyen, S. Park, J. Park, and D. J. Lee, “A novel robotic platform for aerial manipulation using quadrotors as rotating thrust generators”. *IEEE Transactions on Robotics*, in press, 2018.

[87] A. Suarez, G. Heredia, and A. Ollero, “Vision-based deflection estimation in an anthropomorphic, compliant and lightweight dual arm”, in Robot 2017: Third Iberian Robotics Conference, vol. 2, pp. 332.344 (2018).

[88] A. Suarez, G. Heredia, and A. Ollero, "Lightweight compliant arm for aerial manipulation," *IEEE/RSJ International Conference on Intelligent Robots and Systems (IROS)*, Hamburg, 2015, pp. 1627-1632.

[89] A. Suarez, G. Heredia, and A. Ollero, “Compliant and lightweight anthropomorphic finger module for aerial manipulation and grasping,” in Robot 2015: Second Iberian Robotics Conference, pp. 543-555. Springer International Publishing.

[90] A. Suarez. G. Heredia, and A. Ollero, "Cooperative virtual sensor for fault detection and identification in multi-UAV applications, " in Journal of Sensors, vol. 2018, Article ID 4515828, 19 pages, 2018.

[91] A. Suarez, G. Heredia and A. Ollero, "Cooperative sensor fault recovery in multi-UAV systems," *2016 IEEE International Conference on Robotics and Automation (ICRA)*, Stockholm, 2016, pp. 1188-1193.

[92] A. Albu-Schäffer, C. Ott, and G. Hirzinger, “A unified passivity-based control framework for position, torque and impedance control of flexible joint robots,” in The International Journal of Robotics Research, 2007, vol. 26(1), pp. 23-39.

[93] C. Ott, “Cartesian Impedance Control of Redundant and Flexible-Joint Robots,” in Springer Tracts in Advanced Robotics, 2008.

[94] F. Ficuciello, L. Villani and B. Siciliano, "Variable Impedance Control of Redundant Manipulators for Intuitive Human–Robot Physical Interaction," in *IEEE Transactions on Robotics*, 2015, vol. 31, no. 4, pp. 850-863.

[95] A. Albu-Schaffer and G. Hirzinger, "Cartesian impedance control techniques for torque controlled light-weight robots," *Proceedings 2002 IEEE International Conference on Robotics and Automation (Cat. No.02CH37292)*, 2002, pp. 657-663 vol.1.

[96] A. Ajoudani, M. Gabiccini, N. G. Tsagarakis and A. Bicchi, "Human-like impedance and minimum effort control for natural and efficient manipulation," *2013 IEEE International Conference on Robotics and Automation*, Karlsruhe, 2013, pp. 4499-4505.

[97] V. Lippiello and F. Ruggiero, "Exploiting redundancy in Cartesian impedance control of UAVs equipped with a robotic arm," *2012 IEEE/RSJ International Conference on Intelligent Robots and Systems*, Vilamoura, 2012, pp. 3768-3773.